MULTISENSOR MICROWAVE REMOTE SENSING IN THE CRYOSPHERE

by

Quinn P. Remund

A dissertation submitted to the faculty of

Brigham Young University

in partial fulfillment of the requirements for the degree of

Doctor of Philosophy

Department of Electrical and Computer Engineering

Brigham Young University

August 2000

BRIGHAM YOUNG UNIVERSITY

GRADUATE COMMITTEE APPROVAL

of a dissertation submitted by

Quinn P. Remund

This dissertation has been read by each member of the following graduate committee and by majority vote has been found to be satisfactory.

Date	David G. Long, Chair
Date	David V. Arnold
Date	Brian D. Jeffs
Date	Michael A. Jensen
Date	A. Lee Swindlehurst

BRIGHAM YOUNG UNIVERSITY

As chair of the candidate's graduate committee, I have read the dissertation of Quinn P. Remund in its final form and have found that (1) its format, citations, and bibliographical style are consistent and acceptable and fulfill university and department style requirements; (2) its illustrative materials including figures, tables, and charts are in place; and (3) the final manuscript is satisfactory to the graduate committee and is ready for submission to the university library.

Date

David G. Long
Chair, Graduate Committee

Accepted for the Department

A. Lee Swindlehurst
Graduate Coordinator

Accepted for the College

Douglas M. Chabries
Dean, College of Engineering and Technology

ABSTRACT

MULTISENSOR MICROWAVE REMOTE SENSING IN THE CRYOSPHERE

Quinn P. Remund
Electrical and Computer Engineering
Doctor of Philosophy

Because the earth's cryosphere influences global weather patterns and climate, the scientific community has had great interest in monitoring this important region. Microwave remote sensing has proven to be a useful tool in estimating sea and glacial ice surface characteristics with both scatterometers and radiometers exhibiting high sensitivity to important ice properties. This dissertation presents an array of studies focused on extracting key surface features from multisensor microwave data sets. First, several enhanced resolution image reconstruction issues are addressed. Among these are the optimization of the scatterometer image reconstruction (SIR) algorithm for NASA scatterometer (NSCAT) data, an analysis of Ku-band azimuthal modulation in Antarctica, and inter-sensor European Remote Sensing Satellite (ERS) calibration. Next, various methods for the removal of atmospheric distortions in image reconstruction of passive radiometer observations are considered. An automated algorithm is proposed which determines the spatial extent of sea ice in the Arctic and Antarctic regions from NSCAT data. A multisensor iterative sea ice statistical classification method which adapts to the temporally varying signatures of ice types

is developed. The sea ice extent and classification algorithms are adopted for current SeaWinds scatterometer data sets. Finally, the automated inversion of large-scale forward electromagnetic scattering models is considered and used to study the temporal evolution of the scattering properties of polar sea ice.

ACKNOWLEDGMENTS

I am grateful to my advisor, Dr. David G. Long, for his countless hours of guidance and instruction. Over the past several years, he has been an excellent mentor and friend. I would also like to thank Dr. Mark Drinkwater of the Jet Propulsion Laboratory. His expertise in sea ice remote sensing was an invaluable resource in my research. Thanks also go to each member of my doctoral committee for their insightful guidance.

I am fortunate to be a part of a strong family. I express my gratitude to my parents for the many years of inspired direction. Finally, and most importantly, I am thankful for my wife Allison. Without her love and support I would not be where I am today.

Contents

List of Tables

List of Figures

Chapter 1

Introduction

In late 1914, Ernest Shackleton and his small crew of explorers, mariners, and scientists entered the Antarctic ice pack aboard the British vessel "The Endurance." Their objectives were simple. First and foremost, they sought to be the first explorers to ever cross the Antarctic continent on foot. In addition, they hoped to collect new and important scientific data to help the world better understand the last unconquered continent on earth. They soon learned, however, that the enormous Antarctic region is hostile and dangerous. Their ship was caught in the ice pack before even reaching the continent. The immense forces of giant ice floes grinding against one another crushed the Endurance leaving the men to fight for their lives with very little shelter or provisions. After struggling for survival for one and a half years, the men finally reached safety. Miraculously, all the men escaped the disaster alive.

Today, the advances of modern technology allow researchers to monitor the polar regions of the earth without enduring the trials of Shackleton and his crew. While *in situ* measurements still play an important role, satellite remote sensing has given scientists the ability to study these critical regimes on a very large scale with high observation frequency.

Perhaps the most valuable spaceborne sensors in studying polar sea ice are microwave radiometers and scatterometers. Among the earliest microwave radiometers, the Nimbus-5 Electronically Scanning Microwave Radiometer (ESMR) monitored the passive microwave emissions from sea ice and other surfaces. Later the Nimbus-7 Scanning Multichannel Microwave Radiometer (SMMR) added to the dataset of passive microwave observations of the earth. These instruments were later complimented by the Special Sensor Microwave Imager (SSM/I) series of sensors aboard Defense Meteorological Satellite Program (DMSP) platforms.

In contrast, active microwave scatterometers have not enjoyed such an extended period of uninterrupted remote observation. In 1978, the Seasat-A Scatterometer (SASS) was the first wide swath scatterometer to be launched. Though the instrument failed after only about three months in operation, it demonstrated the value of microwave scatterometer measurements of ocean, land, and sea ice. Several years later the Active Microwave Instrument (AMI) aboard the European Remote Sensing Satellite (ERS-1) continued the time series of scatterometer observations. ERS-1 was followed by the NASA scatterometer (NSCAT) aboard the ADEOS-I platform, ERS-2, and SeaWinds on QuikSCAT. A second SeaWinds instrument will be launched aboard ADEOS-II in late 2001.

Microwave instruments have an added advantage over optical and infrared sensors since the lower frequencies inherent to the microwave portion of the spectrum are much less sensitive to atmospheric distortions such as cloud cover and precipitation than optical or infrared instruments. This is a great benefit in regions with frequent cloud cover such as the Arctic and Antarctic. In addition, microwave sensors do not require solar illumination thus allowing them to operate effectively day or night. Since the polar regions experience months of complete darkness each year, this is another critical feature of polar remote sensing instruments.

For the past few decades, researchers have sought to extract critical information from data collected by microwave instruments. While a significant amount of effort has been expended in ocean and land surface studies, much less has occurred in the field of cryosphere remote sensing. This dissertation presents the development and analysis of several techniques and methodologies in inferring important geophysical parameters from observed microwave signatures.

1.1 The Importance of the Cryosphere in Global Geophysical Processes

The earth's cryosphere consists of the polar regions and ice-covered areas of the globe. For decades, scientists have had a keen interest in monitoring the properties of these areas due to their direct influence on short-term weather patterns, long-term climate change, and other important global geophysical processes. Perhaps the most critical factors in this system are the properties of sea and glacial ice. These two ice regimes modulate geophysical processes in many ways. First, they affect the global radiation budget. The typically high albedo of ice surfaces results in the reflection of a large amount of incident solar radiation back out into space. Thus, the extent and surface reflectivity of sea and glacial ice influence the amount of solar energy absorbed by the planet. Next, sea ice acts as an insulator between the warmer ocean and cooler atmosphere inhibiting heat transfer between the two. This process is an important part of the global heat exchange cycle. Also, polar sea and glacial ice are sources of fresh water which directly influence the population distributions and sizes of polar biota. Finally, many scientists believe that polar ice is a sensitive indicator of long term global climate change [1]. That is, if the earth is experiencing a long term warming or cooling trend, the symptoms will first be observed in polar ice property changes. For example, small increases in mean global temperature are observed in the polar regions in the form of decreased annual sea ice extent and increased melting in Greenland [2]. Hence the interest in monitoring the earth's cryosphere.

The harsh environment and vast size characteristic of the polar regions preclude the collection of *in situ* surface measurements with sufficient spatial and temporal sampling. However, satellite remote sensing presents an ideal method for surface property measurement in these regions. The instruments typically achieve complete coverage of the polar regions in just a few days. While some sensors have relatively lower resolution, all of them provide information that is otherwise unavailable.

Over the past few decades, the relatively young field of cryosphere remote sensing has matured as more research is performed to relate remotely sensed signatures to geophysical surface parameters. However, many questions still remain to be answered. The research described in this dissertation will answer some of these questions by providing new insight and developing new methods for understanding and applying remotely sensed data to cryosphere studies. The resulting contributions are an additional step in understanding these critical regions of the earth.

1.2 Description of the Problem

A number of sea ice properties are of interest to the scientific community. Each provides essential information needed to understand global geophysical processes. Among the important sea ice properties are

1. Spatial extent
2. Distribution and dynamics of ice type
3. Concentration (spatial coverage of ice vs. open water)
4. Thickness (important in heat transfer)
5. Salinity (due to brine content)
6. Age and melt rates
7. Surface flooding
8. Snow cover
9. Surface roughness (influences internal stresses)
10. Ice motion and dynamics.

An accurate knowledge of each of these parameters with sufficient spatial and temporal sampling is critical to understanding the polar regions and how they affect the rest of the planet. Methods for relating microwave signatures to these parameters are the focus of the polar remote sensing field.

Microwave remote sensing provides an excellent means for monitoring polar sea ice. Microwave sensors do not require solar illumination to collect measurements of the surface. Both active and passive microwave signatures are much less sensitive to atmospheric distortions than measurements collected at optical frequencies. This is particularly true in the Arctic and Antarctic where extensive cloud cover is common. Many research studies have shown that microwave signatures of sea ice are sensitive to surface parameters [3, 4]. However, for current sensors such as SSM/I, ERS-1/2, NSCAT, and SeaWinds, these benefits come at the expense of spatial resolution. Other microwave sensors such as synthetic aperture radars (SAR) offer higher resolutions, but lower coverage.

In order to enhance the spatial resolution of these low resolution snesor data, image reconstruction techniques are used. These methods use multiple passes of a satellite instrument (in effect trading temporal for spatial resolution) to increase surface sampling in an effort to raise the side lobes in the spatial frequency domain. However, to effectively implement the reconstruction, several conditions must be met. First, since microwave observations are commonly collected over a wide range of azimuth angles, their azimuthal dependence must be negligible. Azimuthal modulation can result in ambiguous reconstructed estimates of surface backscatter or brightness temperature. Second, validating the integrity of inter-sensor calibration ensures that signature variations are surface parameter dependent and not sensor dependent. For example, when the ERS-2 satellite replaced ERS-1, scatterometer measurement biases were observed during the brief period of mission overlap. This lack of consistency between the two instruments causes confusion in interpreting the observations. Consequently, the development of methods for determining the source of these discrepancies is critical. Further, reconstruction algorithms commonly have a number of tuning parameters that affect their convergence characteristics. These parameters must be optimized for each individual instrument to maximize image quality and minimize computational requirements. Finally, atmospheric distortion for higher frequency microwave instruments can cause ambiguous results which effectively mask the true surface signatures. These effects must be minimized to prevent biases in the reconstructed imagery. Each of these problems are addressed in this dissertation to enhance the ability to extract geophysical parameters.

Through the process of inverse modeling, surface parameters are inferred from remotely sensed signatures. Several techniques have been developed to achieve this. Direct methods attempt to derive a mathematical relationship between observed measurements and metrics of different surface features. Others draw on estimation theory, multivariate analysis, and signal processing principles. The various methods developed and analyzed in this dissertation use a combination of these to extract crucial sea ice information such as sea ice extent, sea ice type, and other surface parameters that influence instrument observations.

One of the complicating factors in surface parameter extraction is the temporal variability of observed microwave signatures. For example, a given ice type may exhibit a temporally varying backscatter due to variations in surface temperature, snow cover, and water content. As a result, an effective inversion technique must have the ability to adaptively compensate for temporal changes in the observed signatures. This often leads the algorithm development efforts into iterative methodologies which allow perturbations in the preceding signatures to estimate present conditions.

1.3 Research Contributions

Several contributions are made by this research to better understand microwave signatures of the earth's cryosphere. Valuable contributions are made in a number of areas related to remote sensing such as polar sea ice image reconstruction, geophysical property extraction, data fusion for multisensor studies, and model inversion.

The first set of contributions are in the area of polar backscatter image reconstruction, including the optimization of the scatterometer image reconstruction (SIR) algorithm for the NASA scatterometer. Similar optimization techniques can be used to fine tune the algorithm for other sensors as well. The results allow for the generation of enhanced resolution imagery with minimal computational requirements and maximum image quality. In an observational study, the azimuthal modulation of backscatter signatures of sea ice is shown to be negligible for Ku-band scatterometer data. This is a critical factor requiring verification before the multiple pass reconstruction method can be successfully applied. Also, techniques for determining the source of inter-sensor observation variability are presented. These ensure that variations in microwave signatures are a function of actual surface changes and not calibration discrepancies between instruments. These studies have been published as reports distributed by NASA [5, 6].

The next major element of this dissertation work is the development of multiple methods to reduce the effects of atmospheric distortion in image reconstruction. Each method is derived and compared including the modified maximum average, second-highest, and hybrid techniques. While the applicability of these methods is limited in sea ice image generation due to ice motion, they work well for stationary target scenes such as land and glacial ice as well as vegetated areas. The algorithms find greatest value in the reconstruction of higher frequency microwave imagery that exhibit increased sensitivity to cloud cover and precipitation. The result is improved image quality and reduced ambiguity in image interpretation that can be caused by atmospheric induced biases. This work was published in the *IEEE Transactions on Geoscience and Remote Sensing* [7].

Another contribution of this dissertation to cryosphere remote sensing is in large scale ice extent mapping. This research shows the utility of various parameters derived from Ku-band scatterometer data in mapping the spatial distribution of sea ice. The derived algorithm applies maximum likelihood techniques to segment sea ice pixels from open ocean pixels in polar imagery. A primary value of this technique is its ability to adaptively compensate for variations in the signatures of the two regimes throughout the polar seasonal cycle. It is demonstrated that the resulting ice extent maps correlate well with the commonly used NASA Team algorithm applied to radiometer data to identify sea ice regions. Good agreement is also found with high resolution SAR imagery of sea ice edges. The benefit of the Ku-band scatterometer method over the NASA Team method is the increased resolution inherent to reconstructed imagery from the Ku-band instruments used in this study. This technique is currently used by the Jet Propulsion Laboratory in near real-time wind processing.

The ice edge products are also used by the National Ice Center to monitor the seasonal evolution of polar sea ice edges. The NSCAT ice extent research was published in the *Journal of Geophysical Research* [8]. A follow on study adapted a modified version of the algorithm for Ku-band data from the SeaWinds scatterometer. A paper detailing this has been submitted to the *IEEE Transactions on Geoscience and Remote Sensing* and is currently in review.

While surface features such as sea ice extent can be determined from single sensor data sets, more complex parameters such as sea ice type require multiple instruments to obtain the information needed. Multisensor data fusion studies are relatively few in the field of microwave cryosphere remote sensing. One of the primary contributions of this research is the development of an algorithm that uses the synergy of multiple sensor data sets to infer sea ice type. The method is derived using two statistically based approaches: maximum likelihood and maximum *a posteriori*. Like the ice extent algorithm, this technique is designed to adapt to temporal changes in the signatures of each of the various sea ice classes. The study shows that the method is effective, stable, and more accurate than standard clustering techniques which have historically been used. This portion of the dissertation research has been accepted for publication in the *IEEE Transactions on Geoscience and Remote Sensing* and is currently in press [9].

The sea ice extent and ice type estimation studies described in the previous two paragraphs require Ku-band NASA scatterometer (NSCAT) data. Unfortunately, the NSCAT instrument is no longer operational precluding the use of these techniques in current and future sea ice studies. However, the SeaWinds scatterometer aboard the QuikSCAT satellite was launched in 1999 and is currently providing Ku-band observations of the polar regions. Since SeaWinds and NSCAT are significantly different instruments, substantial algorithm modifications are required to ensure the quality of the resulting estimates. These changes allow for continued analysis of polar sea ice packs using data sets containing Ku-band observations. The sea ice extent portion of this study has been submitted to the *Journal of Geophysical Research* and is currently in review.

The final contribution is in large scale microwave backscatter modeling. An in-depth study of a simple backscattering model is performed including the development of a new technique for model inversion. The inverse model algorithm is based on steepest descent optimization of an objective function which iteratively alters model parameters to fit observed signatures. The novelty of the technique lies in the combination of enhanced resolution imagery with the model for large scale feature extraction. The inverse model is applied to reconstructed imagery allowing for the estimation of important surface parameters on a large scale with a relatively small temporal resolution of only a few days. The value of the inversion technique is illustrated through its application in understanding backscatter anomalies in the Antarctic and Arctic sea ice packs. This work is currently in review for the *Journal of Geophysical Research.*

This dissertation research provides important contributions to the field of microwave cryosphere remote sensing. Through a combination of concepts from multivariate stochastic signal processing, detection and estimation theory, and electromagnetic theory, techniques and methodologies are developed and analyzed to answer important remote sensing questions. The final results are being applied in both on going scientific research and operational weather forecasting.

1.4 Dissertation Outline

The research documented in this dissertation covers a spectrum of studies in cryosphere remote sensing. The various chapters address different but related problems in the field through detailed analysis and the development of applicable solutions. These studies range from the resolution of image reconstruction issues to the inversion of microwave backscatter models for surface feature extraction. A brief overview of each chapter is given in the following paragraphs.

Chapter 2 presents general background information for the studies to be considered. An overview of the history of polar microwave remote sensing is given. Important specifications of the various instruments used to collect microwave measurements of the surface are reported. Also, the scatterometer image reconstruction algorithm used to generate enhanced resolution imagery for each study is described in more detail.

In Chapter 3 a number of critical issues in microwave sensor image reconstruction are considered. The first portion of this chapter deals with the optimization of the scatterometer image reconstruction algorithm for data collected by the NASA scatterometer. Following this segment, a study of azimuthal modulation in Ku-band backscatter over sea ice is presented. Last, a study of discrepancies between the ERS-1 and ERS-2 AMI scatterometers illustrates the important issue of inter-sensor calibration in the interpretation of reconstructed imagery.

Chapter 4 addresses another important aspect of image reconstruction - biases induced by atmospheric distortion. While microwave measurements are much less sensitive to atmospheric occurrences than optical or infrared sensors, this phenomenon still occurs at higher microwave frequencies. In this chapter, various methods for the removal of distorted measurements are presented and compared. Results are given illustrating the utility of the techniques. While originally developed for passive radiometer data, the methods can also be applied to scatterometer data sets.

While the first few chapters deal with critical image reconstruction issues, the remaining chapters focus on using reconstructed imagery to infer important geophysical parameters. The first of these, Chapter 5, discusses the theory, development, and implementation of an algorithm which estimates the spatial distribution of sea ice using only Ku-band scatterometer data. Several Ku-band measurement parameters are sensitive to the presence of sea ice or open ocean are exploited to map sea ice extent and features. The algorithm development is detailed showing its adaptive properties. Results are obtained using a large set of NSCAT imagery. The method is validated with high resolution SAR imagery and comparisons with results from the NASA Team algorithm.

While Chapter 5 presents a method for surface feature extraction using a single instrument, Chapter 6 takes the next step through the development of a multi-sensor sea ice classification algorithm. General sea ice classes are described as well as their role in geophysical processes. The classification data sets are presented along with the scattering and emission mechanisms that enable the ice type segmentation. Maximum likelihood and maximum *a posteriori* classification algorithms designed to adapt to temporally varying signatures are developed and implemented.

Chapter 7 describes the adaptation of the ice extent and ice classification techniques to SeaWinds data sets. Due to differences in instrument designs and configurations, significant modifications to the ice extent mapping method are required. This chapter discusses those changes and the implementation of the algorithm with current SeaWinds data sets. Multisensor sea ice classification using SeaWinds and SSM/I data is also considered. A first step at a “fuzzy” classifier is also presented.

In Chapter 8, a simple forward scattering model is analyzed. The model predicts backscatter based on three general sea ice parameters. These parameters are estimated from observed backscatter signatures through the development of a model inversion technique. The method is based on steepest descent objective function optimization and the computational requirements are moderate enough to use on large scales. The inversion technique is used to generate large scale maps of critical surface features. The results are applied to interpret backscatter anomalies occurring in the Antarctic and Arctic ice packs. Sensitivities for the forward and inverse models are analyzed.

Finally, Chapter 9 contains a summary of the research as well as important conclusions that are drawn. Contributions to the field are enumerated and several lines of future research are presented.

Chapter 2

Background

Remote sensing has proven a valuable tool in studying the earth's cryosphere. A number of past and current instruments have demonstrated the utility of microwave instruments in monitoring these critical regimes. In this chapter, a brief background is given of the history of low-resolution spaceborne microwave remote sensing instruments. The various instruments are described as well as some of the important results derived from the corresponding data sets. Since microwave scatterometer and radiometer data have inherently low spatial resolution, resolution enhancement algorithms are employed. The primary image reconstruction method used in this dissertation is also introduced.

2.1 Active Microwave Cryosphere Remote Sensing

Historically, spaceborne scatterometers have been employed in inferring ocean surface wind vectors. Wind induced roughness on the water increases σ^o, the normalized radar cross-section of the ocean's surface. Through measurements taken at several azimuth angles, estimates of the wind vectors are obtained. Rapid repeat coverage makes such instruments valuable in these applications. The low spatial resolution of these sensors is suitable for studying such large scale phenomena. Spaceborne microwave scatterometers have also been used to study non-ocean surface parameters [2, 4, 7, 10, 11].

Microwave scatterometers are active radar instruments that observe backscattered power from a transmitted microwave pulse. The transmitted and received powers are related through the radar equation [12],

$$P_r = \frac{P_t G^2 \lambda^2 A}{(4\pi)^3 R^4 L} \sigma^\circ \tag{2.1}$$

where P_r is the received backscattered power, P_t is the transmitted power, R is the slant range to the surface, L represents system losses, G is the scatterometer antenna gain, λ is the wavelength of the transmitted pulse, A is the illuminated surface area, and σ^o is the normalized radar cross section (NRCS) of the surface. The first seven of these parameters are related to the sensor and its measurement collection configuration. However, σ^o is function of surface as well as system parameters. In general, σ^o can be considered a function of several primary sensor parameters: incidence angle θ, azimuth angle ϕ, polarization, and frequency. The σ^o responses versus these parameters are often used to infer geophysical parameters from observed signatures. Scatterometer backscatter is a strong function of the surface geometry (roughness) and dielectric properties which dictate the observed scattering properties. For sea ice, there are several important factors affecting the scattering mechanisms [12],

- Surface roughness,
- Multilayer structure (including thickness) and the effective permittivities of those layers,
- Water content,
- Volume scatterer shape, distribution, size, and permittivity.

Scatterometer cryosphere remote sensing consists primarily of estimating such parameters from scatterometer data sets.

Over a limited incidence angle range of [20°, 55°], σ^o (in dB) is approximately a linear function of θ,

$$\sigma^o(\theta) = A + B(\theta - 40^\circ) \tag{2.2}$$

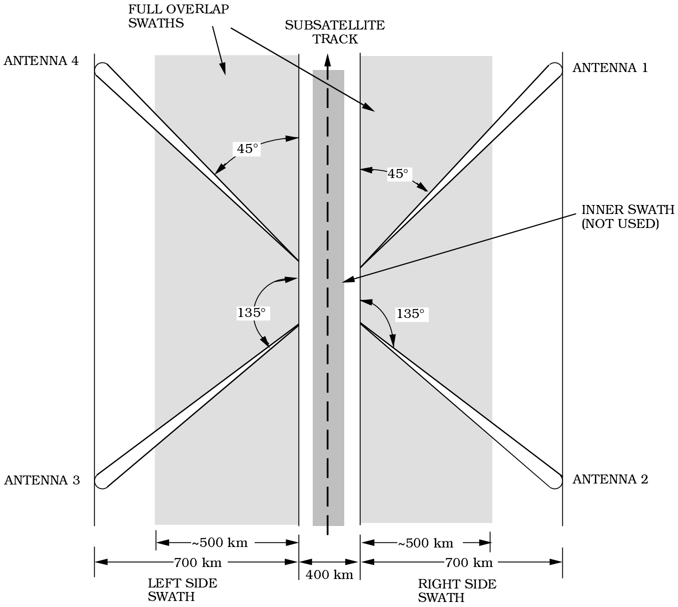

Figure 2.1: SASS multiple fan beam geometry.

where A and B are functions of surface characteristics, azimuth angle, and polarization. A is the σ^o value at 40° incidence and B describes the dependence of σ^o on θ. A and B provide valuable information about surface parameters. 40 degrees is chosen as a mid-swath value, but any interior swath angle can be used. A and B are commonly used to define σ^o measurements collected at multiple incidence angles.

Several microwave scatterometers have demonstrated the utility of these instruments in monitoring sea and glacial ice. The following sections describe the various scatterometer sensors which supply the datasets used in this dissertation.

2.1.1 The Seasat-A Scatterometer (SASS)

The first spaceborne scatterometer to monitor the cryosphere regions of the earth was the Seasat-A scatterometer (SASS). SASS was a dual-polarization Ku-band (14.6 GHz) scatterometer. The fan beam configuration allowed for the collection of σ^o measurements over a wide area from two side-looking swaths [13]. Figure 2.1 shows the SASS fan beam footprint geometry on the surface of the earth. The long fan beam footprints are further resolved through the use of Doppler filtering resulting in a number of 25-50 km nominal resolution measurement cells for each beam.

Launched in 1978, this instrument was designed to estimate surface wind speeds and directions from measured σ^o values over the ocean. However, researchers soon found that SASS data exhibited important variations over land and sea ice that can be used in monitoring critical surface features in the cryosphere. For example, Long and Drinkwater used enhanced resolution SASS σ^o observations to monitor glacial ice in Greenland [2]. The study used forward scattering techniques to determine surface characteristics and resulted in the ability to map different ice facies over all of Greenland. Since SASS was the first earth remote sensing scatterometer, it has also been used in multidecadal change studies in the Antarctic and the Arctic. One such study used SASS, ERS-1/2, and NSCAT reconstructed imagery to detect long term changes in polar ice sheets [14]. In another paper, Drinkwater and Carsey characterized the summer to fall transition in sea ice σ^o [15] illustrating the effects of freezing on backscatter signatures. Later, Winebrenner et al. monitored the progression of melt and freeze cycles of Arctic sea ice [16].

Unfortunately, the SASS mission was terminated early due to a system failure. Although only about 100 days of data were collected, this pioneering mission conclusively proved the value of scatterometers in ocean, land, and ice studies.

2.1.2 The European Remote Sensing Satellites (ERS-1 and ERS-2)

The loss of the Seasat satellite was followed by over two decades without an active orbiting scatterometer. The gap was filled when the European Space Agency launched the first European Remote Sensing Satellite (ERS-1) in 1991. Among other instruments, ERS-1 carries a C-band (5.3 GHz) scatterometer called the active microwave instrument (AMI) [17]. The AMI measures vv-polarization (vv-pol) σ^o at several azimuth and incidence angles. The instrument has a single side looking swath with beams at various azimuth angles as shown in Figure 2.2. The fan beam resolutions are broken into measurement cells using range gating with an effective cell spatial resolution of approximately 50 km. The AMI scatterometer aboard ERS-1

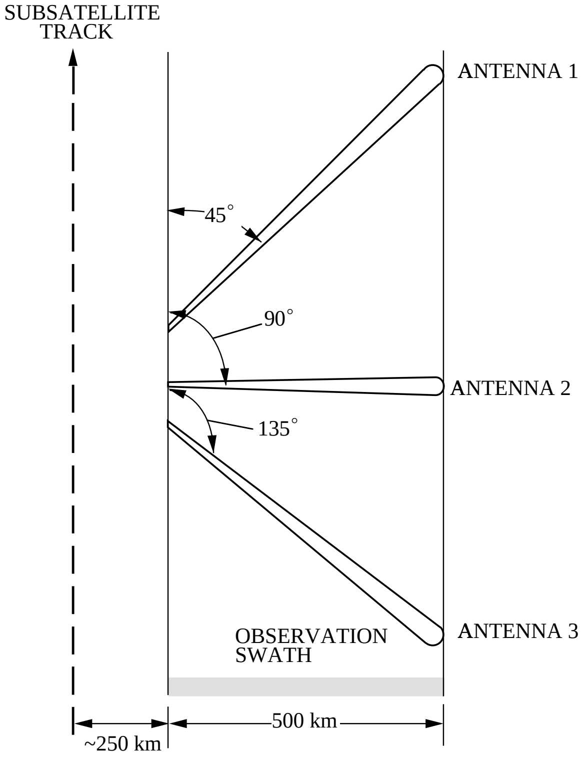

Figure 2.2: ERS AMI scatterometer multiple fan beam geometry.

was later followed by a similar satellite platform, ERS-2, in 1996 carrying an identical scatterometer.

The ERS scatterometer data sets have also shown great utility in cryosphere studies. Gohin and Cavanie used ERS-1 data in an effort to identify sea ice types [18]. In [19], ERS-1 signatures of Antarctic sea ice were compared with passive signatures to determine similarities and differences in sensor sensitivities to sea ice features. ERS-1 scatterometer enhanced resolution imaging of Antarctic sea ice packs is considered in [20]. Lecomte et al. used ERS-1 σ^o measurements to identify sea ice zones [21]. Furthermore, Early and Long evaluated azimuthal modulation levels at C-band over Antarctic ice. The study showed negligible modulation over sea ice but a significant azimuthal dependence of σ^o in glacial ice regions. Finally, Ulander et al. examined the effects of frost flowers on the surface of young ice. Such wind generated features cause SAR σ^o signatures very similar to older deformed ice types [22].

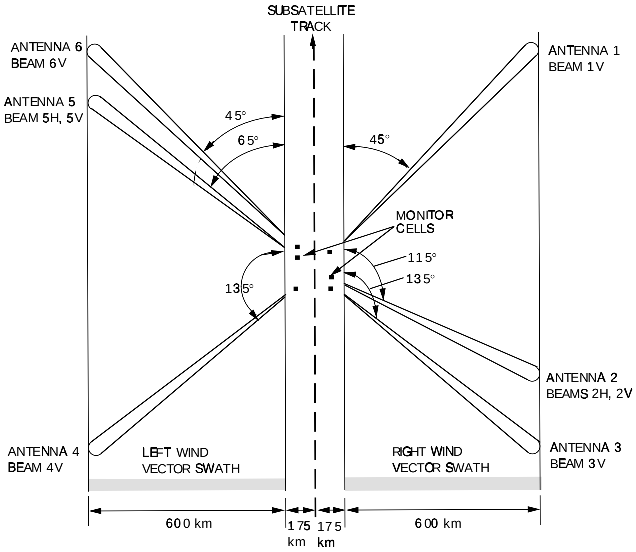

Figure 2.3: NSCAT multiple fan beam geometry.

2.1.3 The NASA Scatterometer (NSCAT)

Another Ku-band instrument, the NASA scatterometer (NSCAT) was launched in 1996 aboard the Advanced Earth Observation Satellite (ADEOS). Similar to SASS, NSCAT is a dual-polarization, dual-swath, fan-beam scatterometer that collects measurements at multiple azimuth and incidence angles [23]. However, the NSCAT instrument uses 6 fan beams rather than the SASS four-beam configuration as shown in Figure 2.3. Operating in the Ku-Band (14 GHz), NSCAT has 6 vv-pol and 2 hh-pol beams as each middle beam collects dual-polarization measurements. Doppler filtering is used to segment each fan-beam footprint into cells with resolution on the order of 25 km. Figure 2.4 shows a sample NSCAT cell along with the beam width and Doppler filtering responses.

NSCAT data sets have also demonstrated their usefulness in the estimation of polar surface parameters. Long and Drinkwater considered a number of cryosphere applications of this data set such as monitoring sea ice edges and examining the correlation of NSCAT σ^o with local temperatures and precipitation events [4]. In

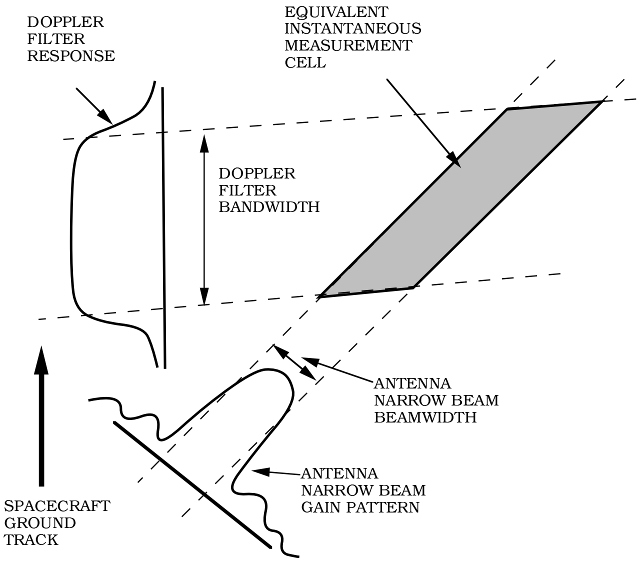

Figure 2.4: NSCAT cell geometry.

another study, Yueh and Kwok used NSCAT observations to estimate Arctic sea ice extent and melt onset [25]. Further, Drinkwater and Liu used a combination of NSCAT reconstructed imagery and wavelet analysis to monitor sea ice motion in the Antarctic and the Arctic [26].

The NSCAT mission lasted only about 10 months due to a catastrophic solar panel failure. Consequently, comprehensive studies of the annual cycles of Ku-band σ^o have not been possible. Still, the NSCAT data has proven its sensitivity to critical surface parameters.

2.1.4 SeaWinds on QuikSCAT

With the failure of NSCAT, NASA initiated a “quick recovery” mission designed to continue the Ku-band active observations. In 1999, the SeaWinds scatterometer aboard QuikSCAT was launched into a polar orbit. Since then, this instrument has provided a nearly continuous data set of observations of ocean, land,

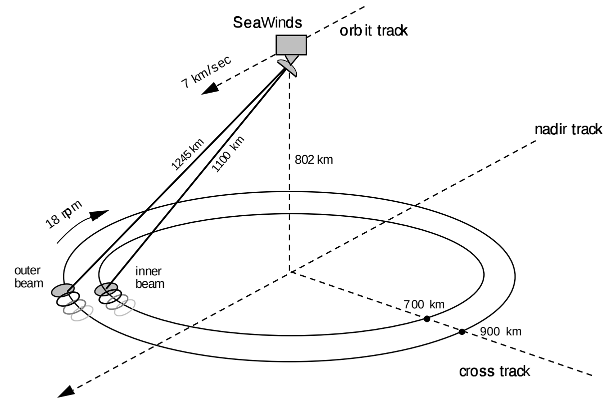

Figure 2.5: SeaWinds measurement collection configuration.

and sea ice. SeaWinds is a 13.4 GHz dual-polarization scanning pencil beam scatterometer with two spot beam scans shown in Figure 2.5 [27]. The outer scan (at 54° incidence) measures v-pol σ^o while the inner scan (46° incidence) measures h-pol σ^o. The resulting swath is 1800 km wide with no nadir gap. Consequently, SeaWinds covers approximately 90% of the earth's surface and 100% of the polar regions each day. In contrast, NSCAT required 2-3 days to obtain complete v-pol coverage. The significant increase in temporal resolution is extremely valuable in observations of sea ice since ice packs can move dozens of kilometers in a single day. Hence, SeaWinds reconstructed imagery is much less subject to blurring caused by sea ice motion and evolution.

SeaWinds has two spatial resolution "modes." The SeaWinds measurement cells (also called "eggs") have a nominal resolution of 25-50 km and are collected at various azimuth angles. These cells are further resolved through Doppler-filtering, splitting each cell into several elongated "slices" approximately 6-8 km wide by 25 km long. Science data products can be made from either egg or slice measurements.

2.2 Passive Microwave Cryosphere Remote Sensing

In contrast, microwave radiometers are passive instruments that observe natural microwave emissions of the earth's surface. The brightness temperature, T_B, is measured by radiometers and is a function of the emissivity of the surface, e, and surface temperature, T_s,

$$T_b = eT_s. \tag{2.3}$$

This proportional relationship is derived from the Rayleigh-Jeans approximation to Planck's Law of Thermal Radiative Emission [28]. The Rayleigh-Jeans approximation is valid in the microwave portion of the spectrum. The emissivity relates the amount of radiation emitted compared to a black-body radiator for which $T_b = T_s$. Like σ^o, the emissivity is a function of a number of instrument and surface dependent parameters [29]. For example, sensor frequency, polarization, incidence angle, and beam width are important. Emissivity is also strongly dependent on a several critical sea ice characteristics. For example, emissivity increases with water content. The presence of brine also influences emissivity with higher salinity resulting in higher emissivity. In addition, snow accumulation rates also affect e.

Similar to scatterometers, passive microwave radiometers have proven to be extremely useful in monitoring the ice covered regions of the earth. Many different radiometer instruments have flown as described below.

2.2.1 Early Radiometers

Among the earliest satellite microwave radiometers was the Electrically Scanning Microwave Radiometer (ESMR). The 19.35 GHz h-pol instrument flew aboard the Nimbus 5 platform from late 1972 to late 1982 [28]. With a swath width of 3,000 km, ESMR could achieve complete coverage of the polar regions in a single day though frequent instrument down time often raised the requirement to three days.

ESMR data provided the first concrete results demonstrating the utility of microwave radiometers in detecting sea ice concentration [30]. In sea ice classification efforts, little contrast was observed in the 19.35 GHz observations. A later version of ESMR aboard the Nimbus 6 satellite used a 37 GHz frequency which significantly increased the contrast between younger and older ice types. However, the electrical scanning configuration of the instrument increased noise levels such that the radiometric resolution was limited.

The knowledge gained from the ESMR experiments was used to develop second generation passive microwave radiometers. One such instrument was the Scanning Multichannel Microwave Radiometer (SMMR). Launched in 1978 aboard the ill-fated Seasat satellite, SMMR collected dual-polarization measurements at five different frequencies: 6.63, 10.69, 18, 21, and 37 GHz. The channel at 21 GHz was chosen at region of the microwave spectrum which is sensitive to the presence of atmospheric water vapor. This channel was primarily used for atmospheric corrections. Though designed to measure sea surface temperature and wind speed (but not direction) over the ocean, the multispectral nature of SMMR greatly enhanced its ability in studies of sea ice types. Using the 18 and 37 GHz SMMR channels estimates of ice concentration were improved [31, 32].

2.2.2 The Special Sensor Microwave Imager (SSM/I)

The Special Sensor Microwave Imager (SSM/I) aboard the Defense Meteorological Satellite Program series of satellites is another example of an imaging microwave radiometer. SSM/I is a total-power, seven channel, four frequency radiometer [33]. It utilizes an integrate-and-dump filter as the antenna scans the ground track [34]. The conical scan geometry is shown in Figure 2.6. The channels are h- and v-pol at 19.35, 37.0, and 85.5 GHz and v-pol at 22.235 GHz. Brightness temperature measurements are collected from each channel. The 3 dB antenna footprints range from about 15-70 km in the along-track direction and 13-43 km in the cross-track direction (see Table 2.1). The 3 dB antenna footprints, which are different for each frequency, have an elliptical shape on the surface of the earth due to the elevation angle of the radiometer [35]. SSM/I has flown on several DMSP satellites from 1987.

SSM/I data sets offer improvements over SMMR in estimates of sea ice extent and concentration. Geolocation is also improved with the SSM/I instrument.

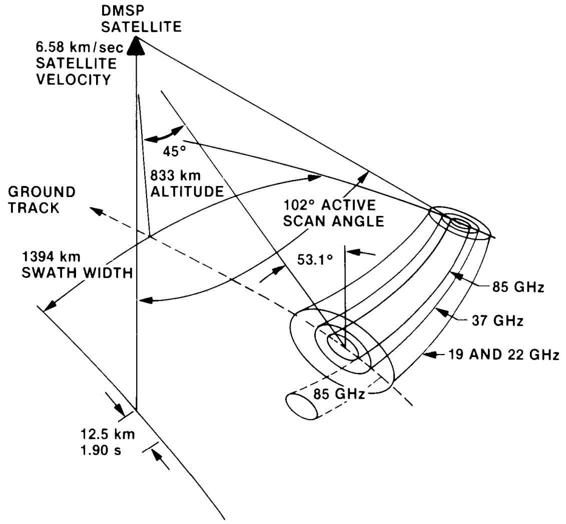

Figure 2.6: SSM/I scanning measurement geometry [28].

The NASA Team algorithm uses SSM/I polarization and gradient ratios computed from the 19 and 37 GHz channels for the estimation of total sea ice concentration in both the Arctic and Antarctic regimes [31, 36]. The NASA Team products are widely used in the cryosphere remote sensing field. Resolution enhancement of SSM/I data is considered in [37] and [38]. Both offer significant improvements over the nominal footprint resolutions through the use of multiple passes of the satellite.

2.3 Resolution Enhancement

While the inherent resolutions of the various instruments are sufficient for the study of large scale phenomena such as surface winds or atmospheric parameters, they are too low for use in some studies. In an effort to ameliorate this problem and to place the data on compatible grids, the Scatterometer Image Reconstruction (SIR) algorithm is used to enhance the spatial resolution [38, 39]. SIR is an iterative block multiplicative algebraic reconstruction technique that increases the resolution of reconstructed imagery through the use of data from multiple passes of the satellite. SIR utilizes the increased sampling, though irregular, to raise the side lobes of

Table 2.1: SSM/I channels.

SSM/I Channel		3 dB Footprint (km)	
Frequency (GHz)	Pol.	Along-track	Cross-track
19.35	V	69	43
19.35	H	69	43
22.235	V	50	40
37.0	V	37	28
37.0	H	37	29
85.5	V	15	13
85.5	H	15	13

the antenna pattern in the spatial frequency domain and thus increase the spatial resolution.

For scatterometers, SIR creates images of the A and B parameters discussed above. NSCAT images are reconstructed on a 4.45 x 4.45 km grid with an effective resolution on the order of 8–10 km. NSCAT imagery is reconstructed with the SIR with filtering (SIRF) algorithm [39] which includes a median filter. For ERS-1/2, the median filter is not used. ERS-1/2 images are generated on a 8.9 x 8.9 km grid with an effective resolution of 20–25 km. SeaWinds imagery is also constructed though the incidence angle parameter B cannot be estimated from fixed-incidence angle SeaWinds data. For the egg data sets, the 4.45 km resolution is used with a resulting surface feature resolution of about 8–10 km. Slice imagery is produced on 2.225 km grids yielding the highest resolution (effectively 4–5 km) currently available for spaceborne microwave scatterometers. SIRF reconstructed imagery compared with SAR imagery has demonstrated the resolution enhancement abilities of SIRF [40].

Figure 2.7 shows examples of NSCAT A_v and B_v images of the world. While the images are not displayed at full resolution, they demonstrate the important variations present in these parameters over land and ice surfaces. The regions with lowest backscatter are generally in the desert regions such as the Sahara Desert in Northern Africa. Rain forest regions in the Amazon and Central Africa have significantly higher A_v values. The highest backscatter is observed in the glacial ice areas of Greenland and Antarctica. Though somewhat more noisy, the B_v world image also contains important information about land and ice surfaces. As with A_v, desert regions have very low B_v indicating rapid σ^o fall-off with increasing incidence angle. The rain forests and glacial ice regimes are characterized by high volume scattering contributions. Consequently, the σ^o versus incidence angle is much more isotropic. That is, σ^o is a weak function of incidence angle.

A univariate version of SIR can be applied to radiometer data such as SSM/I [38]. The lower side lobes of SSM/I make resolution enhancement more difficult. However, a clear improvement in resolution is observed in the reconstructed imagery. That is, surface features are more clearly defined in SIR imagery than in nonenhanced images on the same grid. SSM/I brightness temperature SIR images are reconstructed on a 8.9 x 8.9 km grid for all channels except 85V and 85H which have a pixel spacing of 4.45 x 4.45 km.

SIR enables comparison of sensors on compatible grids with similar resolution. While the SIR algorithm increases the resolution of the reconstructed imagery of a particular instrument, ice motion during the imaging period is a concern. In a six day period, sea ice can potentially move tens of kilometers. This represents several pixels in the reconstructed imagery. As a result, the pixels in reconstructed imagery represent the average surface responses during the imaging interval.

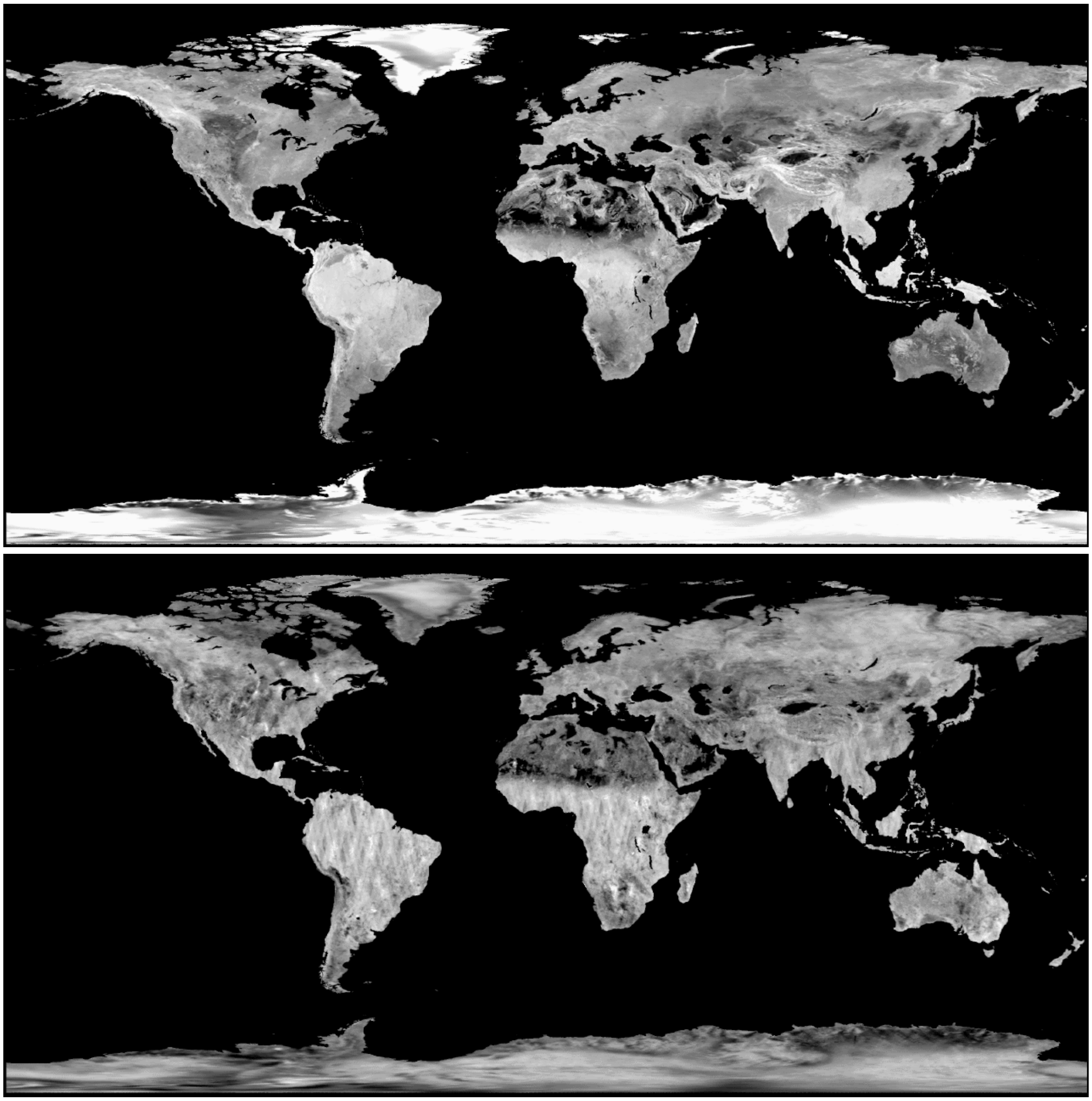

Figure 2.7: Sample NSCAT A_v (top) and B_v (bottom) SIRF images of the world. The original image have much greater spatial resolution than can be displayed here. Ocean pixels have been masked out of the imagery.

Chapter 3

Image Reconstruction Studies

While scatterometer and radiometer signatures show high sensitivity to important sea ice characteristics, the low inherent resolutions of these data limit their use in cryosphere studies. However, image reconstruction techniques such as the Scatterometer Image Reconstruction (SIR) algorithm have been developed that enhance the spatial resolution of the data through various deconvolution techniques. The resulting imagery are much more useful in efforts to determine surface parameters. This chapter discusses three important studies related to enhanced resolution image reconstruction.

In Section 3.1, the SIR algorithm is optimized for NSCAT data. The SIR and SIRF methods, as well as the parameters affecting algorithm convergence, are described in more detail . The parameters are modified to ensure the fastest possible convergence rate. The proposed techniques can be used for the tuning of SIRF for other instruments as well such as SSM/I and SeaWinds.

Since image reconstruction methods like SIRF use multiple measurements collected at various azimuth angles to generate pixel estimates, azimuthal modulation of σ^o is a key issue. Section 3.2 discusses the levels of azimuthal modulation present in NSCAT σ^o measurements of sea and glacial ice. The results are used to determine the error levels in SIR σ^o estimates caused by the modulation.

Another source of error in image reconstruction is inter-sensor variations in σ^o. For example, the ERS-1 scatterometer was replaced by ERS-2 in 1996. For a short period, both sensors were operational collecting σ^o measurements at similar times. Discrepancies in the calibration observations in the two instruments must be resolved to ensure the proper interpretation of ERS-1 and ERS-2 temporal image sets. Section 3.3 addresses this important calibration issue.

Each of these research activities offer results and methods which improve the quality and interpretation of reconstructed microwave imagery. The image products are used in following chapters in which surface parameters are extracted from enhanced resolution imagery.

3.1 Optimization of SIRF for NSCAT

The Scatterometer Image Reconstruction with Filtering (SIRF) algorithm was developed [39] to enhance scatterometer data resolution by combining data from multiple passes of a satellite. This is done under the assumption that the observed surface region has minimal σ^o temporal variability during the observation period. This is generally the case for land and ice regions. From an initial estimate, SIRF iteratively updates estimates of σ^o until satisfactory convergence is reached. Since SIRF was originally developed for SASS data, the algorithm needs to be "tuned" for NSCAT.

Several SIRF algorithm parameters influence its effectiveness in resolution enhancement. Initialization values, update weighting, iteration number, and data incidence angle sampling all influence the functionality of the SIRF algorithm. This section describes the procedure taken to optimize SIRF for NSCAT data. First, an overview of the SIRF algorithm is given. Next, the generation of simulated data for optimization tests is described. B value weighting and convergence in the algorithm are then discussed. SIRF initialization is then examined. Nonhomogeneous simulated SIRF images are created and statistical correlation and error analyses are performed. Incidence angle sampling issues are addressed. Finally, the conclusions drawn from this study are given.

3.1.1 SIRF Algorithm

The SIRF algorithm generates estimates for the A and B values for a given pixel from NSCAT σ^o and incidence angle (θ) measurements. Over a limited θ range of [20°-60°], σ^o (in dB) is a approximately a linear function of θ as described in Eq. (2.2). This equation parameterizes the σ^o vs. θ response with two parameters, A and B. A is the σ^o value at 40° incidence and B describes the dependence of σ^o on θ. A and B provide valuable information about the surface.

In this section, the method for obtaining enhanced resolution radar images of A and B in Eq. (2.2) from the low resolution scatterometer measurements is described. The method is based on the spatial overlap of the σ^o measurements from multiple scatterometer passes and on image reconstruction techniques. In order to develop the technique we first describe the enhanced resolution measurement model. We consider the effects of the scatterometer measurement noise and then describe methods for resolution enhancement of A and B. A sample image outputs from SIRF are shown in Figure 2.7.

An understanding of NSCAT swath and cell geometry is needed to implement the SIRF algorithm using NSCAT data. Figures 2.3-2.4 show the NSCAT antenna patterns and cell geometry. As the satellite travels forward, measurements are taken from two swaths, one on each side of the subsatellite track. Both the right and the left side swaths are 600 km wide with a gap of 350 km in between. Figure 3.1 shows the cell locations and geometries for 11 actual NSCAT measurements from each antenna. The monitor cells at 10° incidence were not plotted since they are not used in the imaging process. SIRF uses the overlap of these cells from multiple beams and multiple orbital passes of the satellite to enhance the resolution.

Enhanced Resolution σ^o Measurement Model

Consider a rectilinear grid of resolution elements on the earth's surface with a resolution element size of $S_x \times S_y$. The six-sided integrated resolution cells of the scatterometer measurements are imposed on this small-scale grid of resolution elements (refer to Fig. 3.2). Assuming a noise-free measurement, the value of σ^o measured by the scatterometer (denoted by ϱ_k where k is the measurement number) is a weighted average of the σ^o's of the individual resolution elements covered by the

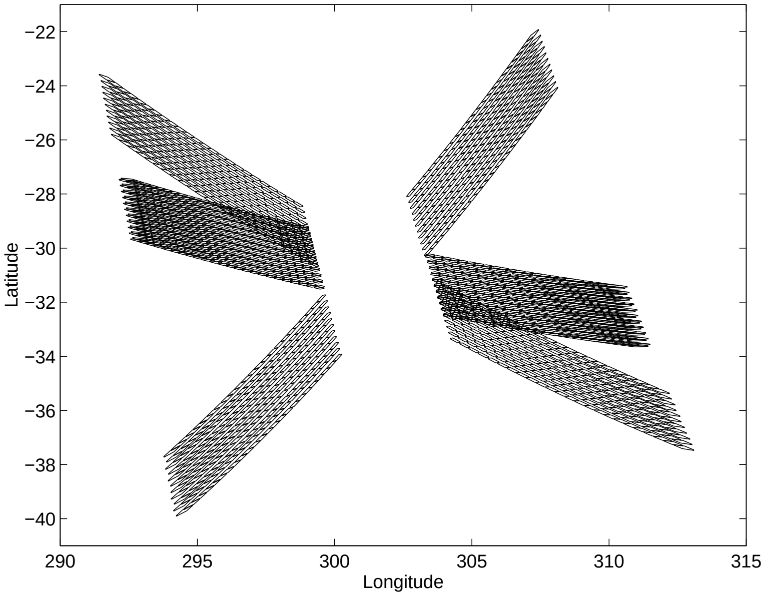

Figure 3.1: Actual NSCAT cell locations and geometries for 11 antenna cycles.

measurement cell, i.e.,

$$\varrho_k = \sum_{c=L_k}^{R_k} \sum_{a=B_k}^{T_k} h(x, y; k)\sigma^o(x, y; k) \tag{3.1}$$

where L_k, R_k, T_k, and B_k define a bounding rectangle for the k^{th} hexagonal σ^o measurement cell, $h(x, y; k)$ is the weighting function for the $(x, y)^{th}$ resolution element $(0 \leq h(x, y; k) \leq 1)$, and $\sigma^o(x, y; k)$ is the σ^o value for the $(x, y)^{th}$ resolution element. The incidence angle dependence of σ^o and h is subsumed in the k index. (Over a given scatterometer measurement cell the incidence angle θ is approximately constant.) h is a function of the cell location and shape.

The dependence of σ^o on θ can be expressed as [see Eq. (2.2) for definitions of A and B]

$$\sigma^o(\theta) = \alpha_o^A[\beta_o(\theta)]^B \tag{3.2}$$

with

$$\begin{aligned} \alpha_o &= 10^{1/10} && (3.3) \\ \beta_o(\theta) &= 10^{(40-\theta)/10}. && (3.4) \end{aligned}$$

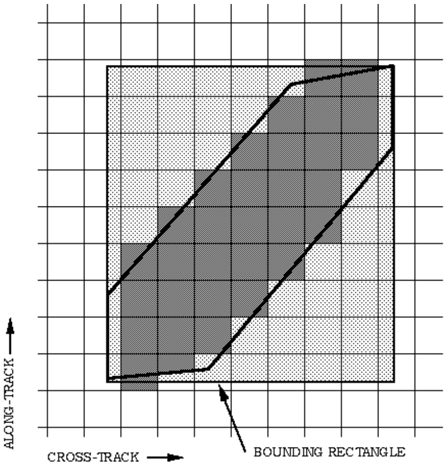

Figure 3.2: An integrated NSCAT σ^o cell overlaying the high resolution grid. Only the shaded square grid elements have nonzero $h(x, y; k)$. The bounding rectangle is also indicated.

Using this relationship Eq. (3.1) can be written as

$$\varrho_k = \sum_{c=L_k}^{R_k} \sum_{a=B_k}^{T_k} h(x, y; k) \alpha_o^{A(x,y)} [\beta_o(\theta_k)]^{B(x,y)}. \tag{3.5}$$

The actual scatterometer measurements are noisy. Let z_k denote the noisy measurement of ϱ_k, then

$$z_k = \varrho_k + \nu_k \tag{3.6}$$

where ν_k is a zero-mean Gaussian random variable with variance

$$\text{Var}[\nu_k] = \alpha \varrho_k^2 + \beta \varrho_k + \gamma \tag{3.7}$$

where α, β, and γ are from the k_p equation

$$k_p = \alpha \sigma^{o2} + \beta \sigma^o + \gamma \tag{3.8}$$

where α, β, and γ are known constants which depend on the measurement geometry (via the radar equation and the SNR) as well as the instrument parameters and calibration accuracy [23].

The resolution enhancement problem can then be posed as the following reconstruction problem: Given noisy measurements z_k of ϱ_k for $k \in [1, N]$, determine

$A(x,y)$ and $B(x,y)$ for each element of the enhanced resolution grid. The method for solving this problem is described in the next section.

The key to successful resolution enhancement of $A(x,y)$ and $B(x,y)$ is taking advantage of the overlap in multiple measurements of the same general region. As will be discussed further, the ultimate A and B image resolutions are determined by this measurement overlap and the measurement location spacing [24]. While measurements from the fore- and aft-facing antennas in a single orbit provide some measurement overlap, this overlap is generally insufficient to adequately apply the technique (the measurements do not completely cover the surface); hence, data from multiple orbits must be used.

In order to use data from multiple orbits we must assume the radar characteristics of the target region remain constant for each pass. Additionally, we assume that A and B have no azimuthal dependence. These and other requirements and assumptions needed (for SASS, but also applicable to NSCAT) are explored more fully in [10].

Reconstruction Approach

The Scatterometer Image Reconstruction algorithm (SIR) is based on multiplicative algebraic reconstruction techniques. In SIR, each measurement is compared to a predicted (forward projection) value computed from the current image estimate. A multiplicative correction factor is then applied each pixel covered by the measurement causing the forward projection to equal the measurement. Subsequent measurements further alter the pixel values. Over multiple iterations, the correction factors ideally converge to a value of unity and all the forward projections match the measurements. SIR has been optimized for noisy scatterometer measurements and to estimate both A and B in multivariate image reconstruction [39].

Initial estimates of A and B, A_{init} and B_{init} images, are made by setting $B_{init}=$ the global average of B and $A_{init}=$ the global average of A. The initial values affect the convergence of the algorithm to the final solution. In the k^{th} iteration of the SIR algorithm, the previous B estimate image is used to normalize the σ^o measurements from which an estimate of A is generated. Linear regression of the update terms (expressed at the measurement incidence angle) is then used to update the previous estimate of B. The new B estimate is determined as a weighted average of the previous B estimate and the B estimate update. The multivariate SIR algorithm is given below [39].

We express the measurements z_j in dB so the forward projection f_j^k is computed in normal space (then converted to log space) while the A and B estimates are in log space, i.e.,

$$f_j^k = 10\log_{10}\left[\frac{1}{q_j}\sum_{n=1}^{N} h_{jn}10^{a_n^k/10}\right] \tag{3.9}$$

where q_j is defined as

$$q_j = \sum_{l=1}^{M} h_{jl}. \tag{3.10}$$

Define d_{ij}^k as

$$d_{ij}^k = \left(\frac{z_j - b_i^k(\theta_j - 40^\circ)}{f_j^k}\right)^w, \tag{3.11}$$

where $w = 1/2$ is used in SIRF. The A estimate update term, u_{ij}^k, is computed,

$$u_{ij}^k = \begin{cases} \left[\frac{1}{2}\frac{1}{f_j^k}\left(1 - \frac{1}{d_{ij}^k}\right) + \frac{1}{a_i^k d_{ij}^k}\right]^{-1} & d_{ij}^k \geq 1 \\ \left[\frac{1}{2}f_j^k\left(1 - d_{ij}^k\right) + a_i^k d_{ij}^k\right] & d_{ij}^k < 1 \end{cases} \tag{3.12}$$

with the A estimate, a_i^k, updated according to

$$a_i^{k+1} = \frac{1}{p_i}\sum_{j=1}^{N} h_{ji}u_{ij}^k, \tag{3.13}$$

where

$$p_i = \sum_{l=1}^{N} h_{li}. \tag{3.14}$$

To compute the B estimate, let

$$r_i = \sum_{j=1}^{N} h_{ji}\theta_j^2 \tag{3.15}$$

$$t_i = \sum_{j=1}^{N} h_{ji}\theta_j \tag{3.16}$$

and

$$\zeta_{ij}^k = u_{ij}^k + b_i^k(\theta_j - 40^\circ). \tag{3.17}$$

Then, the linear regression of the A updates, u_{ij}^k, provides an update for B,

$$c_i^k = \frac{1}{p_i r_i - t_i^2} \left(p_i \sum_{j=1}^{N} h_{ji} \theta_j \zeta_{ij}^k - t_i \sum_{j=1}^{N} h_{ji} \zeta_{ij}^k \right). \tag{3.18}$$

This update is only usable if the range of incidence angles (θ_j) used in Eq. (3.18) is sufficiently wide. Since a wider incidence angle range implies greater confidence in the B estimate update [39], the B estimate is updated using a weighted average of c_i^k and the previous B estimate. The weighting factor is a simple function of the variance of θ, i.e., let

$$x_i = \frac{p_i}{t_i^2} \sum_{j=1}^{N} h_{ji} \theta_j^2 - 1 \tag{3.19}$$

then the B estimate image is updated according to

$$b_i^{k+1} = \frac{1}{x_i + 1} \left(x_i c_i^k + b_i^k \right). \tag{3.20}$$

This system of equations is iterated over k until convergence. Convergence is discussed in following sections.

The subjective quality of the final images can be improved by applying an edge-preserving 3 × 3 median filter to the A and B images. The image noise can be significantly reduced, with only a small reduction in the image resolution, by application of a hybrid median-linear filter to the image estimates at each stage of the iteration. The SIR algorithm with the added filtering is termed SIRF.

In the hybrid filter, the image values within a moving 3 × 3 window are ordered and the median determined. If the difference between the second highest and second lowest values within the window is less than 0.25, the center pixel is replaced with the average of the middle seven values of the ordered window pixels. Otherwise, the center value is replaced with the median value. Effectively, this hybrid filter acts like a linear filter when the algorithm is near convergence and the region is smooth but operates as a median filter otherwise. The edge-preserving properties of the median filter maintain resolution while providing noise suppression.

SIRF was originally developed for use with Seasat scatterometer (SASS) data [39]. The B updates were heavily damped in the original version of SIRF and may not be appropriate for NSCAT data. For NSCAT B value convergence can be accelerated by weighting these updates appropriately.

Equation (3.20) defines the iterative update for B based on a linear regression of the A updates c_i^k (Eq. (3.18)) and a weighting factor x_i determined by the variance of incidence angles (Eq. (3.19)). To facilitate convergence of the B values, the updates are further weighted with an acceleration factor b_{acc}. Using this approach, Eq. (3.19) becomes

$$x_i = b_{acc}\left(\frac{p_i}{t_i^2}\sum_{j=1}^{N} h_{ji}\theta_j^2 - 1\right) \tag{3.21}$$

where b_{acc} is the acceleration factor ($b_{acc} > 1$). The selection of b_{acc} is described in a later section.

AVE Algorithm

As described in [39], a very simple approach to simultaneous estimation of A and B may be derived from the unweighted MART algorithm. For a constant initial value, the first iteration of unweighted MART is

$$a_i^1 = \frac{1}{p_i}\sum_{j=1}^{N} h_{ji}z_j. \tag{3.22}$$

Remembering that h_{ij} is either one or zero, we see that a_i^1 is the average of the measurements covering the i^{th} pixel. This averaging approach (which will be referred to as AVE) provides a smoothed initial image estimate which, in effect, is improved by later iterations of SIRF [39]. In AVE the A and B estimates for a given pixel are computed by linear regression of the σ^o measurements (in dB) which cover the pixel. We note that the AVE resolution is better than the measurement cell resolution and is significantly better than conventional "binning" where the minimum resolution element size is effectively limited to the maximum size of the measurement cells; however, AVE resolution is not as good as SIR or SIRF.

3.1.2 Generating Simulation Data

The values of b_{acc}, the number of iterations of SIRF, A_{init}, and B_{init} affect the estimated image accuracy and quality. In this section, simulations are used to select optimum parameter values. To examine the effects of these parameters, synthetic A and B truth images are created. The images are created at higher resolution (approximately 4.5 km per pixel) than the nominal resolution of the satellite (25 km) with dimensions of approximately $8^\circ \times 8^\circ$. Constant value images are used for both parameters. Two simulations are performed. The first has truth values A=-10.0 B=-0.1 and the second uses A=-20.0 B=-0.2.

NSCAT L1.5 data records contain geolocation, azimuth angle, incidence angle, σ^o, and noise information for each measurement cell. Simulated data is generated using 10 days of actual NSCAT data (1996 JD 301-310) taken from the Amazon Basin (latitude range of 2.0°S to 10.0°S, longitude range of 62.0°W to 70.0°W) combined with the truth images. The actual data provides geolocation and incidence angle information and the truth images are used to create synthetic σ^o and variance values. σ^o is computed from effective A and B values in the measurement footprint (see Figure 3.2),

$$A_{eff} = \sum_{c=L_k}^{R_k} \sum_{a=B_k}^{T_k} h(x,y;k) A_{truth}(x,y;k) \tag{3.23}$$

$$B_{eff} = \sum_{c=L_k}^{R_k} \sum_{a=B_k}^{T_k} h(x,y;k) B_{truth}(x,y;k) \tag{3.24}$$

where L_k, R_k, T_k, and B_k define a bounding rectangle for the k^{th} hexagonal σ^o measurement cell, $h(x,y;k)$ is the weighting function for the $(x,y)^{th}$ resolution element ($h(x,y;k)$=0 or 1 for NSCAT), $A_{truth}(x,y;k)$ is the A value for the $(x,y)^{th}$ resolution element, and $B_{truth}(x,y;k)$ is the corresponding B value. The noiseless σ^o then becomes

$$\sigma^o_{nl} = A_{eff} + B_{eff}(\theta - 40^\circ). \tag{3.25}$$

Realistic noise is added to σ^o_{nl} by using actual variance values of the data. The variance of σ^o is a function of σ^o , α, β, and γ. The simulated σ^o is given by

$$\sigma^o = \sigma^o_{nl}(1 + k_p \nu) \tag{3.26}$$

where

$$k_p = \alpha\sigma_{nl}^{o2} + \beta\sigma_{nl}^{o} + \gamma \tag{3.27}$$

and ν is a zero-mean Gaussian random variable with unity variance. This is performed for all of the measurements cells in the study region during the time period 1996 JD 301-310.

3.1.3 B Weighting

The effects of B acceleration are studied by using the synthetic images described above. The truth image is A=-10.0 and B=-0.1. SIRF is implemented repeatedly with different B weighting values b_{acc}. Initialization values of A=-10.0, -30.0 and B=-0.1, -0.3 are used to evaluate worst case convergence scenarios.

The first case considered is A_{init}=-30.0 and B_{init}=-0.1 (the true B value). Figure 3.3 displays the means and standard deviations of the A and B values for the SIRF images at each iteration and B weighting. The A mean converges to its actual value nearly identically regardless of the B weighting (b_{acc}), achieving its true value after approximately 25 iterations. Increasing the B weighting slightly increases the A noise level as indicated by the A standard deviation. The mean for the B images diverges slightly from the true value for all B weights although the worst error after even 75 iterations is small (on the order of .0002 dB/deg). The B noise level also increases with B weighting although the noise is small.

Another simulation is run with A_{init}=-10.0 (the true A value) and B_{init}=-0.3 to observe the effects of B convergence alone. Figure 3.4 plots the results. The mean A value first diverges from its true value for the first several iterations. It then recovers and begins to converge back to the desired value at a rate determined by the B acceleration value. Higher B weights result in quicker convergence. The A standard deviation in the images initially increases for the first 5-15 iterations, then decreases converging to the same final value as in the A_{init}=-30.0 B_{init}=-0.1 case. Convergence is achieved more quickly for higher B acceleration values. From Figure 3.4 we see that B weighting is required to achieve convergence in less than 75 iterations. Increased B weighting speeds the convergence.

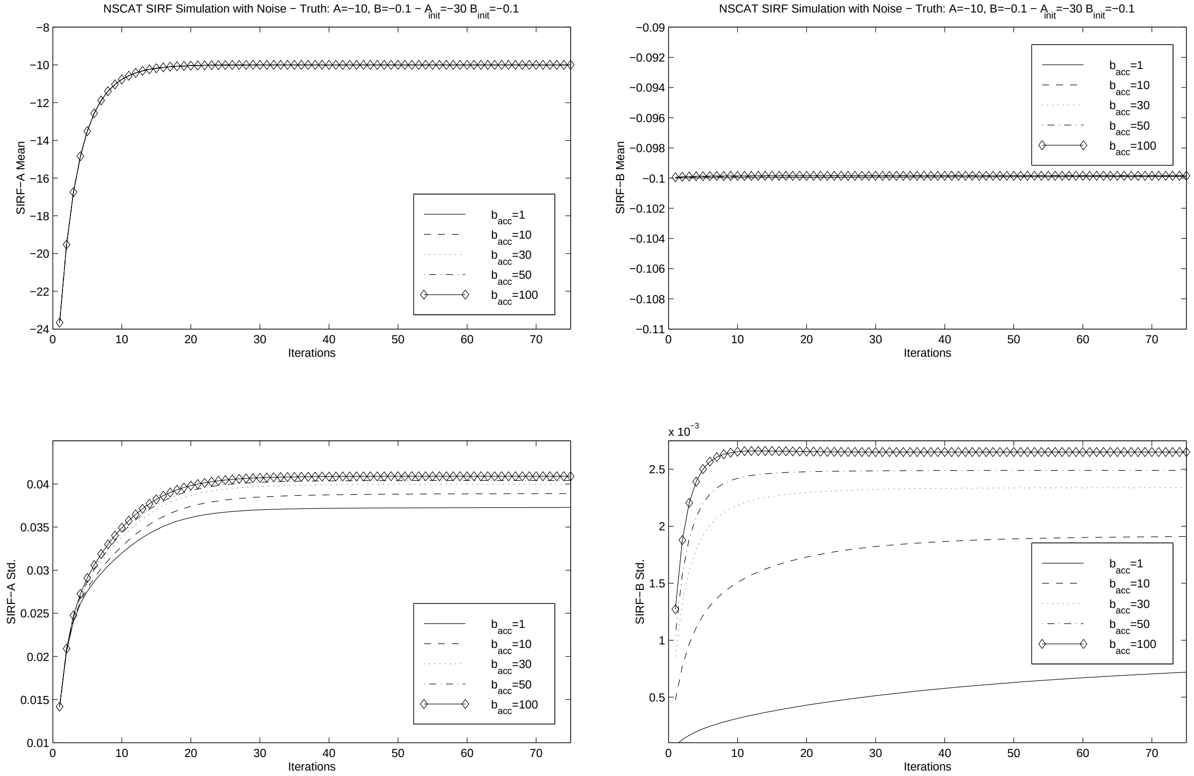

Figure 3.3: Means (top) and standard deviations (bottom) of the SIRF simulation A (left) and B (right) images with constant truth images A=-10.0 and B=-0.1. Initialization values are A_{init}=-30.0 and B_{init}=-0.1. Different values of B update weight are used.

These simulations indicate that increasing the B weighting yields quicker convergence though excessive acceleration can increase the noise level of the image. If 50 iterations are used, a B update weight of 30 is sufficient to reach convergence in mean and standard deviation.

3.1.4 SIRF Initialization

SIRF requires initial values of A and B. The algorithm iteratively updates the estimate by comparing the previous estimate with raw data values. The algorithm continues for N iterations. If a poor initialization value is used, the A and B values

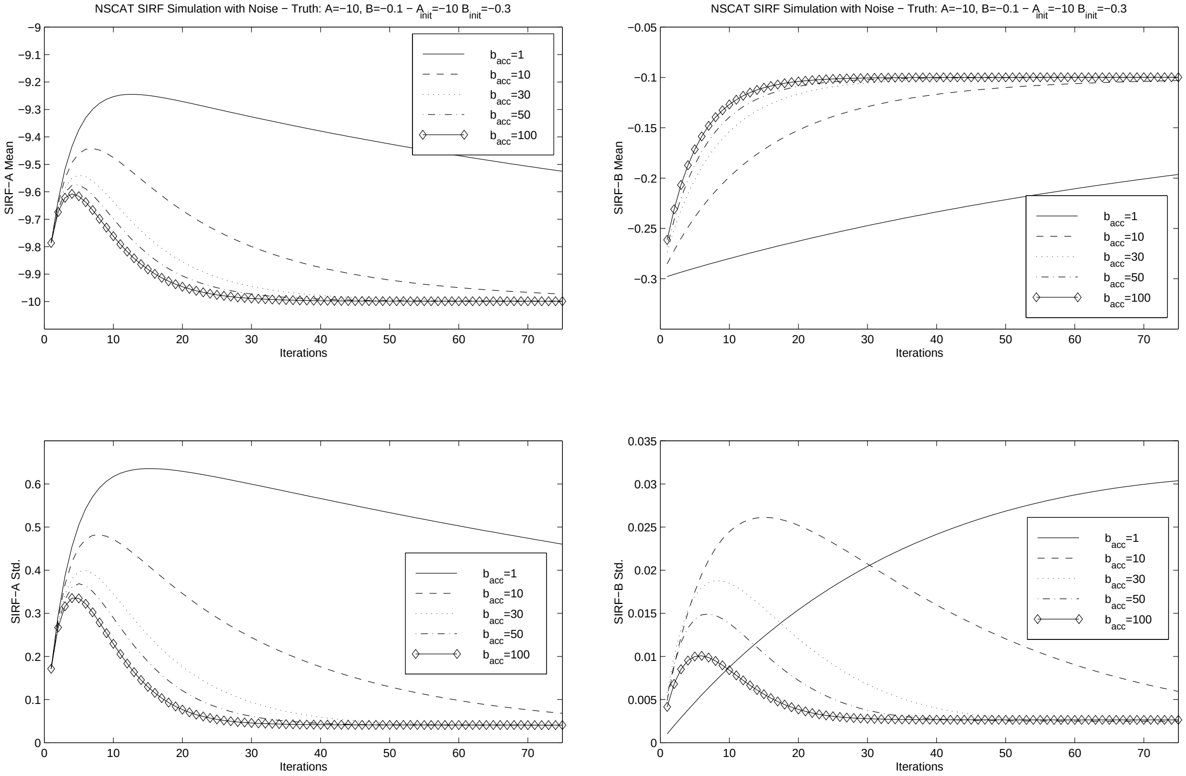

Figure 3.4: Means (top) and standard deviations (bottom) of the SIRF simulation A (left) and B (right) images with constant truth images A=-10.0 and B=-0.1. Initialization values are A_{init}=-10.0 and B_{init}=-0.3. Different values of B update weight are used.

may not converge sufficiently accurately to the desired value within a given number of iterations or may yield different solutions.

To study the effects of different initialization values, simulated measurements are used to produce enhanced resolution SIRF images. SIRF is implemented several times for each image using different initialization values. For A_{init}, values from -30.0 to -1.0 are used while B_{init} is set to various values in the range -0.3 to 0.0. B update weighting is set to b_{acc}=30 to ensure proper convergence of the B values. The mean and standard deviation of the resulting images are observed after each iteration.

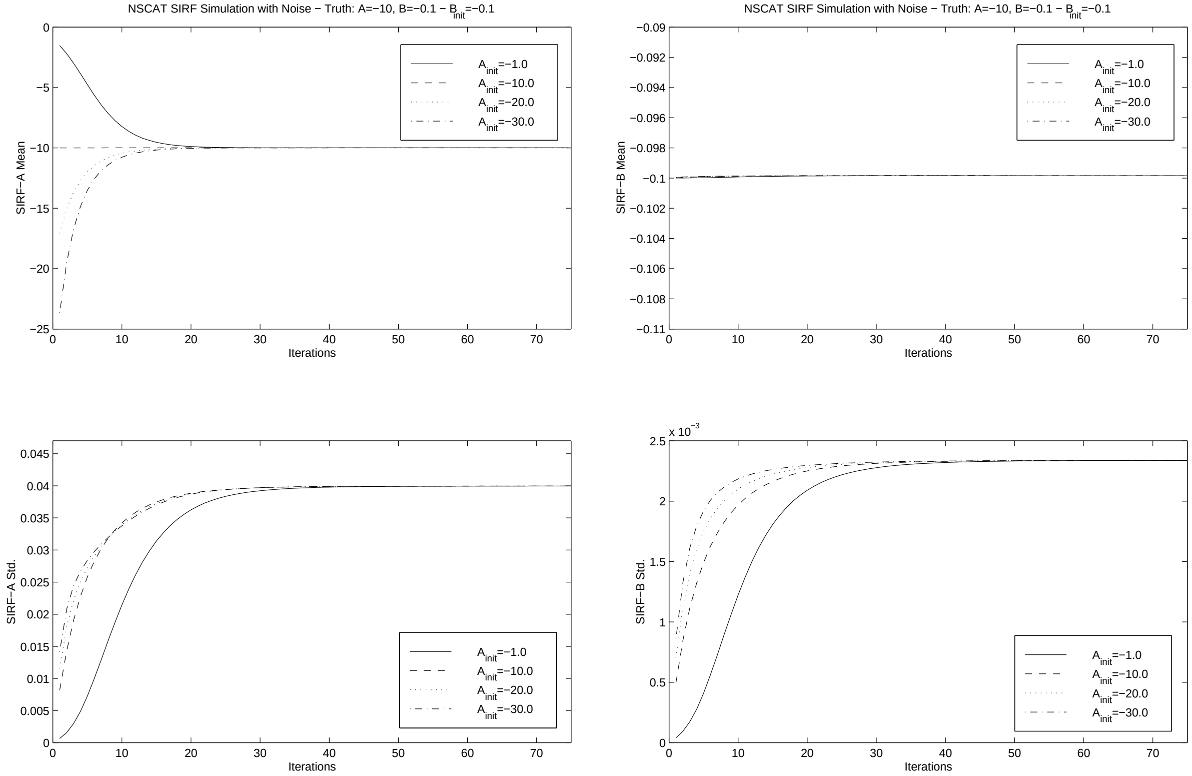

Figure 3.5: Means and standard deviations of SIRF initialization simulation A (left) and B (right) images with constant truth images A=-10.0 and B=-0.1. Different A_{init}'s are used and B_{init} is held at the true B value. b_{acc}=30 for all plots.

The first case observed uses truth images with A=-10.0 and B=-0.1. Figure 3.5 illustrates the convergence trends of the means and standard deviations of the A and B images with iteration using different A_{init} values. The mean A converges to the true value for all A_{init}'s by the 30th iteration. In general, the further A_{init} is from the true value, the longer it takes to converge. However, when A_{init} is less than the true value, the updates approach the desired value more quickly than if A_{init} is greater. The noise level in the image behaves similarly for all A_{init} values increasing with iteration number. Similar trends are noted for B.

Figure 3.6 shows the results of various B_{init} for the same truth images. A_{init} is set to the true value while B_{init} ranges from -0.3 to 0.0. The mean A value

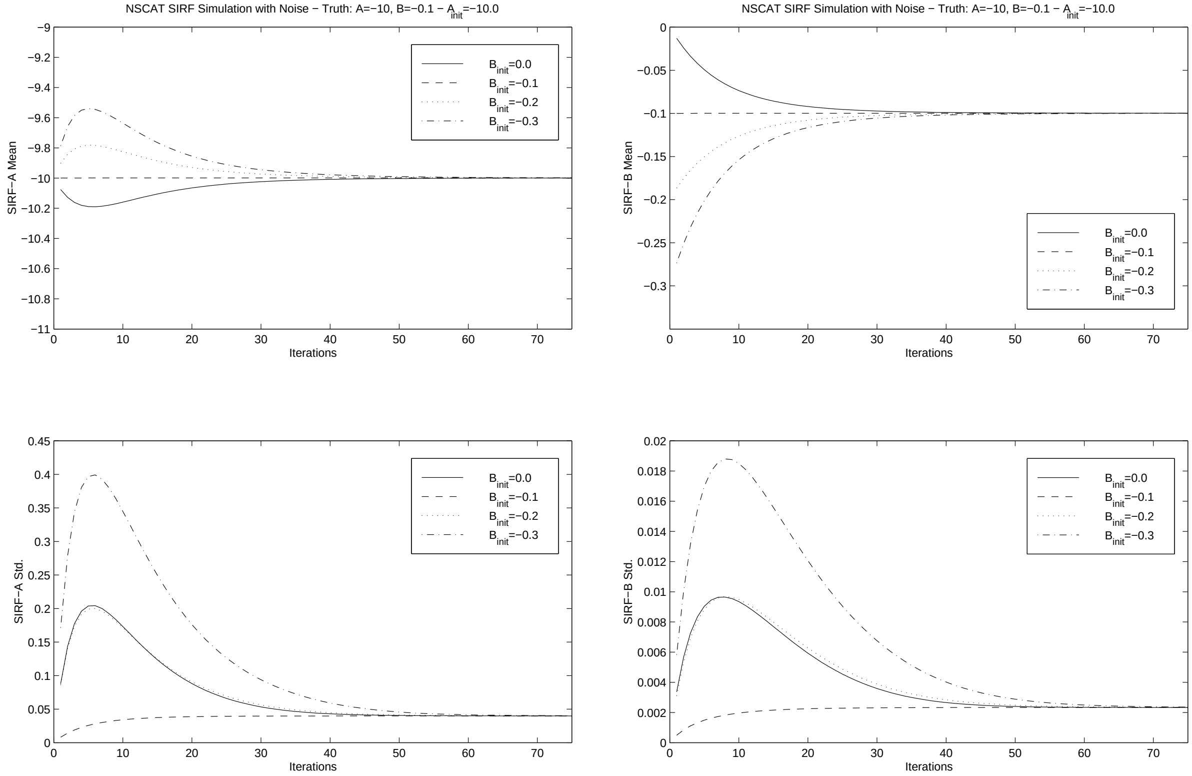

Figure 3.6: Means and standard deviations of SIRF initialization simulation A (left) and B (right) images with constant truth images A=-10.0 and B=-0.1. Different B_{init}'s are used and A_{init} is held at the true A value. b_{acc}=30 for all plots.

of the SIRF image initially diverges from the true value but returns to the true value by the 50th iteration. The noise in the A image is significantly higher during the initial iterations when B_{init} is further away from the true B. However, the noise levels converge for later iterations. Similarly, the mean B converges to the actual value by about the 50th iteration. The B noise level converges to a common value for all B_{init} values.

The same experiment is conducted for the case with true values of A=-20.0 and B=-0.2 and the same initialization values. Very similar results were obtained to the A=-10.0 and B=-0.1 case. Consequently, the corresponding plots are not included.

Several conclusions are drawn from this portion of the project. First, it is desirable for the initialization values to be close to the true values since they will converge more quickly. By setting A_{init} or B_{init} lower than the true value, convergence can be achieved earlier in the process. However, this effect is small and insignificant. Noise level is initially higher for these lower initialization values, but converges to a common value for all initializations for later iterations. These simulations were performed for constant A and B images. In a more realistic case the truth images will be nonhomogeneous with a wide range of A and B values. In an effort to balance the trade-off between convergence time and noise level, it was decided to use the means of the observed A and B images as the initial values.

To determine the optimum A_{init} and B_{init} for NSCAT SIRF images, accelerated B SIRF images are created for all land regions of the earth using NSCAT data during the period 1996 JD 276-281 to determine average A and B values. The averages are approximately A=-8.4 B=-0.14 (excluding polar regions). These values are chosen to be the A_{init} and B_{init} constant initialization images for SIRF.

3.1.5 Statistical Analysis of Simulated Images

With SIRF initialization values, number of iterations, and b_{acc} selected, the next step is to simulate SIRF using nonhomogeneous images and observe the statistical error and correlation properties between the SIRF images and the true images. Synthetic A and B truth images are created to emulate features that might be observed in actual scatterometer observations of the earth. The A and B truth images are shown in Figure 3.7 along with some simulation results discussed later. The features of these images simulate features in actual NSCAT data. The darker area simulates a river body of water with characteristically low A or B values. The large feature in the top right quadrant of the A image represents an area with gradually increasing σ^o to a common center point. The two dots represent small features that SIRF will attempt to resolve. The rest of the image is assigned an average background value. The B image features are mirrored with respect to the A image to observe the effects of SIRF on A and B individually. The images are 192x192 pixels with a span

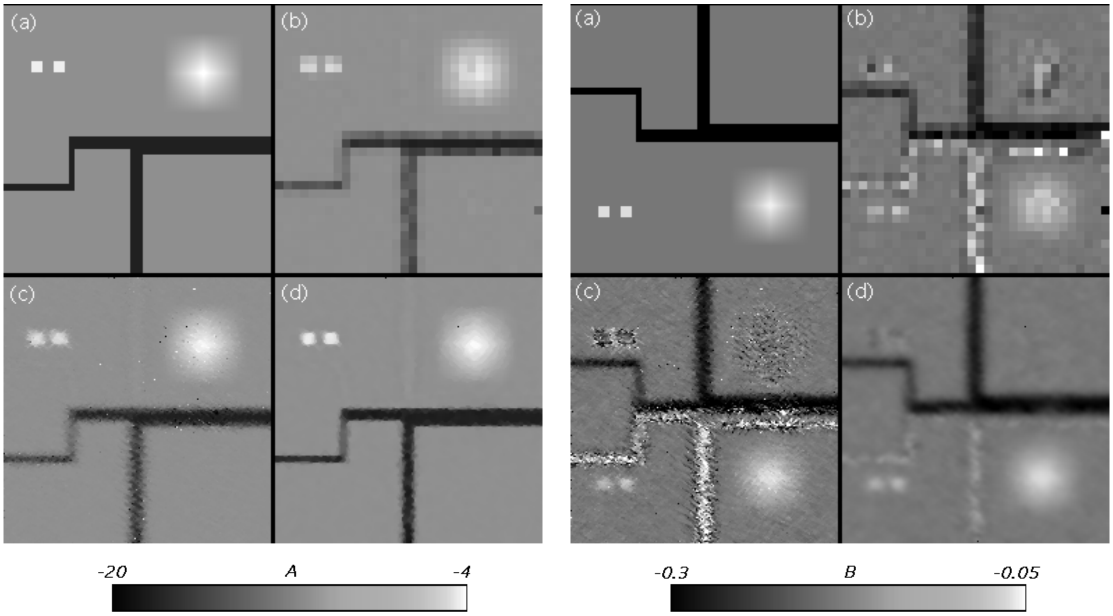

Figure 3.7: Reconstructed simulation A (left) and B (right) images with noise added. (a) Truth images, (b) Nonenhanced images, (c) AVE images, and (d) SIRF images using optimum SIRF parameters.

in latitude and longitude of 8°×8°. The resolution of the images is approximately 4.5 km/pixel.

SIRF Statistics

NSCAT data is simulated by using 10 days of real NSCAT data records over the Amazon Basin and replacing the σ^o values with synthetic σ^o values computed from the A and B truth image according to Eq. (2.2). Noisy data sets are generated. SIRF is run using the A and B initialization values determined previously (A_{init}=-8.4, B_{init}=-0.14). Several B weighting values are used and images are created after each iteration. Every image is then statistically compared with the truth image to determine error and correlation properties. The various metrics used in this development are the mean error, standard deviation of the error, RMS error, and correlation coefficient.

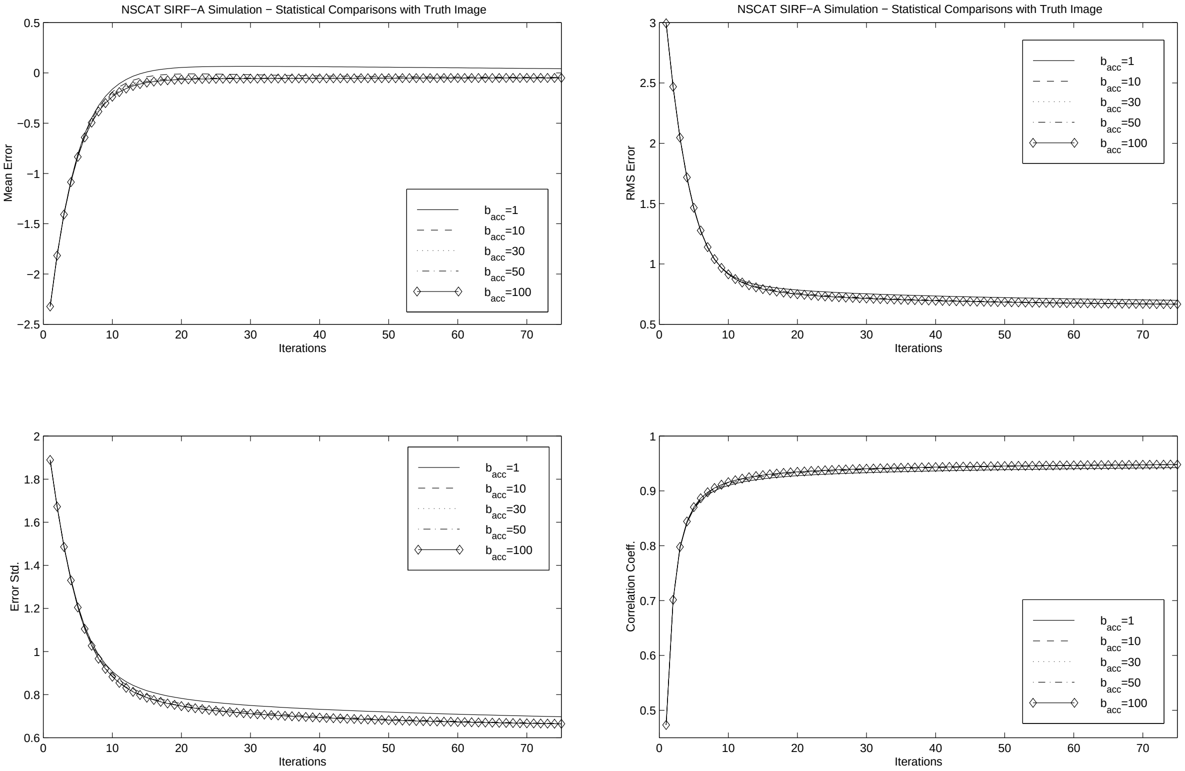

Figure 3.8: Mean error, error standard deviation, RMS error, and correlation coefficient of the SIRF A images for the noiseless and noisy cases.

Figures 3.8-3.9 depict the statistical error and correlation values for the SIRF A and B images as a function of iteration number and B update weighting. In all scenarios, all of the statistical metrics converge toward a final value as the algorithm iterates. The errors decrease and the correlation rises reaching their final values by the 50th iteration. The statistics for the A image behave similarly as iterations increase despite the different accelerated B values. On the other hand, the B image statistics are dependent on B update weighting. The mean error, error standard deviation, RMS error, and correlation coefficient reach their final optimum values more quickly for higher B acceleration. After 50 iterations, all of the error/correlation statistics are virtually the same for all cases in which the B weighting greater than or equal to 30.

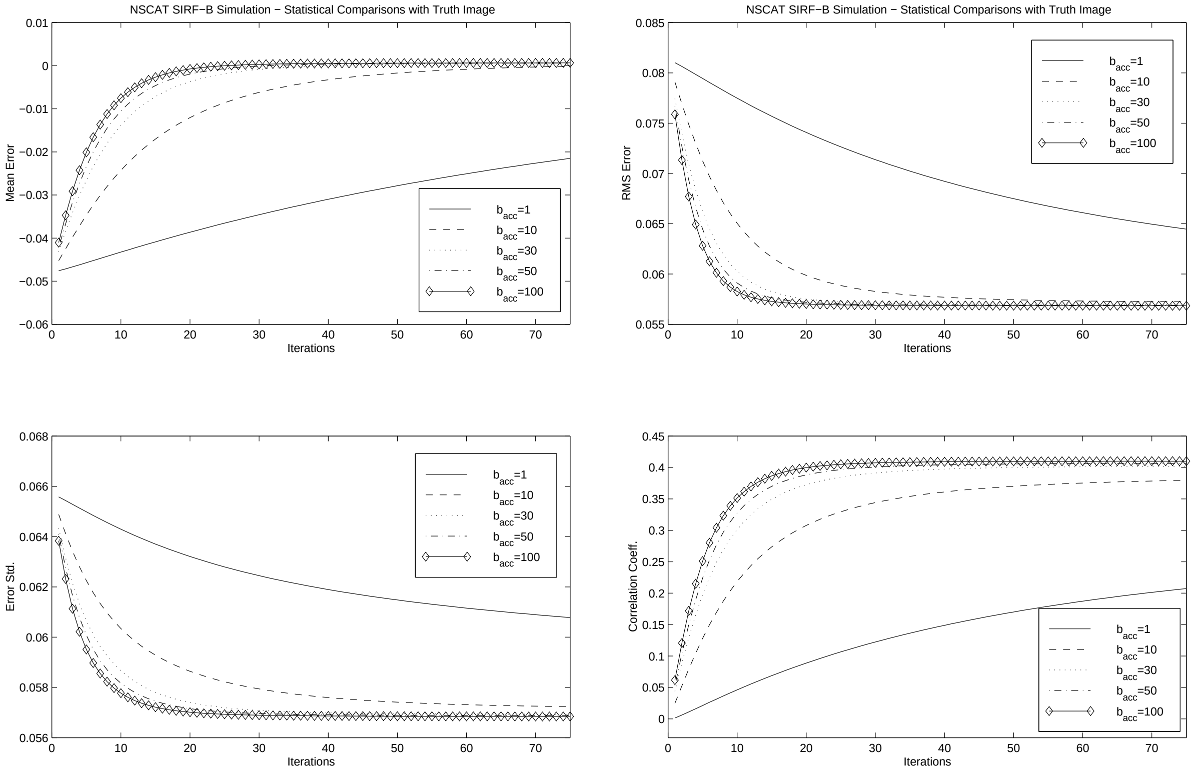

Figure 3.9: Mean error, error standard deviation, RMS error, and correlation coefficient of the SIRF B images for the noiseless and noisy cases.

The correlation coefficient for the A images approaches 0.95 while values of only about 0.40 are reached for the B images indicating that SIRF has excellent ability to estimate A but less accurate in determining B. B estimate error may be the result of excessive σ^o noise or an insufficient distribution of incidence angles of the samples to accurately determine the σ^o incidence angle dependence. This problem is addressed in the next section.

Comparison of SIRF with Other Reconstruction Methods

A and B images of the simulation region are created using other reconstruction methods as well. Nonenhanced images are produced by gridding the NSCAT footprint σ^o values onto a 25 km grid and doing linear regression. AVE images [39] are created on the same high resolution grid that SIRF uses and is essentially equivalent to the first iteration of SIRF [39].

Figure 3.7 illustrates the A value truth, nonenhanced, AVE, and SIRF images. The SIRF image uses b_{acc}=30, N=50 iterations, A_{init}=-8.4, and B_{init}=-0.14. The nonenhanced image shows the general features, but does not define the smaller features well. The AVE image reveals more high frequency information but the edges still appear low-pass filtered. The SIRF image has sharper edges and more defined features. Still the source of the distortion in the average and SIRF images is due to the filtering of the surface truth data by the aperture of the scatterometer antenna as well as by the inherent scatterometer noise. Note that the dots stand out above the noise in the average and SIRF images.

The reconstructed B images are also shown in Figure 3.7. An interesting ghost image phenomenon appears in all of the reconstructed images. That is, the A truth image features appear in the reconstructed B images and vice versa. This occurrence is most pronounced in the nonenhanced and AVE images but does not effect the SIRF images. Since the AVE image is essentially the output of the SIRF algorithm after one iteration, it is apparent that repeated iterations damp the distortion effects of A value on B. The B images have lower correlation to the truth image since the slope of σ^o vs. θ is very sensitive to σ^o noise.

Statistical error and correlation metrics for each of these images are computed and given in Table 3.1. SIRF has lower errors and higher correlation coefficients for virtually all of the metrics. In every case, SIRF has a higher correlation coefficient and lower RMS error indicating that it was most successful in reconstructing the A and B images.

3.1.6 Sampling

The accuracy of SIRF A and B estimates is highly dependent on the number of σ^o samples for a given pixel. B contains incidence angle dependence information and cannot be properly estimated unless several measurements are obtained from a variety of incidence angles. Thus, incidence angle distribution as well as the number

Table 3.1: Error and correlation statistics of reconstructed noisy images as compared to the true images. SIRF was implemented using A_{init}=-8.4, B_{init}=-0.14, b_{acc}=30, and 50 iterations.

Image	Mean Error	Error Std.	RMS Error	Corr. Coeff.
Nonenhanced A	-0.09	1.09	1.10	0.86
AVE A	-0.10	1.07	1.07	0.86
SIRF A	-0.05	0.68	0.68	0.95
Nonenhanced B	-0.00004	0.093	0.093	0.233
AVE B	0.004	0.140	0.140	0.187
SIRF B	0.0004	0.057	0.057	0.40

of measurements affect of the SIRF algorithm to reconstruct microwave scatterometer data.

The incidence angle dependence of σ^o is described by the B parameter. SIRF uses several σ^o measurements of a pixel to estimate this value. To get a good estimate of B SIRF requires a sufficient number of different incidence angle (θ) measurements as well as a good distribution of θ. An experiment is conducted in which SIRF is run for a a simulation region with constant A and B values. Simulated σ^o measurements are generated from the true values. A=-10.0 and B=-0.1 are used as the actual values. The θ values for measurements over a small 3×3 pixel subregion are set to have a uniform distribution in the range [20°-60°]. SIRF A and B estimates are computed for various numbers of measurements. Figure 3.10 displays example A and B mean values in the subregion that SIRF predicts as a function of number of measurements. The plot demonstrates that for a low number of measurements, the SIRF estimates are inaccurate. When SIRF has about 5 σ^o samples or more, the estimates are close to the true value with error a function of the noise in the measurements.

The incidence angle distribution of the measurements affect the accuracy of SIRF estimates. The dependence of estimate error on this is examined by implementing a similar simulation as described above but the incidence angles are modified

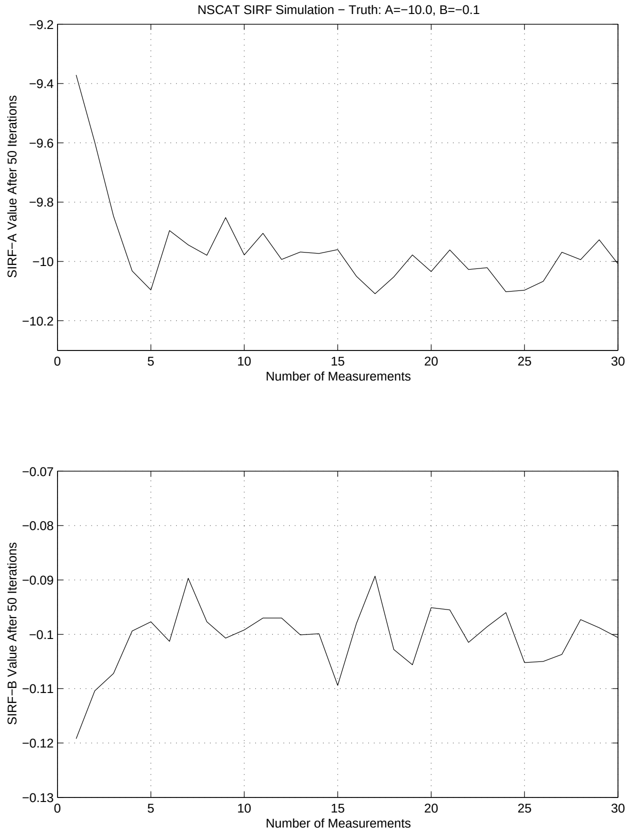

Figure 3.10: SIRF A and B estimates plotted vs. the number of measurements. The true values are A=-10.0 and B=-0.1. The estimates may be poor unless there are at least 5 samples.

to various distributions. Different realizations of random distributions of incidence angles are used and the estimates observed. The true values are A=-10.0 and B=-0.1. For each simulation, 8 measurements are used. SIRF computes A and B estimates for several measurement sets with different θ distributions. For each θ distribution set, SIRF is run 5 times (individual cases differing only in random σ^o noise) to exhibit the general trends. Figure 3.11 shows a plot of A estimates vs. B estimates for different distributions. Nearly every SIRF A estimate is within 0.1 dB of the actual value regardless of the θ distribution. Similarly, all of the B estimates have an error of less than 0.01 dB/deg. Hence, SIRF yields good estimates of A and B for NSCAT even if the θ distribution is narrow, at least for a surface where the linear σ^o model applies.

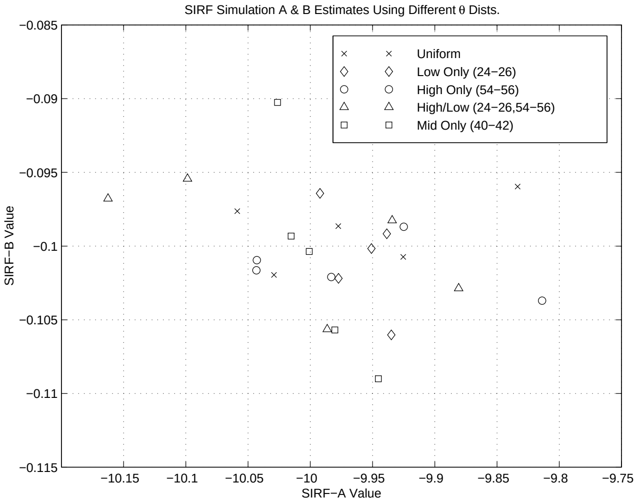

Figure 3.11: Plot of estimates of A and B values with different measurement incidence angle distributions. Eight measurements were used for each SIRF estimate. The true values are A=-10.0 and B=-0.1.

3.1.7 SIRF Optimization Conclusions

The Scatterometer Image Reconstruction with Filter (SIRF) algorithm is an effective method for high resolution image reconstruction. Several parameters of this algorithm affect its ability to enhance intrinsically low resolution scatterometer data to make it useful for non-oceanic studies. Through a non-linear procedure, SIRF iteratively updates A and B estimates to describe σ^o normalized to 40° and σ^o dependence on incidence angle.

Heavy damping of the B updates in the algorithm slow the convergence of B to the true value. B update weighting is used to speed this process. Simulations show that accelerating these updates reduces convergence time. Both A and B noise levels diverge for several iterations and then decrease, converging to a final value. This convergence occurs more quickly for higher B update weighting. After approximately 50 iterations, there is little difference in the error and noise properties of the reconstructed image as long as the B acceleration is 30 or higher.

SIRF initialization values strongly influence the convergence trends of the algorithm. When the initial values are close to the true values, convergence occurs more rapidly. When A_{init} and B_{init} are set below the true values rather than above, convergence is achieved slightly earlier in the iterations but noise level is increased. However, if enough iterations are used, convergence is to a common value for all initializations. This trade-off motivated the original choice of the mean A and B values of nonhomogeneous regions for the initialization [39]. A_{init}=-8.4 and B_{init}=-0.14 were found to be the mean global values for NSCAT land data (excluding polar regions) and thus chosen as the optimum initialization values.

Nonhomogeneous synthetic images are used to study the error and correlation properties between SIRF images and their ground truth counterparts. The statistical metrics continuously improve with increased iterations until a convergent value is reached after about 50 iterations.

In addition to these parameters, the measurement geometry can influence SIRF's effectiveness in estimating A and B. In particular, the incidence angle distribution is critical to achieving good B values. Assuming a uniform distribution of θ in the effective range of [20°-60°], SIRF requires about 5 or more samples to produce quality A and B estimates. SIRF produces good estimates for relatively narrow θ distributions as well as wide distributions.

With each of the aforementioned parameters optimized, the SIRF algorithm produces scatterometer imagery with minimum convergence time and maximum quality. An example is shown in Figure 3.12 which depicts an NSCAT SIRF A_v image of Antarctica for 1996 JD 258-263. Ice pixels have been excluded from the image. Figure 3.12 illustrates the high levels of σ^o variability contained in cryosphere regions. This information will be used in later chapters to extract critical geophysical characteristics.

3.2 Azimuthal Modulation of Polar σ^o Measurements

Image reconstruction methodologies such as SIR require an ensemble of measurements to generate an estimate of the A and B SIR parameters. An inherent

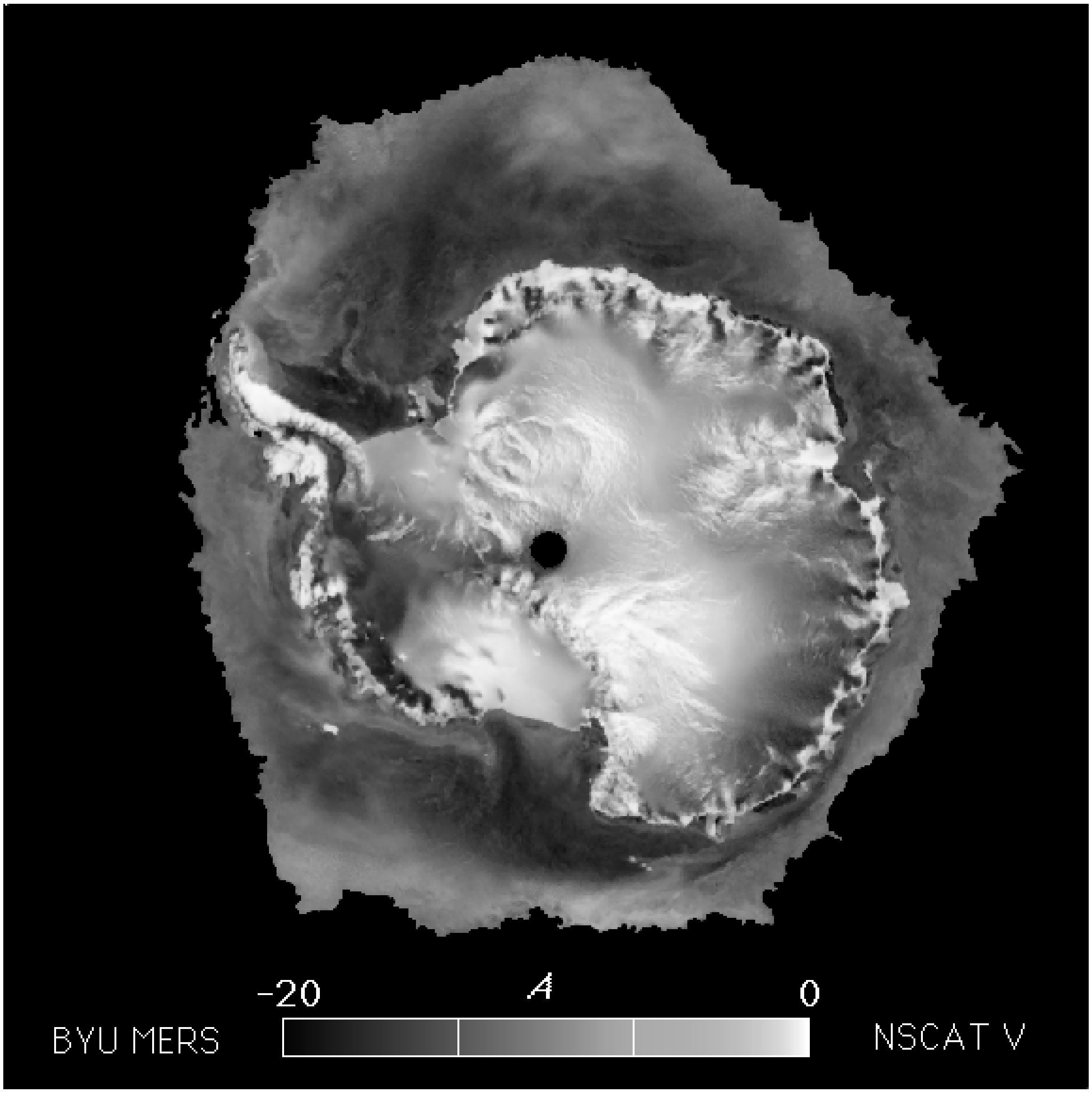

Figure 3.12: A polar stereographic projection image of Antarctica. The image is generated from 6 days of NSCAT data from JD 258 to JD 263 1996. An ice mask has been applied to the image.

assumption to the algorithm is that variations in observed σ^o measurements are only due to incidence angle or surface features. However, σ^o dependence on azimuth angle, ϕ can cause ambiguous estimates in the reconstruction. While azimuthal modulation is not expected over land and vegetated regions, it is not clear that sea ice measurements fit the azimuthal isotropy assumption. This section examines the azimuthal modulation characteristics of Antarctic sea and glacial ice to determine the applicability of this image reconstruction algorithm to the Southern Ocean region of the earth. The methods in this study follow those of Early and Long in which C-band azimuthal modulation was examined in the Antarctic [63]. The following section discusses characteristics of ice types in the Antarctic and how these characteristics contribute to the level of azimuthal modulation. The analysis process, which uses two methods to detect azimuthal modulation, is then described. Conclusions are then given.

3.2.1 Azimuthal Modulation Related Characteristics of Antarctic Ice

The Antarctic is a region of diverse ice types and characteristics. The sea ice pack fluctuates in an oscillating seasonal cycle. During the winter freeze up, the ice pack thickens and grows outward. Antarctic summer causes the ice to recede toward the continent. The ice pack itself is composed of several different ice types. Nilas, first-year ice, multi-year ice, and icebergs are examples. Continental Antarctica also consists of different ice types such as glacial ice and is much less dynamic in its nature.

Azimuthal modulation of σ^o has been observed in Antarctic glacial ice sheet. Remy et al. found a close relationship between azimuth modulated signatures at katabatic winds over the continent [42]. The sustained winds cause azimuthally oriented patterns in the snow surface that that yield higher σ^o at certain azimuth angles. Long et al. produced enhanced resolution of imagery of first and second order azimuth modulation parameters [43]. The first order terms were correlated well with continental surface slope features with the highest σ^o observed when the scatterometer measurement was oriented up slope. Second order estimation of azimuth modulation over glacial ice was strongest in areas which typically experience katabatic winds.

Figure 3.13: Photograph of pancake ice taken near the Antarctic ice pack edge. Note the edges on the pancakes which are formed by wind and wave action forcing pancakes together and piling up the edge. Courtesy of Dr. Mark Drinkwater, JPL.

Sea ice is significantly different than land ice in structure and composition. Since sea ice floats on the ocean surface, large scale slopes do not exist like those found over the continent eliminating one source of azimuthal modulation. Consequently, the only potential azimuthal modulation inducing features lie in the deformation and composition of sea ice media. These characteristics are a strong function of sea ice age and dynamics.

In order to understand potential sources of azimuthal modulation, sea ice make-up is first considered. Two basic sea ice regimes define the Antarctic ice pack. The periphery of the Antarctic sea ice pack is called the marginal ice zone (MIZ).

This region is characterized by newly formed ice floes surrounded by open water and slush [44]. During fall and winter, sea ice forms rapidly in these areas as the ice pack grows outward. Ice formation begins with grease and frazil ice which consist of slushy mixtures of water and newly formed ice crystals. Grease and frazil ice combined with ocean wave action and thermodynamic cooling begin to congeal into small floes called pancakes. Pancakes are the predominant ice form in the MIZ in early winter [45, 46]. A photograph of pancake ice in the Antarctic is shown in Figure 3.13. As cooling continues, the floes grow in size and begin to freeze into a solid ice pack. Though MIZ ice floes damp small scale waves, large surface swells can propagate into the ice pack [47]. Though transient, the swell-waves may cause limited levels of azimuthal modulation.

The dominant form of ice further within the Antarctic sea ice pack is various forms of first year ice. Antarctic first year ice ranges in thickness from approximately 30 cm to 2 m and is characterized by relatively high brine content. Surface roughnesses in this region are primarily caused by ocean wave action, inner ice pack sheering forces, and wind roughening of snow cover. Katabatic winds originating on the Antarctic continent may also cause sastrugi-like roughening of snow-covered sea ice. However, the dynamic nature of sea ice reduces the probability that these features maintain a preferential azimuth orientation. The motion and sheering forces of sea ice packs increasingly randomizes the constituent scattering elements.

3.2.2 Analysis

The study regions used in this project represent various types of sea and glacial ice. A description of these regions is given in Table 3.2. A graphical representation is given in Figure 3.14. The regions are chosen in a manner to ensure that they have little temporal variation and are spatially homogeneous. Twenty regions were chosen in the sea ice areas of Antarctica while five were chosen from the land ice and glacier areas. As described above, it is expected that little azimuthal modulation will occur over sea ice and more will occur over the glacial ice.

Table 3.2: Azimuthal modulation test regions with associated σ^o statistics.

File Name	lon	lat	deg lon	deg lat	Julian Days	Mean	Std Dev
I1	312°	-75°	8°	4°	320-330	-14.93	0.773
I2	308°	-68°	10°	4°	320-330	-13.39	2.29
I3	0°	-70°	14°	3°	320-330	-16.97	2.32
I4	200°	-76°	10°	2°	320-330	-15.87	1.41
I5	196°	-74°	8°	4°	320-330	-15.77	1.54
I6	70°	-68°	8°	3°	320-330	-16.86	2.72
I7	192°	-73°	18°	5°	320-330	-15.70	1.61
I8	324°	-72°	10°	4°	320-330	-15.08	0.904
I10	322°	-76°	8°	3°	320-330	-15.79	1.95
I11	318°	-76°	8°	3°	320-330	-14.32	1.91
I12	314°	-76°	8°	3°	320-330	-13.93	1.91
I13	310°	-76°	8°	3°	320-330	-14.70	1.704
I14	306°	-76°	8°	3°	320-330	-15.31	1.01
I15	302°	-76°	8°	3°	320-330	-15.02	2.45
I16	322°	-73°	8°	3°	320-330	-14.72	0.79
I17	318°	-73°	8°	3°	320-330	-14.77	0.84
I18	314°	-73°	8°	3°	320-330	-15.25	0.88
I19	310°	-73°	8°	3°	320-330	-15.53	0.92
I20	306°	-73°	8°	3°	320-330	-15.90	1.16
I21	302°	-73°	8°	3°	320-330	-16.70	1.11
G1	140°	-78°	10°	2°	320-330	-4.03	0.90
G2	120°	-72°	10°	2°	320-330	-13.66	2.25
G3	40°	-74°	10°	2°	320-330	-7.25	1.91
G4	40°	-78°	10°	2°	320-330	-7.37	0.76
G5	80°	-72°	10°	2°	320-330	-12.09	3.35

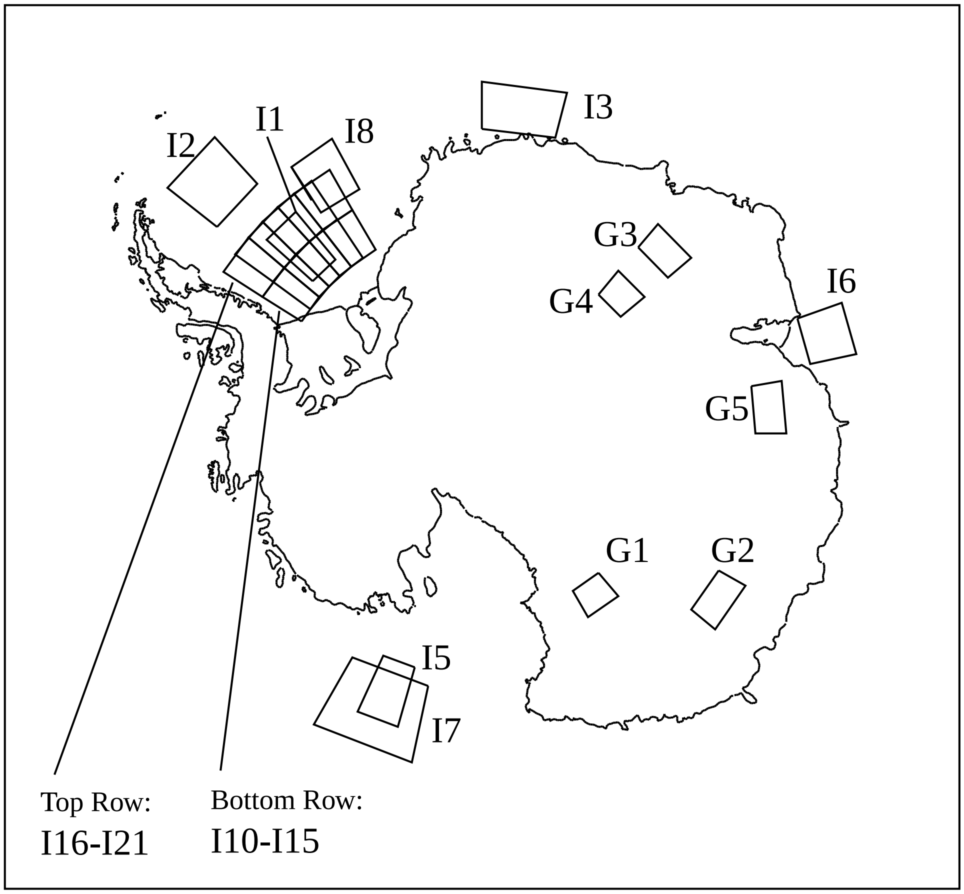

Figure 3.14: Antarctic sea ice and glacial ice study regions. From [63].

Removal of Incidence Angle Dependence

This study is performed to determine if azimuthal modulation is incidence angle dependent. If there is no incidence angle dependency, then one incidence angle range can be used for the rest of the study. If this dependency does exist, representative ranges of incidence angles need to be used in the study for the different swath regions (near, mid, and far).

For this project, 5 degree wide incidence angle ranges are used. The following are the ranges: 20-25, 25-30, 35-40, 40-45, 45-50, 55-60. For each of the ranges (for a given region), a histogram of record azimuth angles is produced to determine if there is enough azimuth angle diversity in the sampled data. Also, a σ^o time history is plotted to evaluate temporal dependencies. The mean and standard deviation of this history are computed. Finally, a scatterplot of σ^o versus azimuth angle is plotted to visually detect any azimuthal modulation.

Figure 3.15a illustrates an example of these plots for sea region I1 for the incidence angle range [40°-45°]. The histogram demonstrates that the measurements for this region have good azimuth angle diversity. The time plot supports the argument that this region is relatively temporally invariant. Finally, the σ^o versus azimuth angle plot shows that there is little variation of σ^o with azimuth angle and thus little azimuth modulation. In contrast, Figure 3.15b shows the same plots for region G2 - a glacial region. Again, there is good azimuth angle diversity. However, azimuth modulation is observed since σ^o is clearly a function of azimuth angle. A difference of 5 dB in σ^o is observed at different angles. In the interest of space, only sample plots are included in the analysis.

The number of records, mean, and standard deviations of all the regions are plotted as a function of incidence angle in Figures 3.16-3.18. Invariably the incidence angle range of 40-45 degrees has the most records and the most azimuth angle diversity. This suggests that these incidence angle ranges are the best to use for the study since we can get the most σ^o samples in the shortest amount of time. Of course, the azimuthal modulation study of an exclusive range of incidence angles can only be done if there is low incidence angle dependence in the azimuthal modulation.

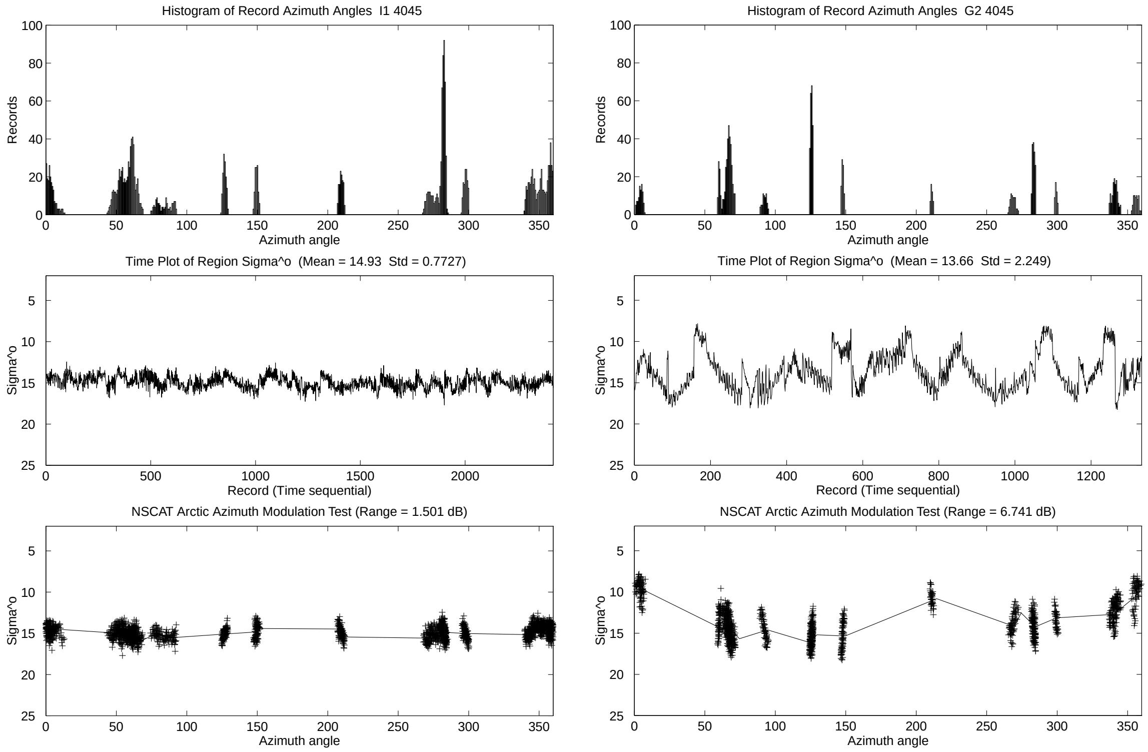

(a) (b)

Figure 3.15: Plots illustrating the azimuth angle diversity, σ^o temporal dependence, and σ^o vs. azimuth angle for sea ice region I1 (a) and glacial ice region G2 (b). All measurements have incidence angles in the range [40°-45°].

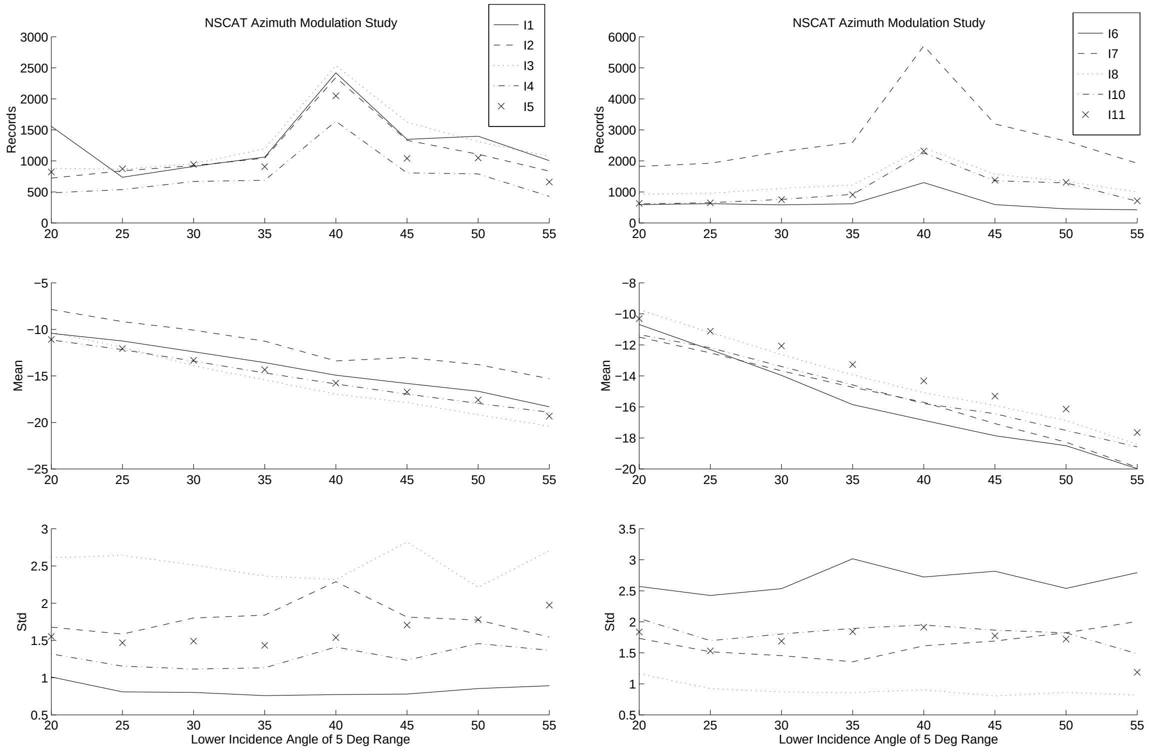

(a) (b)

Figure 3.16: Plots of the number of records, mean σ^o value, and σ^o standard deviation values vs. incidence angle for sea ice regions 1-5 (a) and 6-11 (b).

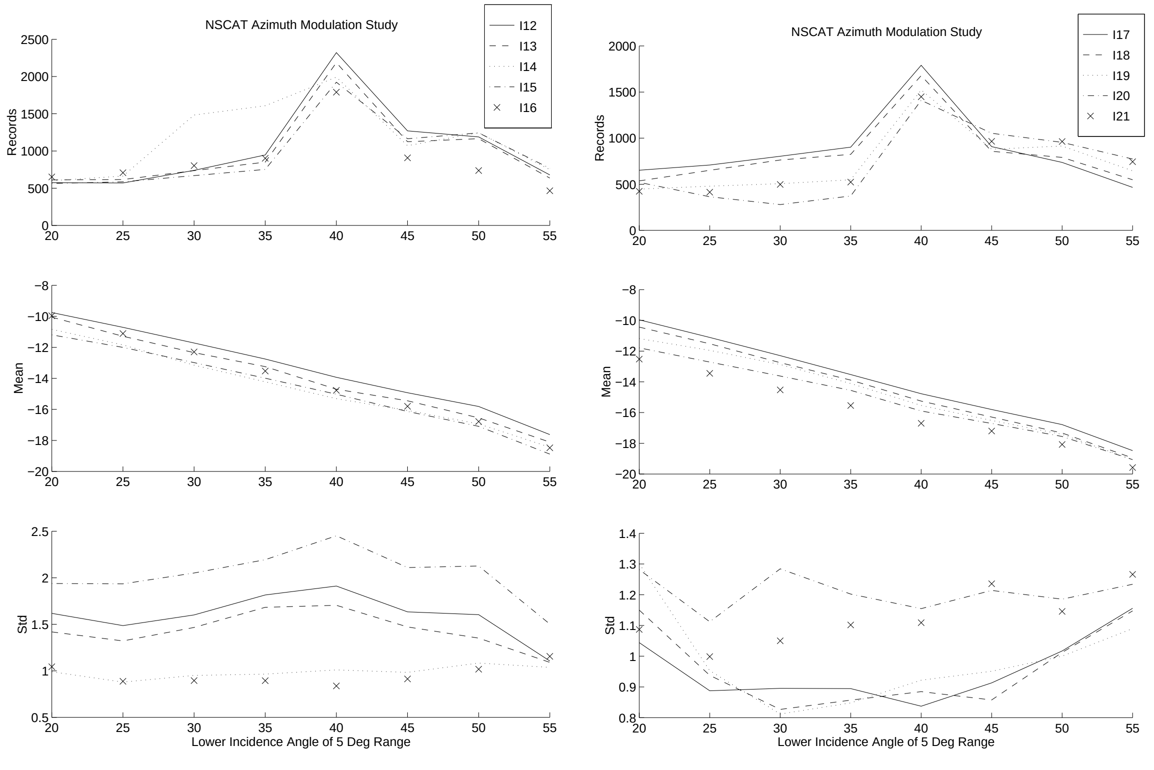

(a) (b)

Figure 3.17: Plots of the number of records, mean σ^o value, and σ^o standard deviation values vs. incidence angle for sea ice regions 12-16 (a) and 17-21 (b).

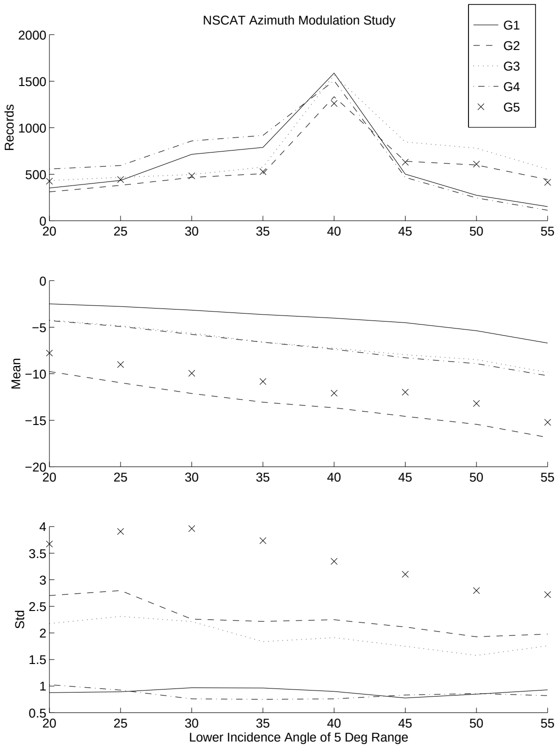

Figure 3.18: Plots of the number of records, mean σ^o value, and σ^o standard deviation values vs. incidence angle for glacial ice regions 1-5.

The plots also show that the σ^o time history mean for each region is nearly linearly dependent on incidence angle with higher incidence angles yielding lower σ^o. For sea ice, the slope of the lines are nearly always the same for different regions - just shifted up or down from one another. The glacial regions have less constant slope as different regions are observed. Also, the slopes are flatter in general than the sea ice regions.

The standard deviations of the data from each region and at each range of incidence angles seem to be relatively flat. That is, as incidence angle is changed, the standard deviation is essentially constant, normally within a .5 dB range (between max std and min std). If the standard deviation is any indication of azimuthal modulation, this result suggests that the azimuthal modulation is not incidence angle dependent. However, this metric does not provide conclusive results about azimuthal modulation dependence on incidence angle. Thus, a more in depth study is done by manually interpretting the data for each region and at each incidence angle.

Ku-band σ^o versus Azimuth Angle

The σ^o versus azimuth angle scatterplots described above give a good visual indication of azimuthal modulation. If the σ^o values are a function of the azimuth angles, modulation exists to some degree. As a metric of this phenomenon, the mean of every σ^o within 5 degree azimuth bins is computed and plotted over the top of the scatterplot. The range (max - min) of this curve gives a rough indication of how much σ^o changes through the possible range of azimuth angles. This range is computed for each region and each incidence angle range and plotted for each of these ranges. Two factors must be considered in the interpretation of the range plots. First, the overall levels of the curves is an indication of the level of azimuthal modulation present. The second factor is the amount of variability in the range as incidence angle changes. This latter consideration reveals any incidence angle dependence of the azimuthal modulation.

The range metric versus incidence angle plots for each region is given in Figure 3.19. As shown in the plots, sea ice regions have relatively low ranges (from

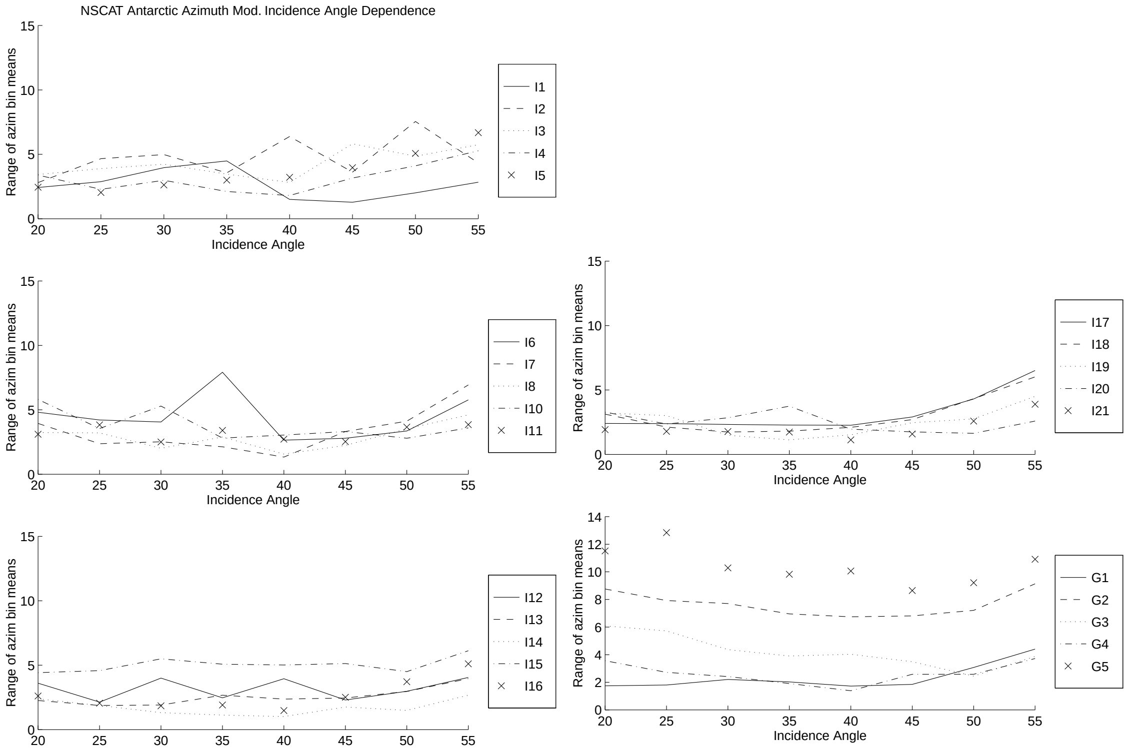

(a) (b)

Figure 3.19: Plots of range of σ^o values at different azimuth angles versus incidence angle for sea ice regions 1-16 (a) and for sea ice regions 17-21 and glacial regions 1-5 (b).

about 1 to 5 dB) when compared with some of the glacial regions. The latter have a range from around 1 to 15 dB. This leads to the conclusion that less azimuthal modulation occurs for sea ice than for some glacial regions.

The mean σ^o range metric can be used to draw a second conclusion about azimuthal modulation - azimuthal modulation has low dependence on incidence angle. This is due to the fact that the range parameter changes only slightly with incidence angle for all observed regions (about 1-2 dB). Most regions follow the general trend of constant spread in the near and mid swath (20-45 deg) and gradual increase in the far swath (45-60 deg) possibly suggesting slightly more azimuthal modulation at the higher incidence angles.

Fore-Aft Difference Analysis

I next investigate the fore-aft difference in σ^o values. Since the fore and aft beams are about 90 degrees offset in azimuth angle from one another, taking the difference between fore beam cells and aft beam cells in the same surface region and at the same incidence angle can yield and indication of azimuthal modulation. The observed σ^o can be viewed as the sum of a signal random variable with a noise random variable having a zero mean Gaussian distribution. The difference between the fore and aft beam measurements may be modeled by:

$$D = (\sigma^o_F + N_F) - (\sigma^o_A + N_A) \tag{3.28}$$

where N_F and N_A are independent Gaussian noise terms associated with the fore and aft beam measurements, respectively. For an azimuthally isotropic medium, $\sigma^o_F - \sigma^o_A = 0$ since the incidence angles for each measurement are equal, and D becomes the difference of the noise terms:

$$D = N_F - N_A. \tag{3.29}$$

When the difference is taken over an area with no azimuthal modulation (identical σ^o signal random variable values) the signal terms cancel one another and the difference in noise terms remains. Since the difference of two Gaussian random variables is a Gaussian random variable, we conclude that in regions with no azimuthal modulation the distribution of the fore-aft σ^o difference will be zero mean Gaussian.

Next, plots are considered which contain: 1) a histogram of the difference measurement azimuth angles, 2) a histogram of fore-aft difference values, and 3) a scatterplot of the fore-aft difference versus azimuth angle. For the fore-aft difference histogram, a Gaussian distribution (dotted line) with the same mean and variance was also plotted. Samples of these plots are shown in Figure 3.20 for regions I2 and G2. I2 is a sea ice region while G2 is a glacial ice region.

Examination of the histograms for all the regions reveals that for the sea ice regions, the distributions are almost invariably near zero mean Gaussian as predicted. This indicates the absence of significant azimuth modulation in the backscatter signatures of these regions. For each of these fore-aft histograms, the mean and standard

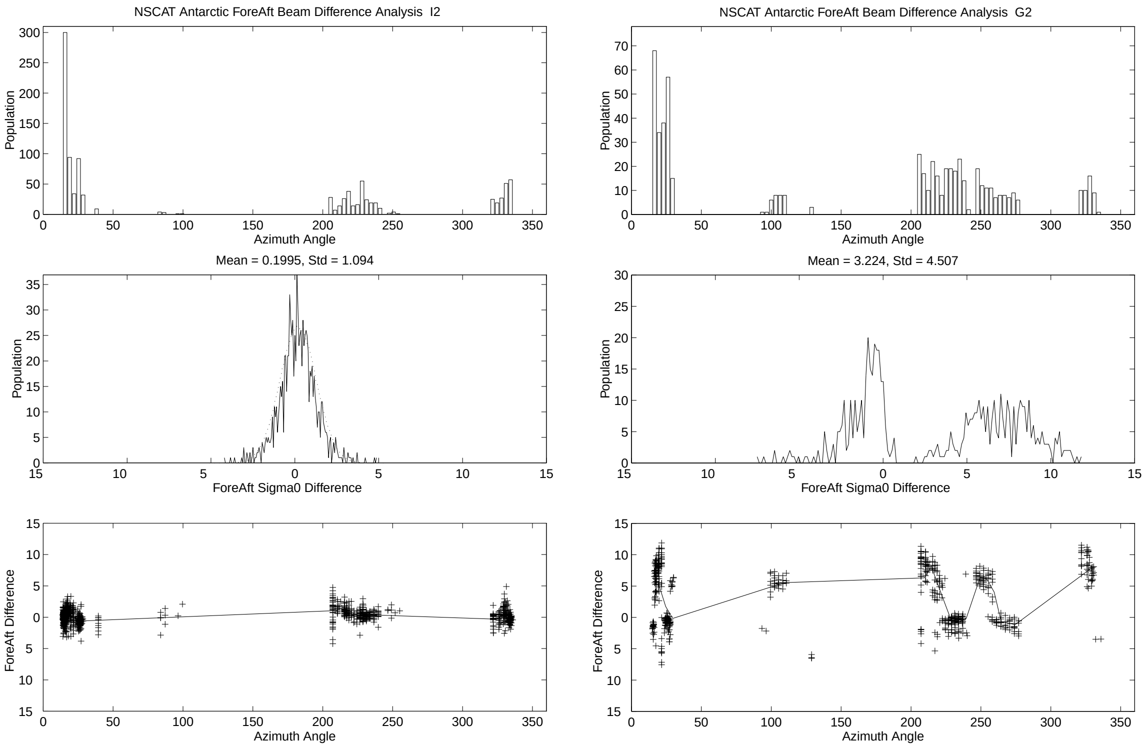

(a)

(b)

Figure 3.20: Plots illustrating azimuth angle diversity, the distribution of the fore-aft σ^o difference, and the fore-aft σ^o difference versus azimuth angle for sea ice regions I2 (a) and G2 (b). Note in (a) that the fore-aft σ^o difference is approximately zero-mean Gaussian indicating the absence of azimuth modulation. In contrast, (b) is not zero-mean Gaussian indicating the presence of azimuth modulation.

deviation is given at the top of the plots. With only two exceptions, the means of these distributions are below 0.6 dB. We conclude from this that less than 0.6 dB of azimuthal modulation occurs in the sea ice regions of Antarctica. The non-zero mean may result from two sources. First, it may be caused by a low level of azimuthal modulation. Second, it may be an artifact of the incomplete calibration of the NSCAT data at the time of this study. Without proper beam balancing some bias will appear in the fore-aft difference. It is expected that after the data is processed with the correct calibration factors, the results will be more accurate.

An observation of similar plots of the glacial ice regions reveals some interesting features. Two of the five regions have distributions very similar to the characteristic sea ice distribution. That is, nearly zero mean Gaussian indicating low azimuthal modulation. The other regions have bimodal distributions leading to the conclusion that in the difference the signal terms do not cancel one another and more than just noise remains. We conclude from this that these areas have microwave properties conducive to azimuthal modulation in the backscatter signatures.

3.2.3 Conclusion

From this study we conclude that little azimuthal modulation (less than 1 dB) occurs in the sea ice regions of Antarctica for NSCAT scatterometer data. Some glacial regions exhibit a significant level of modulation in the data. These results support those of Early's ERS-1 C-Band study [63]. Two methods were used to assess the level of azimuthal modulation for a given region. The first technique observed variations in σ^o versus azimuth angle. Azimuthal modulation appears as changes in σ^o levels at different azimuth angles. The second involved an analysis of the fore-aft beam difference. The distribution of the difference reveals the level of azimuthal modulation. The conlusion that can be drawn from this experiment is that azimuthal modulation can be neglected for sea ice for NSCAT data. That is, modulation in these regions will not significantly affect applications that require isotropic responses such as resolution enhancement.

3.3 Inter-instrument Scatterometer Calibration

While the previous two sections have dealt with issues of image reconstruction, this section considers an important topic in the proper interpretation of reconstructed scatterometer imagery - inter-instrument calibration. Various remote sensing programs have launched the same sensor design aboard different satellite platforms. Examples are the SSM/I instruments which fly on the DMSP platforms and the AMI scatterometers on ERS-1 and ERS-2. If identical instruments exhibit significant differences in measurements coregistered in space and time due to instrument calibration, signature interpretation becomes difficult. This section considers one such scenario in the ERS-1 to ERS-2 sensor transition.

The European Space Agency's (ESA) ERS missions consist of two remote sensing satellites, ERS-1 and ERS-2. The first was launched in July 1991 and collected data until June 1996. The second was put into orbit in April 1995, but was not fully commissioned until April 1996. ERS-2 is still in operation. Both of these satellites carry the active microwave instrument (AMI) scatterometer described in Chapter 2.

A critical issue in the use of data from the ERS-1 and ERS-2 AMI scatterometers is proper calibration. This ensures a seamless transition from one instrument to its successor and provides confidence that signatures obtained from each are consistent. Several months of the ERS-2 mission were devoted to this task when both ERS-1 and ERS-2 were simultaneously operating. However, analysis of the data during the brief instrument overlap period indicates that a calibration problem may exist. The following section describes and resolves the discrepancy.

3.3.1 ERS-1/ERS-2 Data Collection

The ERS-1 and ERS-2 AMI scatterometer data sets overlap during approximately 1996 JD 123-155. This is an opportune time to measure similarity in the σ^o signatures measured by the two instruments. In a study of the transition from ERS-1 to ERS-2, an inconsistency is observed in the overlapping data. Figure 3.21 illustrates the problem. This plot was generated by looking at enhanced resolution average σ^o values normalized to 40° incidence in a small region of the Ronne Ice Shelf. The characteristic seasonal signature from early 1992 through mid-1996 is evident. During the cross-over period in which both ERS-1 and ERS-2 σ^o data are available, there is only a slight discrepancy between the signatures observed by the two instruments. However, immediately after ERS-1 was switched off, the ERS-2 trend decreases rather than increases as in previous seasons. A 0.2 dB upward shift of the ERS-2 signature would make it more believable during this portion of the year.

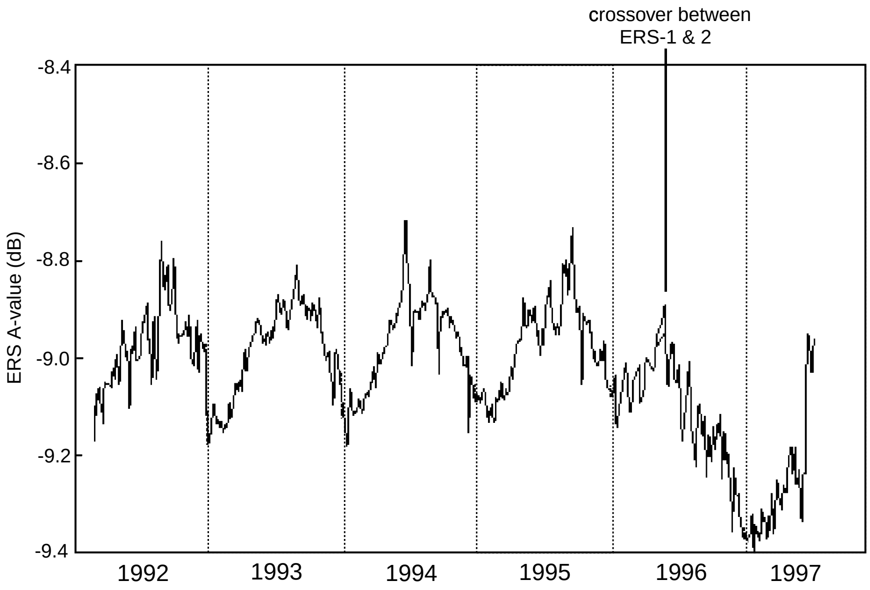

Figure 3.21: Plot of ERS-1 and ERS-2 average SIR-A (σ^o at 40° incidence) as a function of time using the JPL defined region of the Ronne Ice Shelf. From A. Bingham, JPL.

3.3.2 Possible Sources of the Discrepancies

Several possible explanations for the observed discrepancy may exist. These include diurnal variations of σ^o signatures, azimuthal modulation, calibration problems, actual differences in the seasonal σ^o response of 1996 compared to previous years, or a combination of these.

The first explanation is the possibility of diurnal variations in the study region. If ERS-1 and ERS-2 observe this region during different times of the day, and if there is a slight time of day dependence of σ^o, it is expected that differences in signatures would exist. For example, suppose ERS-1 collects measurements during a portion of the day in which the surface has very little melt with characteristically high σ^o values. Now suppose ERS-2 observes the same region during a time of the day when water content is slightly higher and σ^o values are correspondingly lower. The overlap period of occurs during Antarctic fall. In addition, the study region in the Ronne Ice Shelf is quite far south. These two factors would seem to indicate that the temperature in this region should rarely rise to levels that would allow any water content to accumulate during any portion of the day. However, for completeness, the issue of diurnal variations was considered.

The next possibility is azimuthal modulation of σ^o. Azimuthal modulation occurs when the σ^o signature of a distributed target is not only a function of incidence angle, but also azimuth angle. The azimuth angle dependence is exploited in determining ocean wind vectors from σ^o measurements taken at multiple azimuth angles. Due to the orbit geometry and beam configuration of the ERS-1/2 satellites, a region on the earth typically is observed at several azimuth angles (or ranges of azimuth angles) repeatedly over an extended period of time. While the satellites are in very similar orbits, any slight differences would cause a particular region to be observed at slightly different azimuth angles by the two scatterometers. If the study region exhibits azimuthal modulation of σ^o, a discrepancy is σ^o values would be observed.

Another source to be considered is a calibration problem between the two instruments. This should appear as a bias in ERS-2 σ^o over ERS-1 σ^o regardless of incidence or azimuth angle.

The final source of the discrepancy may be due to actual changes in the surface σ^o trend of the Ronne Ice Shelf in 1996 from previous years. While not likely, changes in ice shelf climate during this year may have produced the observed differences. This is consistent with the observations of Bingham that the differences of σ^o signatures for ERS-1 and ERS-2 were quite small during the overlap period (*A. Bingham, personal communication*).

Each of these possibilities have the potential to cause the discrepancies observed in ERS-1/2 σ^o signatures. The next section examines raw data taken from these two instruments in an effort to determine if one or a combination of these factors are responsible for the problem.

3.3.3 Data Analysis

In an effort to duplicate the results of Bingham shown in Figure 3.21, a small subregion of the Ronne Ice Shelf was defined. The region is bounded by -58.0°

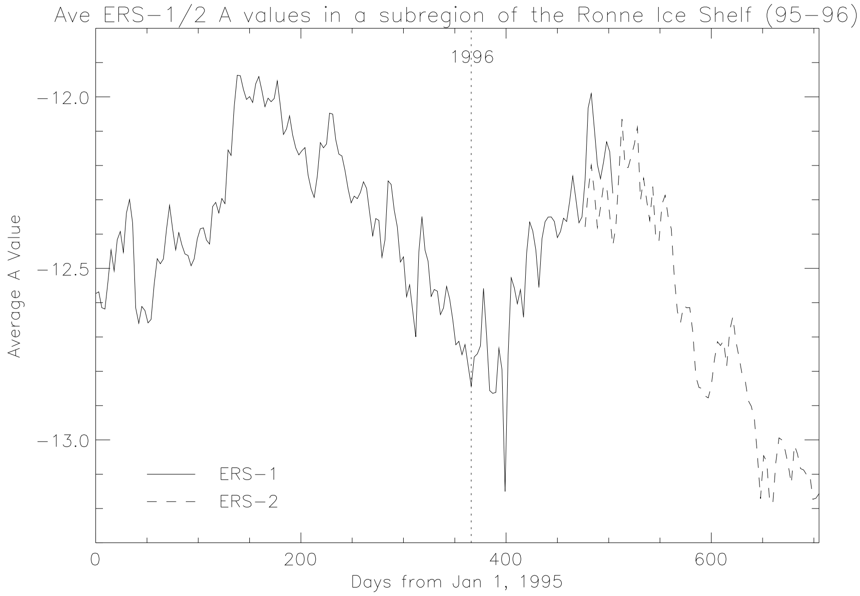

Figure 3.22: Plot of ERS-1 and ERS-2 average SIR-derived A (σ^o at 40° incidence) as a function of time using the BYU defined region of the Ronne Ice Shelf.

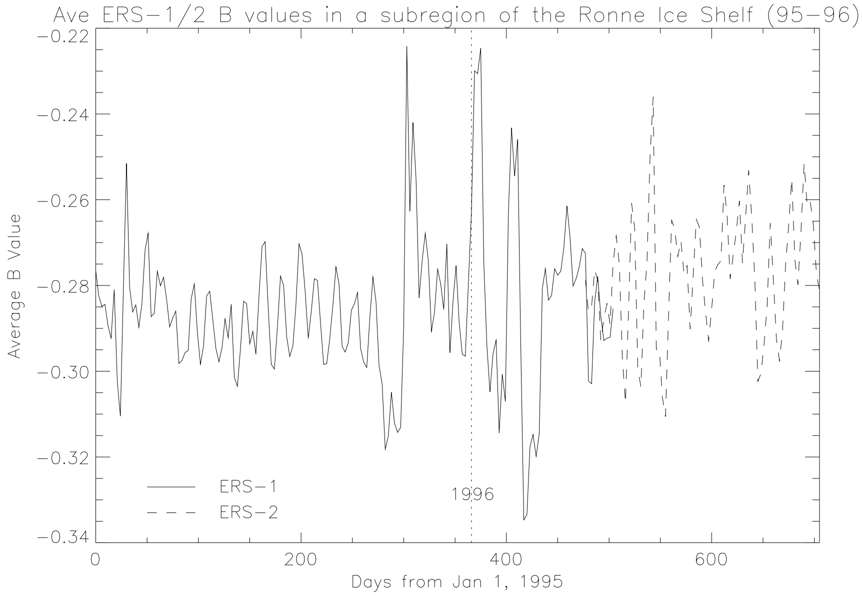

Figure 3.23: Plot of ERS-1 and ERS-2 average SIR-derived B (incidence angle dependence of σ^o) as a function of time using the BYU defined region of the Ronne Ice Shelf.

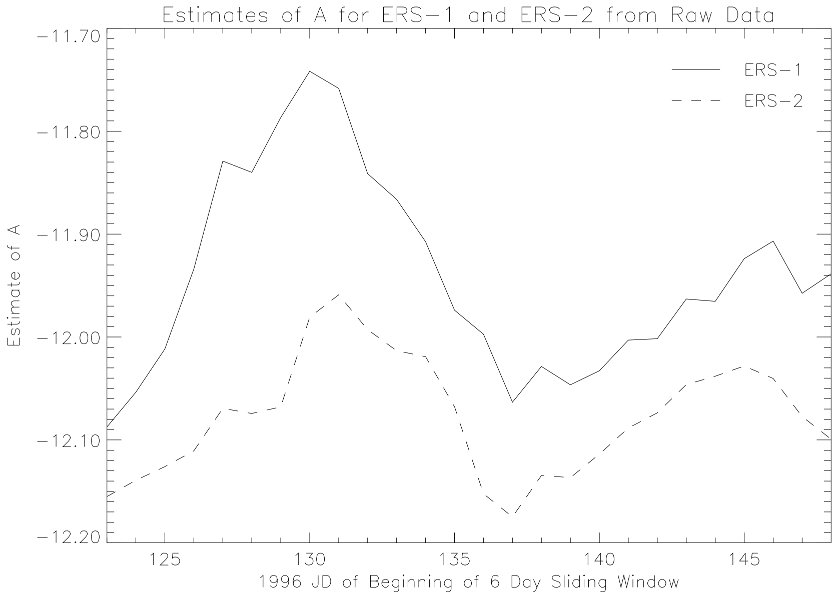

Figure 3.24: Plot of ERS-1 and ERS-2 raw data *A* values computed with a linear regression on data in a 6 day sliding window as a function of time.

to -56.0° longitude and -77.0° to -76.5° latitude. ERS-1 and ERS-2 SIR *A* images were examined in this region for all of 1995 and 1996. For each 6 day image, the average *A* value was computed in this region and plotted as a function of time. The result is shown in Figure 3.22. The corresponding *B* plot is shown in Figure 3.23. While it includes only 1995-1996 data and is likely from a different subregion than was used by Bingham, Figure 3.22 is similar to the results found in Figure 3.21. That is, the ERS-2 trend seems to be 0.2-0.3 dB lower than ERS-1 exhibited during the previous year. However, in Figure 3.22 the discrepancy exists during the overlap period as well. Indeed a 0.2 to 0.3 dB upward shift of the ERS-2 data produces better agreement to ERS-1 during both the cross-over time and afterwards.

The data for Figures 3.21 and 3.22 are taken from images reconstructed using the scatterometer image reconstruction (SIR) technique. To guarantee that the discrepancy in question is not an artifact of the reconstruction algorithm, *A* and *B* values are estimated from the raw data in the study region during the overlap period.

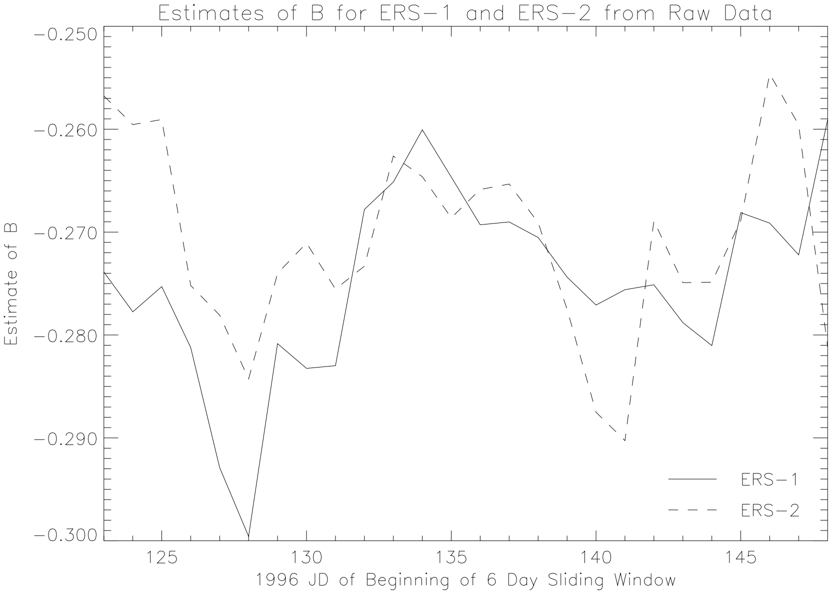

Figure 3.25: Plot of ERS-1 and ERS-2 raw data B values computed with a linear regression on data in a 6 day sliding window as a function of time.

This is done by performing a simple linear regression on all of the data in a 6 day sliding window. The results are shown in Figures 3.24 and 3.25. The plot of the A values clearly shows that the discrepancy exists in the raw data as well as the SIR reconstructed images.

The next step is to examine possible sources of the discrepancy as described in the previous section. These are diurnal variations, azimuthal modulation, and incorrect calibration. Since Figure 3.22 seems to rule out the hypothesis of actual differences in surface response in 1996 over previous years, it is not explicitly addressed in this section.

Diurnal Variation Hypothesis

The first hypothesis considered is that a combination of diurnal variations in σ^o responses and differences in typical observation times of ERS-1 and ERS-2 cause the discrepancy. To evaluate this hypothesis, the time of day for each measurement is

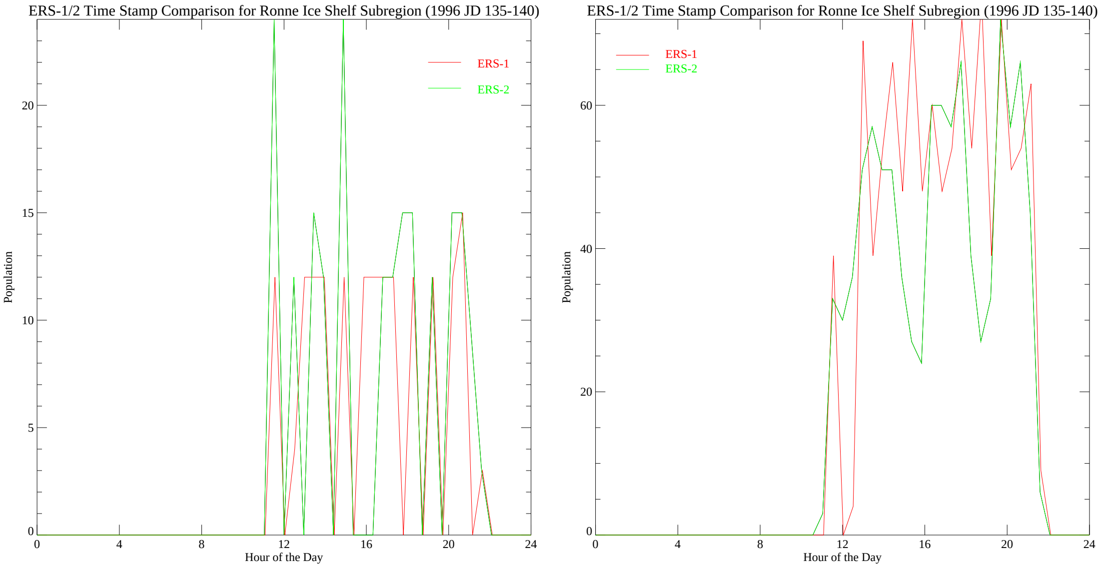

(a) (b)

Figure 3.26: Histograms of measurement time for ERS-1 and ERS-2 during 1996 JD 135-140 (a) and 1996 JD 123-155 (b).

examined for each instrument. Figure 3.26a is a histogram of the hour of the day in which measurements were taken of the study region during 1996 JD 135-140 for both instruments. From this we see that both ERS-1 and ERS-2 collect measurements of this region between 11 am and 10 pm. Several discrete times within this range are typical observation times. Both instruments cover the time range and the discrete times match well with some minor differences. ERS-1 has a bias towards the earlier measurement times during JD 135-140 which may cause some bias in σ^o values if diurnal variability is present. However, this was not typical of the entire overlap period as shown in Figure 3.26b. The absence of any obvious difference in the typical observation times of ERS-1 and ERS-2 seem to indicate that this is not a major factor in the discrepancies detailed above.

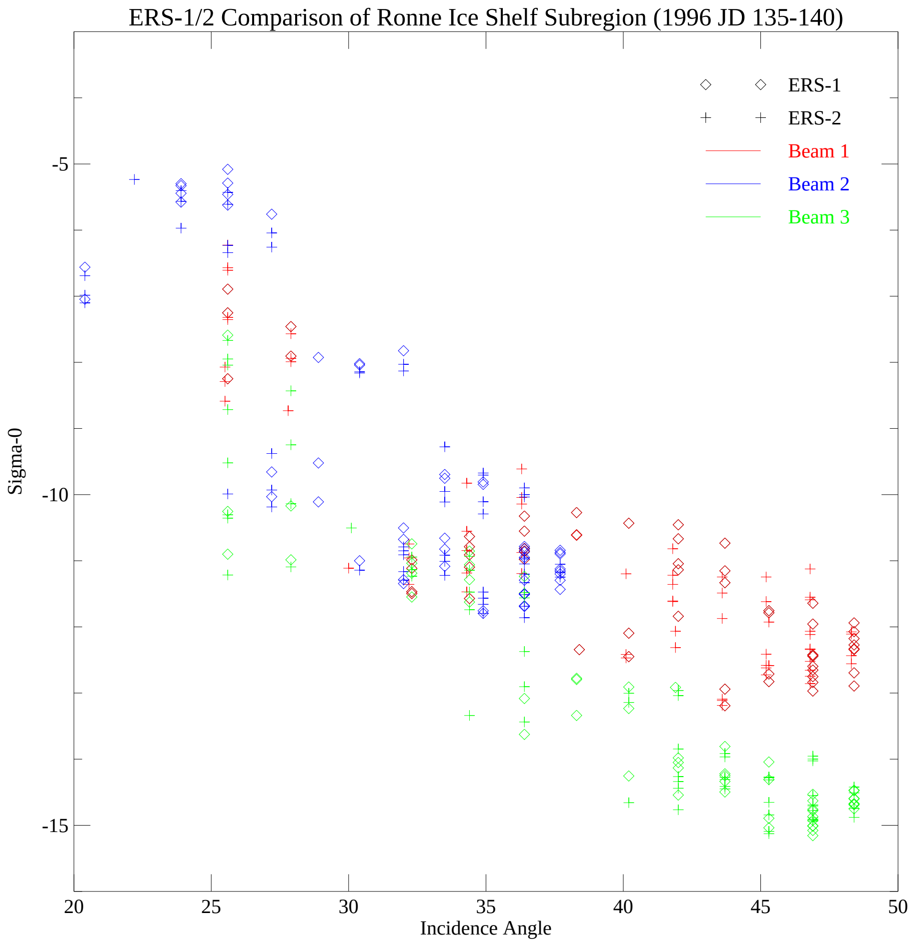

Figure 3.27: Scatter plot of σ^o vs. incidence angle for each beam of ERS-1 and ERS-2 during 1996 JD 135-140. The beams are color coded. The data from different instruments can be differentiated by plot symbol.

Azimuthal Modulation Hypothesis

In addition to temporal dependence of σ^o, azimuth dependence may also be a factor in discrepancies between the two instruments. It is conceivable that if the orbits of ERS-1 and ERS-2 are not identical, the azimuth angles at which σ^o measurements are collected will not be identical. Figure 3.27 is a scatter plot of σ^o vs. incidence angle for all beams of both scatterometers. The color denotes beam number while the instruments are differentiated by the plot symbols. A similar plot is shown in Figure 3.28 where all σ^o values for a particular instrument and

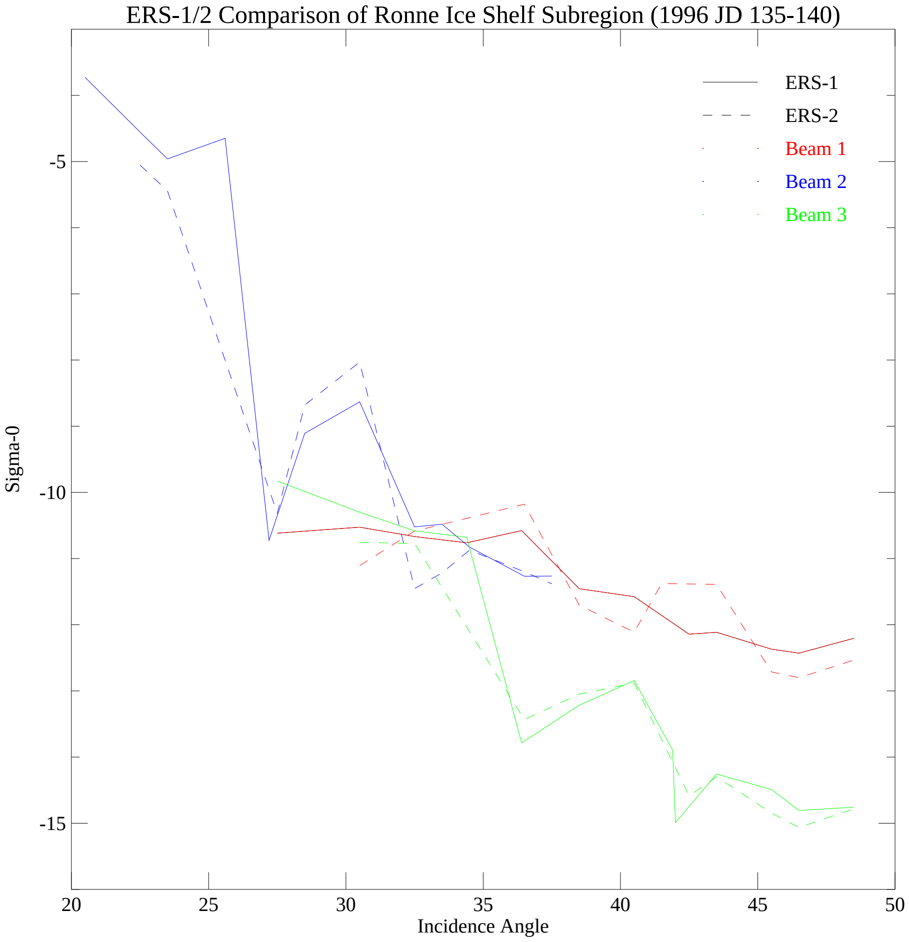

Figure 3.28: Plot of average σ^o (in 1° incidence angle bins) vs. incidence angle for each beam of ERS-1 and ERS-2 during 1996 JD 135-140. The beams are color coded. The data from different instruments can be differentiated by line styles.

beam have been averaged in 1° incidence angle bins. These plots indicate that either the beams are not cross-calibrated well or azimuthal modulation is present in the study region. The latter is now considered. In Figure 3.29 a contour plot of the two dimensional histogram of measurement incidence vs. azimuth angles for ERS-1 and ERS-2 is shown. This figure indicates that while the azimuth angles are similar in form, there are some subtle differences. In fact, the average azimuth angle of observations from each individual beam is found to be two degrees higher for ERS-2 than ERS-1. Since the presence of azimuthal modulation in the study region has

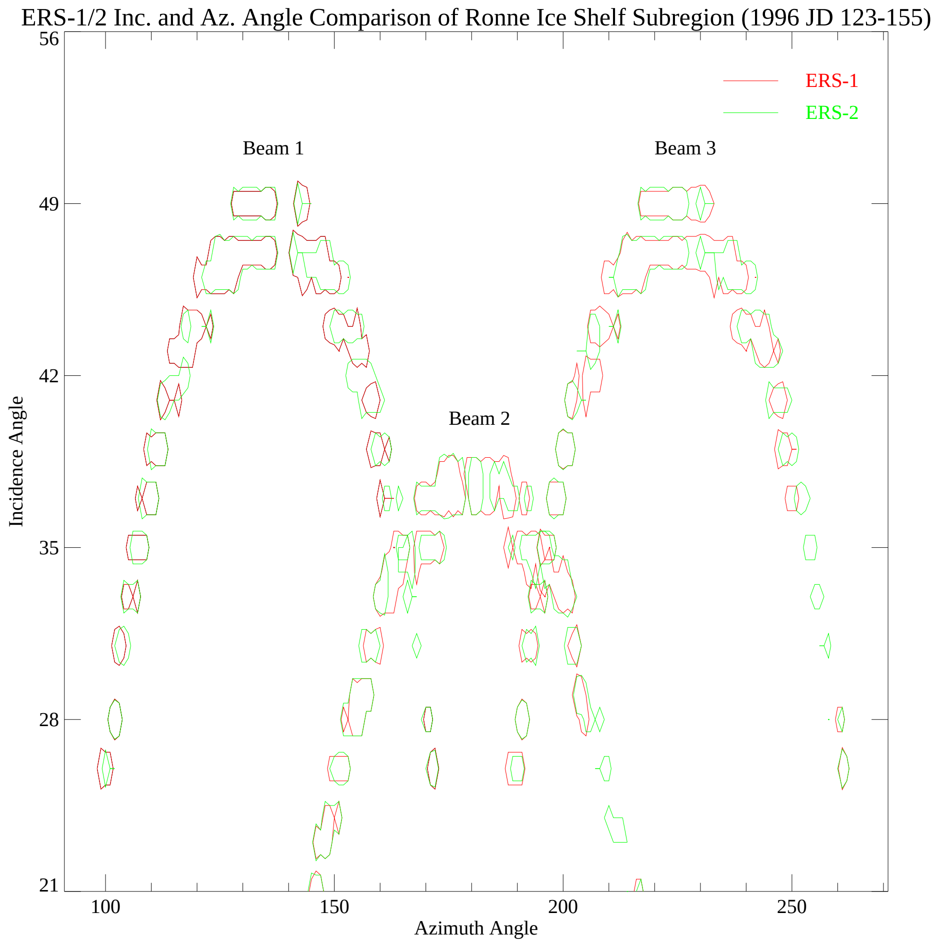

Figure 3.29: Contour plot of measurement incidence angle vs. azimuth angle for all ERS-1 and ERS-2 data during the overlap period.

been established, these differences in azimuth angle are likely responsible for some discrepancy in σ^o values. The level of discrepancy possible in this subregion due to azimuthal modulation is estimated by plotting σ^o values vs. azimuth angle where incidence angle and temporal dependence has been minimized. Such a plot is shown in Figure 3.30. In generating this plot, the incidence angle dependence is reduced by only plotting σ^o values from one degree incidence angle ranges. The long-term temporal dependence was minimized by using 6 days of data. A strong azimuth angle dependence is observed in the σ^o data points. In the azimuth angle range of 150° to

250° there is roughly a 3 dB drop in σ^o corresponding to a 0.03 dB/deg σ^o dependence on azimuth angle. The two degree bias in ERS-2 measurements would result in only a 0.06 dB drop in σ^o in this range of azimuth angles.

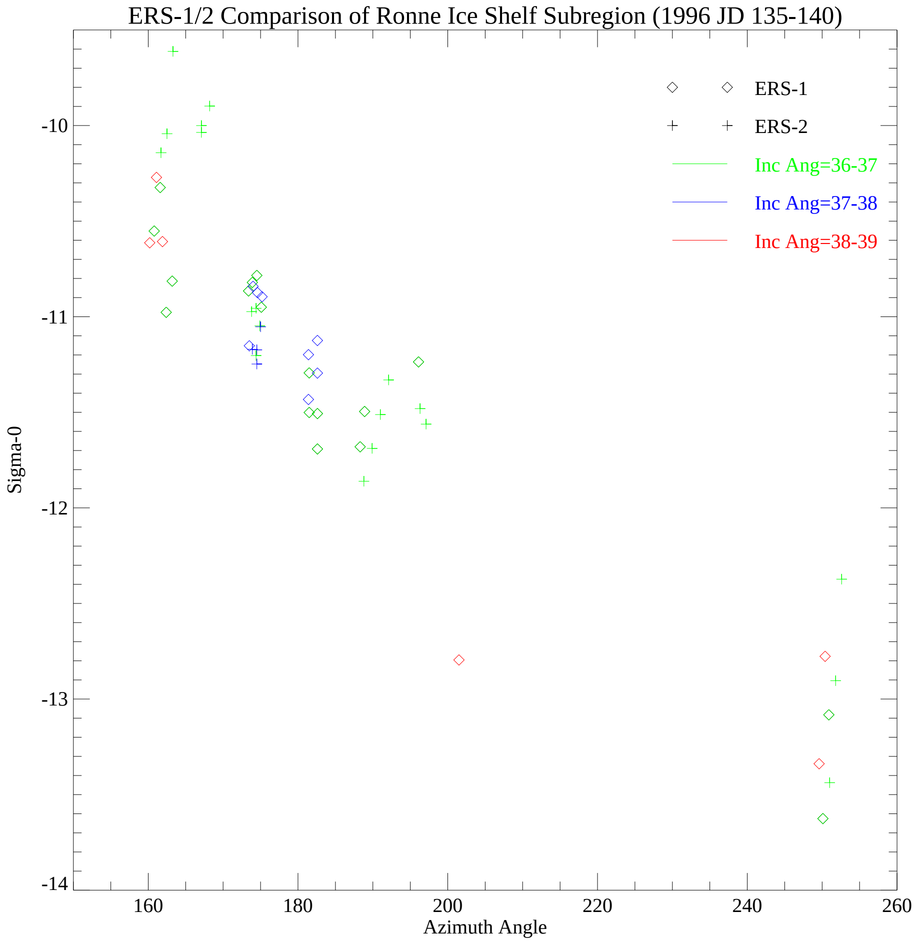

Figure 3.30: Scatter plot of σ^o vs. azimuth angle for 1996 JD 135-140.

Calibration Hypothesis

The final possibility is a calibration problem between scatterometers. Figure 3.30 shows a scatter plot of σ^o at various azimuth angles for measurements taken at several mid-range incidence angles for both instruments over the study region. This plot should provide the information needed in determining if calibration is an issue. If calibration is a problem, a clear trend should be observed regardless of azimuth or incidence angles. At a given azimuth angle, σ^o values are plotted without incidence angle or temporal variability induced ambiguity. While differences are observed, there is no clear trend in ERS-1 σ^o values compared to ERS-2 σ^o values. Hence, no obvious calibration problem appears to be present in the study region.

3.3.4 ERS Instrument Calibration Conclusions

This study has defined discrepancies of ERS-1 σ^o with ERS-2 σ^o in a region of the Ronne Ice Shelf of Antarctica. Several possible sources of the observed differences were proposed and explored including diurnal variations, azimuthal modulation, and calibration. The measurement times of the two instruments were found to be very similar indicating that diurnal variability is likely not a major contributor to the discrepancies. Azimuth modulation was found to exist in the study region. In addition, slight differences in measurement azimuth angles were found. While it appears likely that this is responsible for some portion of the drop in ERS-2 σ^o, it does not appear to be enough to account for the full 0.2-0.3 dB discrepancy. Finally, a clear trend that would be indicative of a calibration problem was not observed.

Since the discrepancy in question is so small, it is difficult to accurately pin point its source in the presence of noise. However, it has been established that there are distinct although slight differences in the time and azimuthal characteristics of measurements of ERS-1 and ERS-2 σ^o. In the final analysis, both of these along with the possibility of slight calibration problems likely combine to cause the observed differences.

3.4 Image Reconstruction Conclusions

The research described in this chapter addresses a number of important issues in image reconstruction from spaceborne scatterometer and radiometer measurements. The first study detailed the optimization of the SIRF algorithm for NSCAT data ensuring proper convergence of the iterative technique with minimal computational requirements. In the next section, analysis was performed of azimuthal modulation over Antarctic sea ice and glacial ice regions. Azimuthal modulation levels are found to be negligible for sea ice indicating minimal effect on image reconstruction. In contrast, significant levels of modulation are observed in some glacial ice areas due to surface slope and wind induced sastrugi on the snow surface. Consequently, reconstructed imagery of these regimes exhibit moderate estimate errors. Finally, a study of inter-sensor calibration issues between the ERS-1 and ERS-2 sensors was considered. The study concluded that slight beam miscalibrations and azimuthal measurement characteristics are likely the source of the observed discrepancies. These differences must be considered when interpreting combined ERS-1 and ERS-2 reconstructed image sets.

Chapter 4

Atmospheric Distortion Reduction in Image Reconstruction

4.1 Introduction

The previous chapter addressed several issues in image reconstruction. Another factor affecting reconstructed image quality is a sensor sensitivity to atmospheric distortions. Due to shorter wavelengths, this phenomenon is a significant problem for instruments with relatively high microwave frequencies such as those used by the SSM/I. This chapter considers the effects of those distortions in SSM/I imagery and methods for their removal. While the methods are applied to images of vegetated regions, the same techniques can be used over polar glacial ice regions as well. This study considers vegetated areas since the effects of atmospheric distortions are much more pronounced there than in the cryosphere. The work presented in this chapter was published in the *IEEE Transactions on Geoscience and Remote Sensing* [7].

Microwave radiometers such as SSM/I [33, 35] have wide application in atmospheric remote sensing over the ocean and provide essential inputs to numerical weather prediction models. SSM/I data has also been used for land and ice studies including measurements of soil and plant moisture content [48, 49], land surface temperature [50], atmospheric moisture over land [51], snow cover classification [52], and mapping polar ice [53].

Because the surface brightness observed by the SSM/I may be adversely affected by spatial variations in the atmospheric profile over the surface, algorithms for cloud removal have been developed [51, 54]. In this chapter, several new algorithms are compared which generate cloud-free composite images from multiple passes of the study region. Simulations to determine the effectiveness of these algorithms are performed. Actual SSM/I data is analyzed by exploring the effects of compositing algorithms on the pixel surface brightness temperature distributions.

This chapter is organized as follows: After a brief background discussion, the production of no-cloud composite images is discussed. The next section introduces the modified maximum average (MMA) and hybrid algorithms. A simulation experiment to compare the cloud-removal algorithms is then presented. Analysis of actual SSM/I data is performed. Finally, the conclusions are given.

4.2 SSM/I Remote Sensing

An in-depth background of the SSM/I instrument is given in Chapter 2. SSM/I observes T_B at four different frequencies and both polarizations. Channels with higher frequencies typically exhibit more sensitivity to atmospheric distortions such as water vapor, cloud cover, and precipitation.

The brightness temperatures observed by the SSM/I are a function of the effective brightness temperature of the Earth's surface and the emission, scattering, and attenuation of the atmosphere. Because of the spatial and temporal variability of the surface brightness, which is a function of the properties of the soil and overlaying vegetation and their physical temperatures, it is difficult to decompose the observed brightness into its individual components. The most crucial factors affecting a radiometric measurement, however, are the surface emissivity and temperature, the vegetation canopy, and the atmospheric conditions [29].

4.3 Generation of Cloud-Free Images

One of the challenges in mapping the surface brightness from space-borne radiometer data is atmospheric distortion. Cloud cover and precipitation are two primary sources of this distortion. Although cloud and rain cause little microwave attenuation for frequencies less than 10 GHz, the higher microwave frequencies of the SSM/I (19.35, 22.235, 37.0, and 85.0 GHz) show substantial atmospheric loss due to scattering from hydrometeors and water vapor. Over the ocean the atmospheric signal is used to deduce cloud water content from the change in brightness. For studies of the land surface, however, these atmospheric effects may be unwanted [55].

Clouds and precipitation affect surface brightness measurements in two ways. First, the cloud scattering non-uniformly lowers the measured brightness temperature for all frequencies of the SSM/I with higher frequencies progressively more sensitive. The reduction in brightness temperature can be confused with surface features. Second, the clouds attenuate the polarization differences caused by the geometric or chemical composition of different surface types. This prevents the surface polarization difference from being used to discriminate between vegetation types and/or standing water.

Figure 4.1 illustrates examples of atmospherically distorted brightness temperature images in a region of the Amazon Basin for all vertical polarization SSM/I channels. These images, like all in this chapter, were generated by assigning to each pixel covered by the swath the value of the nearest measurement. Other single-pass imaging techniques can also be used, e.g. [37, 39]. The distortions are evident in the temporal variation of surface brightness temperature in different areas. Note that, as expected, the distortions are more pronounced in the higher frequency channels. This follows the trend of increased atmospheric scattering due to clouds and precipitation with increasing frequency. The distortions of pixel values can be as high as 60 K for the higher frequency channels. These distortions can greatly hinder the application of SSM/I data to land studies.

While multi-channel and/or multi-sensor based algorithms for cloud removal have been previously used (e.g., [52, 55, 56, 57]), a single channel algorithm similar to [54] in this study. By using only single frequency information to generate a "cloud-free" image of the surface, the introduction spurious correlation between the channels is avoided. For example, since each frequency has a different footprint size, using lower frequency data to remove atmospheric distortion effects in higher frequencies may exclude undistorted values in the higher frequency channels [54].

The algorithm is based on the assumption that temporal surface brightness variations over an area are caused by small-scale, atmospheric effects rather than

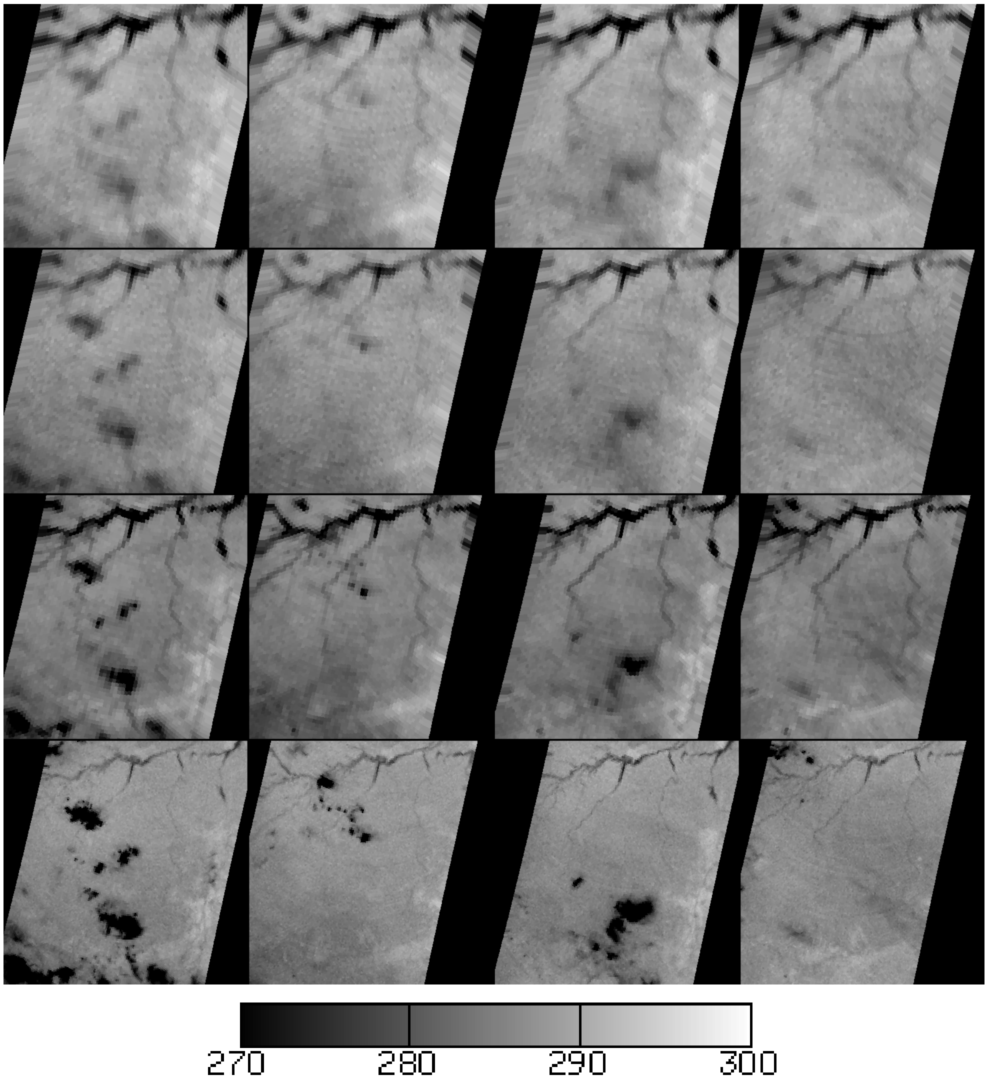

Figure 4.1: Individual SSM/I swath examples of temporal atmospheric distortions. These images were created by assigning the closest measurement value to each pixel. Columns (from left to right) correspond to 1992 Julian Days 245, 248, 261, 264 of the passes. Rows (from top to bottom) indicate SSM/I channels 19V, 22V, 37V, 85V.

temporal changes in the surface brightness. A composite image is generated using multiple passes which represents the effective surface brightness temperature over a multi-day period. The composite image is generated from images created from each descending pass, though ascending passes can also be used.

In the example data which follows, twenty days of descending pass SSM/I data (Sept. 1992) over South America are used. During this period each pixel is observed from 5 to 10 times. The value of the composite pixel is computed from this ensemble. The study region is considered a worst-case example, with frequent rain and distortion events occuring up to several times during the compositing interval. For this region twenty days offers a good balance between the number of undistorted measurements in the ensemble and temporal variations due to seasonal radiometric surface response variations. This is somewhat less than the 30 days used by previous investigators [54] but provides adequate results. Areas with less frequent distortion events may be able to use shorter periods.

Choudhury and Tucker [54] removed temporal atmospheric distortion by using the second-highest pixel value from the ensemble as the composite pixel value. Since the atmospheric distortion generally lowers the brightness temperature measurements over land, high pixel values have the least atmospheric influence. They reason that since the highest value is often strongly influenced by noise or processing artifacts they used the second-highest pixel value.

Choosing the second-highest value is an example of a rank order statistic [58]. Another rank order technique is the median filter [59]. As an estimator, a rank order statistic is noise-reducing but is sensitive to the underlying distribution of the samples [60]. Thus, the second-highest value technique's ability to reduce noise is strongly influenced by the measurement distribution.

Unfortunately, the distribution function for the SSM/I data is not known precisely and it is not possible to analytically determine the estimator variance. However, it is known that in the presence of atmospheric distortion over land, the distribution is skewed low, while the desired estimation parameter is the mode on the high end of the distribution [56]. This strongly suggests that the rank order statistic needed for this application is a value closer to the highest value than to the median value. Given this insight, the second-highest value method is a reasonable approach.

4.4 Modified Maximum Average Algorithm

In an effort to improve the performance of a cloud removal algorithm, a modified maximum average (MMA) technique was developed. This algorithm attempts to estimate the cloud-free surface brightness of a pixel by choosing a subset of pixel values from the ensemble of measurements of that pixel and then averaging the selected values together. By properly selecting the subset from the ensemble, the cloud distortion is eliminated. Averaging of the subset reduces the noise and attenuates any residual bias.

To select pixel values from the ensemble in the MMA technique, the sample mean of the entire pixel ensemble is first computed. Measurements greater than the sample mean yield a subset of the complete ensemble corresponding to its highest values. The highest value of this subset is then eliminated. The remaining values consist of those values which are above the ensemble mean but less than the maximum value of the ensemble. This is the MMA subset. The estimated pixel value is then determined as the mean of this subset.

Analyzing this technique statistically is challenging for two reasons: 1) the distribution of pixel values when distortions are included is not clearly known and 2) the algorithm combines both box averaging statistics and order statistics. To qualitatively justify this approach, consider a simple model for the pixel measurements. In this model, the measurement is the sum of a Gaussian distributed surface brightness temperature and a weighted binary random variable:

$$z = \eta(\mu, \sigma) - p_d \Delta \tag{4.1}$$

where z is the measured brightness temperature, η is the Gaussian distribution with mean μ and standard deviation σ, p_d is a binary-valued random variable of the probability that a measurement contains cloud distortion (less than 30% based on a simple examination of SSM/I in the study region described later), and Δ is a positive random

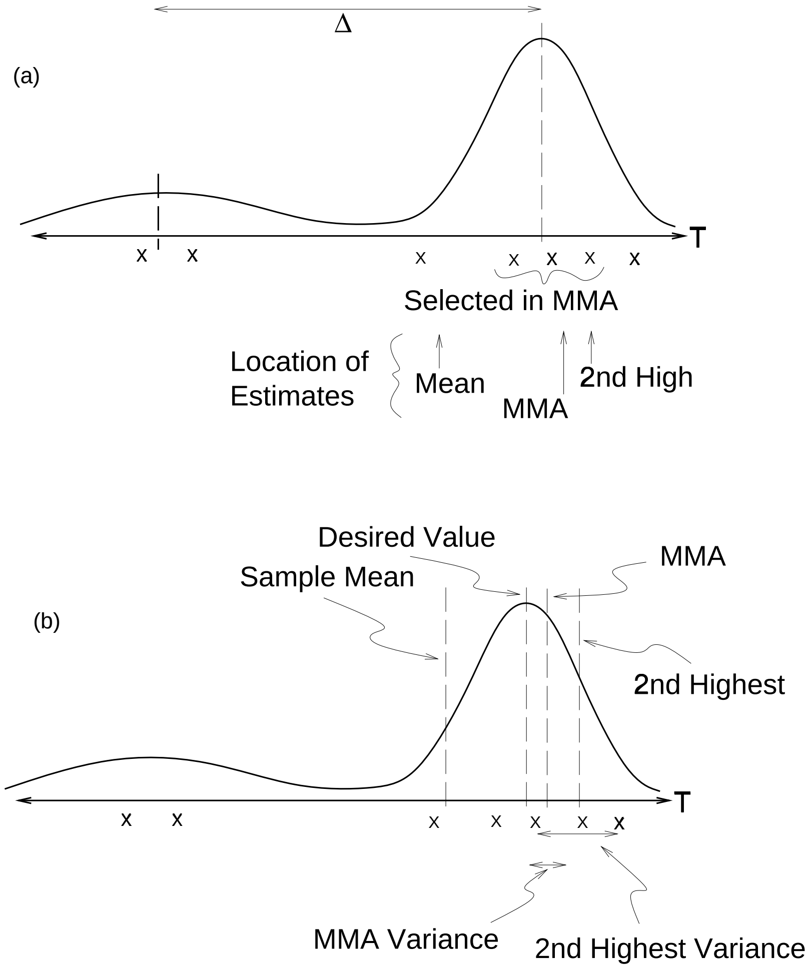

Figure 4.2: Illustration of hypothetical radiometric measurement distribution for a cloudy region. (a) Sample discrete ensemble. (b) Variance of the modified maximum and second highest value.

variable representing the drop in brightness temperature due to a cloud (Δ depends on the cloud thickness, water content, etc., the statistics of which are unknown). A schematic example of the distribution of z is given in Figure 4.2a where $\Delta = 10$ K and $p_d = 30\%$. The right mode corresponds to the distribution of surface brightness while the lower mode represents the distribution of cloudy pixels. The "X" marks below the temperature axis illustrate an ensemble of seven random measurements for a given pixel. Also illustrated are the results from applying the MMA and second-highest value techniques.

Good metrics for comparing estimation algorithms include the mean estimate error (bias) and the estimate variance. Ideally, the estimate should have no bias and minimum variance. To compare the variances of the MMA algorithm and the second-highest value technique, consider Figure 4.2b. As in Fig. 4.2a the "X"'s represent an ensemble of seven samples taken from the distribution. The variance of the second-highest value technique is governed by the average temperature difference between the highest and third highest value of the ensemble. The variance of the MMA algorithm depends on the variances of the second, third, and fourth measurement. Graphically, one may see that the averaging of these values lowers the estimate variance more than just using the second-highest value.

Like the second-highest value estimate, the MMA estimate in this example is biased high, and is whenever the ensemble includes more than one sample from the lower mode of the mixture distribution. However, it is clear that the MMA bias is less than the second-highest value estimate. Further, the estimator variance is smaller for MMA.

While MMA produces a less biased estimate for pixels with high cloud contamination than the second-highest value, it is still biased high for pixels with little or no contamination. Figure 4.3 depicts a hypothetical distribution of brightness temperatures for a non-cloud-affected pixel. In this case, the second-highest value and MMA estimates are biased high. The desired value is the mean of the overall distribution in the absence of clouds or precipitation. As previously noted, a simple examination of SSM/I data reveals a probability of less than 30% that a measurement

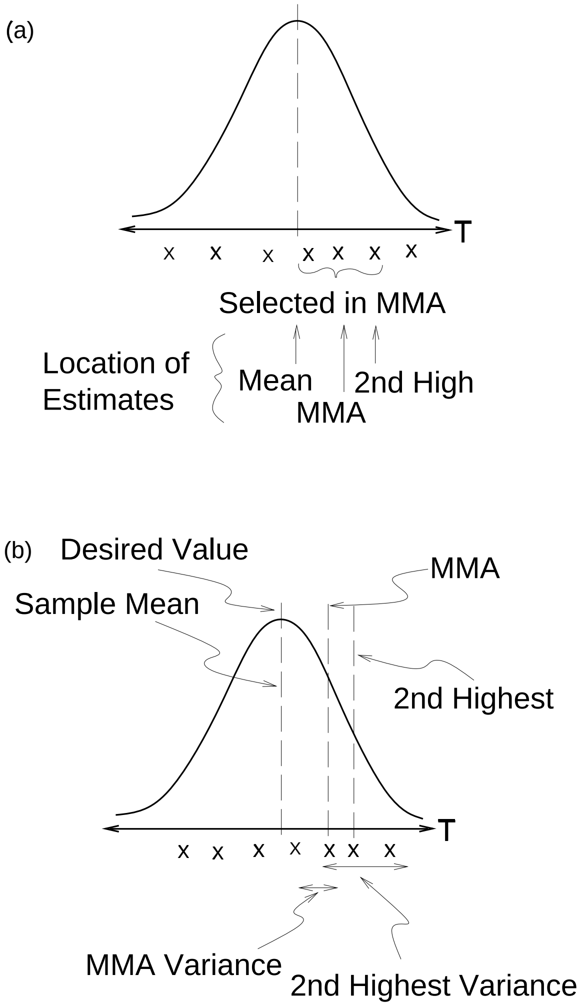

Figure 4.3: Illustration of hypothetical radiometric measurement distribution for a clear region. (a) Sample discrete ensemble. (b) Variance of the modified maximum and second-highest value.

is distorted by clouds or rain. Thus, MMA may be unnecessarily biased somewhat high for many of the measurements.

In an effort to ameliorate this problem, a hybrid of the mean and MMA methods has been developed. Ideally, this hybrid implements MMA in the presence of clouds and takes the mean in their absence. This reduces the overshoot of MMA for low atmospheric distortions and provides a better estimate of the actual surface brightness temperature.

To implement the hybrid algorithm, a metric is required for the decision making process. The chosen metric is the temporal standard deviation of the values for a particular pixel. The presence of clouds skews the brightness temperature distribution low for affected passes, thus increasing the standard deviation. Figure 4.4 shows a mean SSM/I composite image along with its corresponding temporal standard deviation image for the 85 GHz vertically polarized channel. This visually illustrates that the high standard deviation regions correlate well with low T_B regions indicative of atmospheric distortion. Areas that appear darkened in the mean composite image exhibit relatively high values in the standard deviation image.

In the standard deviation image of Figure 4.4 the areas with low values correspond to regions with little or no atmospheric distortion. A small 2°x2° spatially-homogeneous subregion, which will be more explicitly defined in a later section, is chosen as an example of an area with low temporal variation and thus low atmospheric distortion. The temporal mean and standard deviation of all swath pixel values are calculated for each vertically polarized SSM/I channel in this subregion and are shown in Table 4.1. The standard deviations represent the temporal variance of surface brightness temperature in the absence of atmospheric distortion. According to the previous discussion, any kind of temporal variation, such as atmospheric distortion, will cause the standard deviation to rise above these values. All channel standard deviation values are similar with the 19V channel exhibiting the highest and 37V the lowest. Ideally, optimum values should be used for each channel in implementing the hybrid algorithm. However, since the temporal standard deviations are similar and for the sake of simplicity, the highest of these values is chosen, 1.25 K, as the hybrid

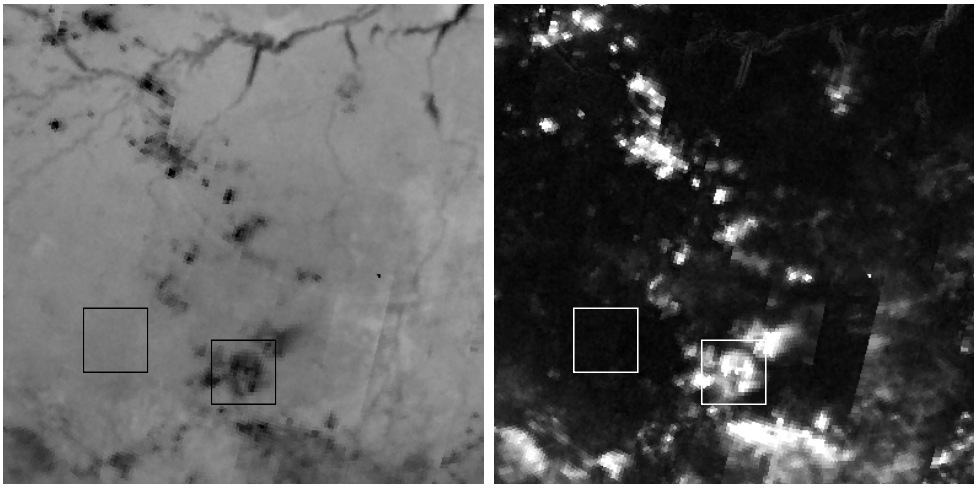

Figure 4.4: Temporal mean and standard deviation images of the 85 GHz vertically polarized SSM/I channel. These were generated using 44 descending single pass images corresponding to days 245-264 of 1992. The left panel is the mean image and the right panel is the standard deviation image. The boxes define two 2°x2° subregions used later in the assessment of algorithm effectiveness. One is an example of a cloudy region and the other is a region with little or no distortion. The band in the lower-right area of the standard deviation image results from atmospheric distortions affecting only some passes.

threshold metric for the results presented in this chapter. In the hybrid algorithm, the standard deviation is computed for each pixel ensemble of brightness temperatures. If it is above 1.25 K, the MMA algorithm is used to produce the composite value for that particular pixel in order to select only nondistorted measurements. Otherwise, the mean is used. This threshold has been chosen for use in the study region and while it is adequate for most regions, the threshold can and should be tuned for other regions.

4.5 Simulation

To further compare and contrast the mean, second-highest value, MMA, and hybrid algorithms, a simple Monte Carlo analysis for a single pixel is presented. This simulation assumes that the true pixel brightness for a geographical area is 280 K. An ensemble of seven pixel values is then created by adding a Gaussian random

Table 4.1: Temporal means and standard deviations of pixel brightness temperatures in a 2°x2° distortion-free subregion of the Amazon Basin.

Channel	Mean	Std.
19V	287.2	1.25 K
22V	284.9	1.23 K
37V	283.2	1.14 K
85V	284.6	1.20 K

variable of standard deviation 1 K to the "true" value. This represents the radiometric "noise" ΔT inherent to the radiometer measurements. Seven pixels simulate the average number of radiometric measurements in the twenty day study period. Two of the ensemble measurements then have simulated atmospheric distortion added. The first measurement is reduced by T_{dis} and the second measurement by $T_{dis}/2$. This models a pixel which is contaminated by clouds at two different times with one cloud twice as distorting as the other. The seven member ensemble is then processed by each algorithm and the results are saved. The results of 1000 simulations are then analyzed to give the results in Figure 4.5. For comparison, the ensemble mean is plotted along with the windowed mean. The windowed mean is the mean of values within one standard deviation of the ensemble mean.

For pixels with little or no atmospheric distortion, the mean or windowed average is closer to the 280 "true" value than MMA or the second-highest value. For ensembles which have greater ($>$ 5 K) atmospheric distortion, the second-highest value and MMA techniques are superior. The MMA technique has the smallest bias of the two. Since it also has the smallest variance, the MMA algorithm is considered superior to the second-highest value algorithm. The hybrid algorithm combines the strengths of the mean method for low distortion temperatures and MMA for high distortion temperatures. This is evident in Figure 4.5 by the closer estimates to 280 K for small T_{dis}. Simulation results show that MMA is superior in the presence of high distortion and that mean is best with low distortion. The hybrid algorithm combines the two in a manner that uses the correct algorithm for each pixel.

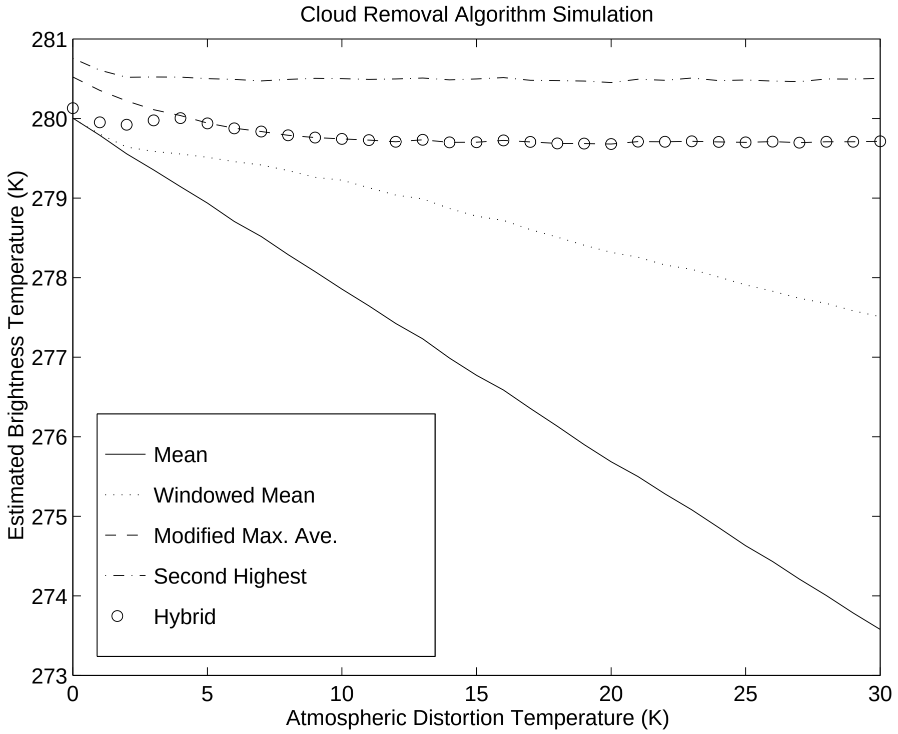

Figure 4.5: Simulation results of atmospheric distortion removal (the true value is 280 K).

4.6 SSM/I Data Analysis

To validate the algorithms with actual data, a region of the Amazon Basin was chosen for SSM/I data analysis. The region lies primarily within Brazil and is bounded by the coordinates: 48° to 63° W longitude and 1° to 16° S latitude. Its characteristic high precipitation levels make it a good study region representing a worst case scenario with frequent rain and distortion events. The mean, second-highest value, MMA, and hybrid composite images of this region were created for all vertically polarized SSM/I channels. Examples are presented in Figures 4.6-4.7. In the interest of space, only the 37V and 85V images are shown here. Due to smaller 3dB antenna footprints, the higher frequency images exhibit better effective resolution.

Two small nearly spatially-homogeneous regions were chosen from the larger study region for brightness temperature distribution analysis. Each is 2° square in latitude and longitude. The first region, with bounding coordinates of 54.5° to 56.5°

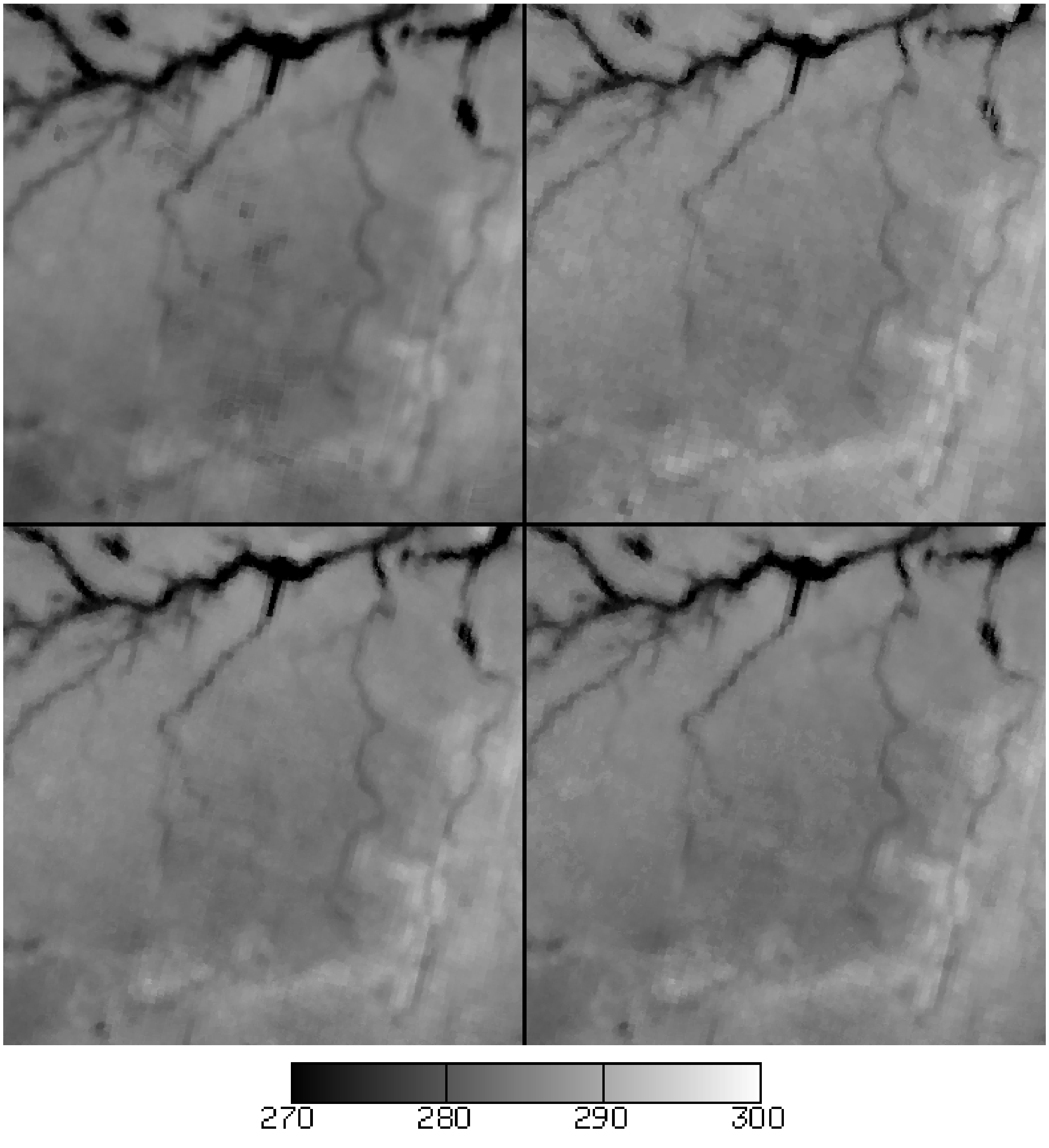

Figure 4.6: SSM/I 37V Brazil region composite images. From top left to bottom right: mean, second-highest value, MMA, and hybrid.

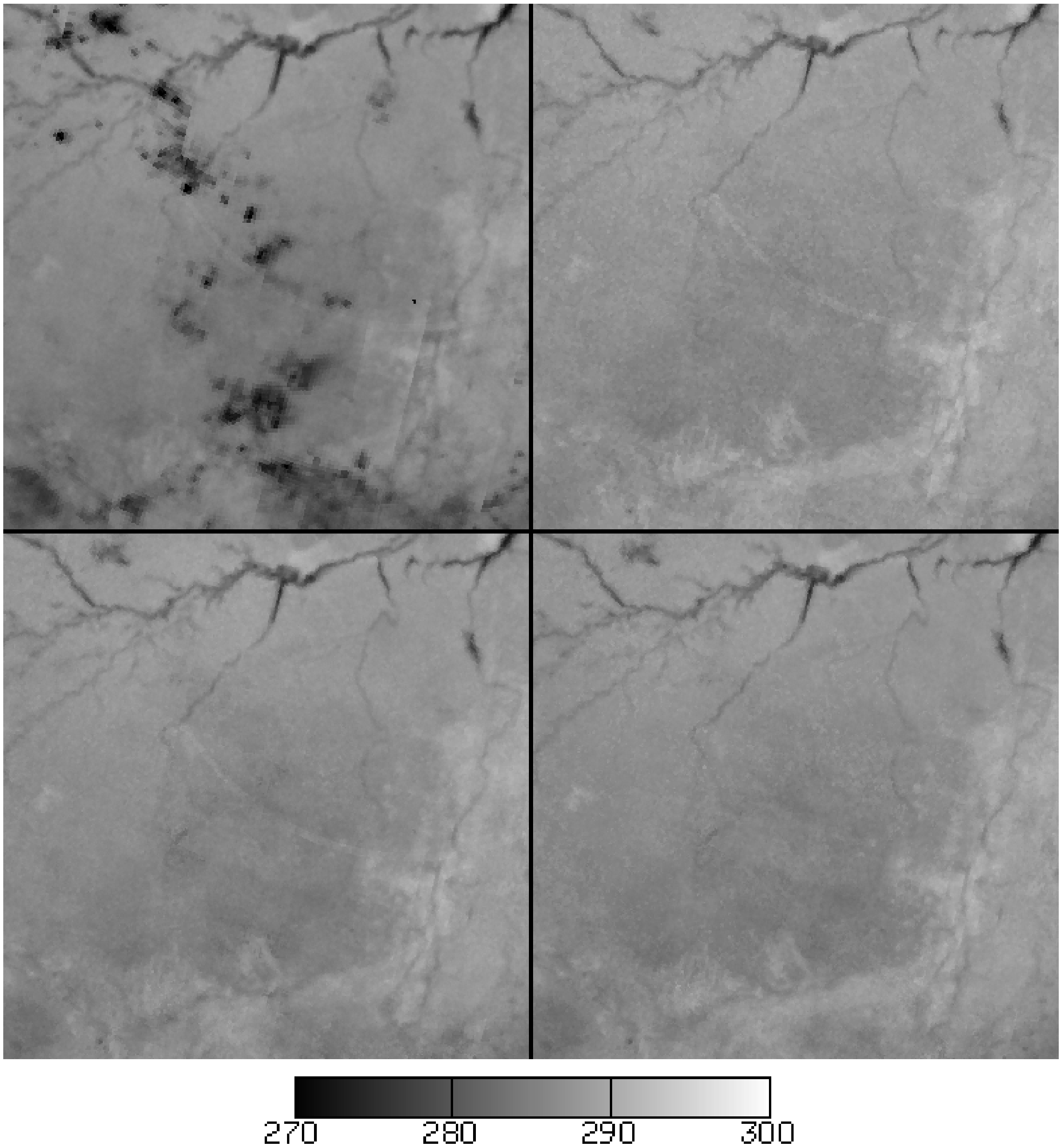

Figure 4.7: SSM/I 85V Brazil region composite images. From top left to bottom right: mean, second-highest value, MMA, and hybrid.

W longitude and 11.5° to 13.5° S latitude, exhibits temporal variations consistent with atmospheric distortion. The second was chosen for its apparent absence of cloud or precipitation distortion with boundaries of 58.5° to 60.5° W longitude and 10.5° to 12.5° S latitude. Both subregions are shown in Figure 4.4.

The brightness temperature distribution of all of the SSM/I swath measurement data over the small regions is presented in Figures 4.8-4.9. These help validate the distortion model used previously. Figure 4.8 depicts distributions for the cloudy region and Figure 4.9 shows the same for the clear region. Note that a log vertical scale has been used to emphasize the distribution tails. These distributions demonstrate the difference between cloudy and clear regions. The cloudy region distribution has a relatively wide peak at the high end with a long tail of lower temperatures. The peak corresponds to non-distorted brightness temperatures while the tail represents pixels that have experienced some level of atmospheric distortion. For conciseness, only the 85 GHz channel are considered for the rest of the analysis.

The clear region has a clean single-modal distribution with a tight peak and no trailing tail, indicating the absence of any distortion. Hence the effect of atmospheric distortion on the surface brightness distribution is to widen the upper modal peak and add a lower tail of brightness values. A good cloud-removal algorithm would select only values within the mode that represent the undistorted brightness temperatures.

Images for both subregions were created using the mean, second-highest value, MMA, and hybrid algorithms. These images are shown in Figures 4.10-4.11. Since no surface brightness temperature ground truth is available for validation of the estimated surface brightness temperature, it is difficult to objectively assess the effectiveness of each algorithm. However, a visual interpretation of these images yields some important information.

Figure 4.10 illustrates each composite image for the cloudy region at 85 GHz vertical polarization. Here, the presence of clouds and precipitation are evident. Certainly, it can be seen that the second-highest value, MMA, and hybrid algorithms all perform superior to mean. The distortions are still evident in the mean composite

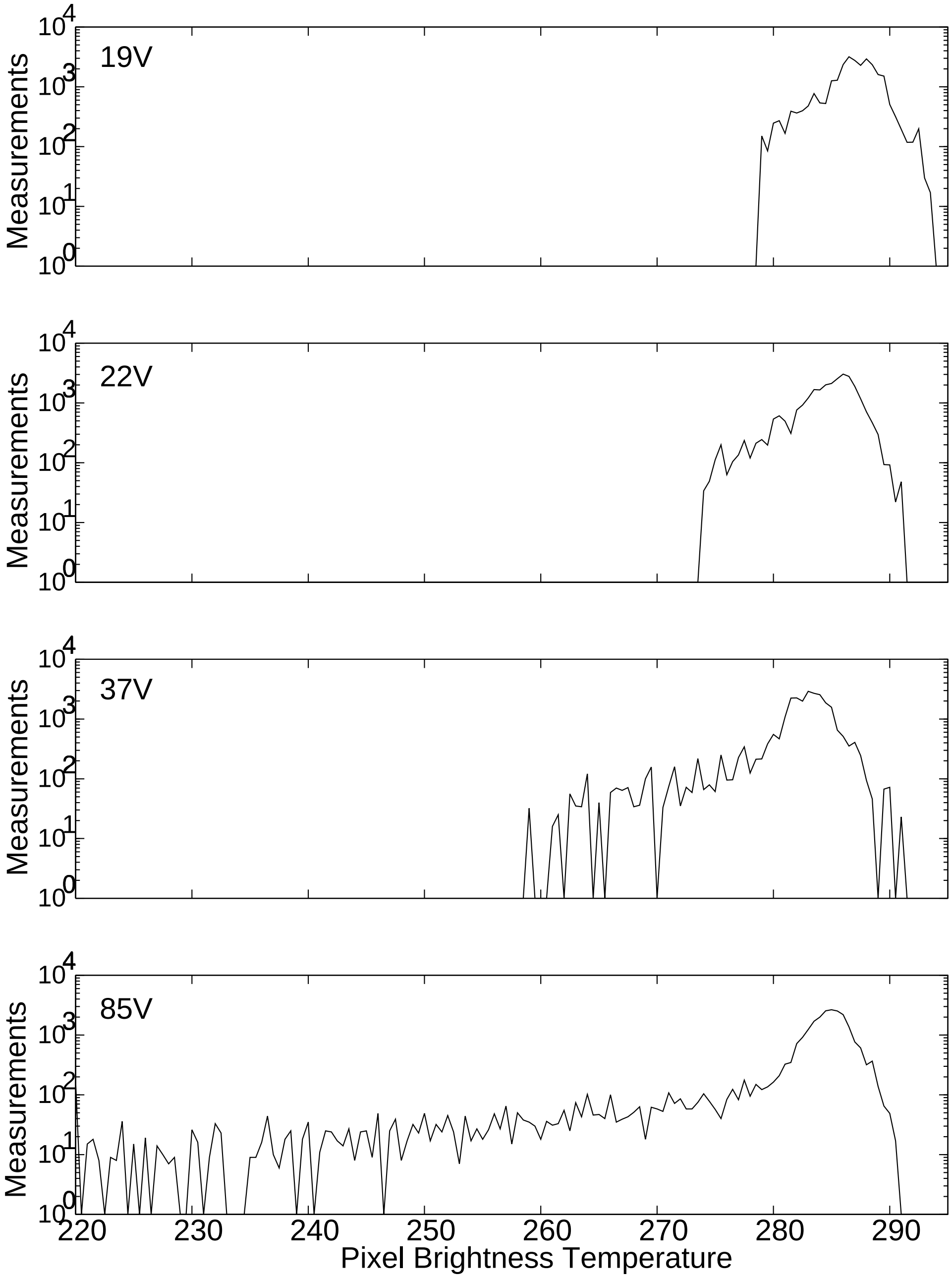

Figure 4.8: Cloudy region temporal and spatial measurement histograms for all SSM/I vertically polarized channels. A log vertical scale has been used to emphasize the tails of the distributions. These tails correspond to atmospheric distortions which lower the overall brightness temperature.

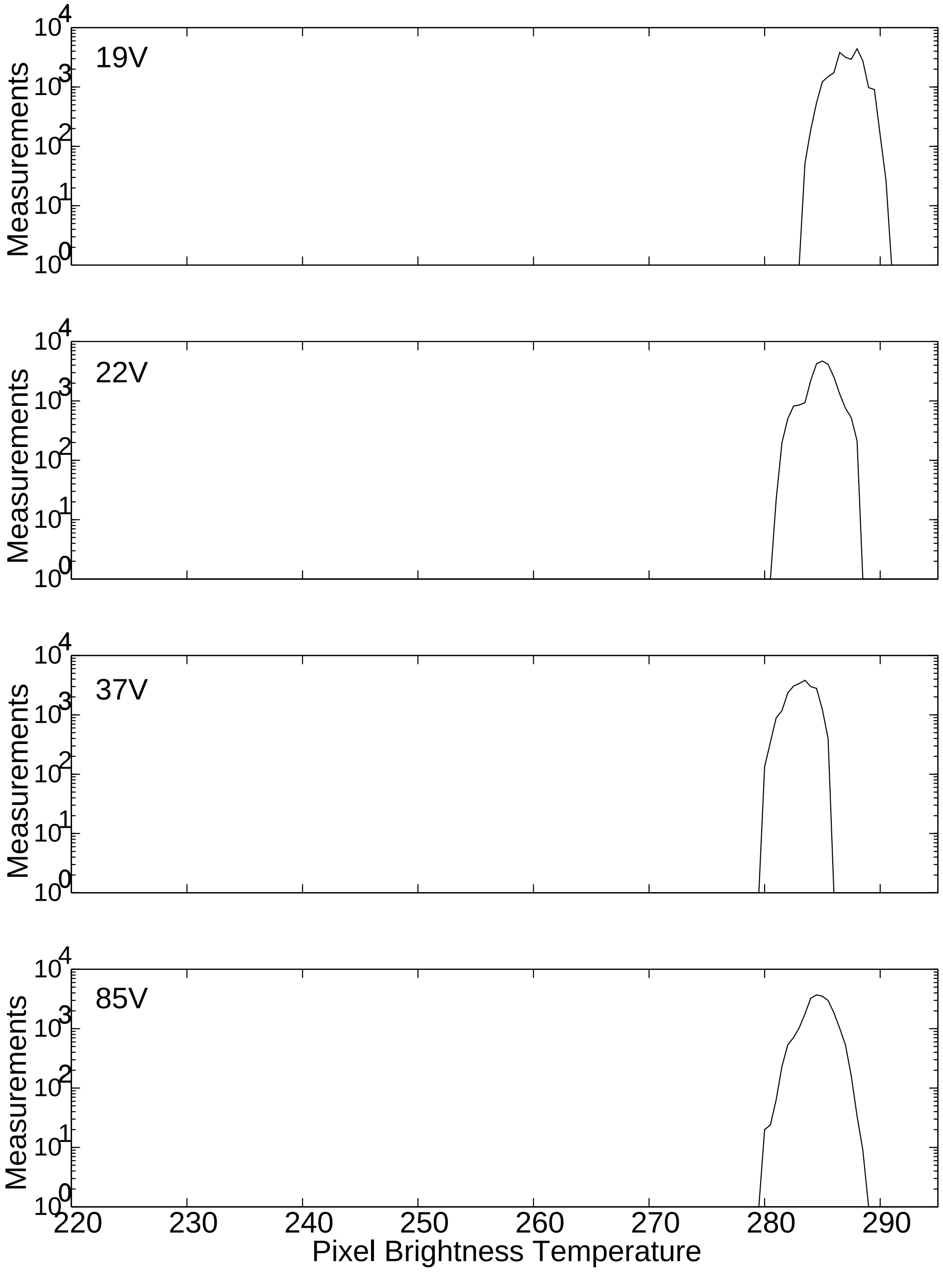

Figure 4.9: Clear region temporal and spatial measurement histograms for all SSM/I vertically polarized channels. Compare these distributions with those in Figure 4.8. The lack of tails on the distributions indicates the absence of significant atmospheric distortions.

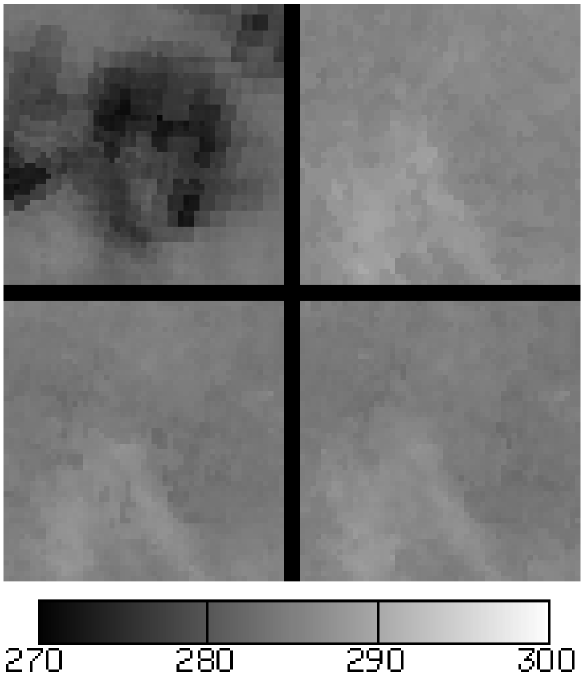

Figure 4.10: SSM/I 85V cloudy region cloud removal composite images. From top left to bottom right: mean, second-highest value, MMA, and hybrid.

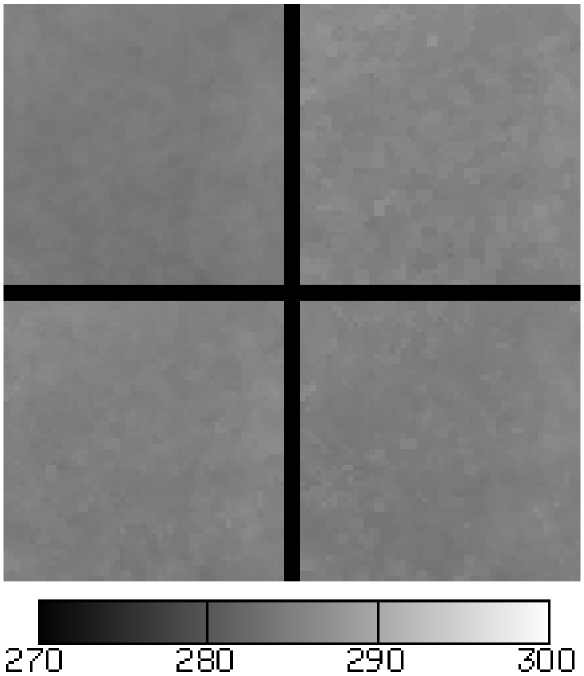

Figure 4.11: SSM/I 85V clear region cloud removal composite images. From top left to bottom right: mean, second-highest value, MMA, and hybrid.

Table 4.2: Pixel value averages and standard deviations of each algorithm composite image for the cloudy and clear regions.

	Cloudy Region		Clear Region	
Algorithm	Ave.	Std.	Ave.	Std.
Mean	279.8	3.259	284.4	0.480
Second Highest	286.2	1.033	285.6	0.551
MMA	284.7	0.973	285.1	0.509
Hybrid	284.7	0.982	284.8	0.523

image while the others appear to remove the distortions to some degree. The average and standard deviation of pixel values were computed for each composite image. The results are given in Table 4.2. Without a knowledge of the true surface brightness temperature, it is not possible to determine the bias in each image. However, the mean image has the highest standard deviation. This is expected since the atmospherically distorted values were included in the mean. Second-highest value standard deviation is governed by the variance of the second-highest value only. As a result, this statistic is greatly improved over the mean image case. MMA yields the lowest standard deviation. The averaging contained in the MMA algorithm provides some additional noise reduction over the second-highest value. The hybrid image has the same mean as MMA and a slightly higher standard deviation indicating that the two algorithms performed similarly for the cloudy region. This shows that, as predicted, the hybrid algorithm effectively chooses MMA in cloudy regions.

Figure 4.11 shows the 85V channel composite images for a clear or distortion-free region. The average and standard deviation of all pixel values for each image are shown in Table 4.2. Since this region has been chosen specifically because it apparently has no distortion problems, the mean image is unbiased - unlike the other algorithms' composite images. Hence, its average can be treated as the ground truth in this instance. With this in mind, the hybrid algorithm provides the best estimate to the true brightness temperature and is the least biased according to its average value. The second-highest value is the most biased with MMA falling in between. Thus, the hybrid provides the closest approximation to the “actual value” with MMA following closely behind. A closer examination of the standard deviation image (Fig. 4.4) reveals that some of the pixels in this area have values higher than the 1.25 K threshold indicating that some subtle temporal variations exist due to minor atmospheric distortions or small seasonal surface brightness temperature changes. Regardless, the hybrid algorithm provides the estimate with the least bias. As in the cloudy region, MMA has a lower standard deviation than the second-highest value. The hybrid noise level is only slightly higher than MMA.

The spatial pixel brightness temperature distributions for the composite images are plotted for both regions after each compositing algorithm is run. Figures 4.12-4.13 present the results. Each of the distributions is plotted over the full temporal and spatial measurement distribution for that particular region. These help validate the assumptions on which the algorithms were based and provide a measure of algorithm performance.

Figure 4.12 illustrates the algorithm composite image brightness temperature distributions of the cloudy region for the 85 GHz channel. Clearly, the MMA and the hybrid most closely match the upper mode of the raw data distribution. Their similar performance indicates that hybrid primarily used the MMA algorithm in the presence of atmospheric distortion.

Distributions for the clear region are given in Figure 4.13. The high bias inherent to the second-highest value method is once again evident. In the clear region, MMA also demonstrates some bias although not as large. This is because MMA removes pixel values regardless of the actual presence of clouds or precipitation. On the other hand, the hybrid distribution has less bias and most closely matches the distribution of the raw data.

4.7 Conclusion

A comparison of several different methods (mean, second-highest value, modified maximum average (MMA), and hybrid) for creating cloud-free temporal composite surface brightness temperature images from SSM/I has been presented.

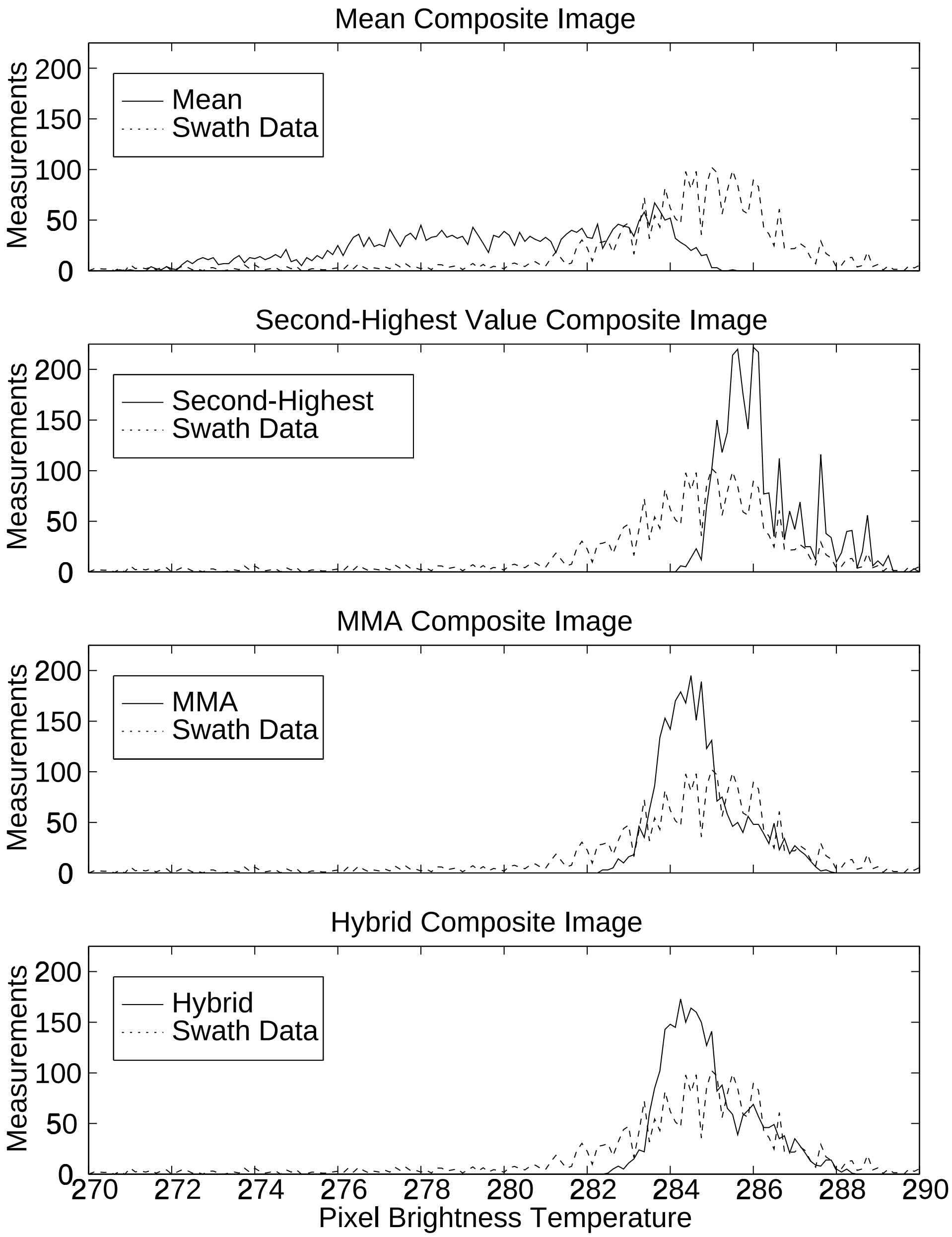

Figure 4.12: SSM/I 85 GHz vertical channel cloudy region spatial brightness temperature distributions for each cloud removal algorithm. The temporal and spatial measurement distribution has been plotted to provide a reference.

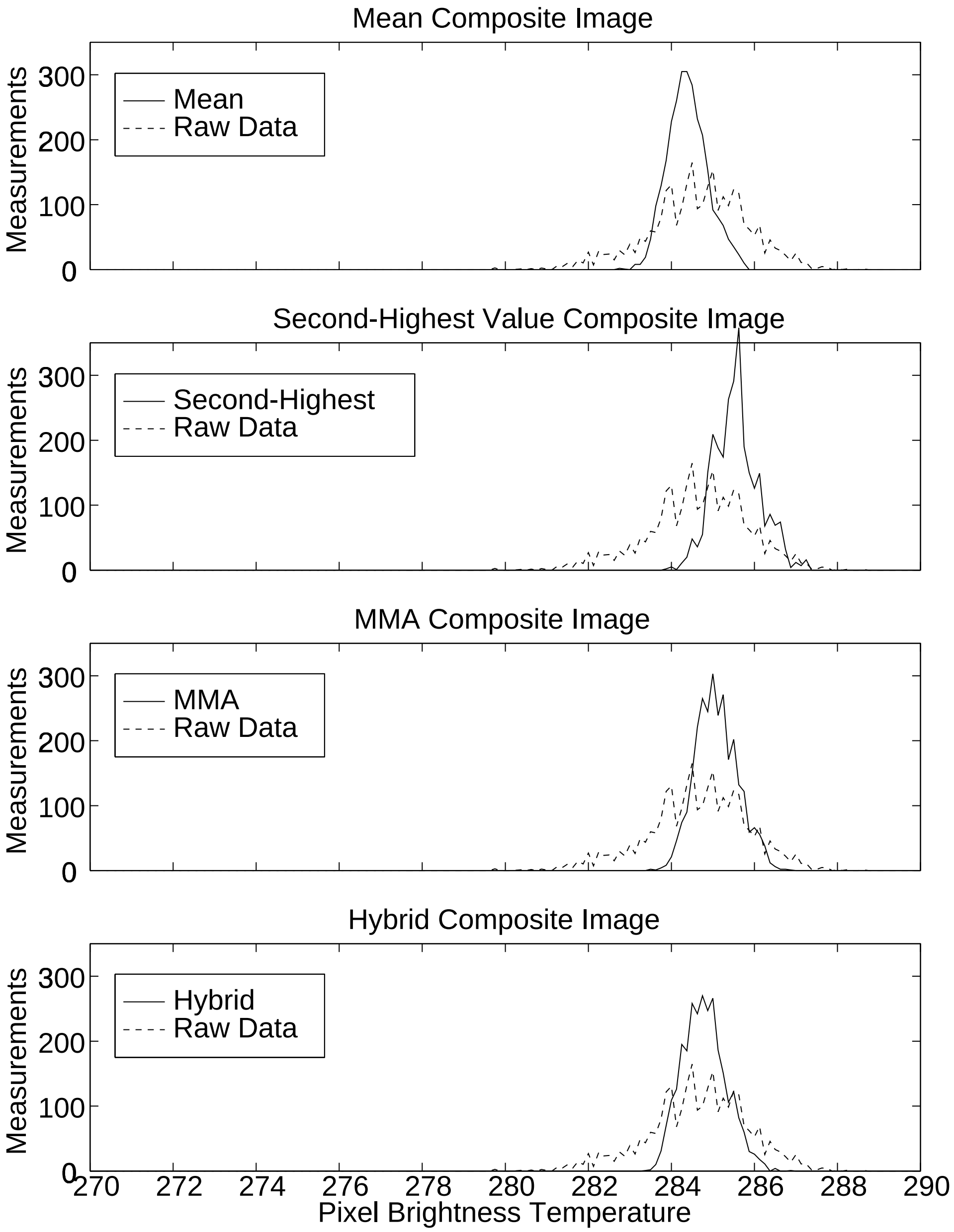

Figure 4.13: SSM/I 85 GHz vertical channel clear region spatial brightness temperature distributions for each cloud removal algorithm. The temporal and spatial measurement distribution has been plotted to provide a reference.

Taking the mean is optimum in the absence of clouds and hydrometeors. The second-highest value algorithm removes distorted pixel brightness temperature measurements, but has an inherent high bias in its brightness temperature distribution. The MMA algorithm more accurately estimates the desired value and has a lower variance; however, it may have an undesirable bias for instances in which no distortion is present. The hybrid algorithm combines the strengths of the mean and MMA algorithms. It contains a decision making routine that switches between the mean and MMA dependent upon the apparent presence of clouds or precipitation. Simulations indicate that the hybrid algorithm more accurately approximates a pixel's actual brightness temperature for different distortion temperatures. Analysis of the composite image distributions also shows that the hybrid most closely approximates the upper mode of the real data distributions for the study region considered.

In the presence of persistent atmospheric distortions, the distortion cannot be removed. However, the effects of the more heavily distorted pixels can still be reduced since MMA and the hybrid algorithms choose only the less distorted pixels in the averaging. It should also be noted that the algorithms can be optimized for specific study regions. Areas with different latitudes may be able to use shorter collection periods to gather the same number of measurements per pixel due to the satellite orbit geometry. The decision threshold for the hybrid can be tuned for specific regions according to the expected number of local atmospheric distortion events.

This chapter considered the development and implementation of atmospheric distortion reduction techniques applied to imagery of vegetated land regions rather than over sea or glacial ice. Land regions are chosen for this study since the effects of atmospheric distortion are significantly greater than in the cryosphere. The method can be applied observations of stationary ice forms such as land ice, glaciers, and ice shelves. Unfortunately, ice motion precludes the application of the algorithm in sea ice areas using current sensors. Future sensors offering greater temporal and spatial sampling may may have sufficient temporal resolution to facilitate the use of these methods for sea ice.

Chapter 5

Multivariate Ice Extent Mapping from Scatterometer Data

5.1 Introduction

Previous chapters have addressed various key issues in scatterometer and radiometer image reconstruction. Reliability in σ^o or T_B estimates contained in enhanced resolution imagery is critical to ensuring accuracy in parameter extraction studies. This chapter discusses one such application of reconstructed scatterometer images - the estimation of polar sea ice extent. This work was published in the *Journal of Geophysical Research* in 1999 [8].

Several factors motivate the interest in monitoring the extent of sea ice. Sea-ice extent is a critical input to global climate and geophysical models. Polar ice sheets act as insulating layers between the relatively warm ocean and cool atmosphere and can radically change the albedo of the Earth's surface. It also plays a vital role in the planetary water exchange cycle. Moreover, sea-ice extent may be used as a sensitive indicator of global climate change [1]. Hence, monitoring the extent of sea ice is of great interest to the remote sensing community.

In addition to climatological reasons, sea-ice mapping is needed for retrieval of ocean wind velocities from scatterometer measurements. The NASA scatterometer (NSCAT) was designed to infer surface wind speed and direction over the ocean. If measurements are included that are corrupted by non-ocean surfaces such as sea ice, the wind estimates are degraded. Thus, an accurate knowledge of the location of sea ice is required. In this chapter, an adaptive technique for mapping the sea-ice extent using NSCAT data is developed and compared to Special Sensor Microwave

Imager (SSM/I) derived ice maps. Using the methods discussed in this chapter, six day average ice extent maps are processed every three days over the nine months of NSCAT data. The ice maps are used in the final reprocessing of the NSCAT data.

As discussed in Chapter 2 the Scatterometer Image Reconstruction with Filter (SIRF) algorithm was developed to enhance scatterometer image resolution by combining data from multiple passes of the satellite [39]. Estimates are obtained for the two primary parameters (A and B) characterizing the near-linear depedence of σ^o (in dB) on incidence angle, θ (see Eq. (2.2)). SIRF generates images of both A and B from scatterometer σ^o measurements. These values provide valuable information about surface parameters.

This chapter describes the development and implementation of an adaptive sea-ice extent mapping method and its comparison to SSM/I derived maps. Section 5.2 describes the resolution enhanced parameters used in the multivariate analysis of the data. Section 5.3 gives an overview of the sea-ice mapping technique and discusses each of the steps in detail. The technique is applied to NSCAT polar data and the results are given in section 5.4. The final section contains the conclusions drawn from the analysis.

5.2 Polar NSCAT Data

As described in Chapter 2, the NASA Scatterometer (NSCAT) launched in August of 1996 is a real aperture dual polarization Ku-band radar scatterometer designed to measure the normalized radar backscatter coefficient (σ^o) of the Earth's surface. Using the SIRF algorithm, dual polarization A and B images with an effective resolution of 8-10 km can be generated with six days of data. NSCAT v-pol images can be produced with only three days of data since there are more v-pol antenna beams than h-pol beams. However, six days are used to ensure that the h-pol data provides enough coverage to create the reconstructed image. Since the v-pol images are reconstructed with more measurements, the qualities of the A and B estimates are subjectively superior to the h-pol images. Sea-ice dynamics may cause the ice edge to change significantly during a six day interval. As a result, the ice maps generated by this technique must be regarded as average ice extents during the imaging period. The method can be applied with data over shorter intervals (especially in the Arctic region) with some loss of coverage and degradation of the h-pol image quality.

The dual polarization A and B values for each pixel provide four parameters that can be used to detect sea ice. In addition, σ^o error standard deviation is also useful. These parameters are described in the remainder of this section. Their utility in the discrimination between sea ice and open ocean is also discussed.

5.2.1 Copol Ratio

A useful parameter in the discrimination of sea ice and ocean is the copol ratio, defined as the ratio of σ^o_{vv} and σ^o_{hh} [25]. This can be extended to a copol ratio of the incidence angle normalized σ^o values. For the purposes of this chapter, the copol ratio γ is defined as the ratio of the A_v and A_h values:

$$\gamma = A_v / A_h. \tag{5.1}$$

In log space, this is equivalent to taking the difference between the V and H components. Sample A_v and A_h images are shown in Figures 5.1a-b. The corresponding γ image is shown in Figure 5.1e.

The copol ratio is sensitive to the surface scattering mechanisms. For smooth, conductive surfaces such as calm sea water, the reflection coefficients for vertically and horizontally polarized incident waves differ. In general, vertically polarized waves reflect more than their horizontal counterparts. Thus, the copol ratio in dB is positive. For rough surface dielectric layers with randomly oriented scatterers such as ice or snow, multiple reflections of the incident radiation tend to depolarize it. As a result, vertical and horizontal waves are scattered similarly and the copol ratio is closer to 0 dB. Further, the copol ratio is sensitive to the presence of ice or water even in single (Bragg) scattering situations. In these scenarios, the polarization ratio is determined by the relative permittivity of the material. Since sea ice has a much lower permittivity than ocean water, γ is also much lower. Because of these differences in scattering mechanisms, γ is useful in discriminating between different

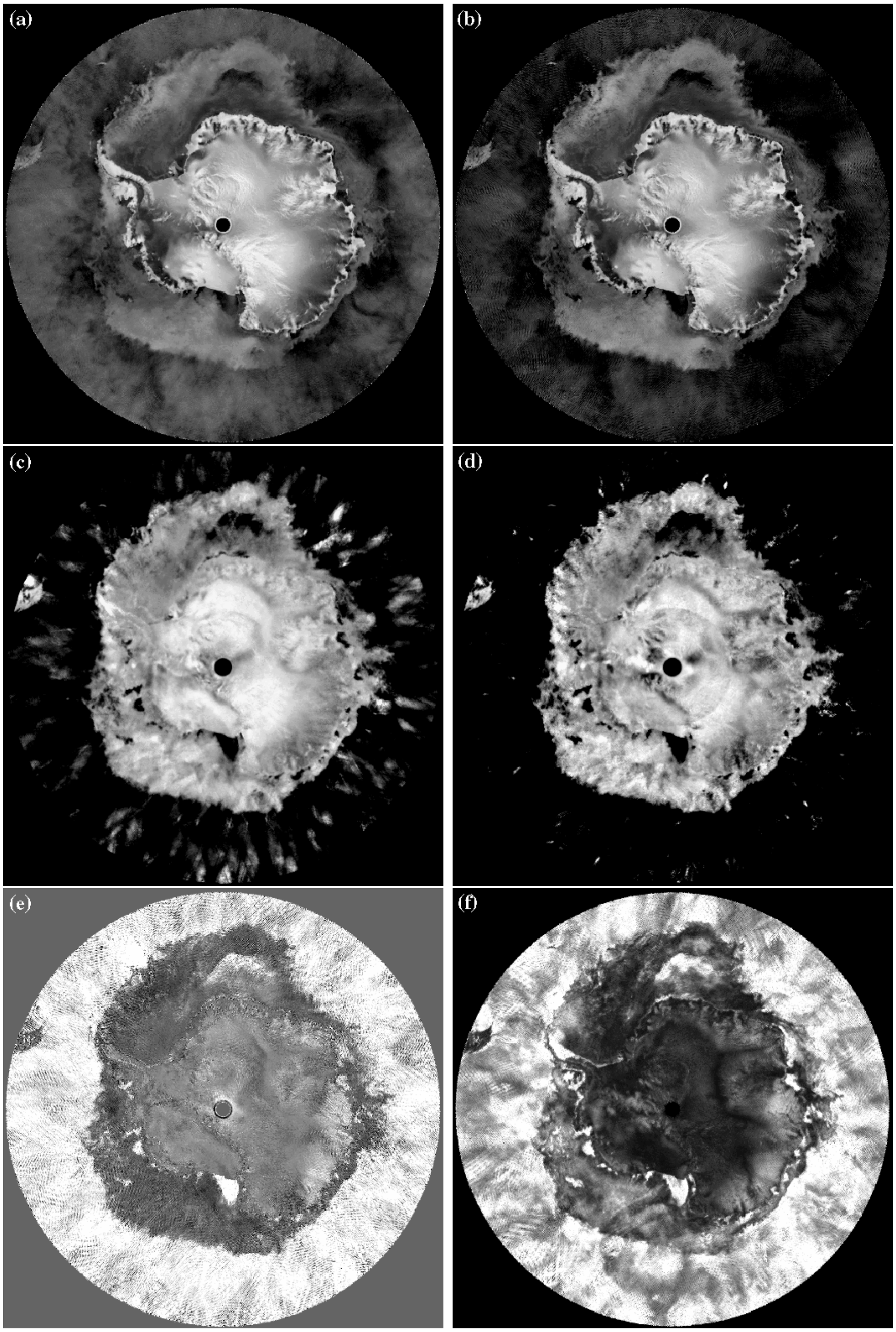

Figure 5.1: SIRF enhanced resolution NSCAT Antarctic images for the day range 1996 JD 337-342. The image panels contain (a) A_v, (b) A_h, (c) B_v, (d) B_h, (e) copol ratio, and (f) σ^o error standard deviation. Each image demonstrates that it contains information about the presence of sea ice.

ice and ocean surfaces. While the ocean generally has high γ values and sea ice (with low water content) generally has low values, in high wind conditions some ocean areas may exhibit low copol ratios. The winds induce roughness on the ocean surface which depolarizes the scattering and drives γ down. In order to overcome this, other parameters are used to assist in the classification.

5.2.2 Incidence Angle Dependence

The incidence angle dependence of σ^o, represented by B, is also sensitive to the presence of sea ice [18, 19, 61, 62]. Figures 5.1c-d give examples of B_v and B_h enhanced resolution images, respectively. Due to the increased scattering isotropy of sea ice [63] relative to the ocean, these regions tend to have less incidence angle dependence. On the other hand, ocean σ^o measurements are strongly dependent on incidence angle with the low incidence angles exhibiting higher σ^o. Thus, this parameter can be used to limited degrees of accuracy in differentiating between the ice and ocean. While it may be useful to use both B_v and B_h, this study found a strong correlation between B_v and B_h. Noting that B_v values are less noisy than B_h due to the greater number of vertical polarization measurements, only B_v is used for the discriminant analysis.

5.2.3 σ^o Estimate Error Standard Deviation

In addition to the copol ratio and incidence angle dependence, the standard deviation of the error in the σ^o estimates also contains information about polar surfaces. This metric, denoted κ, is a measure of the amount of surface response change over the ensemble of σ^o measurements due to temporal or azimuthal variability.

In order to understand κ, the measurement collection process and its relation to image reconstruction are examined. For NSCAT, each fan beam antenna illumination pattern is resolved in the along beam direction through Doppler filtering along isodoppler lines in the footprint [23]. The beam is resolved into 25 cells at different incidence angles. The size of each cell depends upon its relative location in the beam with near nadir cells covering a smaller area on the surface. The cells have a hexagonal shape determined by the Doppler filtering, motion of the satellite, and azimuth beamwidth of the antenna [23].

Figure 5.2 shows an example NSCAT cell overlaid on a SIRF resolution grid. SIRF produces A and B estimates for each resolution element. The forward projection of the A and B values yields an estimate for σ^o given by

$$\widehat{\sigma}^o = \frac{1}{N} \sum_{i=L_k}^{R_k} \sum_{j=B_k}^{T_k} h_k(i,j)[A(i,j) + B(i,j)(\theta - 40^o)] \tag{5.2}$$

where N is the number of pixels in the cell, L_k, R_k, T_k, and B_k define a bounding rectangle for the k^{th} hexagonal σ^o measurement cell, $h_k(i,j)$ is the weighting function for the $(i,j)^{th}$ resolution element (for NSCAT a simplified weighting can be used),

$$h_k(i,j) = \begin{cases} 1 & Pixel\ in\ k^{th}\ cell \\ 0 & otherwise \end{cases} \tag{5.3}$$

$A(i,j)$ is the A estimate for the $(i,j)^{th}$ resolution element, and $B(i,j)$ is the B estimate for that pixel (see Fig. 5.2). For each NSCAT σ^o measurement, the associated forward projection $\widehat{\sigma}^o$is computed. The difference between the measured and forward projected σ^o, (σ^o-$\widehat{\sigma}^o$) for each pixel is computed. The parameter κ is defined as the standard deviation of the measurements in the ensemble of this random variable for each pixel:

$$\kappa = \sqrt{\sum_l (\sigma_l^o - \widehat{\sigma}_l^o)^2} \tag{5.4}$$

where the σ_l^o are the vertical polarization measurements touching the pixel. While this study used the SIRF A and B estimates to compute κ, estimates obtained from linear regression and simple binning may also be used although the resulting κ images would have lower spatial resolution.

Figure 5.1f illustrates an example κ image. Ideally, the standard deviation, κ, would be zero if SIRF perfectly reconstructed the measurements into the A and B images. However, temporal change of the surface, noise in the σ^o measurements, and azimuthal anisotropy of σ^o may cause κ to increase though, unfortunately, the time and azimuth components are inseparable in this metric. The ocean response tends to be very dynamic in both time and azimuth due to varying wind induced surface roughness resulting in large κ values. Although higher κ values are expected in ocean

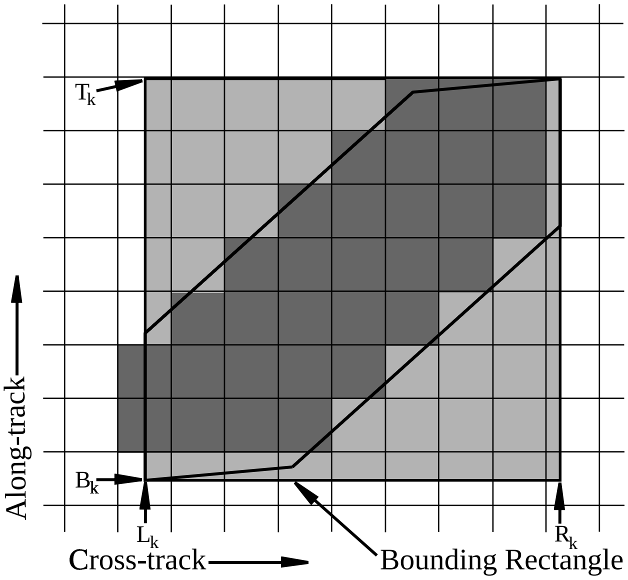

Figure 5.2: An integrated NSCAT σ^o cell overlaying the high resolution grid. Only the shaded square grid elements have nonzero $h(x, y)$. The bounding rectangle is also indicated.

regions than for sea ice, consistently calm ocean areas during the data collection period may produce low κ values. Sea-ice response, on the other hand, is less time dependent, although ice melt/freeze events or ice motion may cause some variance. Azimuthal anisotropy in sea-ice regions is generally less than 1 dB for C-band ERS-1 data [63]. Albeit in a different year and season, a similar study detailed in Chapter 3 was performed for NSCAT data and showed that the anisotropy was less than 0.6 dB in the chosen study regions [6]. Though sea ice conditions may be different in these study regions due to the different data time frames, it is expected that azimuthal variability is much lower for sea ice than open ocean.

5.3 Sea-Ice Extent Mapping Technique

The parameters discussed above provide the information needed to map sea-ice extent in the polar regions. Through proper processing, the presence or absence of sea ice can be inferred from the γ, B_v, and κ images. This section discusses a technique for generating polar ice extent maps from these parameters. First, an overall strategy is described by enumerating the individual steps. Next, a description and analysis of each step is presented.

5.3.1 Technique Overview

Several steps are combined to define an ice extent mapping technique that adaptively handles the time variant parameter distributions. The technique can be summarized as follows:

1. Produce the enhanced resolution γ, B_v, and κ images.
2. Generate γ vs. B_v bivariate distribution of the images.
3. Perform linear discrimination (LD) to obtain a first estimate of the sea-ice extent.
    (a) Find the optimal linear discrimination boundary.
    (b) Pixel by pixel classification.
4. Compute the means, variances, and covariances of the ice and ocean regions for both parameters.
5. Perform the Mahalanobis distance (MD) discrimination.
    (a) Find the Mahalanobis quadratic discrimination boundary.
    (b) Pixel by pixel classification.
6. Apply the κ correction by thresholding κ at 3.3 for all pixels for which the LD and MD estimates differ.
7. Perform edge filtering to reduce noise.
    (a) Region growing removes isolated noise patches.
    (b) Erosion/dilation techniques low-pass filter the edge.

Illustrative examples of the binary output images at different stages of the detection technique are shown in Figure 5.3 for one quadrant of the Antarctic image. Figure 5.4 illustrates an A_v image masked by the ice extent estimate generated by our method.

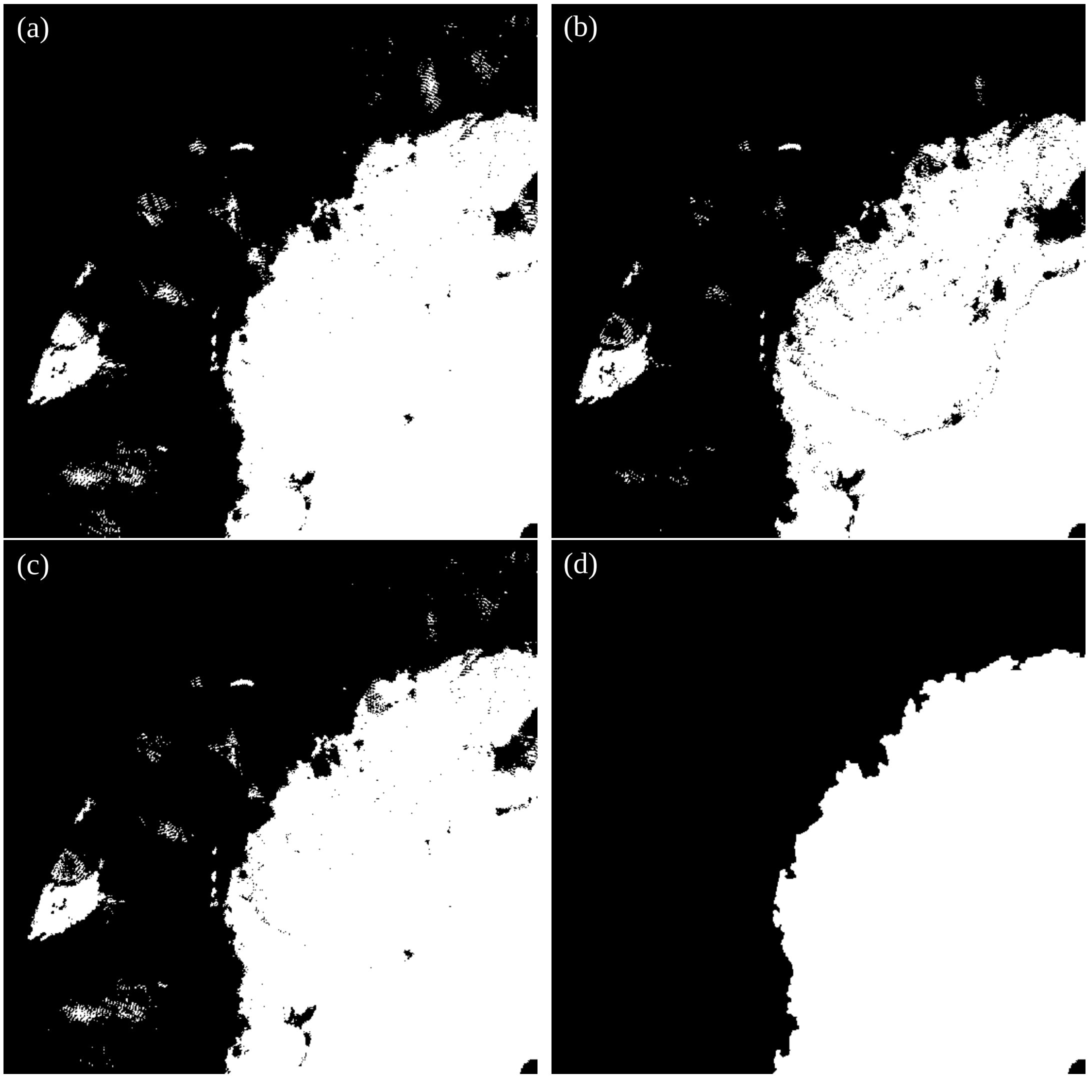

Figure 5.3: Binary images at different stages of the ice/ocean discrimination process for a single quadrant of the Antarctic 1996 JD 337-342 image. The images are (a) linear discriminant estimate, (b) Mahalanobis distance estimate, (c) κ correction applied, and (d) the result of the erosion, region growing, and dilation procedures.

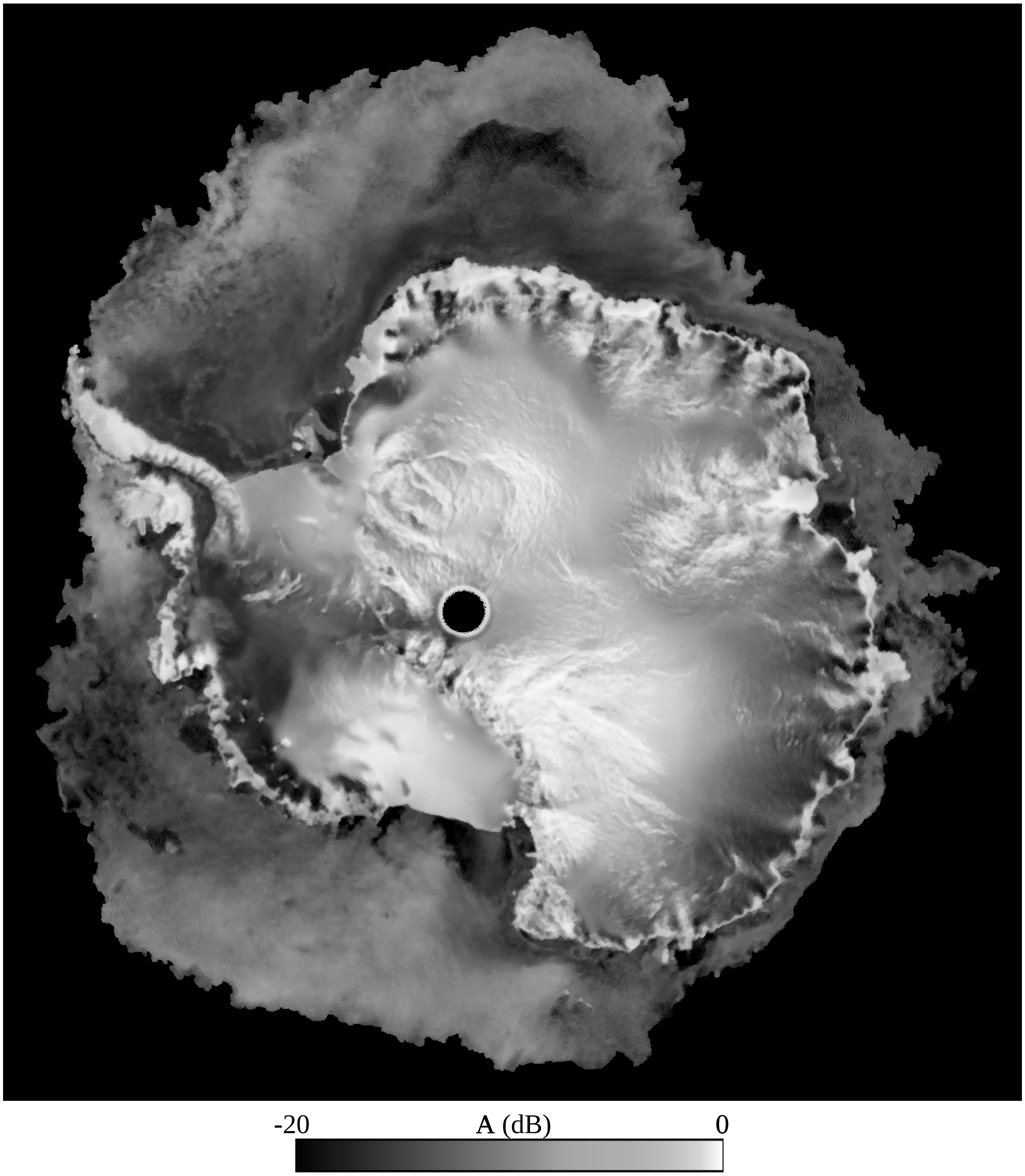

Figure 5.4: Antarctic ice masked image using the NSCAT technique for 1996 JD 337-342.

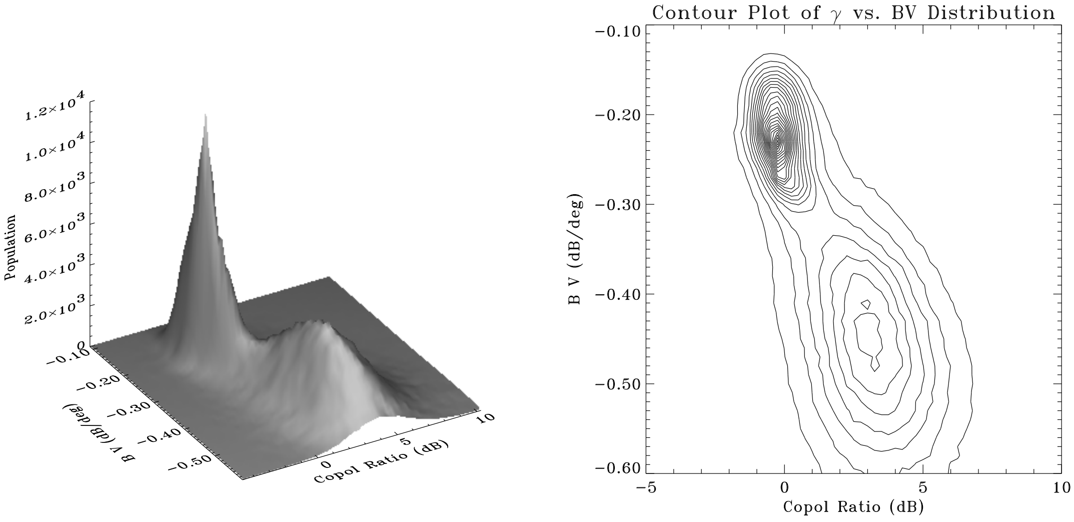

Figure 5.5: Two-dimensional distribution of γ vs. B_v values and its corresponding contour plot for NSCAT data from 1996 JD 337-342. The two modes represent ice and ocean pixels. Each mode clearly has different mean and variance values. The upper left mode is sea ice, the other represents ocean pixels.

5.3.2 Multi-Parameter Discrimination

The three parameters, γ, B_v, and κ contain varying degrees of information about the surface response which can be used to differentiate between sea-ice and open ocean pixels in the images. Of the three parameters, γ and B_v are the most sensitive to sea ice presence. This can be seen in the example images in Figure 5.1. The κ image has the most ambiguity in differentiating between the different surfaces. Indeed, when a simple threshold discrimination is implemented with each parameter individually, κ has the weakest performance. For this reason, γ and B_v are used as the primary discrimination parameters. However, the κ images can be used to reduce residual errors in localized regions when the other two are used. This will be shown in a later section.

The two-dimensional distribution of non-land pixels for the two primary parameters contains two distinct modes that separately correspond with sea-ice and ocean pixels. An example is shown in Figure 5.5 with its corresponding contour plot.

Through the proper choice of a discriminant boundary, the modes can be separated to obtain an ice extent estimate. Due to the seasonal variations in ice extent and scattering characteristics, the distribution is season dependent. Thus, the optimal mode-separating boundary must adapt to the specific distribution for each six day imaging period.

Two major steps are used in the sea-ice extent mapping technique: linear discrimination and Mahalanobis distance discrimination. The first uses a linear boundary to separate the modes of the bivariate data while the second uses a quadratic boundary.

Linear Discrimination

If the underlying ice and ocean component distributions of the joint distribution are Gaussian, the optimum linear discriminant boundary passes through the saddle point of the distribution function and is perpendicular to the line passing through the peaks of the two modes. This line can be found in an automated fashion. First, the mode peaks are located by a 5x5 bin search of the bivariate distribution. These are found by starting two separate searches in regions of the γ-B_v plane known to be in the different modes of the distribution. The search procedure ascends to each local peak. A 5x5 window is used to ensure that the search does not get hung on any local maxima. The saddle point is then located along the line connecting the two peaks of the distribution at the bin with the minimum value along the line. The linear discriminant boundary is computed as the line passing through the saddle point and perpendicular to the peak-to-peak line.

Using the linear boundary, each pixel is classified as ice or ocean by observing its associated parameter values. Pixels on one side of the line are considered ice while the others are classified as ocean. Figure 5.6 shows the γ vs. B_v distribution contour plots of images from four different NSCAT time frames. The linear discriminant boundary is also plotted. Note that as the distribution characteristics change with season, the technique adaptively assigns an optimum decision boundary. The result of the linear discrimination is a binary image of ice and ocean locations.

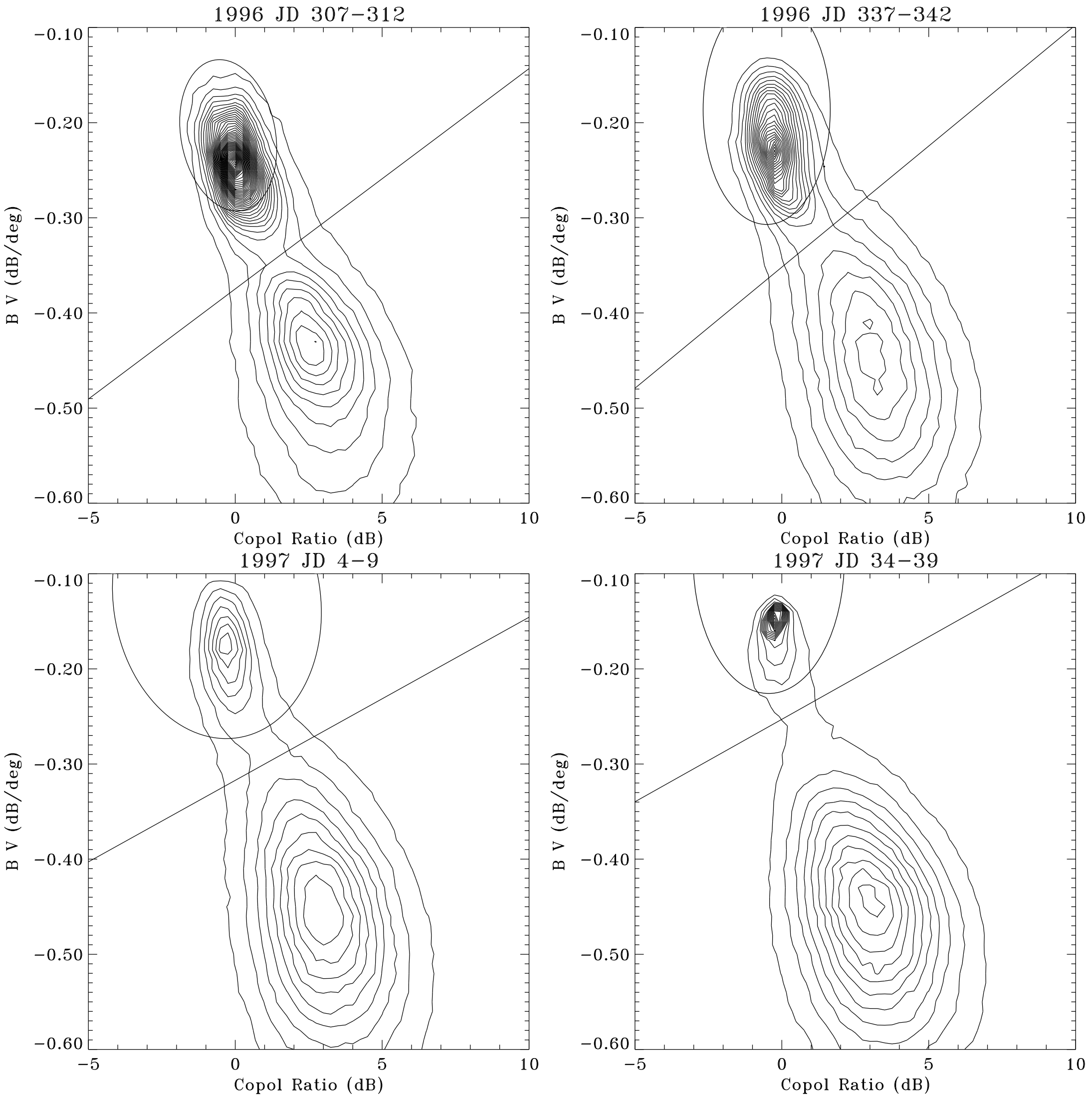

Figure 5.6: Contour plots of 4 γ vs. B_v distributions. The Mahalanobis and the linear discriminant boundaries are also plotted. The decision boundaries are adapted to be optimum for each individual distribution.

Once an ice extent estimate image is produced, the means, variances, and covariances are computed for the ice pixels and the ocean pixels. These are used as statistical estimates for the Mahalanobis distance classification.

Mahalanobis Distance Discrimination

The Mahalanobis distance aids in separating the modes of a multimodal distribution where each component distribution is Gaussian with different variances [64]. It accounts for the variance differences through the use of a quadratic rather than a linear boundary. The squared Mahalanobis distance is given by

$$r^2 = (\vec{x} - \vec{\mu})^T \Sigma^{-1} (\vec{x} - \vec{\mu}) \tag{5.5}$$

where $\vec{x}$ is the vector of parameters for the test pixel, $\vec{\mu}$ is the reference vector containing the component distribution means, and Σ is the covariance matrix.

Subjectively noting that the underlying component distributions of the bivariate γ-B_v distribution appear nearly Gaussian, the Mahalanobis distance can be applied in the discrimination of sea ice and ocean pixels. For each pixel of interest, two Mahalanobis distances are computed: r_{ice} and r_{ocean}. If r_{ice} is less than r_{ocean}, the pixel is flagged as ice, otherwise the pixel is considered ocean. Figure 5.6 shows the distribution contours plotted with the Mahalanobis and the linear discriminant boundaries. Clearly, the boundaries adapt for the particular characteristics of a given imaging period distribution.

5.3.3 κ Correction

The linear discriminant (LD) and Mahalanobis distance (MD) binary ice extent images both provide visually good estimates of the ice extent. In general, the same ice edges are observed in the LD and MD estimates with the exception of relatively small localized errors. Local errors in the LD estimates tend to overestimate the ice edge. On the other hand, the MD edges usually do not show these overestimation errors, but have some localized regions where the ice edge is underestimated. As described previously, consistently high winds during the data collection period may drive γ down resulting in false ice detection when the LD method is applied. The same weather mechanism that causes this error also increases κ since high winds over the time frame of the data collection induce higher azimuthal anisotropy and temporal variance of σ^o. The overestimation error regions of the LD images have characteristically high κ values. The correlation between LD errors and high κ suggests that κ can be used as a secondary discrimination parameter to correct for errors in the LD and MD images.

The κ correction is applied to the set of all pixels for which the LD and MD images disagree. Thus, κ becomes the deciding factor when LD and MD yield different discrimination outputs. The set consists of all LD overestimation pixels and all MD underestimation pixels. An empirical analysis of the κ data over this set of pixels for several sample images showed that κ is generally above 3.3 for the LD error pixels. The correction is then applied by thresholding κ over the error set using the following discrimination rule:

$$pixel_{i,j} = \begin{cases} ice & \kappa_{i,j} < 3.3 \\ ocean & \kappa_{i,j} \geq 3.3 \end{cases} \tag{5.6}$$

where $\kappa_{i,j}$ is κ for the i,jth pixel in the set of pixels for which LD and MD disagree.

5.3.4 Ice Map Filtering

The κ correction results in a binary image illustrating the location of sea-ice and ocean regions. However, some residual high wind induced noise over the ocean can cause ocean pixels to be misclassified as ice for reasons previously addressed. This noise is manifested in the binary image as patches of ocean that have been classified as sea ice. Other physical mechanisms may also cause patches of ice to be misclassified as ocean. The former is much more common than the latter. These anomalies often occur in isolated regions disconnected from the actual edge but may also occur on the edge itself. Each of these is handled separately in the filtering step.

Region growing techniques are used to eliminate the isolated misclassification patches in the ocean and ice. The region growing method starts with a small region known to be within the ice area (the land mass for the Antarctic region). It then expands this region within the ice area of the binary ice mask image. The region continues to grow until it gets to the outer edge of the ice region and cannot expand further. This eliminates all the isolated patches of pixels misclassified as ice in the ocean. The region growing method is then inverted to grow from the outer edge of the image inward until it reaches the binary threshold edge. This eliminates all the patches of pixels misclassified as ocean in the ice.

Once the region growing is complete, some residual noise exists on the edge itself as high spatial frequency edge characteristics and as small lobes attached by only a few pixels to the main body of ice. To remove these, image erosion and dilation techniques are used [65]. Two erosion iterations separate the smaller misclassified lobes from the main body. Region growing is then performed again to eliminate these separated lobes. To restore the edge (a low pass filtered version), two iterations of image dilation are performed. It is noted, that small fingers of ice extending from the main ice pack may be filtered out along with the edge noise. The result is a binary image mask that can be applied to the original A or B images (see Figure 5.3).

The filtering operation is designed to map the sea-ice extent rather than absolute sea-ice coverage. Consequently, open water regions within the ice pack are filtered out by the inverse region growing step. The filtering can be modified to preserve these regions by eliminating the inverse region growing step.

5.4 Results

The technique is implemented for all data during the NSCAT mission. Each enhanced resolution image is constructed using six days of data with three days of overlap in consecutive time frames. The result is a long time series of sea-ice extent images that can be used in a variety of applications including the ice masking needed in wind retrieval reprocessing of NSCAT data. In this section, the NSCAT and NASA Team algorithm SSM/I derived ice maps are compared and the seasonal ice extent as generated by both methods is observed.

5.4.1 Comparison with NASA Team Algorithm SSM/I Derived Ice Maps

To provide one source of validation for our technique, the NSCAT ice maps are compared with SSM/I-derived ice concentration images. This product is derived from passive multi-frequency, dual-polarization Special Sensor Microwave Imager (SSM/I) observations using the NASA Team algorithm [31, 36]. The NSCAT images use a polar stereographic projection similar to the projection used for the SSM/I images but are produced at a higher pixel resolution. Daily SSM/I ice concentration images were obtained from NSIDC. For each NSCAT image, the corresponding six SSM/I images were averaged together. For comparison with NSCAT results, the SSM/I average ice concentration image for the same time period is thresholded at the desired concentration level to create a binary ice map. This image is then interpolated to the NSCAT pixel resolution by determining which NSCAT pixels correspond to each SSM/I pixel and filling them with the associated SSM/I pixel value.

Four sample time periods were used for the validation. The images are each spaced by approximately one month to illustrate the changes in sea-ice extent throughout the yearly melt cycle. The resulting ice extent maps are compared with various NASA Team algorithm ice concentration images thresholded at various levels from 10% to 50%. To provide a quantitative measure of correlation between the two ice maps, the disagreement percentage is used. While this is not an ideal metric, it is easily defined as the ratio of the area of the pixels where the NSCAT and the NASA Team methods disagree and the area of the pixels that are classified as ice by either method. Figure 5.7 shows this metric as a function of NASA Team algorithm ice concentration for the four sample images. In most cases, the minimum occurs at approximately 30%. Consequently, it is concluded that the NSCAT ice edge corresponds most closely with a 30% ice concentration.

Figure 5.8 shows several sample SIRF A_v images for a quadrant of Antarctica with the associated NSCAT and NASA Team 30% ice edge estimates. These images consist of the quadrant of Antarctica from 90° west longitude (lower edges of the images) to 0° longitude (right edges of the images). Subjectively, there is a high correlation between the edges. For the images with time periods 1996 JD 307-312,

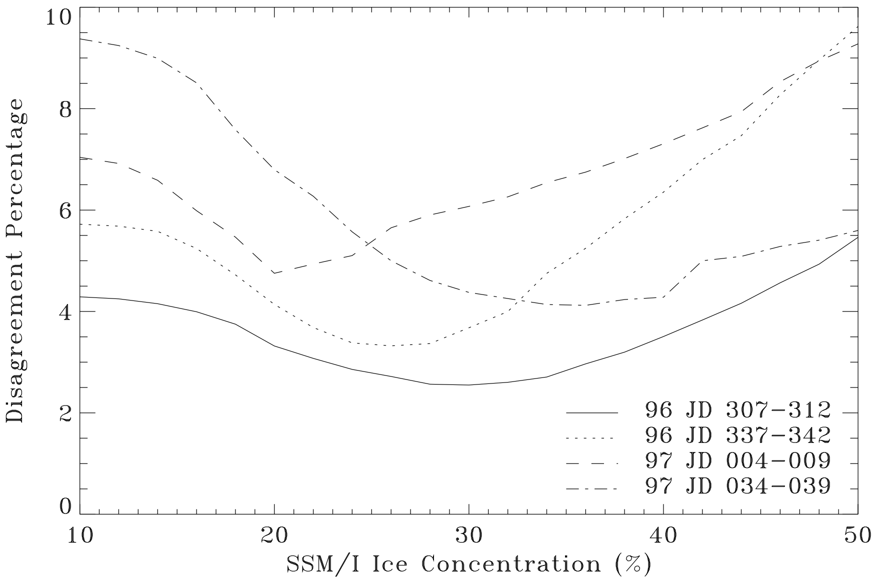

Figure 5.7: Percentage of the sea-ice area that the NSCAT and SSM/I ice extent maps disagree as a function of SSM/I ice concentration. This metric is computed by finding the ratio of the area for which the two methods disagree to the area classified as ice for either method. Four sample NSCAT images were used. The minimum generally occurs very close to 30%.

337-342, 1997 4-9, and 34-39, the disagreement percentages are 2.19%, 3.24%, 5.47%, and 3.56%, respectively. Some of the disagreement is due to the differences in image resolutions and pixel spacing since the enhanced resolution NSCAT images have higher spatial resolution than the SSM/I images.

The disagreement percentage metric is also calculated for every image in the NSCAT data set using the corresponding NASA Team 30% ice concentration images and is shown in Figure 5.9. The set consists of 80 images spanning the time period from 1996 JD 277-282 to 1997 JD 166-171. For the most part, the disagreement percentage is between 2% and 5%. The mean value is 3.34% and the standard deviation is 1.01%. The correlation between the NSCAT and NASA Team (SSM/I-derived) ice mapping techniques is strong throughout the NSCAT mission period.

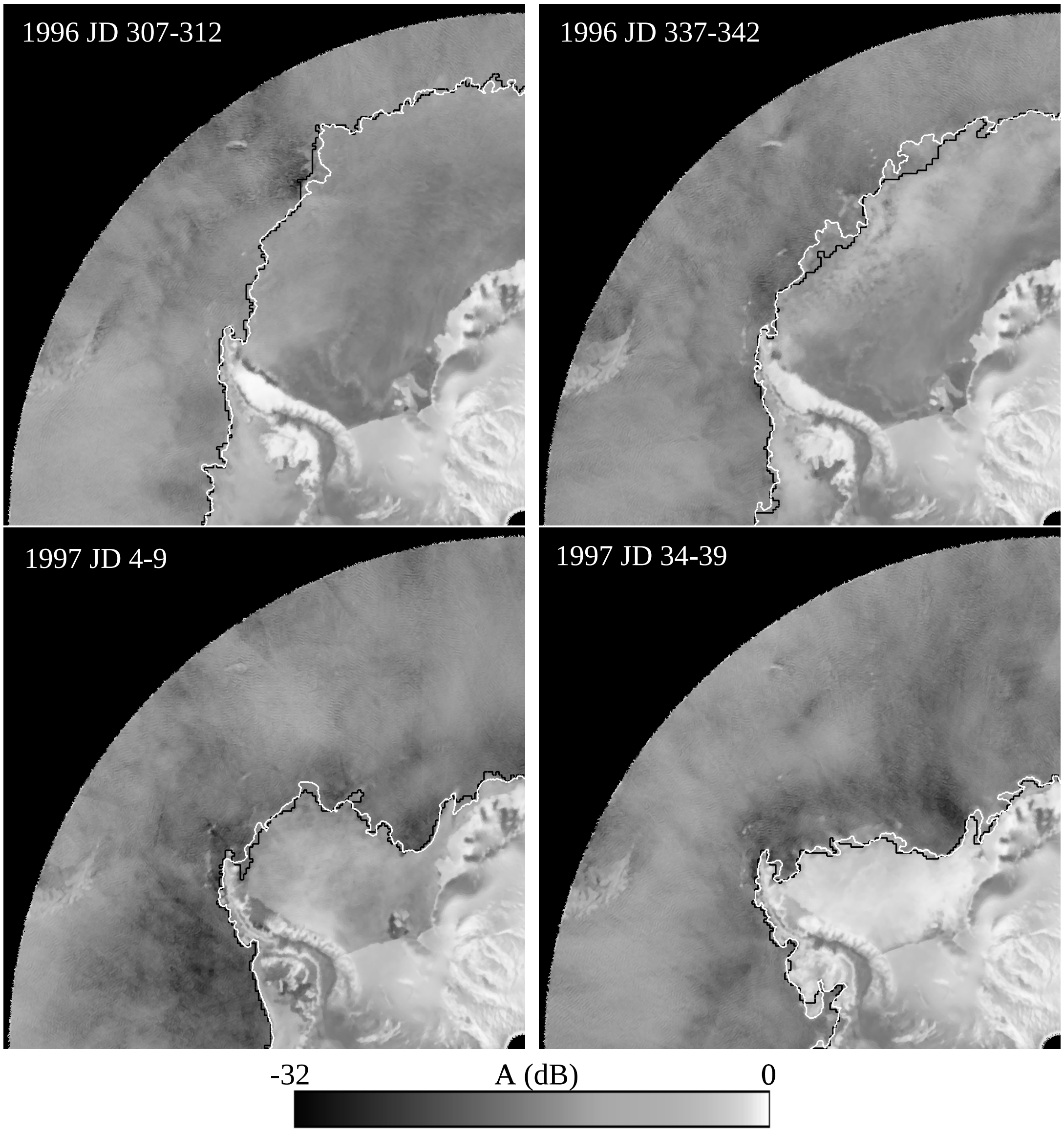

Figure 5.8: NSCAT SIRF resolution enhanced A_v images of a portion of Antarctica. The NSCAT ice edge is plotted in white. The NASA Team algorithm SSM/I derived 30% ice concentration edge is plotted in black.

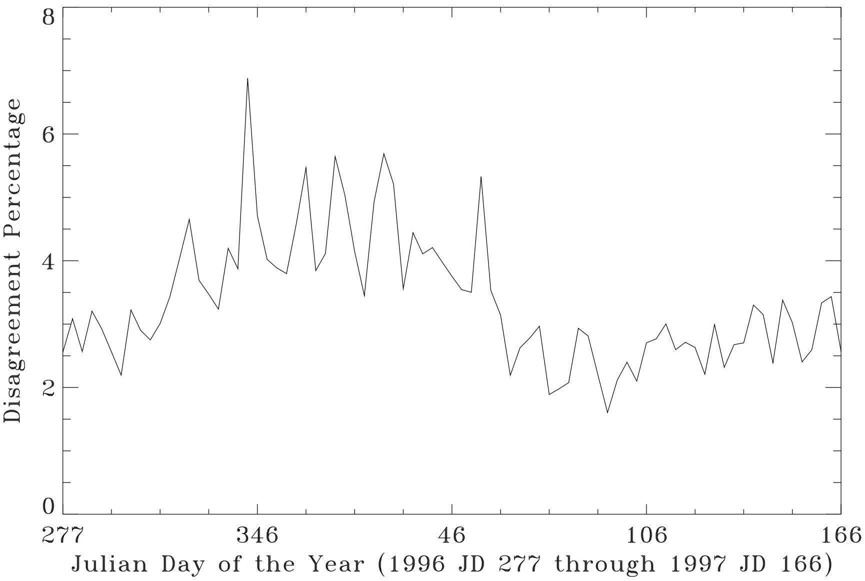

Figure 5.9: Plot of disagreement percentage metric computed by taking the ratio of surface area where the two methods disagree and the area for which either method classifies the surface as sea ice. The images each represent six days of data with three days of overlap between consecutive images. The Julian days given on the horizontal axis correspond to the first days of each imaging period.

The time period when the disagreement percentage is the greatest is during the ice retreat phase. During this time, the NSCAT estimated ice extent is generally greater than the SSM/I ice extent. The top right panel of Figure 5.8 illustrates this effect. The NSCAT edge identifies a portion of the ice pack that the SSM/I does not. In [66] a similar trend was observed in comparing NASA Team and Geosat radar altimeter ice edges.

5.4.2 Comparison with Radarsat SAR Imagery

For further validation, Radarsat SAR imagery is used. The inherently higher resolution of SAR data makes it optimal for validating the estimated sea ice edge in regions for which the actual edge is well defined. Since Antarctic sea ice SAR data is rare, only a single SAR image frame is used in the following comparison.

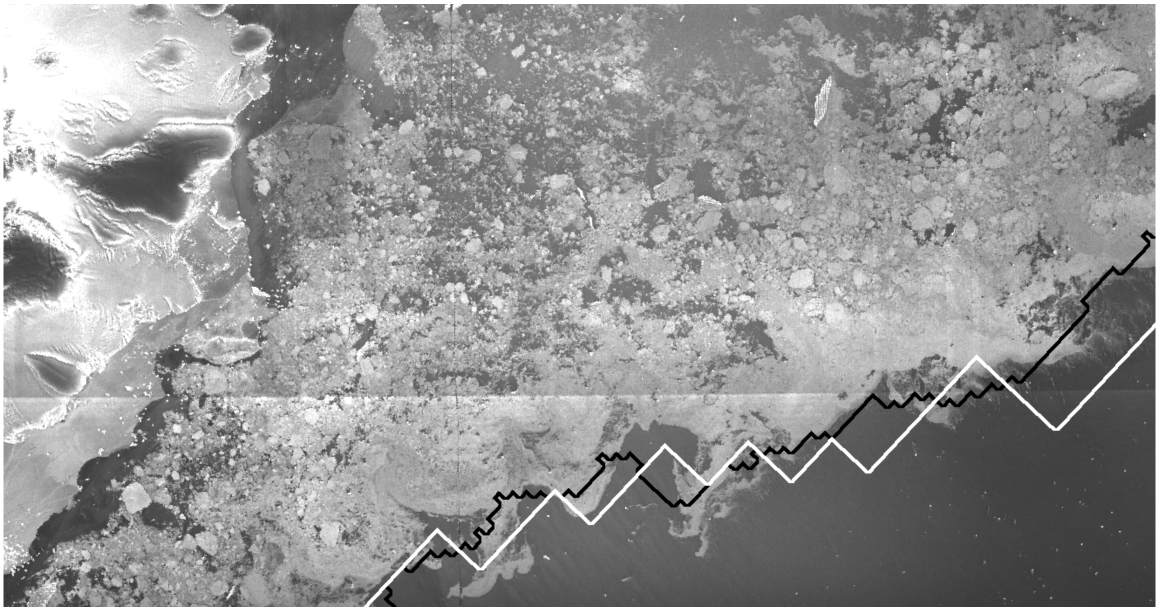

Figure 5.10: Ice edge comparison with NSCAT edge (black) and NASA-Team 30% ice edge (white) plotted over a RADARSAT SAR mosaic (uncalibrated) of a sea ice region [Radarsat data © Canadian Space Agency, 1996]. A portion of Saunder's Coast is evident on the left of the image on 20 February 1997.

Figure 5.10 shows the NSCAT and NASA-Team ice edges plotted over a C-band hh-pol RADARSAT SAR image. The NASA-Team edge was generated by averaging six days of data to be consistent with the NSCAT imaging interval. While the RADARSAT image is not calibrated and some obvious geolocation errors exist, a clearly defined ice edge is observed. Although both edges are relatively good estimates of sea ice extent, the NSCAT curve most closely follows the actual ice edge in this particular case.

5.4.3 Seasonal Sea-Ice Extent

The seasonal area of the sea-ice extent as computed from the NSCAT and NASA Team ice maps is now considered. The sea-ice extent area for a particular image is computed by finding the area for each ice flagged pixel according to the polar stereographic projection. These areas are summed to obtain the total extent.

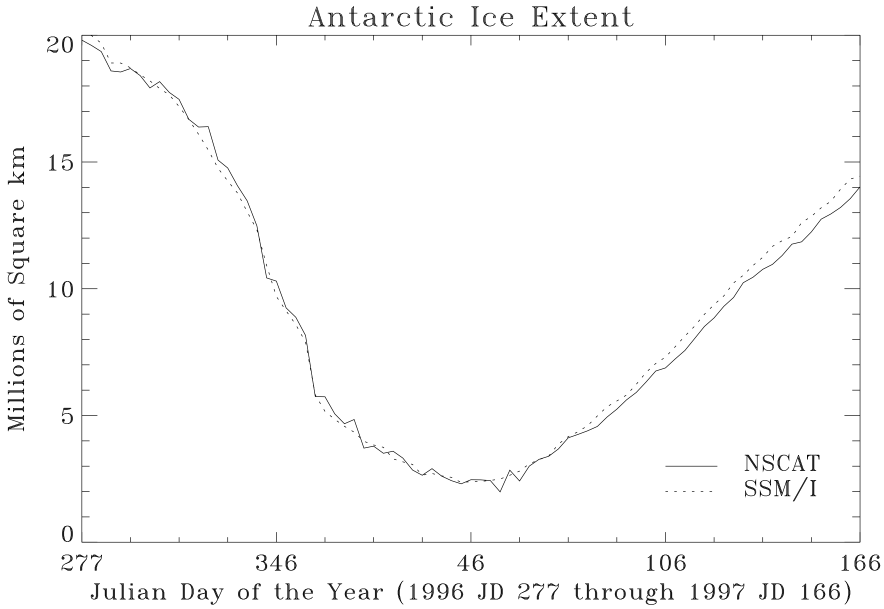

Figure 5.11: Seasonal Antarctic sea-ice extent in square kilometers using both the NSCAT and NASA Team methods. The data set extends from 1996 JD 277-282 to 1997 JD 166-171. The first Julian day of each imaging period is represented on the horizontal axis.

It should be noted that this is the total ice extent rather than the total ice area since polynyas are not masked out in the images. Figure 5.11 shows the seasonal ice extent computed for the complete NSCAT data set. The NSCAT and NASA Team signatures are very similar. For both, the melt cycle along with a portion of the freeze cycle is evident. These results are similar in form to those of [67] in which the ice extent was computed using the Scanning Multichannel Microwave Radiometer (SMMR) from 1978-1987 although the maximum and minimum of the cycle are more extreme in 1996-1997.

During the ice retreat phase NSCAT often estimates a greater ice extent than the NASA Team algorithm. This result is similar to the findings of [66] during midsummer in which the Geosat altimeter measured a greater ice extent than the NASA Team SSM/I derived product. During ice advance, the NASA Team method

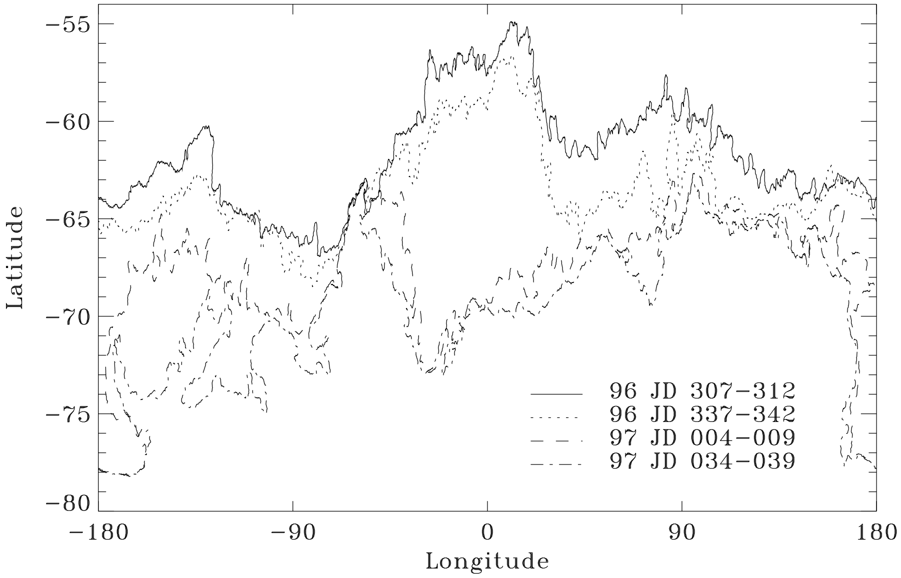

Figure 5.12: Latitude of the sea-ice edge as a function of longitude for four sample images illustrating yearly melt. The edges were generated using the NSCAT ice extent mapping technique.

consistently predicts a larger sea ice extent than NSCAT. The differences occur primarily in the Weddell and Amundsen Seas. The geographical correlation suggests that a geophysical cause is responsible for the discrepancy. Both of these areas are regions of rapid ice advance. The physical mechanisms behind these differences are presently not understood, but may be related to differences in the detection of new ice formation for active and passive sensors similar to the differences noted by Fetterer during ice retreat. The evolution of the sea-ice extent is shown in Figure 5.12. The latitude of the four sample ice edges is plotted as a function of longitude illustrating the recession of the ice edge from October to February.

The ice extent mapping technique can also be applied to Arctic NSCAT data. Figure 5.13 shows an example Arctic SIRF A_v ice masked images for 1997 JD 4-9 with the associated NASA Team edge plotted over it. Again, the resulting ice edge is similar to the NASA Team algorithm SSM/I-derived edge.

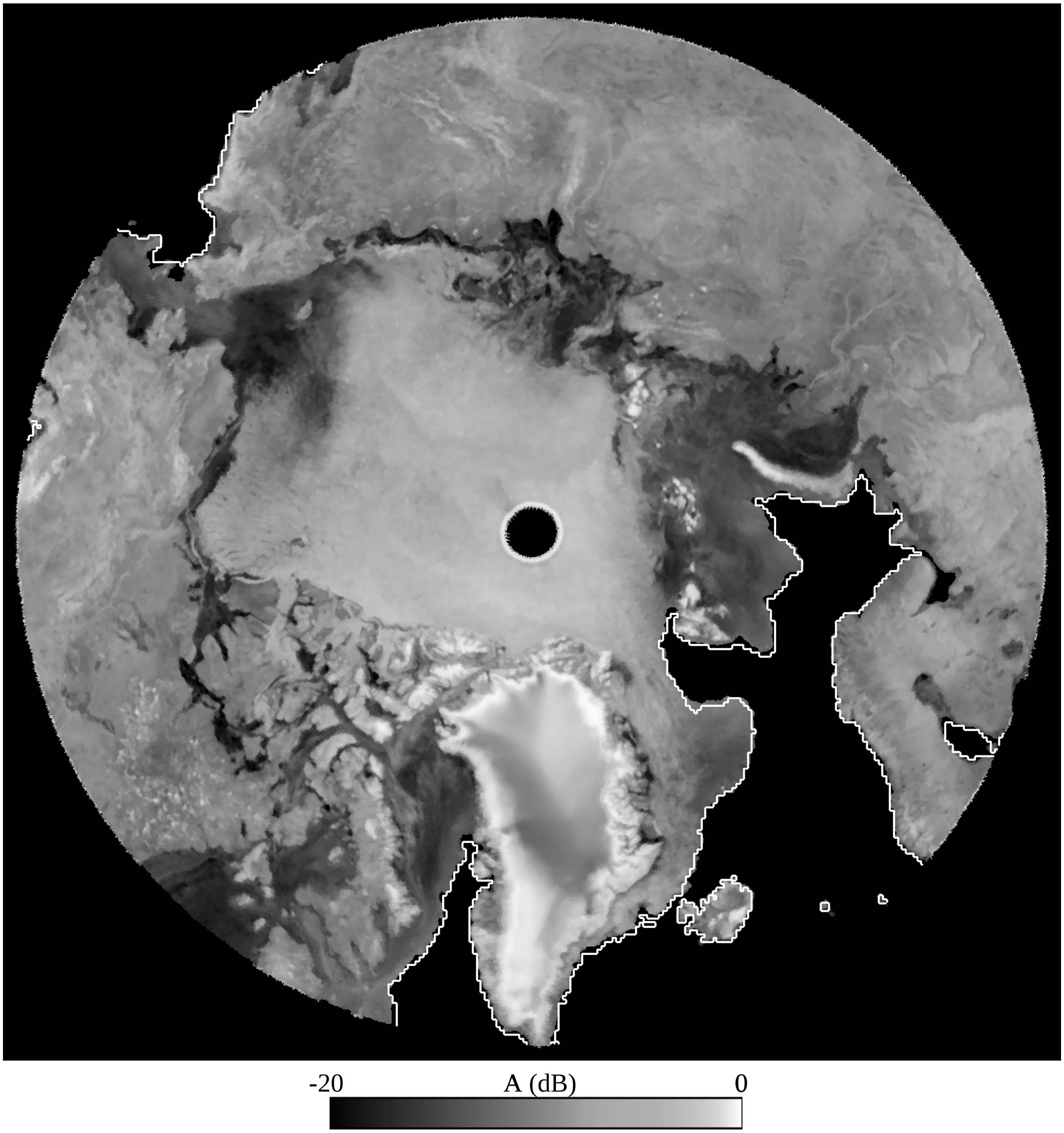

Figure 5.13: Arctic ice masked image using the NSCAT technique for 1997 JD 4-9. The SSM/I derived ice edge is plotted in white over the top of this image for comparison.

5.5 Conclusions

NSCAT dual polarization Ku-band data in concert with the SIRF resolution enhancement algorithm can be used to effectively determine sea-ice extent in the polar regions. The copol ratio and the incidence angle dependence of σ^o are used as primary classification parameters since they appear to be the most sensitive to the presence of sea ice. The κ parameter on the other hand is useful for correcting errors in the linear and quadratic ice extent estimates due to its sensitivity to classification error inducing high winds in ocean regions. The technique requires no *a priori* information and adapts to the temporal variability of the underlying parameter distributions. When applied, the sea ice detection method closely matches the NASA Team algorithm SSM/I-derived 30% ice concentration extent. In a comparison with a Radarsat SAR image, the NSCAT and SSM/I-derived methods both show good correlation with the actual sea ice edge. However, the higher resolution of the NSCAT edge results in a better match. While only scatterometer data has been used to estimate the sea-ice extent, scatterometer data can be coupled with radiometer data to improve the accuracy of ice maps and ice classifications.

Application of the described technique has resulted in a large data set comprised of six day average ice extent images every three days of the polar regions during the nine month NSCAT mission. This data set can be applied to a wide range of studies, including global climate studies and wind processing. By excluding regions with ice cover, the probability of error in extracting wind speed and direction from the backscatter data goes down.

The loss of the ADEOS satellite prematurely terminated the flow of NSCAT data. While the ice mapping technique was developed to be used with NSCAT data, it can be adopted to work for other Ku-band scatterometers. One current and one future scatterometer are of interest: SeaWinds on QuikSCAT was launched in 1999 and SeaWinds on ADEOS-II is scheduled to fly in 2001. These differ from NSCAT in several ways. First, they are dual polarization scanning pencil beam scatterometers. The inner scan is at 46° incidence and is horizontally polarized ($A_h(46)$) while the outer scan operates at 54° and is vertically polarized ($A_v(54)$) [27]. Hence, they do not contain the information needed to obtain an estimate of σ^o incidence angle dependence. Also, since the vertical and horizontal σ^o data are at different incidence angles the copol ratio is undefined for QuikSCAT and SeaWinds. However, by using two different primary classification parameters, A_h and $A_v(54)/A_h(46)$, the ice mapping technique can still be applied. It was found that using simulated SeaWinds data, the sea ice can still be mapped although the occurrence of error went up slightly. Chapter 7 discusses the development of an adopted version of this algorithm for SeaWinds data.

An advantage of the QuikSCAT and SeaWinds instruments over NSCAT is the increased coverage of the earth's surface. Both have a wider swath than NSCAT and have no nadir gap allowing QuikSCAT and SeaWinds polar images to be produced using only 1-2 days of data rather than the six days required for NSCAT. As a result, the ice extent maps can be produced at 1-2 day intervals with quality and resolution similar to the NSCAT six day ice extent estimates. In this case, sea ice dynamics become less of a factor in discrimination errors near the edge. Alternatively, six days of QuikSCAT or SeaWinds data can be used resulting in a higher confidence ice extent map due to the increased quality of parameter estimates.

Chapter 6

Multisensor Sea Ice Classification

6.1 Introduction

Chapter 5 presented an automated adaptive algorithm that estimate polar sea ice extent using only NSCAT data. As previously discussed, the spatial distribution of sea ice is an important parameter in understanding many geophysical processes. This chapter takes the next step in determining a more detailed cryosphere characteristic, the sea ice class. The work presented here has been accepted for publication in the *IEEE Transactions on Geoscience and Remote Sensing* and will appear in the July, 2000 issue [9].

Through a knowledge of sea ice class or type in combination with sea ice extent, scientists can gain a greater understanding of more processes. For example, sea ice types is closely related to ice age, thickness, and density. These parameters are important in heat transfer studies. Additionally, by identifying sea ice types characterized by significant deformation the dynamic process of ice pack motion and sheering can be better explained. Furthermore, ice type identification can also be used to determine ice brine content or salinity. These factors are key in the fresh water exchange that occurs in sea ice regimes.

Fundamental sea ice characteristics can be grouped into a number of general sea ice classes or types. Various studies have been pursued to classify ice type from observed microwave signatures. A single-band classifier using 33.6 GHz passive high-resolution aerial measurements was used on Beaufort Sea data [68]. Kwok et al.

developed a method for classifying high-resolution ERS-1 SAR imagery using ancillary data from meteorological databases [69]. Rignot and Drinkwater also performed a MAP classification on polarimetric airborne SAR data and compared results to high resolution passive microwave data [70]. Hara et al. proposed an unsupervised polarimetric SAR multi/first year ice classifier using a neural network followed by iterative maximum likelihood classification [71]. The primary strengths of these approaches lie in the high spatial resolution capability of the instruments. Consequently, image pixels are much less likely to contain a mixture of ice types. Lower resolution techniques have also been proposed. Wensnahan et al. proposed a classification method using passive radiometer data [72] to estimate the concentrations of first-year, multi-year, and thin ice in the Arctic. In [73], a classifier was developed that uses single channel 5.3 GHz ERS scatterometer data. Finally, a neural network classifier for sea ice type is given in [74]. These studies are representative of the different work that has been done in microwave sea ice classification.

This chapter presents a multisensor sea ice classification approach which uses multispectral, dual-polarization data collected from both active and passive spaceborne instruments for the segmentation of Antarctic data. In section 6.2, important background information is given describing the instruments from which data is collected, the image reconstruction methodology, the ice extent mapping techniques, and the basic ice type signatures. Section 6.3 introduces the multivariate analysis techniques fundamental to the preprocessing stage of the algorithm including data fusion and principal component analysis. The sea ice classification algorithm is described in detail in section 6.4. A brief derivation of statistical measures as well as convergence metrics are given. Results of the application of the algorithm to actual data are presented in section 6.5. The final section contains the conclusions.

6.2 Microwave Remote Sensing of Sea Ice Types

The proposed ice classification scheme uses data from several different spaceborne instruments. This section provides a brief background of each of the data collecting instruments and the corresponding ice type signatures. In addition, the methodology for image reconstruction is described. Finally, an ice masking algorithm that removes open ocean pixels is summarized.

6.2.1 Spaceborne Microwave Sensors

Data from three different sensors are used in the classification approach which follows. The sensors are chosen for their temporal simultaneity of measurement collection during the target time frame of September-October 1996. In addition, all of the selected instruments have large-scale coverage capability. The first data set comes from the dual-polarization, Ku-band NSCAT that flew from August 1996 to June 1997. The second sensor is the C-band active microwave instrument (AMI) aboard the European remote sensing satellite (ERS-2). One mode of operation of the AMI is the wind scatterometer mode which measures the v-pol normalized radar cross section (σ^o) at several azimuth and incidence angles. Finally, passive radiometer data is used in concert with the active scatterometer data to produce a merged data set. The SSM/I aboard the Defense Meteorological Satellite Program series of satellites is a total-power, seven channel, four frequency radiometer. The channels are h- and v-pol at 19.35, 37.0, and 85.5 GHz and v-pol at 22.235 GHz. Brightness temperature (T_B) measurements are collected from each channel. For more information about these instruments, see Chapter 2.

Each of the three instruments offer a wide spectrum of observations at different frequencies and polarizations. While the inherent resolutions of the various instruments are sufficient for the study of large-scale phenomena such as surface winds or atmospheric parameters, they can be too low for use in some studies. In an effort to ameliorate this problem and to place the data on compatible grids, the scatterometer image reconstruction (SIR) algorithm is used to enhance the spatial resolution of both scatterometer and radiometer data [38, 39] (see Chapters 2 and 3). Consequently, v- and h-pol A and B images are obtained for NSCAT, v-pol A images are produced for ERS-2, and SSM/I T_B images are produced for each of the seven channels.

All images are generated using six days of data with three days of overlap in consecutive images. While NSCAT v-pol and SSM/I can achieve full coverage of the Antarctic ice pack in much less time, ERS-2 and NSCAT h-pol require the full six days. For consistency in pixel spacing between the different images, the 8.9 km images are interpolated to the 4.45 km grid. All parameter images are used in the classification except for the ERS-2 B images which have relatively high noise levels and are thus discarded. The final merged data set consists of 12-dimensions with three A, two B, and seven T_B images. Sample images of all 12 types are shown in Figure 6.1 for 1996 JD 261–266. Figure 6.2 shows two zoomed versions of these images which illustrate the Weddell Sea quadrant of the NSCAT v-pol A and the SSM/I v-pol 37 GHz images. The imagery shown has been masked with an ice extent mapping algorithm discussed in the next section. A significant amount of detail is evident in the sea ice regime of these images. This is exploited in the proposed classification algorithm.

Each of the described images are ice masked using the methods presented in Chapter 5. Open ocean pixels in the reconstructed imagery are masked out for two reasons. First, the sea ice classification algorithm presented below uses statistical preprocessing techniques which take advantage of the covariance structure of the data to reduce the dimensionality of the data space. Since ocean pixels have typically high covariance values in all of the active and passive signatures, undue weight would be given to ocean pixels in the new data space effectively reducing the classification potential. Second, a significant number of the image pixels are open ocean and the removal of these pixels reduces the size of the classification data set.

6.2.2 Ice Type Signatures

Data collected by NSCAT, ERS-2, and SSM/I are used to segment the data into six general ice types or classes. While the following discussion is based on the general behavior of scattering and emission from sea ice, *in situ* measurement averages for the various ice classes can be found in [73] for C-Band scatterometer Antarctic data and [74] for Arctic SSM/I data.

The first ice type to be considered is smooth first-year (SFY) ice. This class represents relatively young ice which has not been roughened by the differential

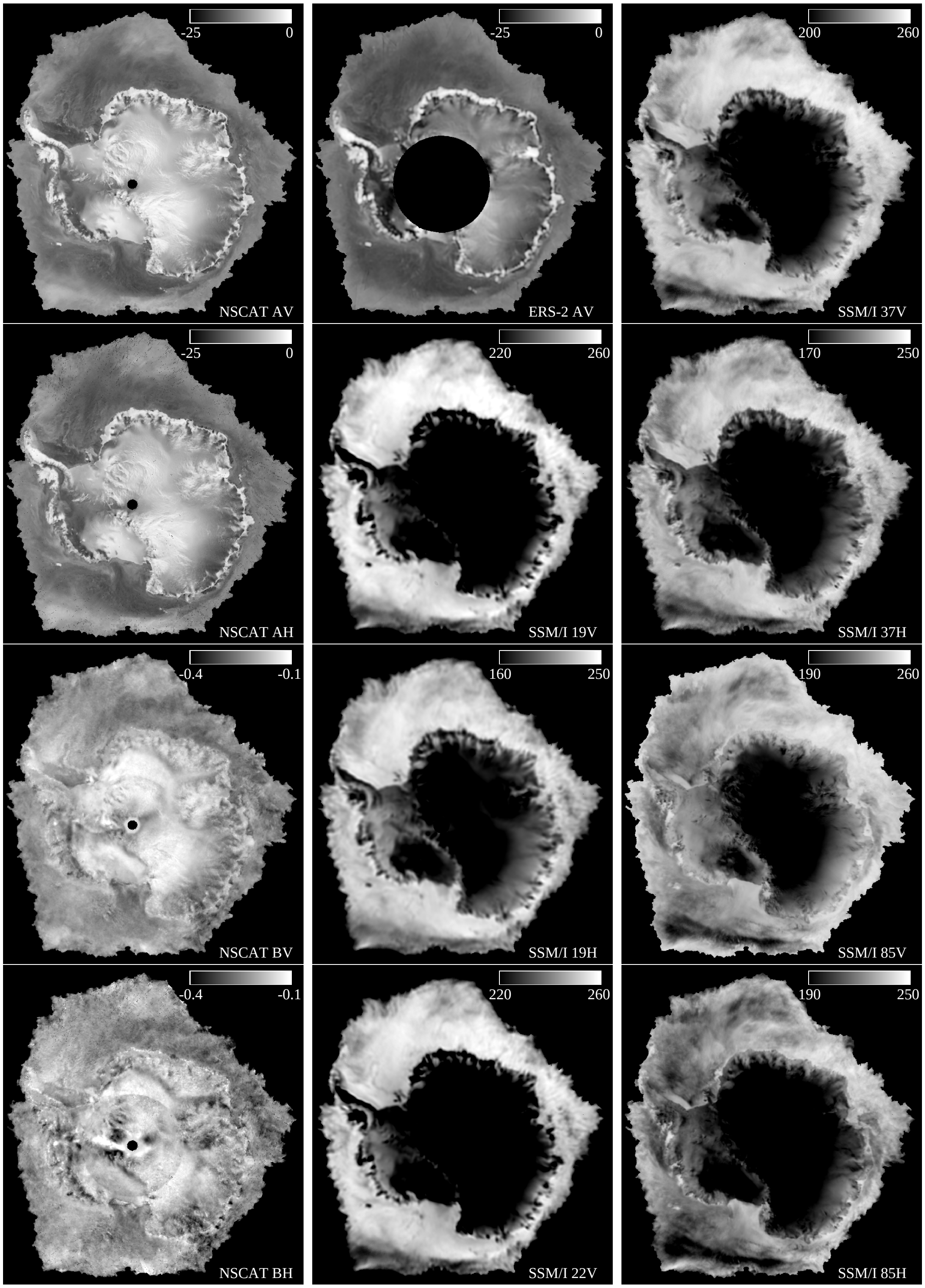

Figure 6.1: Image set for 1996 JD 261-266.

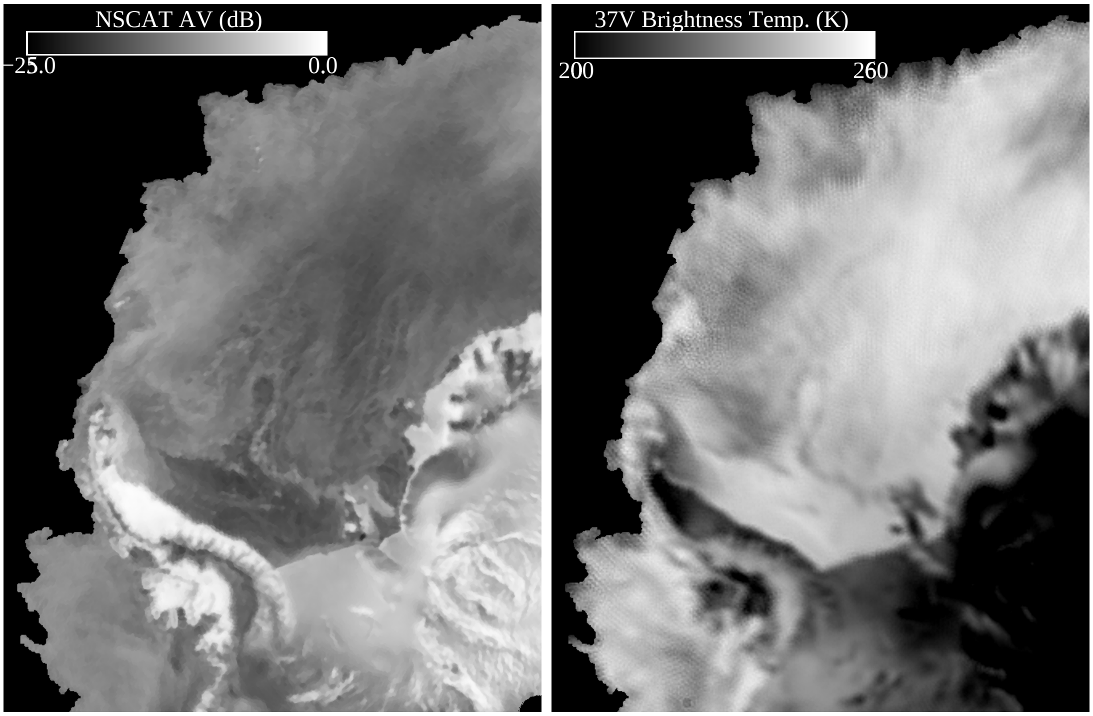

Figure 6.2: Sample Weddell Sea quadrant images of NSCAT A_v (left) and SSM/I 37V (right).

motion and deformation of the ice pack. Ranging in thickness from 10 cm to 1 m, smooth first-year ice is highly saline with a high density of brine pockets caught within the ice crystal lattice. The high salinity causes this ice type to be very lossy and thus dominated by surface scattering and emission at virtually all frequencies used in the study. The active signatures exhibit low A and B values due to the strong incidence angle dependence of smooth surface scattering from level ice. T_B measurements are expected to be relatively high.

Like smooth first-year ice, rough first-year (RFY) ice is very saline and lossy. Surface scattering and emission dominate the signatures. Motion within the ice pack causes extensive roughening of this ice type. In general, the rough surface scattering cause A values to be higher than for smooth ice types and B values to rise (ie, have less incidence angle dependence) [46, 73]. While passive signatures are less sensitive to the difference in RFY and SFY ice classes, T_B values are radiometrically cooler for RFY when compared to SFY ice.

Perennial (PER) ice is another important Antarctic ice type. While multiyear ice is common in the Arctic, less Antarctic sea ice survives more than one summer's melt since the Antarctic continent limits the southern extent. Regardless, a small amount of perennial ice can be found and is included in the classification. Over time, brine drainage results in much lower salinity and hence lower electromagnetic absorption in this ice type. This leads to greater penetration depths and volume contribution to scattering and emission. A and B values are typically higher than those for RFY ice while T_B measurements are lower.

Another sea ice type to be considered in the classification is the iceberg class (IB) consisting of large floating plates of fresh water ice that have calved or broken off from an ice shelf. In the absence of surface melt, this ice class has very low loss resulting in a large contribution from volume scattering and emission especially at lower microwave frequencies Furthermore, these targets may extend vertically out of the water several tens of meters thereby acting as strong reflectors. As a result, A and B are very high and T_B values are very low compared to other ice classes. The volumetric scattering contribution also causes a depolarization resulting in similar response for both v- and h-pol measurements.

Pancake ice is also included in the classification effort because of its unique appearance over extremely large areas of the marginal ice zone during winter ice growth. This ice regime is normally found in the outer portions of the ice pack where wave action aggregates and deforms newly growing frazil ice into small floes called pancakes. The high roughness of this type results in a signature that is very similar to perennial ice in both active and passive signatures [63, 73].

The final ice type is the marginal ice zone (MIZ). This dynamic region of the ice pack consists of mixtures of ice and open water. The open water contribution drives T_B down. Wind roughening of the ocean surface in these regions causes A and B values to often be confused with other ice types. While pancake ice is typically found in the marginal ice zone, the two classes are considered separately in this study in order to discriminate between regions of low ice concentration in the MIZ and high concentration pancake regimes existing only under ice growth conditions.

One of the complicating factors in sea ice classification is the seasonal dependence of the ice type microwave signatures. The signatures are most distinct during the Austral winter months when ice types exhibit negligible surface melt. Hence, the differences due to subsurface contributions are strong. When temperatures rise and water content increases (typically during the mid-November to March Austral summer months), the scattering and emission from lower ice layers become increasingly masked and surface scattering mechanisms begin to dominate. This causes ice type clusters to drift in the 12-dimensional data space with some clusters merging together. For this reason, an effective classification technique must have the ability to adapt to changing signatures in order to maintain a maximal degree of accuracy.

6.3 Multivariate Data Analysis

As previously discussed, the classification data set consists of 12 parameters from which sea ice type is to be extracted. Additional preprocessing is performed on the data to maximize classification accuracy and minimize required computational effort. Since the parameters are measured in very different units, data fusion techniques are used to give equal weighting to all of the data. In an effort to reduce the computational complexity and the noise levels, principal component analysis is implemented.

6.3.1 Data Fusion

The 12-dimensional data space consists of three basic types of data with differing units. The first data type, A, is measured in dB with a typical range of -30.0 to 0.0 dB. The incidence angle dependence of σ^o, given by B, contains dB/deg values ranging from -0.4 to -0.1 dB/deg. The last data type is T_B measured in degrees Kelvin with sea ice values from 150 K to 290 K depending on frequency and polarization. Since each data type is quite different from the others, standardization is required to ensure that each data type is given appropriate weight in the classification. The standard approach is to shift and scale the data so that each of the 12 parameters have zero mean and unit variance. However, this may remove some ice class information that exists between the mean responses of parameters that are within the same data type. In an effort to preserve the ice class dependent biases that exist in each data type, the following standardization technique is applied for a particular observation x

$$x_s = \frac{(x - \mu_{type})}{\sigma_{type}} \tag{6.1}$$

where μ_{type} and σ_{type} are the collective mean and standard deviation of all the parameters belonging to a particular data type (e.g., A, B, or T_B data) and x_s is the new standardized parameter value. Hence, the three general data types, A, B, and T_B are transformed such that they have zero mean and unit variance though specific parameters (e.g., A_v, A_h, etc.) may not have these characteristics. The resulting data resides in a 12-dimensional unitless space in which each data type has similar range and variance.

6.3.2 Principal Component Analysis

The high dimensionality of the classification data set equates with significant computational requirements. To reduce the number of required parameters, principal component analysis (PCA) is implemented. PCA is a powerful data analysis tool that effectively rotates the data space by projecting each observation onto a new orthonormal basis [75]. The resulting basis vectors are chosen such that the first spans the direction of maximum variance in the data. Successive vectors are chosen to span the maximum variance not accounted for by previous vectors.

For the classification problem at hand, data vectors are composed of the 12 standardized values

$$\vec{y} = [y_1 \; y_2 \; . \; . \; . \; y_{12}]^T \tag{6.2}$$

where the y_i represent the standardized versions of the NSCAT, ERS-2, and SSM/I data values. PCA uses an eigenvalue/eigenvector decomposition of the data to construct the necessary orthonormal basis vectors. The eigenvalue/eigenvector equation is given by

$$K\Gamma = \Gamma\Lambda \tag{6.3}$$

where K is the 12 x 12 covariance matrix of the standardized data, Γ is a matrix with eigenvectors of K along the columns (which form a basis for the original 12-dimensional space), and Λ is a diagonal matrix with the eigenvalues of K along the diagonal (which represent the variances spanned by each eigenvector). Once these are obtained, a 12 x 1 data vector $\vec{y}$ containing standardized parameters is transformed through projection onto the new basis

$$\vec{z} = \Gamma^T \vec{y}. \tag{6.4}$$

The elements of $\vec{z}$ are called the principal component scores [75].

The analysis technique is used on land/ice masked imagery to produce 12 principal component images composed of a combination of information contained in the original parameters. The pixel values in individual PCA images represent coefficients of the eigenvector associated with that principal component score. The size of the corresponding eigenvalues determine the variance and informational content of each of the images. For example, the PCA transformation was performed for the microwave data set during the imaging interval 1996 JD 261-266. Figure 6.3 illustrates the resulting eigenvalue spectrum. Clearly, a majority of the data variance is contained in the top few principal component images implying that lower PCA images can be neglected with minimal effect on the final classification. Wensnahan et al. suggest keeping only PCA parameters whose variance is much larger than measurement uncertainty (converted into principal component space) [72]. Such a choice of eigenvectors allows information to be separated from noise. Indeed, the lower principal component images used in this study appear very noisy with image reconstruction artifacts dominating the features. Hence, by ignoring these eigenvectors, undesirable noise is eliminated and data dimensionality is reduced.

Another method for choosing principal component images is to keep the top N PCA transformed images that account for some predetermined percentage of the total variance in the data. For this classification project, the eigenvectors that span 90% of the variance are kept for use in the data segmentation. The 90% threshold

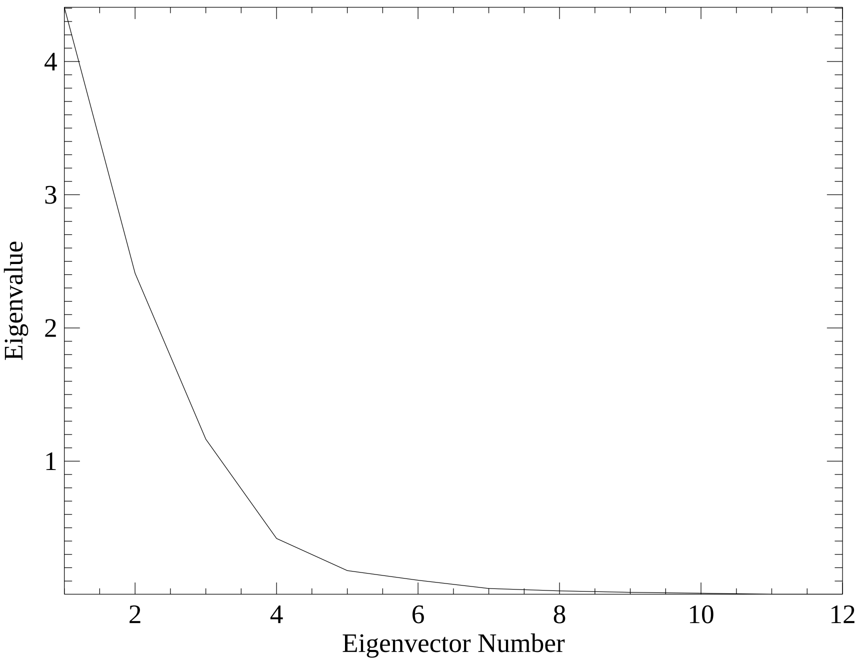

Figure 6.3: Eigenvalue spectrum for the principal component data rotation during the imaging interval of 1996 JD 261-266. A large majority of the data variance is contained in the first few eigenvectors.

was chosen to balance increased computational complexity and increased informational content when including additional individual components. That is, eigenvalues for the principal components beyond the first 90% are typically negligible in comparison. Only three PCA images must be retained in the case of the sample data set representing 1996 JD 261-266 Antarctic sea ice data. These principal component scores are shown in the composite RGB image of Figure 6.4 where the red channel contains the maximum variance principal component score, green contains the second highest variance, and blue contains the third highest. Features from all 12 original data value images are evident in this figure. The training regions are also indicated and will be discussed later.

The composite image is composed of a variety of signatures in the sea-ice annulus around Antarctica. For example, pixels that contain known icebergs are

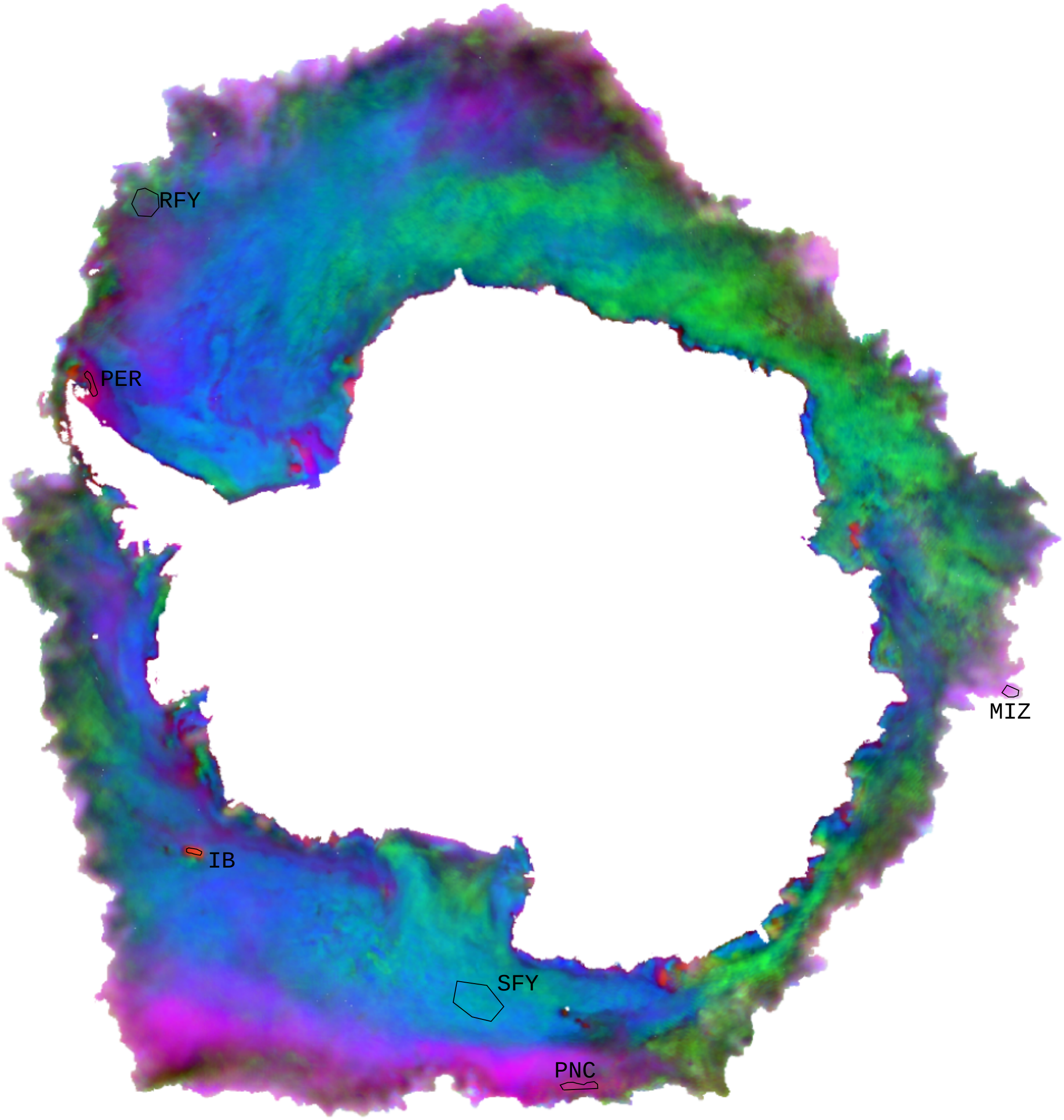

Figure 6.4: RGB composite image of the first three principal components for 1996 JD 261-266. The red channel is the top principal component image, the green is second, and blue is third. This image is useful in evaluating ice type information contained in the top three PCA scores. The six training regions are also indicated.

bright orange in the image. Regions of old perennial ice are visible in locations where a residual amount of old ice have been observed in late winter, such as near to the north-eastern tip of the Antarctic peninsula [46, 76]. Signatures which appear close to that of perennial ice may be observed in other coastal zones. In the southern Weddell Sea, a patch of deformed old ice and fast ice may be found surrounding a number of grounded icebergs [73], with a resulting purple color. Further such regions of deformed ice may be found in the Amundsen and Eastern Ross Seas along the coast. Large portions of the central ice pack have blue and green hues. Blue regions of undeformed medium, snow-covered first year ice are found in the central Weddell and Ross Seas, while green appears more closely related to the younger regions of first-year ice. For instance, recently formed ice in the Ross Sea, just north of the Ross ice shelf, and relatively thinner, saline young ice formed around East Antarctica display larger areas of green hues. One factor that appears to confirm the relationship between principal component three and young ice is the appearance of green in known coastal polynya regions such as along the Ronne ice shelf front in the Southern Weddell Sea [73], and in the wake of the large drifting icebergs, such as those observed off the Terre Adelie Land coast, and those grounded off the Amery ice shelf [77].

Interesting mixtures of browns and cyans are observed predominantly at the outer ice margin. Bright cyan signatures appear to be extensive regions of pancake ice formation, as for instance in the region of maximum northern ice extent in the Amundsen Sea. Brown hues are more extensively found at the ice margin, and likely are associated with mixtures of deformed and wave fractured floes found in the marginal ice zone, together with mixtures of open water and ice signatures.

Although previous classification efforts have identified many of these primary cluster types [61, 73] in single channel datasets, the unique attribute of the top three principal components shown in Figure 6.4 is that they show mixtures of the primary end-members. Pure red may be thought of as the ice with the most typical volume-scattering signatures. This encompasses icebergs, old, thick snow-covered perennial ice, and fast ice - all with low salinity. In contrast, pure green appears to indicate the most different cluster of ice typifying signatures which have the greatest rate of incidence-angle signature change, and the least volume-scattering like signatures. Lastly, the pure blue appears to imply intermediate ice salinity, and the least amount of surface deformations.

PCA can be used not only to reduce the dimensionality and noise levels of the data, but to quantitatively assess the informational content of multisensor data. By observing the relative magnitudes of the elements of the first few eigenvectors, one can determine levels of informational content of the original parameters. An example is given in Figure 6.5 in which the coefficient magnitudes of the top three eigenvectors of the sample data are plotted. The first eigenvector gives very low weighting to the NSCAT B and SSM/I 85 GHz images while high weighting is given to the NSCAT A and SSM/I 19H and 37H images. The eigenvector plot can also be used to determine which parameters can be eliminated from the classification. For example, the first two eigenvectors have very low NSCAT B_v and B_h values indicating that the B data types do not contribute to the majority of data variance. The third principal component eigenvector has a much higher weight on B_h than B_v implying that one of the B parameters could be eliminated without major impact on the classification.

6.4 Classification Algorithm

Several techniques are available for classification of N-dimensional data sets. A nearest-neighbor approach is perhaps the simplest when centroids from training samples or electromagnetic models can be obtained. Iterative clustering algorithms such as k-means or ISODATA represent another methodology and search for natural clusters in the data. The task then remains to label the resulting clusters as different classes. In contrast, the proposed approach is a statistical classification scheme with the goal of maximizing the probability of correctly classifying sea ice type. This section presents the classification methodology through a development of an iterative maximum *a posteriori* algorithm.

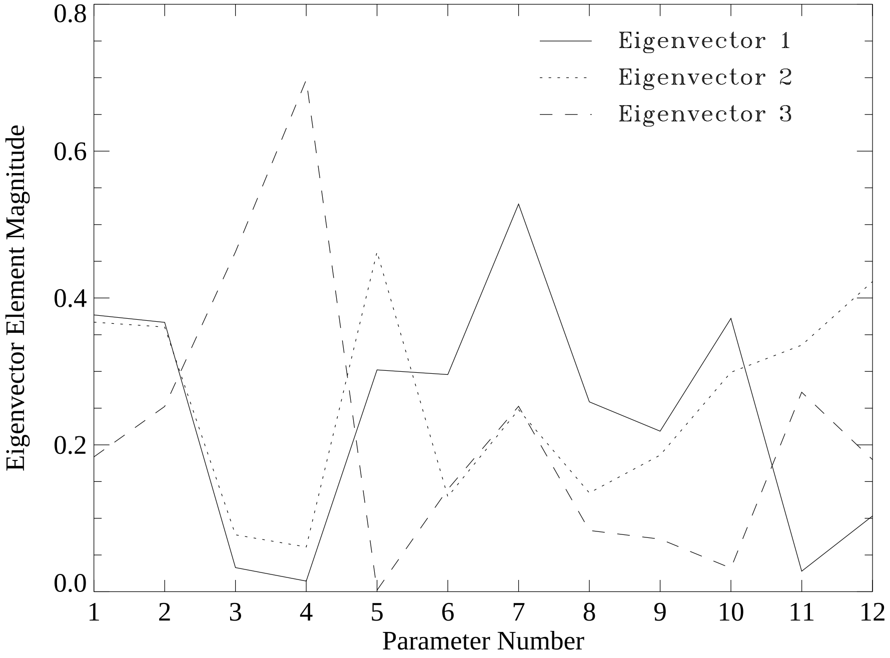

Figure 6.5: Vector element magnitudes for the first three eigenvectors. Eigenvector 1 spans the most data variance, 2 spans the second highest variance, and 3 spans the third highest. The parameter numbers correspond with 1- NSCAT A_v, 2- NSCAT A_h, 3- NSCAT B_v, 4- NSCAT B_h, 5- ERS-2 A_v, 6- SSM/I 19V, 7- SSM/I 19H, 8- SSM/I 22V, 9- SSM/I 37V, 10- SSM/I 37H, 11- SSM/I 85V, and 12- SSM/I 85H.

6.4.1 Statistical Classification

The intrinsic value of statistical methods of classification stems from the ease of interpretation of results. That is, statistical classifiers attempt to maximize a probability measure given some level of knowledge of class distributions. Two primary branches have evolved in the field of statistical classification and estimation: maximum likelihood and Bayesian classification.

Maximum likelihood (ML) methods as applied to discrete classification problems such as the determination of sea ice type choose the solution that maximizes the conditional probability of data vector observation over all possible sea ice types,

$$C_{ML} = argmax_c \; p(\vec{z}|C = c) \tag{6.5}$$

where C_{ML} is the chosen ice class, $\vec{z}$ is the principal component data vector, C is a discrete variable of different ice types, and $p(\vec{z}|C = c)$ is the probability of observing $\vec{z}$ given a particular ice type $C = c$. Hence, the maximum likelihood method can be implemented as long as the conditional distributions are known. Unfortunately, this is rarely the case. A weakness of this method lies in the fact that the occurrence of each sea ice type is effectively considered to be equal. Consequently, classes that occur infrequently such as icebergs are given equal weight in the data segmentation and may be chosen too often.

Bayesian methods represent another class of statistical approaches. This scheme requires the definition of a loss function which assigns a penalty for misclassifications. The Bayes solution then minimizes the expected loss which is also called the Bayes risk. Under a uniform loss function this reduces to a maximum *a posteriori* (MAP) classifier. The MAP technique treats the ice type C as a random variable and maximizes the probability of ice type given the observation vector $\vec{z}$

$$C_{MAP} = argmax_c \; p(C|\vec{z}) = argmax_c \; \frac{p(\vec{z}|C)p(C)}{p(\vec{z})} \tag{6.6}$$

where $p(C)$ is the *a priori* distribution. Since $p(\vec{z})$ is fixed for a particular observation, this reduces to

$$C_{MAP} = argmax_c \; p(\vec{z}|C)p(C). \tag{6.7}$$

MAP classification has an advantage over maximum likelihood techniques in that the probability of each class is included in the derivation ensuring that less likely ice types appear less frequently in the final classification. However, the *a priori* distribution and the conditional distributions are required.

Under a Gaussian assumption, the conditional distributions are

$$p(\vec{z}|C) = \frac{1}{(2\pi)^{n/2}|K_c|^{1/2}} e^{-\frac{1}{2}(\vec{z}-\vec{\mu}_c)^T K_c^{-1}(\vec{z}-\vec{\mu}_c)} \tag{6.8}$$

where $\vec{\mu}_c$ is the mean vector and K_c is the covariance matrix of ice type c, respectively. Hence, the statistical structure of the data for each ice class is completely determined by the mean vectors and covariance matrices. Even if the Gaussian assumption is not entirely correct, it is considered to be an improvement over the simple equal and isotropic distribution assumption inherent to a nearest-neighbor classifier since the Gaussian model can account for covariance between separate principal component scores. This allows the classifier to use cluster shapes in addition to the centroids to segment the data. For the maximum likelihood development, the maximization of Eq. (6.8) can be simplified. After taking the natural log (a monotonic function) and a little mathematical manipulation the equations become

$$C_{ML} = argmax_c \; p(\vec{z}|C) = argmax_c \; [-(log|K_c| + (\vec{z} - \vec{\mu}_c)^T K_c^{-1}(\vec{z} - \vec{\mu}_c))] \tag{6.9}$$

which is equivalent to

$$C_{ML} = argmin_c \; [log|K_c| + (\vec{z} - \vec{\mu}_c)^T K_c^{-1}(\vec{z} - \vec{\mu}_c)]. \tag{6.10}$$

The second term in Eq. (6.10) is the Mahalanobis distance commonly used in Gaussian classification problems [64]. Thus, the ML classification can be interpreted as choosing the class centroid that minimizes a modified Mahalanobis distance.

A similar development applied to the MAP equations yields

$$\begin{aligned} C_{MAP} &= argmax_c \; p(\vec{z}|C)p(C) \qquad (6.11) \\ &= argmax_c \; [-\frac{1}{2}(log|K_c| + (\vec{z} - \vec{\mu}_c)^T K_c^{-1}(\vec{z} - \vec{\mu}_c)) + log(p(C))]. \qquad (6.12) \end{aligned}$$

Both ML and MAP methods are separately used and compared in the sea ice classification given below.

6.4.2 Iterative Approach

In order to fully implement the ML and MAP techniques, the mean vectors $\vec{\mu}_c$ and covariance matrices K_c of the individual ice type clusters are required along with the *a priori* distribution $p(C)$. While a rough estimate of the cluster centroids can be generated from small homogeneous training regions, it is more difficult to obtain reasonable estimates of the K_c matrices. However, estimates can be obtained through an iterative procedure, assuming that the statistical measures converge to the correct values.

Figure 6.6 illustrates the complete process for the classification of a time series of image data. The initial SIR-derived images are first masked to remove all land

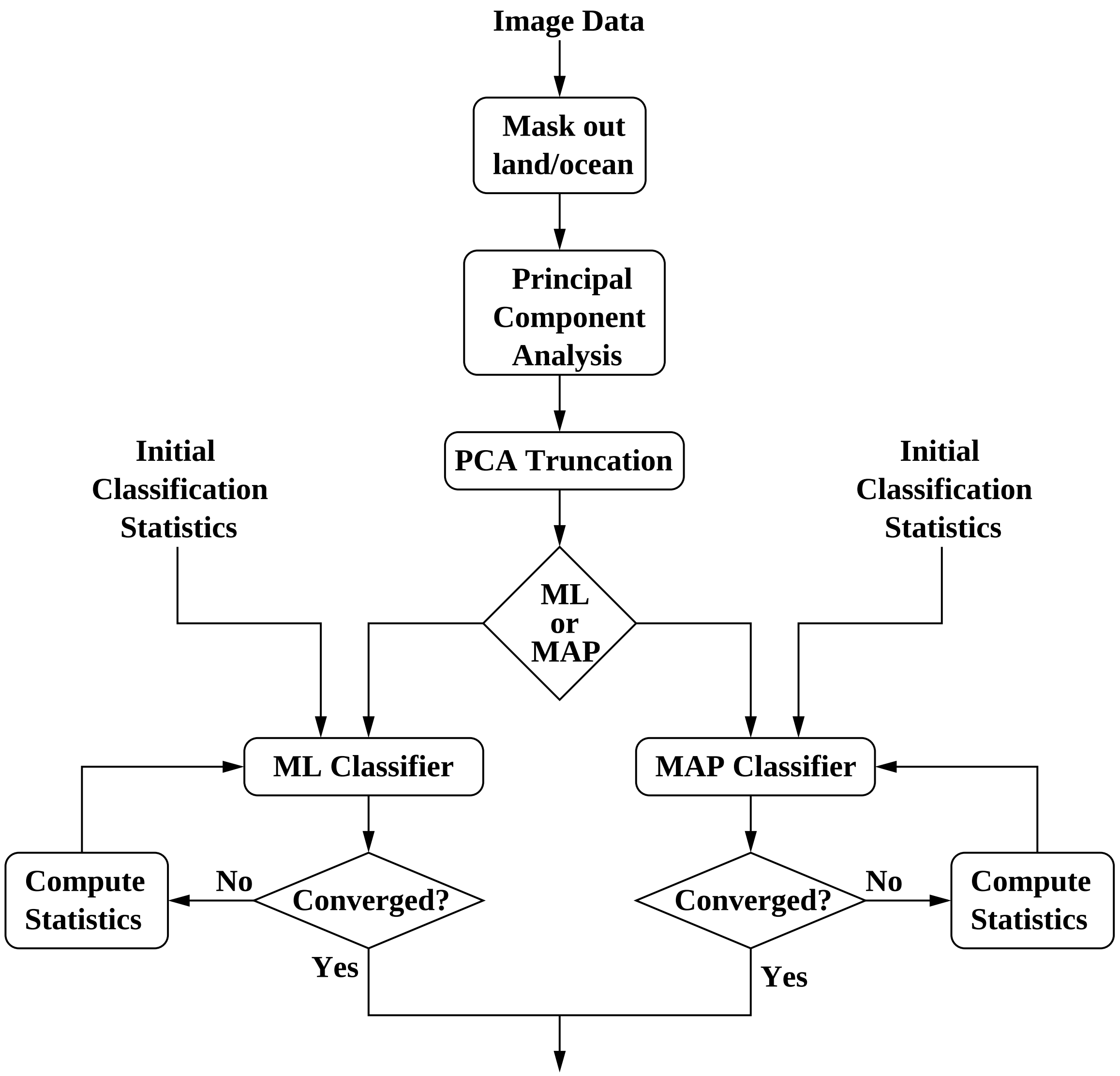

Figure 6.6: Flowchart depicting the iterative ice classification algorithm for both ML and MAP methods.

and ocean pixels using the ice extent mapping procedure defined in an earlier section. The PCA linear transformation is then performed to rotate the coordinate space into ordered maximum variance axes. Next, the resulting 12-dimensional principal component space is truncated by choosing the top N eigenvectors that span 90% of the data variance.

After the preprocessing, an iterative maximum likelihood or maximum *a posteriori* classifier is implemented. The first iteration uses the $\vec{\mu}_c$, K_c, and $p(C)$ statistical measures computed from the classification of the previous image set. Thus, the preceding classification is treated as a training set to obtain initial sea ice type cluster centroids, covariance matrices, and the *a priori* distribution. Due to the seasonal nature of cluster characteristics, the approximated values are likely erroneous. However, they represent a good initial starting point for the iterative procedure. After the first iteration, the statistical measures are updated using the current classification. These are then used in a new classification. The process iterates until predefined convergence criteria are met. The result is a classified image which maps the spatial extent of each sea ice type.

One important issue regarding the MAP algorithm is the behavior of the $p(C)$ estimate during the iterations. It is conceivable that an element of this distribution could go to zero if the corresponding ice class becomes very scarce. If the ice type later becomes more abundant, the zero probability from a previous iteration precludes any pixels from being classified as this ice type. While this phenomenon is not observed in any of the realizations in this study, the problem can be solved by setting some very low value as a lower limit on values of $p(C)$ preventing any of them from becoming zero.

6.4.3 Convergence Metrics

Two metrics are used to determine algorithm convergence. Since the Gaussian clusters are completely defined by the centroid vectors and covariance matrices, appropriate norms are used to obtain scalar measures of individual cluster behavior as a function of iteration. The Euclidean norm is used to measure the behavior of the cluster centroid vectors. The matrix spectral norm of each covariance matrix K_c is computed as a measure of the overall variance structure of each cluster. The spectral norm is equivalent to the square root of the maximum eigenvalue of $K_c^T K_c$. Convergence of both metrics for a particular cluster is a good indication that the cluster remains unchanged from one iteration to the next.

6.4.4 Algorithm Initialization

The algorithm described above is a recursive method that uses the classification result from the previous imaging interval to compute the present sea ice type map. In order to obtain an initial classification result to start the process, the following procedure is used. Cluster centroid vectors are estimated from small homogeneous training regions derived from a basic knowledge of sea ice type spatial behavior and expected microwave signatures. For the ML classifier a simple nearest-neighbor (minimum distance) classification yields the needed initial classification result. For the MAP method, the data is segmented with a weighted nearest-neighbor technique in which the distances to each cluster are inversely weighted by an initial estimate of $p(C)$. While an accurate estimate of the *a priori* distribution is difficult to produce, an educated estimate can be made through a knowledge of sea ice type population in Antarctica. For example, a large majority of the Antarctic ice pack consists of various types of first-year ice. Other classes are much less prevalent. For either ML or MAP, the nearest-neighbor solution is used to compute the necessary statistics for the classifier and initiate the iterative algorithm.

Simulations of the algorithm for both the ML and MAP techniques are performed. The simulation data consists of four different two-dimensional Gaussian distributions with different mean vectors, covariance matrices, and cardinalities. The distributions are chosen to have significant overlap to increase the classification difficulty. Simulation results indicate that the iterative algorithms converge to solutions that are very close to the actual ML or MAP solutions given two conditions. First, the individual cluster centroids must be relatively close to the actual centroids. In the simulations, this means that the centroid estimate merely has to be closer to its

Table 6.1: Training region signatures used in the initial nearest-neighbor classification for 1996 JD 261-266.

	IB	PER	RFY	SFY	PNC	MIZ
NSCAT A_v	-3.19	-5.72	-11.02	-17.35	-6.91	-12.29
NSCAT A_h	-3.77	-5.79	-11.01	-17.34	-6.51	-13.65
NSCAT B_v	-0.20	-0.14	-0.23	-0.25	-0.20	-0.22
NSCAT B_h	-0.23	-0.14	-0.21	-0.24	-0.18	-0.32
ERS-2 A_v	-4.46	-9.25	-14.80	-17.96	-11.19	-13.58
19V T_B	224.6	235.7	249.2	256.6	233.4	191.4
19H T_B	187.5	219.1	218.7	241.4	199.3	126.1
22V T_B	225.5	233.2	247.5	254.2	232.4	199.2
37V T_B	231.2	224.1	242.2	249.6	221.7	213.7
37H T_B	204.0	209.6	218.3	237.2	199.0	160.3
85V T_B	236.9	228.2	239.6	234.3	223.3	240.8
85H T_B	219.5	218.2	224.3	224.2	214.2	206.2

actual centroid than any of the others. Second, for MAP classification, the initial distribution estimate of $p(C)$ must be a reasonable estimate of the actual *a priori* distribution.

6.5 Results

The iterative algorithms are applied to the classification of Antarctic data during consecutive imaging periods in September and October of 1996. The algorithm is initiated with multisensor data from JD 261-266. As noted in the previous section, the nearest-neighbor segmentation is required for the first image of the time series. As indicated in Figure 6.4, small homogeneous training regions are defined through a knowledge of sea ice dynamics and microwave signatures. Table 6.1 contains the cluster centroids obtained from these regions. In addition to the centroids, the MAP algorithm requires an initial estimate of the *a priori* distribution. For the 1996 JD 261-266 image classification $p(C) = [p(IB),\ ,p(PER),\ p(RFY),\ p(SFY),\ p(PNC),\ p(MIZ)] = [0.01,\ 0.02,\ 0.40,\ 0.45,\ 0.07,\ 0.05]$ is used.

Figures 6.7-6.8 show the convergence metrics as a function of iteration for the ML and MAP classifications, respectively. After about 25 iterations, all metrics

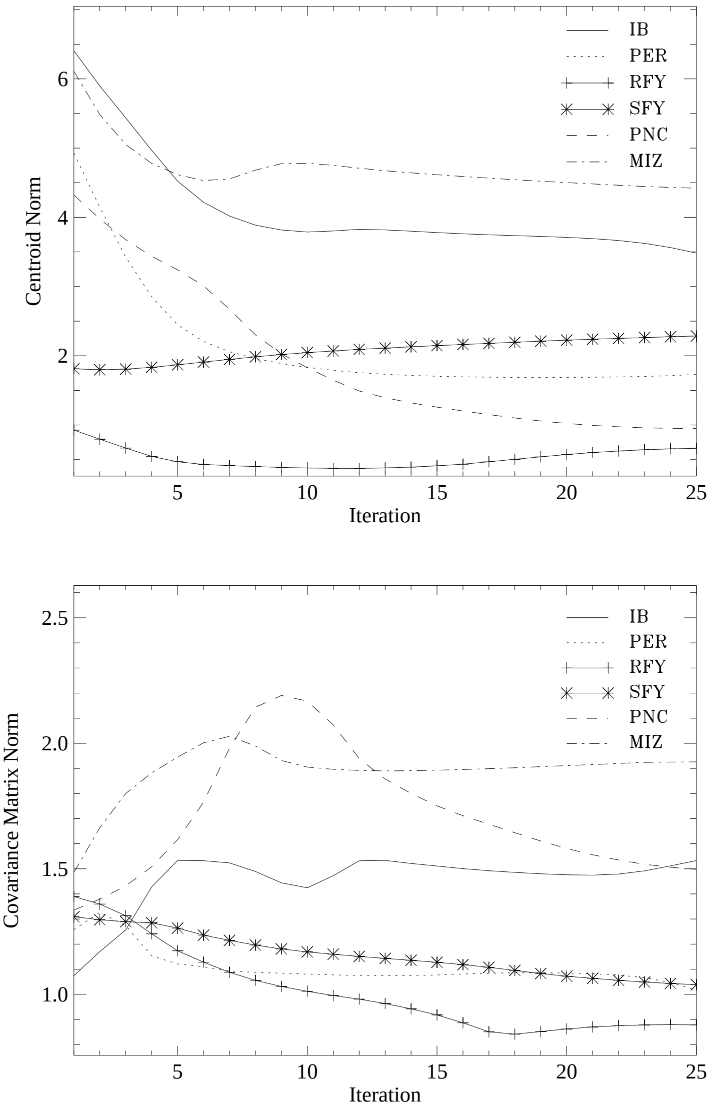

Figure 6.7: Maximum likelihood classification cluster convergence metrics. (Left) The Euclidean norms of each ice type cluster as a function of iteration. (Right) The spectral norms of the covariance matrices.

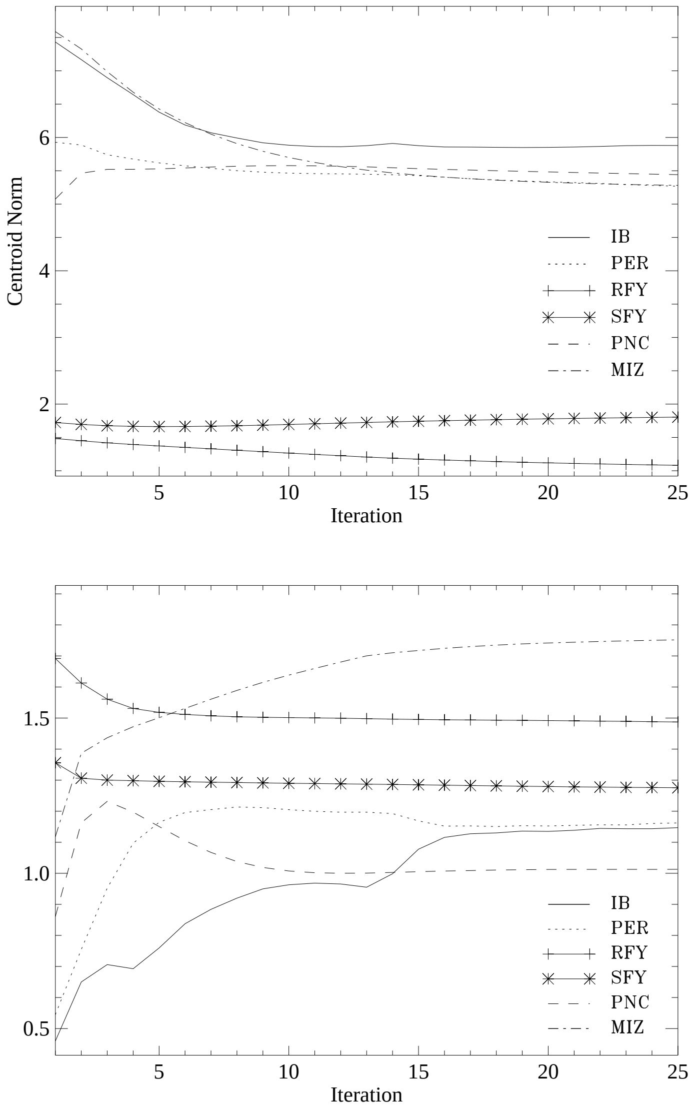

Figure 6.8: Maximum *a posteriori* classification cluster convergence metrics. (Left) The Euclidean norms of each ice type cluster as a function of iteration. (Right) The spectral norms of the covariance matrices.

have converged relatively well. Some minimal centroid drift is still evident in the centroid norm trends. Most of the ML centroid norms shift significantly (and erroneously) during the iterations. On the other hand, only two of the MAP centroid norms move significantly indicating that the original centroids are reasonable estimates of the true values. Figure 6.9 illustrates the centroid drifts in the plane of the top two principal components for the MAP implementation using data for 1996 JD 261-266. The starting points for each centroid are denoted with triangles while the final centroid locations are represented by squares. The effect of the algorithm's iterative nature is evident as each of the points move varying amounts. Isoprobability elliptical contours have also been plotted surrounding each centroid convergence point using the sample covariance matrices from the final classification. The major and minor axes for each ellipse are 2-σ wide. This figure not only shows iterative migration of centroids, but gives a feel for how much separation exists between different ice classes in the plane of the top two principal components. Table 6.2 contains the final MAP cluster centroids in the normal parameter space. Table 6.2 can be compared with Table 6.1 for an indication of how much the initial training signatures were modified by the algorithm.

Table 6.2: Ice type centroid signatures after 25 iterations of the MAP algorithm for 1996 JD 261-266.

	IB	PER	RFY	SFY	PNC	MIZ
NSCAT A_v	-5.35	-6.63	-11.66	-15.17	-7.85	-11.66
NSCAT A_h	-5.85	-6.67	-11.77	-15.27	-7.41	-12.39
NSCAT B_v	-0.201	-0.154	-0.224	-0.229	-0.183	-0.257
NSCAT B_h	-0.218	-0.152	-0.221	-0.225	-0.164	-0.286
ERS-2 A_v	-6.69	-9.47	-13.77	-16.72	-12.18	-12.99
19V T_B	230.3	239.6	246.9	256.2	232.0	213.8
19H T_B	195.8	219.6	217.5	235.8	196.5	160.8
22V T_B	230.6	237.9	245.9	253.9	229.1	219.2
37V T_B	234.1	231.2	241.5	248.3	215.4	226.6
37H T_B	208.2	214.4	219.0	230.8	192.6	184.6
85V T_B	238.4	229.0	236.8	234.5	211.5	243.3
85H T_B	220.5	217.3	223.4	222.3	200.7	215.8

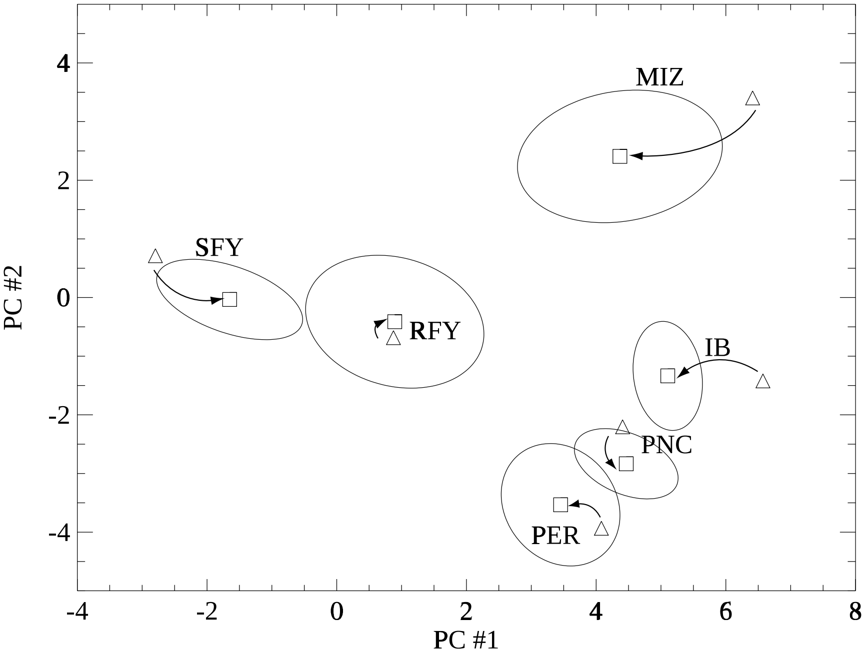

Figure 6.9: Centroid locations in the plane of the top two principal components for the MAP classification of 1996 JD 261-266 data. The initial centroids (triangles) as well as the final converged centroid points (squares) are shown. Also plotted are the isoprobability contours according to the sample covariance matrices obtained from the final classification. The ellipses are 2-σ wide.

Figure 6.10 depicts the final ML and MAP sea ice type images. Since the ML image has large regions classified as icebergs and perennial ice, it is concluded that the ML algorithm performs poorly. The primary source of the error is the ML assumption that all sea ice types are equally likely. This causes clusters that should have low cardinality to grow to sizes similar to more common ice types. This effect is responsible for the undesirable centroid drift discussed above.

In contrast, the MAP result exhibits a much more reasonable spatial distribution. Several icebergs known from the National Ice Center iceberg inventory are classified correctly (see URL www.natice.noaa.gov). The largest concentration of perennial ice is found just off the tip of the Antarctic Peninsula. The ice here has survived the previous melt season by avoiding being swept out to sea by the Weddell

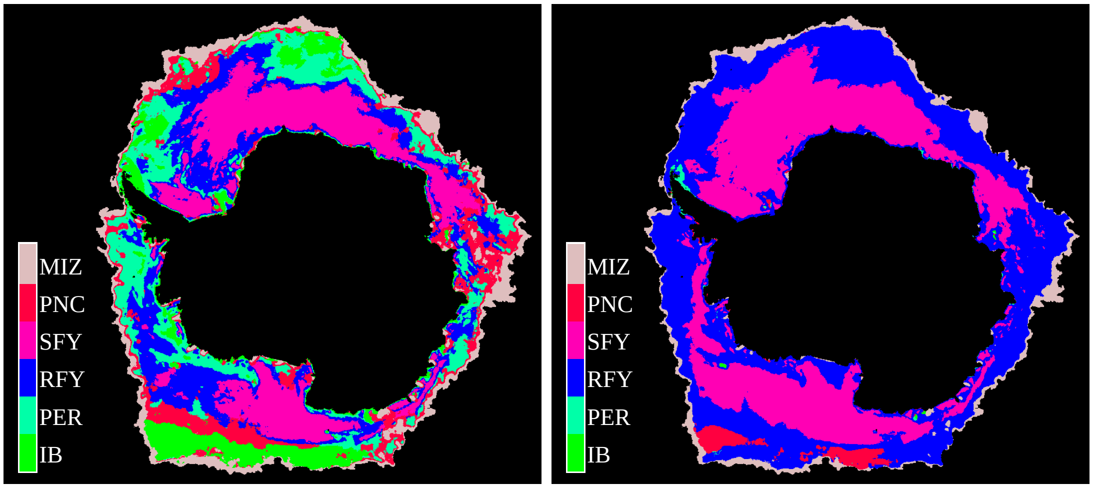

Figure 6.10: ML (left) and MAP (right) sea ice classifications of 1996 JD 261–266 Antarctic data. The ML result is in error because of the assumption that each ice type is equally likely.

Gyre. Rough first-year ice in the classification surrounds smooth first-year ice which is located primarily in the inner portion of the ice pack. This is consistent with the classification results in [73]. In addition, the marginal ice zone exists on the perimeter of the ice pack as expected.

In order to gain an understanding of possible cross-confusion that may occur between classes using this algorithm, the Mahalanobis distance is computed between the final cluster centroids in principal component space. Since the Mahalanobis distance requires a cluster covariance matrix and each centroid comes from a different cluster, one of the centroids is treated as the reference and the other is considered the test vector. In the computation, the covariance matrix of the reference vector is used. The results are given in Table 6.3 for the 1996 JD 261-266 classification. The table contents may be interpreted by observing individual columns corresponding to a test ice type cluster. Each row cell value within a particular column is a measure of dissimilarity between the reference and test vectors. Thus, lower values correspond with higher probability that an ice type will be misclassified as the reference type. For example, the PER column demonstrates that the perennial ice class is substantially

Table 6.3: Mahalanobis distances between centroids for 1996 JD 261-266 providing a measure of dissimilarity between different clusters in the classification. The covariance matrix of the reference centroid is used in each computation.

		Test Centroid					
		IB	PER	RFY	SFY	PNC	MIZ
Reference Centroid	IB	0.0	24.5	25.0	59.1	70.8	111.0
	PER	15.5	0.0	79.1	138.3	46.3	350.2
	RFY	27.0	17.6	0.0	8.0	11.5	21.5
	SFY	119.2	67.0	17.0	0.0	87.9	180.3
	PNC	23.0	12.9	37.9	120.5	0.0	56.6
	MIZ	23.3	16.5	12.6	44.6	11.6	0.0

more likely to be misclassified as pancake (PNC) ice than smooth first-year (SFY) ice.

As previously stated, the MAP algorithm requires an initial estimate of the *a priori* distribution $p(C)$. The technique is designed to use the $p(C)$ resulting from the classification of the previous image set. However, the first classification in the series requires the user to provide an approximate $p(C)$ for initialization. In an effort to determine the sensitivity of the final ice classification to the this parameter, a Monte Carlo analysis is performed. Several random realizations within a neighborhood of a nominal $p(C)$ are used in the 1996 JD 261-266 image segmentation. The study showed that the final spatial distribution of ice types is not particularly sensitive to the original *a priori* distribution.

Figure 6.11 shows classification images generated using two other methods for comparison. Both were implemented using the same training data for initial cluster centroids. The left image is the classification result of the standard k-means clustering algorithm. The k-means approach yields a solution that minimizes the within cluster sum of squared distances under the Euclidean distance metric. Since no regard is given to the probability of ice type, the k-means result has problems similar to the ML image. The second image was generated using a modified form of k-means in which a "MAP distance metric" measured the similarity between data samples and

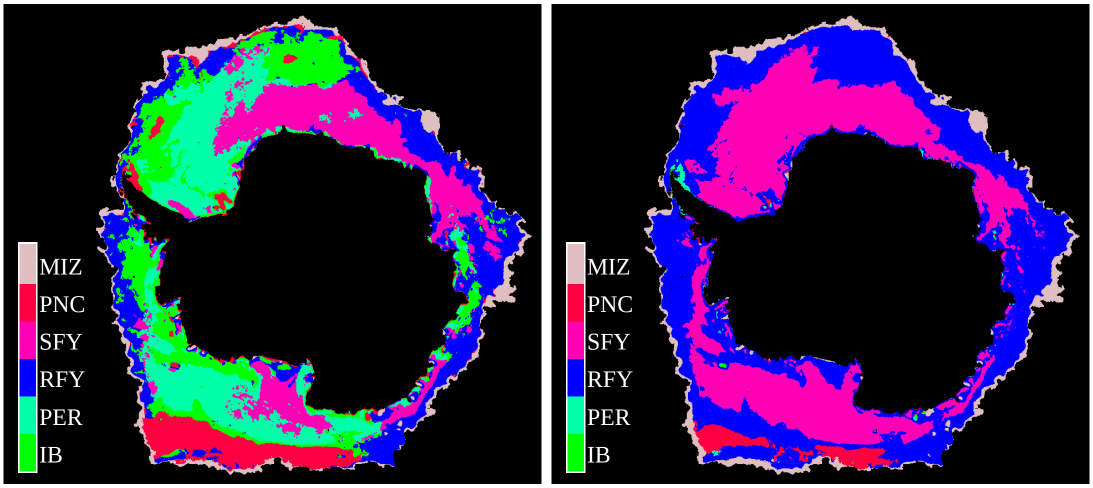

Figure 6.11: K-means clustering classification results of 1996 JD 261–266 Antarctic data using different distance metrics. The left image is the conventional k-means result with the Euclidean distance metric. The right is k-means with the "MAP distance" metric as defined in the text.

the centroids. The MAP distance metric is the negative of the $argmax$ argument in Eq. (6.12). The resulting ice type map is nearly identical to the MAP classification. In fact, the two agree for 96.5% of the image sea ice pixels. The differences primarily occur in the number of pixels classified as pancake ice. Consequently, the modified k-means classifier result is similar to the maximum *a posteriori* technique result.

An obvious error in the MAP classification in Figure 6.10 is the RFY labeled tongue extending from the Ross Ice Shelf. The perimeter of the ice shelf is actually a region of new ice formation and divergence. Consequently, the ice in this regime should have been identified as smooth first year (SFY) ice rather than rough first year (RFY) ice. The source of the discrepancy is likely due to frost flower formation on the surface of smooth ice. Drinkwater and Crocker [78] found that frost flower formation can yield microwave signatures that are very similar to RFY ice. The proposed classifier did not include a classification cluster for this ice type. Consequently, a useful line of future research would include a study of the potential of segmenting frost flower covered ice from RFY ice using the results of Wensnahan [72] and Ulander [22].

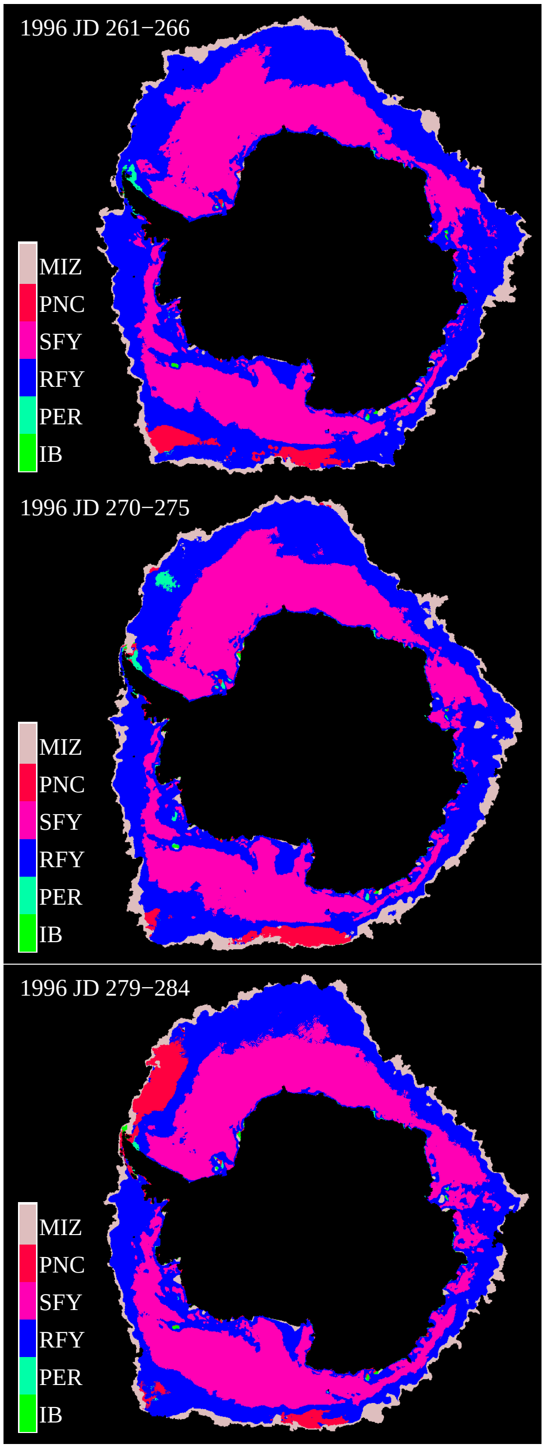

1996 JD 261−266

1996 JD 270−275

1996 JD 279−284

Figure 6.12: MAP ice classification of the image series with day ranges 1996 JD 261–266, 270–275, and 279–284.

Figure 6.12 shows the algorithm results when applied to a time series of images. The original images are generated with three days of overlap between consecutive intervals. The three day spaced classification maps illustrate stability in the ice classes between contiguous images. Since geophysical variability is greater on longer time-scales, results from images separated by three day gaps are shown. The ice maps in Figure 6.12 reveal a number of interesting features. First, the temporal continuity between the spatial distributions of classes such as RFY and SFY ice types indicates that the algorithm is stable. However, some misclassification does occur such as the region of MY ice that appears in the outer ice margin of the Weddell Sea in the JD 270–275 image. In this case, pixels are exchanged between the RFY and MY categories.

Classified imagery can be used to better understand certain geophysical processes. For example, the tongue of "RFY" ice extending from the Ross Ice Shelf exhibits some interesting temporal behavior. As discussed previously, this region is likely not RFY ice, but SFY ice covered with frost flowers formed as off ice-shelf winds drive the ice pack northwards. Hence, temporal changes in the direction of the tongue relate to changes in wind direction over the ice pack through dynamic adjustments to the ice drift direction.

Another region of interest is in the outer Weddell Sea where a large region classified as pancake ice appears in the last frame. Initially, this feature appears to be an error in the classification. However, examination of the original data set images reveals that this classification relates to an actual physical event. From the first image in Figure 6.12 to the last, the scatterometer σ^o values increase several dB and the radiometer T_B values drop significantly. For example, the average NSCAT A_v value in the area rises from -11.2 to -7.4 dB. The SSM/I 37V T_B average decreases from 236 to 210 K. The final signatures are typical of pancake ice. A possible cause for this event is the occurrence of storm induced swells penetrating the ice margin. Under such conditions, intense ice floe fracturing and wave-washing of floes are observed in the field. Subsequent return of the signatures to values more typical of the marginal ice zone, and rough first-year ice confirm that this is an event of transitory nature. If this is indeed the case, it may be possible to relate pancake ice "blooms" in ice margin signatures to increased wave radiation stresses, or to surface flooding events caused by increased swells. Further analysis of this phenomenon could compare the occurrence of such signatures with the significant wave heights observed by altimeters in the region of the Southern Ocean directly off the ice margin at those times. Similarly, these events may be classified as "flooding" in future extensions of the algorithm.

6.6 Conclusions

This study has demonstrated the utility of a multisensor, iterative maximum *a posteriori* sea ice type classification algorithm for Antarctic sea ice. The use of data collected from multispectral, dual-polarization, active, and passive instruments increases the level of information that can be exploited in segmenting the data. Through the use of principal component analysis, not only is the data dimensionality minimized, but the effects of noise and imaging artifacts are reduced. The resulting data set is classified in an iterative manner that utilizes MAP statistical techniques. The MAP classifier performs better than ML and the standard k-means and is very similar to a modified version of k-means with a different distance metric.

The iterative classification algorithm yields ice maps with spatial ice type distributions that are reasonable when general Antarctic sea ice dynamics are considered. However, while the algorithm appears to function well, a more detailed validation study is needed. Unfortunately, Antarctic validation data is difficult to obtain during this period of sensor overlap. Though SAR data exists for continental Antarctica, sea ice SAR imagery during the period spanned by our multisensor data set is scarce. Future research will apply the algorithm to Arctic data where validation data is much more abundant both spatially and temporally, and where current efforts are underway to plot ice drift and dynamics on a Lagrangian grid.

Several implications must be considered in a medium-scale classification such as the method presented in this study. First, the six day imaging period may introduce blurring in the images due to sea-ice motion resulting in ambiguous signatures and misclassification. The limiting factors for this data set are the scatterometers which need more time to achieve full coverage of the Antarctic ice pack. In the future, similar algorithms may be applied using instruments with wider swaths such as the SeaWinds scatterometer on board the QuikSCAT and ADEOS II spacecrafts. Furthermore, AMSR in conjunction with SeaWinds aboard ADEOS II will provide temporally and spatially coregistered active and passive data. This provides many of the channels required for such a method to be applied in the future. Both SeaWinds missions will reach full coverage in one to two days rather than six days. SeaWinds on QuikSCAT is currently in flight while ADEOS II is scheduled for launch before the end of 2001. Also, the relatively low resolution, even in the reconstructed imagery, implies that some pixels may contain a mixture of ice types. Thus, the classification result for a particular pixel is considered the spatial and temporal average behavior of sea ice in that region. A promising line of future research is the extension of this algorithm from a hard to a fuzzy classifier. That is, for each pixel the concentration of each ice type may be estimated. It is conceivable that the MAP probabilities could be used to achieve this. However, a greater understanding of the effects of within-footprint mixtures on observed microwave signatures is first required. Nevertheless, the algorithm yields results consistent with historic ice distributions and expectations.

This study has demonstrated one method for the application of multisensor data sets to classification problems. The use of multiple sensors appears to improve the ability to identify different classes by combining the inherent strengths of each instrument. The three sensors used each add unique information to assist in segmenting the images into separate ice types. The scatterometers, NSCAT and ERS-2, are sensitive to surface roughness, volume inhomogeneities, and other scattering mechanisms which vary across different ice types. In addition, these instruments collect measurements at multiple incidence angles. Incidence angle dependence varies over the spectrum of sea ice types justifying the value of this parameter. NSCAT in particular is valuable in that it collects dual polarization measurements over a wider swath at higher resolution. The primary strength of the C-Band ERS-2 lies in greater penetration depth due to its lower frequency of operation. Unfortunately, both of these sensors require several days of data to obtain complete coverage of the Antarctic. SSM/I also contributes a great deal to the classification. As a passive instrument, the SSM/I sea ice signatures are a more a function of surface emissivity and dielectric properties than their active counterparts. The wide spectrum of frequencies and dual polarization nature of the SSM/I channels offers sensitivity to a larger range of surface properties than single frequency/polarization instruments. Additionally, the SSM/I measurement collection geometry allows complete coverage of the Antarctic usually in one day though at a lower resolution than NSCAT.

Chapter 7

SeaWinds Applications in Cryosphere Remote Sensing

Chapters 5 and 6 presented the theory and methodologies used to determine the location of sea ice and the spatial distribution of sea ice types within the ice pack. Polar sea ice extent was determined using NSCAT data sets alone. In contrast, the sea ice classification required the use the multiple sensor combination of NSCAT, ERS-2, and SSM/I. The unfortunate loss of the ADEOS satellite (and thus NSCAT) has limited the use of these techniques. However, the methods can be modified for use with data collected by the SeaWinds scatterometer. This chapter discusses the use of SeaWinds in sea ice extent detection and sea ice classification. In Section 7.1, sea ice extent mapping using SeaWinds data is considered. Significant changes to the algorithm presented in Chapter 5 are required for adaptation to SeaWinds and improvement of the ice edge estimates. The research detailed in Section 7.1 has been submitted to the *Journal of Geophysical Research* and is currently in review. Section 7.2 presents a brief discussion on the application of the multisensor ice classification methods in Chapter 6 to combined SeaWinds and SSM/I reconstructed imagery.

7.1 SeaWinds Ice Extent Mapping

The ability to accurately map sea ice with Ku-band NSCAT data was demonstrated in Chapter 5 (see also [8]). The study described the development and implementation of an adaptive sea ice extent mapping algorithm. Because NSCAT data is no longer available, the state of the sea ice pack can no longer be observed using this method. However, the ice detection method can be adopted for σ^o data from present and future active Ku-band sensors such as SeaWinds aboard the QuikSCAT and ADEOS-II platforms; the basic concepts behind the algorithm still apply, though significant modifications are required due to the design differences of SeaWinds and NSCAT.

This section describes the adaptation of the NSCAT ice extent mapping algorithm (hereafter referred to as the RL-N algorithm) to SeaWinds scatterometer data. Algorithm implementation and validation are discussed. A comparison of SeaWinds-derived and SSM/I-derived edges is given. In section 7.1.1, some brief background is given about the various instrument specifications and the original RL-N ice edge detection algorithm. Section 7.1.2, describes the SeaWinds data parameters and their levels of sensitivity to the presence of sea ice. The algorithm development is described in section 7.1.3. Implementation results are given in the section 7.1.4 along with detailed validation. Finally, the conclusions are presented.

7.1.1 Ice Extent Mapping Background

The primary advantage of SeaWinds over NSCAT is the rate of surface coverage. The SeaWinds swath is 1800 km wide with no nadir gap. Consequently, SeaWinds covers approximately 90% of the earth's surface and 100% of the polar regions each day. In contrast, NSCAT required 2-3 days to obtain complete v-pol coverage. The significant increase in temporal resolution is extremely valuable in observations of sea ice since ice packs can move dozens of kilometers in a single day. Hence, SeaWinds reconstructed imagery is much less subject to blurring caused by sea ice motion and evolution.

As discussed in Chapter 2, SeaWinds has two spatial resolution modes: eggs and slices. The SeaWinds measurement cells (or eggs) have a nominal resolution of 25-50 km while the slice measurements have dimensions of approximately 6-8 km by 25 km. Science data products can be made from either measurement collection scheme.

Using the scatterometer image reconstruction (SIR) algorithm, SeaWinds measurements are used to create Ku-band σ^o imagery. For SeaWinds, SIR is used to construct v- and h-pol images from egg data on a 4.45 km grid with an effective resolution of approximately 10-12 km. Slice measurements are used to produce enhanced resolution imagery on a 2.225 km grid with an effective resolution of 4-8 km. While the slice images have better spatial resolution, noise levels are inherently higher. For the Arctic and Antarctic regions, both egg and slice images are produced at one day intervals. For other lower latitude land areas, a longer imaging period may be required to achieve complete coverage with adequate sampling for image reconstruction.

Due to the computational complexity of the SIR algorithm, near real-time (NRT) slice image products are reconstructed using the AVE algorithm (see Chapter 3), enabling surface σ^o analysis shortly after data acquisition. The NRT operational processing of polar SeaWinds slice imagery is currently implemented at the Jet Propulsion Laboratory for ocean wind studies and by NOAA and the Brigham Young University Microwave Earth Remote Sensing Laboratory for sea ice pack analysis. Image products are being distributed by the Jet Propulsion Laboratory PO.DAAC. Though SeaWinds egg imagery are used in the ice discrimination method presented in this study, the technique can also be applied to SIR or AVE slice images.

Since the SeaWinds ice extent mapping algorithm presented in this study is based on the RL-N method, the latter is briefly summarized here. An in-depth description of the RL-N algorithm is given in Chapter 5 (see also [8]). The RL-N algorithm uses NSCAT SIR enhanced resolution imagery to generate estimates of the spatial distribution of sea ice. Three basic parameters are used in the RL-N classification. The first is the copol ratio, γ, of v- and h-pol σ^o at 40° incidence. In general, this parameter is low for sea ice and high in open ocean regions [25]. The second metric used in the discrimination is the v-pol incidence angle dependence of σ^o, B_v, exhibiting relatively low and high magnitudes for ice and ocean, respectively [25, 62]. The combination of these two parameters along with statistical classification methods shows great utility in identifying sea ice and ocean regions. The third parameter, the σ^o estimate error standard deviation, κ, is used to further enhance the edge estimate. Residual errors are minimized using binary image processing techniques. The resulting edge correlates well with the NASA Team algorithm 30% ice edge.

Extending the RL-N [8] algorithm to SeaWinds data presents several difficulties due to inherent differences in the instruments. While both are Ku-band scatterometers, SeaWinds differs significantly from NSCAT. The fan beam configuration of NSCAT allowed for the measurement of σ^o at vertical and horizontal polarizations at multiple incidence angles [23]. In contrast, SeaWinds uses the scanning pencil beam geometry discussed in Chapter 2. The distinct, fixed incidence angles of the v- and h-pol beams preclude the computation of the two primary RL-N classification parameters, the copol ratio and the incidence angle dependence of σ^o. However, modified parameters can be constructed that exhibit significant sensitivity to the presence of sea ice. These are described in the following section. The increased coverage of SeaWinds when compared to NSCAT significantly improves the temporal resolution of the sea ice extent estimates: one day's worth of SeaWinds data can be used to make enhanced resolution images in contrast to NSCAT's 3-6 day data requirement.

7.1.2 SeaWinds Ice Extent Mapping Parameters

Four primary SeaWinds SIR images are reconstructed for each one day interval: v-pol σ^o at 54° incidence (A_v^{54}), h-pol σ^o at 46° incidence (A_h^{46}), and the v- and h-pol σ^o estimate error standard deviations (κ_v and κ_h). Sample images are shown in Figure 7.1. For later use each of these parameters is defined and their utility in sea ice detection is discussed.

The Modified Copol Ratio

The first parameter is the modified SeaWinds copol ratio, γ_{sw}, which is defined as the ratio of A_v^{54} and A_h^{46}

$$\gamma_{sw} = A_v^{54}/A_h^{46}. \tag{7.1}$$

This is equivalent to taking the difference in log space of v- and h-pol σ^o. A sample γ_{sw} image is shown in Figure 7.1 to illustrate the sensitivity of this parameter to the presence of sea ice.

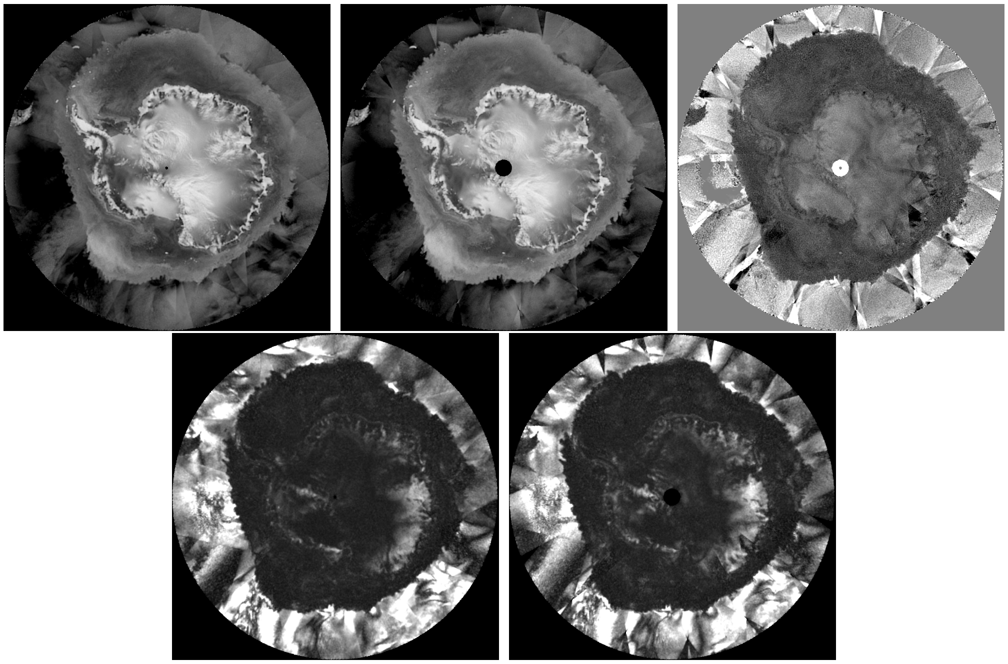

Figure 7.1: Sample SeaWinds egg SIR imagery for 1999 day 245. The images are, from top left to bottom right, A_v^{54}, A_h^{46}, γ_{sw}, κ_v, and κ_h, respectively. The original images contain 1940 x 1940 pixels with a nominal pixel spacing of 4.45 km.

The modified SeaWinds copol ratio metric exhibits a combination of two Ku-band backscatter signature dependencies. The first is the polarization dependence of ocean and sea ice σ^o. The utility of the polarization response has been shown in identifying sea ice [25]. For conductive surfaces such as sea water, the backscattering reflection coefficients for horizontal and vertical polarization waves are different. In general, the vertically polarized waves reflect more than the horizontal waves. Sea ice, on the other hand, behaves quite differently. Sea ice is not as lossy as sea water and thus has greater penetration depths at microwave frequencies. Typical sea ice types are composed of an ice crystal lattice with multiple inhomogeneities such as brine pockets and air bubbles. These act as volume scatterers which effectively depolarize the backscatter. As a result, vertical and horizontal polarization backscatter of sea ice at the same incidence angle are similar.

The modified SeaWinds copol ratio also contains cross polarization incidence angle dependence. This component of the parameter is primarily sensitive to surface roughness levels. Incidence angle dependence has been used by a number of researchers to study sea ice [8, 18, 19, 61, 62]. Sea ice microwave signatures are typically more isotropic in incidence angle than sea water surfaces. Consequently, this dependence can be used to assist in identifying ice pack extent.

To illustrate the parameter sensitivity, Figure 7.2 shows various γ_{sw} values along a 45° West longitudinal transect that extends from deep in the ice pack into open ocean. Overall, the polarization and incidence angle dependence of σ^o combine such that γ_{sw} is low in the sea ice portions of the image and relatively higher in ocean regions. However, while γ_{sw} is the most sensitive of all the parameters to be presented, it is not sufficient alone for the discrimination. Mechanisms such as high wind induced roughness over the ocean can result in ambiguity-induced classification errors. Thus, other parameters are included in the process.

Horizontal Polarization σ^o

The A_h^{46} image is also useful in discriminating between ocean and sea ice pixels. An example enhanced resolution image of this parameter is shown in Figure 7.1. As discussed above, h-pol measurements over the ocean are typically much lower than their v-pol counterparts while the sea ice has similar signatures. Consequently, the h-pol responses of sea ice and open ocean are more easily segmented.

In Figure 7.2 the 45° West transect is given for A_h^{46}. The edge between sea ice and sea water pixels is clearly defined using this metric. Still, the noise levels are higher in the A_h^{46} data than in the γ_{sw} case, making this parameter less sensitive to sea ice presence. In other ice edge regions, the boundary between the two regimes is not as clearly defined, requiring the use of this parameter in concert with others for effective sea ice discrimination. Similar to the copol ratio, wind-induced surface roughness can potentially cause ambiguous signatures.

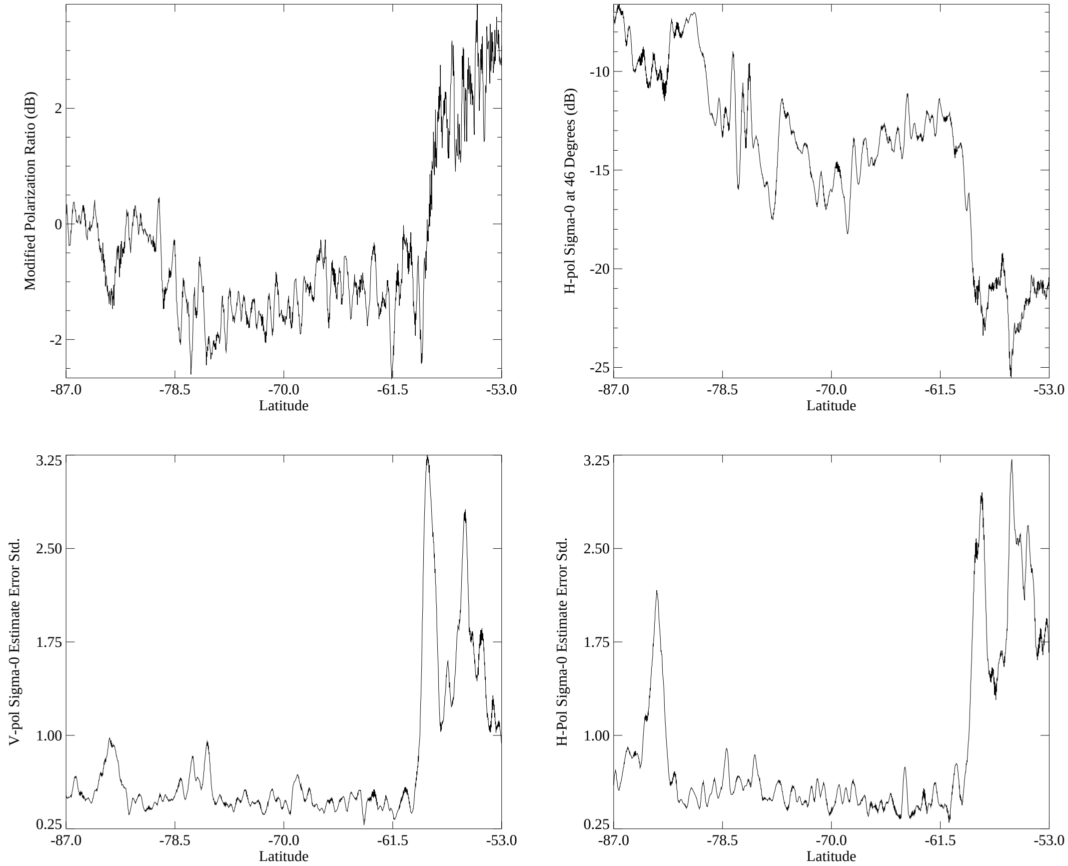

Figure 7.2: Plots of the each classification parameter along 45° West longitude illustrating the differences in sea ice and open ocean signatures. The sea ice extends southward of approximately 62° S latitude. The plots are from top left to bottom right: γ_{sw}, A_h^{46}, κ_v, and κ_h.

Dual-polarization σ^o Estimate Error Standard Deviation

Two additional parameters are used to complement γ_{sw} and A_h^{46} and increase the ability of the algorithm to separate sea ice and ocean pixels: the vertical and horizontal polarization σ^o estimate error standard deviations, κ_v and κ_h. These metrics are reconstructed on the enhanced resolution grid for compatibility with other SIR products. The mathematical definition of κ for a particular pixel is given as

$$\kappa = \sqrt{\sum_l (\sigma_l^o - \widehat{\sigma}_l^o)^2} \tag{7.2}$$

where the σ_l^o are the measurements whose spatial response includes the pixel and $\widehat{\sigma}_l^o$ are the associated forward projections given by

$$\widehat{\sigma}^o = \frac{1}{N}\sum_{i=L_k}^{R_k}\sum_{j=B_k}^{T_k} h_k(i,j)A(i,j) \tag{7.3}$$

where N is the number of pixels in the cell, L_k, R_k, T_k, and B_k define a bounding rectangle for the k^{th} σ^o measurement cell (egg or slice), $h_k(i,j)$ is the antenna gain weighting function for the $(i,j)^{th}$ resolution element, and $A_k(i,j)$ is the σ^o estimate for the $(i,j)^{th}$ resolution element. In general, the κ metric is statistically equivalent the standard deviation of the difference error between the σ^o measurements touching a pixel and their associated forward projections. A more in-depth discussion of κ is given in [8]. Figure 7.1 contains illustrative examples of the κ_v and κ_h images.

The dual-polarization σ^o estimate error standard deviation parameters are functions of variations in observed σ^o during the imaging interval. Since the SeaWinds measurements are at fixed incidence angles, the variations are primarily due to azimuthal and temporal dependence of surface backscatter. The azimuthal component is an excellent differentiator of sea ice and sea water regions. Azimuthal modulation over wind roughened ocean surfaces is a fundamental part of inverting the wind geophysical model function to extract ocean wind vectors. In contrast, sea ice has been shown to have negligible C- and Ku-band azimuthal dependence, generally less than 1 dB [6, 63] (see also Chapter 3). This difference increases ocean κ values when compared to sea ice. However, regions with consistently low winds during the imaging period can exhibit κ values that are similar in magnitude to sea ice observations.

The second component contributing to differences in sea ice and ocean κ measurements is temporal variation. Changes in surface scattering mechanisms of a particular region during the data collection interval cause κ measurements to rise. Open ocean signatures are much more dynamic in time since wind induced surface roughness often changes between satellite passes. On the other hand, sea ice surface properties exhibit much lower temporal variation. Diurnal variations can be observed if significant surface melt occurs, but these effects are typically less pronounced than temporal changes in ocean σ^o. Ice motion can also produce increased κ.

The RL-N ice extent mapping algorithm uses κ as a secondary classification parameter. Because six days of NSCAT data are required to generate enhanced resolution h-pol images of the polar regions, κ was used as a secondary rather than primary classification parameter. The NSCAT κ sea ice values are affected by sea ice motion and temporal change. In contrast to NSCAT, the measurement geometry of the SeaWinds instrument allows for complete coverage of the Antarctic and Arctic regions in a single day. Hence, ice motion and other temporal variations in sea ice signatures are significantly reduced and the κ values are dominated by azimuthal dependence. This facilitates the use of SeaWinds κ_v and κ_h values as primary classification parameters. A longitudinal transect is plotted for these variables in Figure 7.2. While the graphs demonstrate obvious differences at the ice edge along 45° W, plots along other transects do not always exhibit such a clear delineation between the two regimes. Using all four parameters together maximizes the ice discrimination capability.

7.1.3 Multivariate Sea Ice Extent Mapping

Through a combination of various processing techniques the sea ice extent can be effectively mapped using γ_{sw}, A_h^{46}, κ_v, and κ_h imagery. This section describes an algorithm designed specifically for SeaWinds Ku-band data. While based on the fundamental methodology of the RL-N method, significant modifications and improvements are presented. Following the RL-N algorithm, the method can be broken down into five major steps beginning with the reconstructed parameter images:

1. Data fusion and histogram generation.
2. Linear discrimination.
3. Iterative maximum likelihood discrimination.
4. Residual error reduction.
5. Sea ice growth/retreat constraint filtering.

Each of these steps is discussed in detail in the following sections.

Data Fusion and Histogram Generation

Individually, each of the four classification parameters contains valuable information about the presence of sea ice. Taken together, a more accurate classification is possible. These data reside in a 4-dimensional hyperspace of measurement vectors,

$$\vec{x} = [\gamma_{sw}\ A_h^{46}\ \kappa_v\ \kappa_h]^T. \tag{7.4}$$

The data fusion portion of the algorithm ensures that data is weighted to maximizes classification accuracy. The first step consists of data standardization. Each of the three different data types (γ, A_h, and κ) are normalized such that each type has a mean of zero and a variance one. This transforms the hyperspace so each parameter type is given equal weight.

While the standardization is useful for combining feature vector elements with different units of measure in an impartial way, classification parameters contain varying levels of useful information to be exploited in the algorithm. In an effort to maximum classification accuracy, a weighting vector is applied to the all measurements in the observation space which scales the individual measurement vector elements by varying amounts. An empirical analysis of various weighting vectors reveals that the resulting sea ice map is not particularly sensitive to the precise level of the weighting vector components. However, the general magnitude is important to the algorithm performance. Through the consideration of several weighting vectors, it is determined that the vector producing the best results gives equal weight to all standardized parameters except γ_{sw} which is scaled by a factor of four. Since γ_{sw} is the most sensitive to the presence or absence of sea ice, greater weight is given to this dimension in the observation space.

Once the data is prepared through standardization and vector weighting, the distribution of observation vectors is examined through histogram analysis. The 4-dimensional histogram of the data space is generated revealing a bimodal distribution. While it is impossible to show a 4D histogram graphically, a 2D distribution of γ_{sw} vs. A_h^{46} is shown in Figure 7.3 along with the corresponding contour plot. The

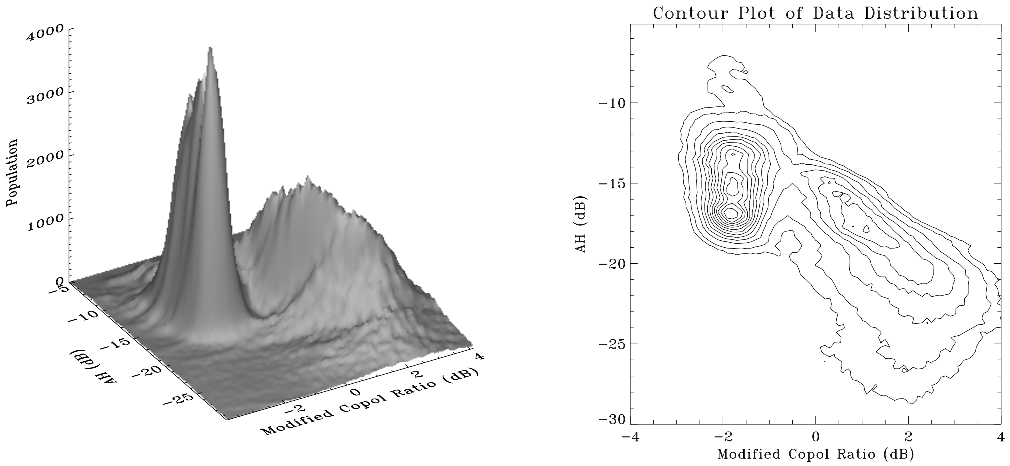

Figure 7.3: Two-dimensional distribution of γ_{sw} vs. A_h^{46} values for Antarctic SeaWinds data from 1999 day 245. The corresponding contour plot is also shown. The highest peak is the mode of the sea ice distribution.

plot illustrates the bimodal nature of the distribution for these two parameters. The two modes correspond with the sea ice and ocean pixel component distributions or clusters. The sea ice distribution has a typically tighter covariance structure than the ocean distribution in both the 2D and 4D histograms. That is, the variance of each of the parameters is lower for the ensemble of sea ice measurements than their ocean pixel counterparts. This is a function of the various mechanism described in section 7.1.2 which described the nature of dynamic ocean signatures compared to the relatively stable sea ice observations.

An important issue in polar sea ice extent mapping is the seasonal variability of the component distributions of ice and ocean. For sea ice, the seasonality of microwave signatures is due to variations in surface properties caused by ice growth and melt, surface deformation, brine drainage, and other mechanisms. For the ocean, the cluster centroid can be modified by changes in prevailing wind characteristics which vary with season. This phenomenon precludes the use of a fixed boundary to segment the two clusters throughout the year. Rather, an effective algorithm must have the ability to adapt to current conditions to provide and optimal estimate of sea ice extent. The following sections detail the iterative portion of the algorithm to achieve automated adaptability.

Linear Discrimination

The main objective of the image segmentation algorithm is to separate the sea ice and ocean clusters with minimal error. The first cut is achieved through linear discrimination. Assuming that the component distributions are Gaussian in the 4-dimensional space, the optimal linear boundary is a hyperplane that passes through the saddle point in the distribution and is perpendicular to the line segment connecting the two modes.

To identify the hyperplane boundary, the distribution modes are first found through an automated histogram search algorithm. The search method is similar to the two-dimensional search performed in Chapter 5 though for SeaWinds, a four-dimensional search window is used. Once the locations of the two modes are identified, the histogram values that fall along the line connecting them are observed. The values along such transects follow a curve illustrating the bimodal nature of the distribution as well as the differing covariance structures associated with each of the component distributions. The hyperplane is chosen to pass through the minimum value of this curve (corresponding with the saddle point of the full distribution) and is perpendicular to the line segment between the two modes.

In identifying the saddle point, noisy histogram values on the ocean side can potentially cause spurious low values that are clearly not the correct saddle point. Though rare, this phenomenon results in a hyperplane placement which is too close to the ocean cluster center causing multiple misclassifications of ocean pixels as sea ice. To ameliorate this problem, the location of the saddle point in relation to the two modes is limited. Since the ice cluster has characteristically lower variance than the ocean mode, the saddle point is always closer to the ice cluster center than the ocean mode. Consequently, if the chosen center point is closer to the ocean cluster mode, the hyperplane tie point is shifted to the center of the mode connecting transect. This

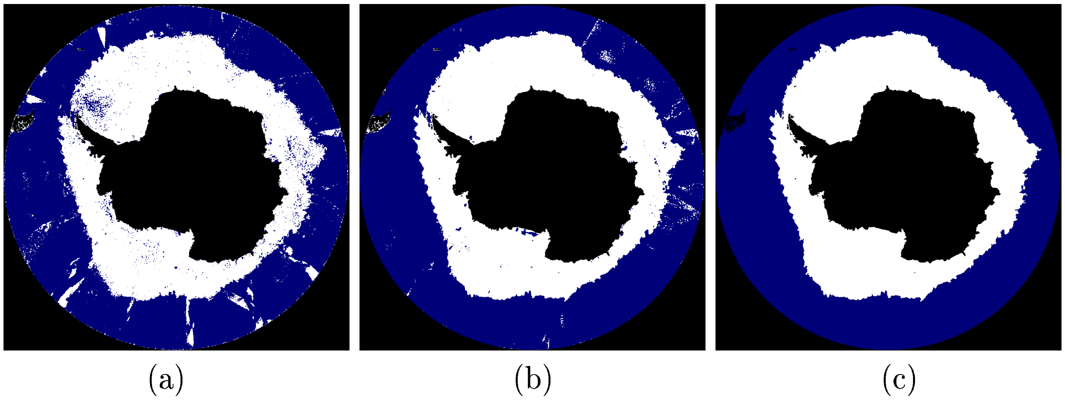
(a) (b) (c)

Figure 7.4: Sample binary Antarctic ice maps for 1999 day 245 at various stages in the algorithm: (a) nearest neighbor estimate, (b) iterative maximum likelihood estimate, and (c) classification error filtered estimate.

placement of the hyperplane boundary results in a simple nearest neighbor linear classification.

Figure 7.4 shows three binary ice masks resulting from various stages of the algorithm for a sample image set in Antarctica. Figure 7.4a depicts the ice extent estimate after the linear discrimination. While the ice edge can be readily observed, significant errors still exist indicating that further processing is required to improve the ice extent estimate. The classification quality is enhanced through the use of iterative maximum likelihood discrimination as described in the following sections.

Maximum Likelihood Discrimination

While the linear method produces a reasonable initial estimate of the ice edge, higher order classifiers can be used to improve the quality of the final sea ice map. In the RL-N method, the Mahalanobis technique is used to provide a better discrimination boundary. For the SeaWinds data, a maximum likelihood classification technique is adopted from a study to identify sea ice types in Antarctica described in Chapter 6 (see also [9]). A maximum likelihood (ML) classifier is derived assuming that the two component distributions are Gaussian in the hyperspace. Maximum likelihood techniques choose the solution that maximizes the conditional probability of observing a given measurement vector over the two possible surface types,

$$C_{ML} = argmax_c \; p(\vec{y}|C = c) \tag{7.5}$$

where C_{ML} is the ML chosen surface type, $\vec{y}$ is a standardized and weighted data vector, C is a discrete binary random variable denoting the surface type (sea ice or ocean), and $p(\vec{y}|C = c)$ is the probability of observing a specific feature vector given a particular surface type. In order to implement such a statistical classifier, the conditional distribution must be known. Under the multivariate Gaussian assumption, these distributions have the form given in Eq. (6.8) which is repeated here for convenience:

$$p(\vec{z}|C) = \frac{1}{(2\pi)^{n/2}|K_c|^{1/2}} e^{-\frac{1}{2}(\vec{y}-\vec{\mu}_c)^T K_c^{-1}(\vec{y}-\vec{\mu}_c)} \tag{7.6}$$

where $\vec{\mu}_c$ is the mean vector and K_c is the covariance matrix of surface type c, respectively. Thus, the conditional distributions are completely characterized by their individual mean vectors and covariance matrices. Sample estimates of these can be computed from the linear discrimination described above.

The maximization of Eq. (7.6) can be simplified to reduce computational complexity. Through some mathematical manipulation, the maximization of the conditional distribution reduces to the minimization of a "maximum likelihood distance metric,"

$$C_{ML} = argmin_c \; [log|K_c| + (\vec{y} - \vec{\mu}_c)^T K_c^{-1}(\vec{y} - \vec{\mu}_c)]. \tag{7.7}$$

The ML method results in a quadratic boundary which accounts for the differences in component distribution variances and covariances. Equation (7.7) is similar to the Mahalanobis distance metric used in the RL-N sea ice detection. In fact, the second term in this equation is the Mahalanobis distance.

Using estimates of the mean vectors and covariance matrices of the two clusters computed from the linear discrimination, the ML classification is employed. After the first implementation of the ML method, the statistics are updated and the ML classification is used once more. Within two iterations, the algorithm converges to an improved estimate of polar sea ice extent. A sample of the resulting binary ice masks is given in Figure 7.4b. Compared with the linear discrimination results

(Figure 7.4a), significant improvements have been made, though some residual errors are still present in the images.

Residual Error Reduction

The ML estimate of the sea ice extent can still contains some misclassifications due to high, persistent winds over a region during the imaging period which can result in ambiguous signatures that confuse the algorithm. Consequently, a small percentage of ocean pixels may be erroneously identified as sea ice. These errors are manifested in the binary image as isolated patches of sea ice in regions that clearly cover open ocean.

In general, the algorithm is most effective in correctly identifying sea ice. The tighter covariance structure inherent to the sea ice cluster in the observation space allows this regime to be mapped more accurately. In addition, since polynyas have signatures very similar to open ocean, the method consistently identifies these features within the ice pack. Unfortunately, a relatively low level of residual misclassification noise still exists.

Isolated regions of misclassified pixels can be eliminated through the use of the binary image processing technique of region growing described more fully in Chapter 5. When complete, the misclassified patches in the ice or ocean regimes are removed. Unfortunately, this portion of the algorithm filters out polynyas as well. Since the objective of this study is to identify the total sea ice extent, polynyas are ignored. However, the processing can be adjusted to retain polynyas along with the infrequent misclassifications within the ice pack by skipping the inverse region growing step. An example of the effect of region growing on the ice extent estimate is shown in Figure 7.4c.

Sea Ice Growth/Retreat Constraint Filtering

An additional source of errors are misclassified “fingers” or “dents” along the ice edge. Since they are connected to the edge itself, the region growing portion of the algorithm does not remove these errors. Though both are encountered relatively infrequently, steps have been added to the algorithm to remove large manifestations of these from the edge.

One important piece of information not exploited in the RL-N ice mapping method is a knowledge of typical sea ice growth and retreat. That is, sea ice edges have physical bounds on the amount of advance or retreat that can occur in a single day. Hence, the previous ice map can be used to constrain the current discrimination. The automated constraint is implemented through the use of binary image dilation and erosion [65, 79] techniques.

The first step in constraining ice growth is to generate a binary difference image between the current and previous ice masks. The difference image is non-zero only where the two masks are dissimilar. Next, the previous ice mask is dilated outward an arbitrary distance that represents an upper threshold on the maximum possible ice advance. For this study, a 200 km maximum advance per day threshold produces good results in eliminating erroneous ice fingers. At this point, the dilated image is compared with the present ice mask. The binary difference of these two images is generated. Non-zero values represent the tips of ice fingers that have exceeded the limit on ice growth. In these regions, the previous ice edge estimate is more accurate. To recover the former edge, the region growing algorithm (which is actually a constrained dilation) is used to expand the remaining tips within the original current/previous mask difference image. Enough dilations are used to reach the previous ice edge. The resulting region is removed from the current ice mask. The effect is to substitute the ice edge in only a small localized region affected by the anomaly.

Less frequently encountered sea ice dents are corrected in a very similar manner. All procedural steps are the same except that the previous image is first eroded a specified amount rather than dilated. For large erroneous sea ice retreats, the local ice edge is replaced with the previous estimate.

Algorithm Summary

Together, the steps described above produce an automated adaptive algorithm using mapping sea ice for Ku-band SeaWinds scatterometer data. The algorithm results in a binary ice map depicting the extent of sea ice in either the Antarctic or the Arctic polar regions. A summary of the algorithm follows.

1. Generate enhanced resolution imagery
2. Standardization and weighting
3. 4-D histogram generation
4. Linear discrimination
    (a) Identify locations of the two distribution modes
    (b) Optimal hyperplane boundary placement
    (c) Cluster segmentation
5. Compute sample Gaussian statistics
    (a) Cluster mean vectors
    (b) Cluster covariance matrices
6. Maximum likelihood discrimination
    (a) Two iterations
    (b) Update statistics in between
7. Region growing to remove isolated misclassifications
8. Ice extent growth/retreat constraining
    (a) Removal of erroneous ice edge "fingers"
    (b) Removal of erroneous ice edge "dents"

The resulting mask is used to remove ocean pixels from polar imagery. Implementation and validation of the algorithm are discussed in the following section.

7.1.4 Ice Extent Results

The algorithm is implemented for all currently available QuikSCAT Antarctic and Arctic data, spanning 1999 day 200 to 2000 day 50 (mid-July to late February). Enhanced resolution imagery is produced on one day intervals resulting in a large time series of ice-masked imagery that can be used for a number of applications. Examples are the removal of sea ice regions in scatterometer wind processing and ice edge evolution studies. In this section, the QuikSCAT generated ice extent maps are validated and analyzed. For validation, comparisons are made with ice edges produced by the NASA Team algorithm applied to SSM/I data in the Antarctic and Radarsat SAR imagery in the Arctic. The evolution of total sea ice extent is also studied during the SeaWinds mission and compared with sea ice extent observed by NSCAT during similar seasons.

Ice-Masked Polar Image Sequences

Figure 7.5 shows four sample ice-masked SeaWinds A_v^{54} images of Antarctica. An animation of the complete image sequence can be viewed at internet address http://www.mers.byu.edu/Seawinds-1.html. The image series demonstrates the dynamic nature of Antarctic sea ice throughout the seasonal cycle. The first image shows the state of the sea ice pack during Antarctic winter as sea ice growth rate begins to decrease. The following image, day 278, shows the distribution of sea ice near the peak of the seasonal sea ice extent. Substantial melting has occurred by the next frame, day 346, in which a number of polynyas have begun to form. Most notable of these are the large polynyas in the Ross Sea and north of the Bellingshausen Ice Shelf. The images from day 346 to day 50 which are not shown in this figure reveal that these two polynyas continue to grow until they break through the ice edge into open ocean. The final image panel demonstrates that significant melting occurs from 1999 day 346 to 2000 day 50 as austral summer begins and the sea ice draws near its minimal yearly extent. At this point, a large majority of the remaining Antarctic sea ice is in the Weddell and Amundsen Seas.

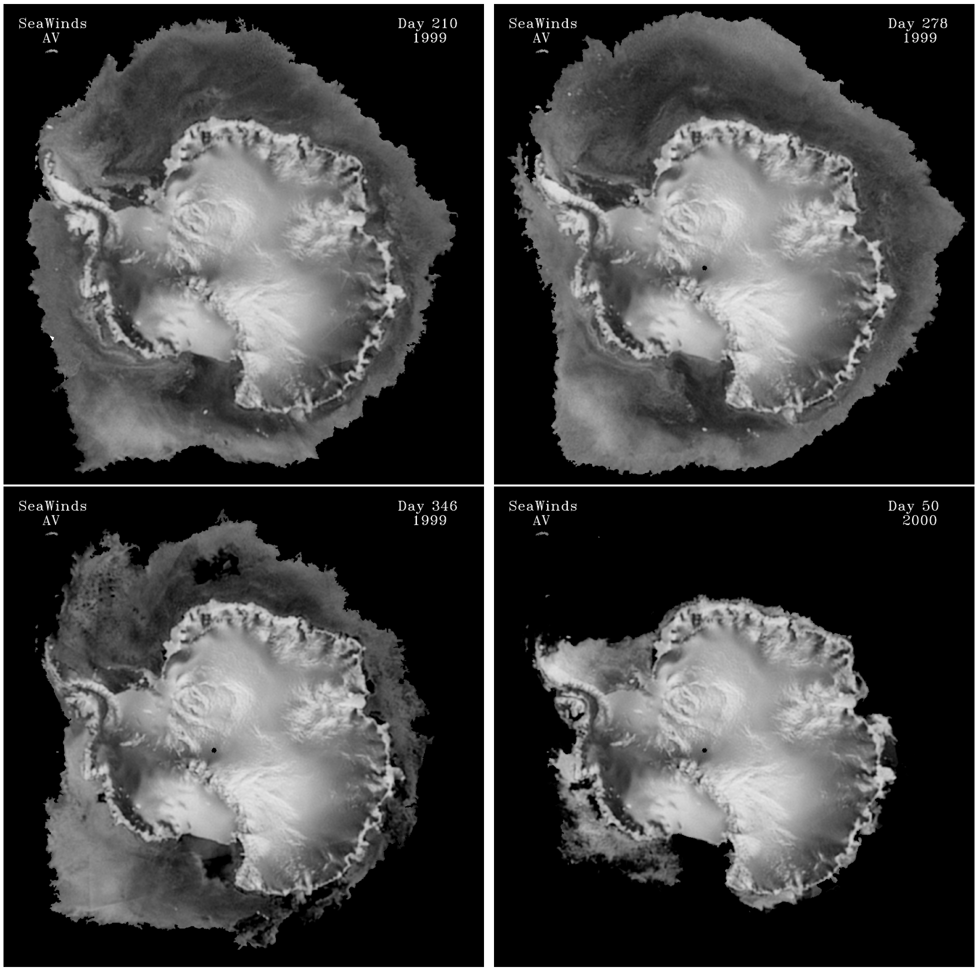

Figure 7.5: Sample ice-masked SeaWinds v-pol images illustrating the seasonal evolution of Antarctic sea ice extent.

Within the ice pack a wide spectrum of σ^o values are observed. The various levels of backscatter are related to important sea ice properties such as surface roughness, snow cover, dielectric loss, and volume scattering due to inhomogeneities. In general, older ice types appear very bright in the imagery due to increased volume scattering as water and brine content drain from the ice. Very rough ice types also exhibit high backscatter. Young, smooth ice forms have much lower σ^o values. Consequently, the evolution of surface features can be monitored to better understand polar sea ice dynamics. For example, from day 210 to 278 brighter relatively old ice moves northwest away from the Ronne Ice Shelf along the Antarctic Peninsula due to ocean currents and prevailing surface winds. Younger forms of ice fill in the gap shown by the low backscatter region along the shelf. Near the eastern-most point of the Ronne Ice Shelf, a number of large grounded bergs oppose sea ice floe motion forced by the Weddell Gyre. As a result, ice floes pile up to the east of the icebergs. The deformed ice rubble eventually overflow to the north of the bergs and travel northwest parallel with the peninsula. This phenomenon is manifest in the day 210 and 278 images as a bright band of sea ice in the southern Weddell Sea.

Figure 7.6 illustrates a similar image series for the Arctic region. Again, the dynamic nature of sea ice extent is observed. The first image frame, representing day 210, shows Arctic sea ice distribution toward the end of the sea ice retreat phase. The darkened sea ice σ^o values are indicative of widespread surface melt. The next frame, day 278, illustrates the ice extent near the minimal point during the year. During this period, high backscatter multi-year sea ice constitutes a large majority of the ice pack. From day 278 to 346, extensive ice growth is observed. Lower backscatter first year sea ice grows southward into the Bering Sea, Baffin Bay, and other areas. The final image panel shows the sea ice pack near maximal extent. These figures illustrate the nonuniform nature of sea ice advance during the Arctic growth cycle. In some regions such as the Bering Sea, Baffin Bay, and Hudson Bay, sea ice extends much further south than in the Barents and Norwegian Seas. Differences in backscatter levels in portions of Greenland due to surface melting and refreezing of glacial ice are also evident.

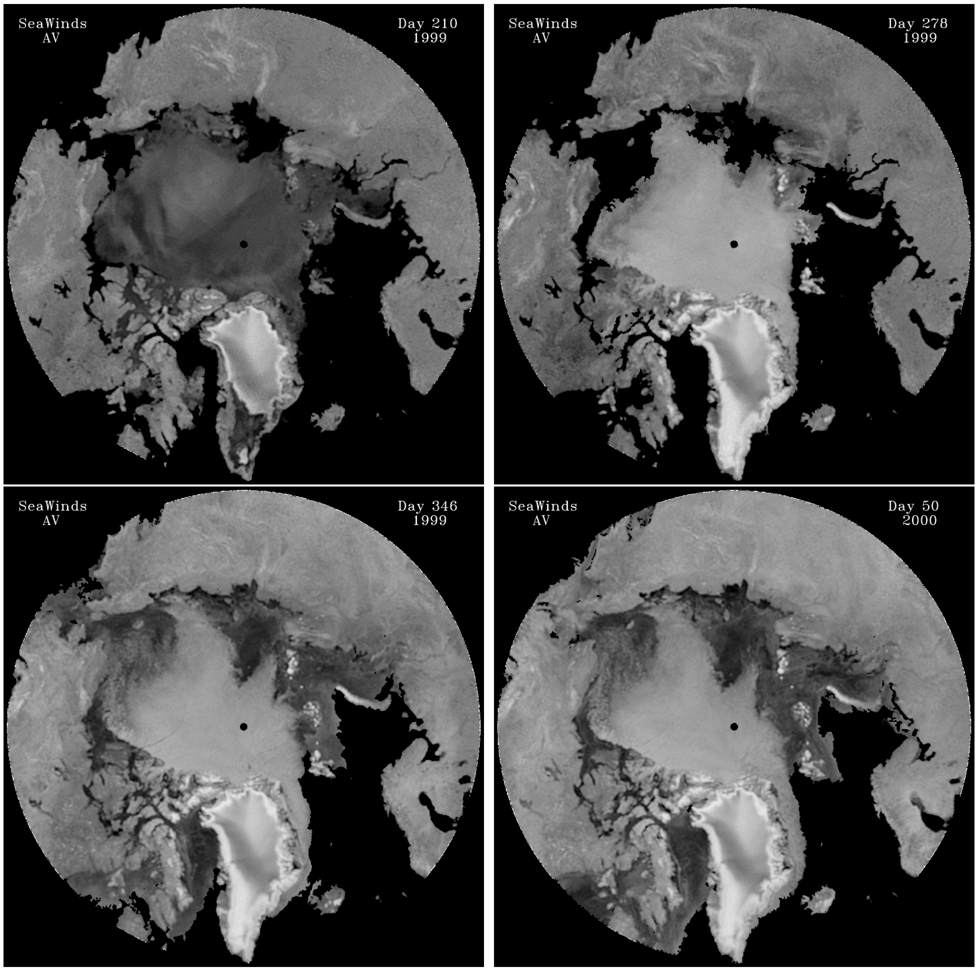

Figure 7.6: Sample ice-masked SeaWinds v-pol images illustrating the seasonal evolution of Arctic sea ice extent.

NASA Team Algorithm Comparisons

In an effort to validate the technique, the SeaWinds ice extent images are compared with SSM/I-derived sea ice concentration imagery produced by the NASA Team algorithm. The images were provided by the National Snow and Ice Data Center. The NASA Team method uses multifrequency, dual-polarization data from the SSM/I radiometer to produce estimates of sea ice concentration on a 25 km grid [31, 36]. Both the NASA Team and SeaWinds images are presented using similar polar stereographic projections. The SeaWinds egg images are produced on a higher resolution grid with pixel spacing of 4.45 km. Daily ice concentration images are compared with SeaWinds data by interpolating the NASA Team imagery to the same pixel grid. These are then thresholded at various concentration levels to obtain multiple ice edges for comparison.

Ideally, all SeaWinds images would be compared with corresponding NASA Team products. However, the near real-time NASA Team ice concentration images have significant processing errors in the Amundsen Sea quadrant of Antarctica (90°-180° West longitude) from 1999 day 274 through the end of the available image set. These artificial errors are unrelated to the NASA Team algorithm and have not been corrected at the time of this writing. Hence, after day 274, the affected quadrant is excluded in the comparisons.

For the correlation analysis, the NASA Team ice concentrations images are thresholded at 5% increments from 5% to 45%. The disagreement percentage is used to provide a measure of similarity between ice edges [8]. This metric is defined as the ratio of the total pixel area for which the two methods disagree and the area of the pixels that are classified as ice by either method. Hence, high correlation in the edges results in low disagreement percentages. Figures 7.7-7.8 shows this metric as a function of NASA Team algorithm ice concentration for the four sample images shown in Figure 7.5. In Figure 7.7, the minima are found at 30-35% concentration. This result is typical of daily imagery up to approximately 1999 day 300 and is similar to the results found for NSCAT sea ice extent mapping [8]. Figure 7.8, illustrates the disagreement percentages for two sample images later in the season. The resulting

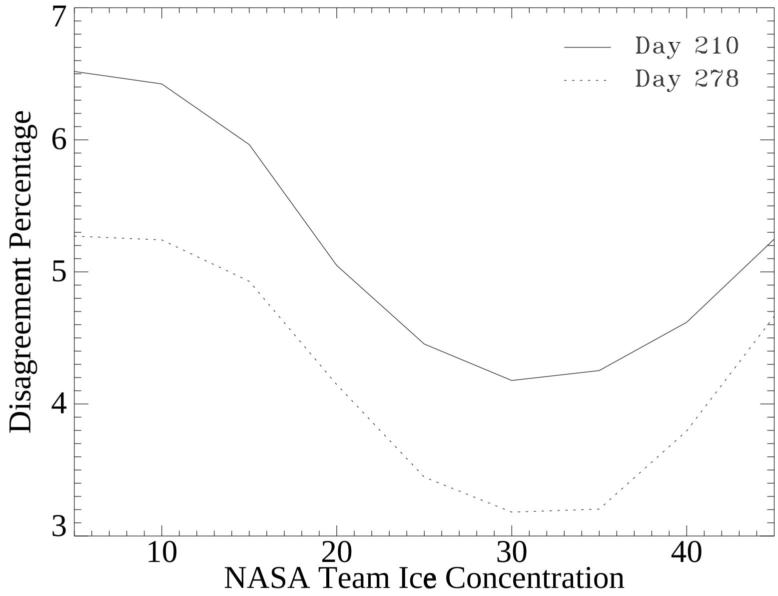

Figure 7.7: Disagreement percentages as a function of NASA Team SSM/I-derived sea ice concentration for two sample days during ice advance and the beginning of ice retreat. Strongest correlation occurs at 30%.

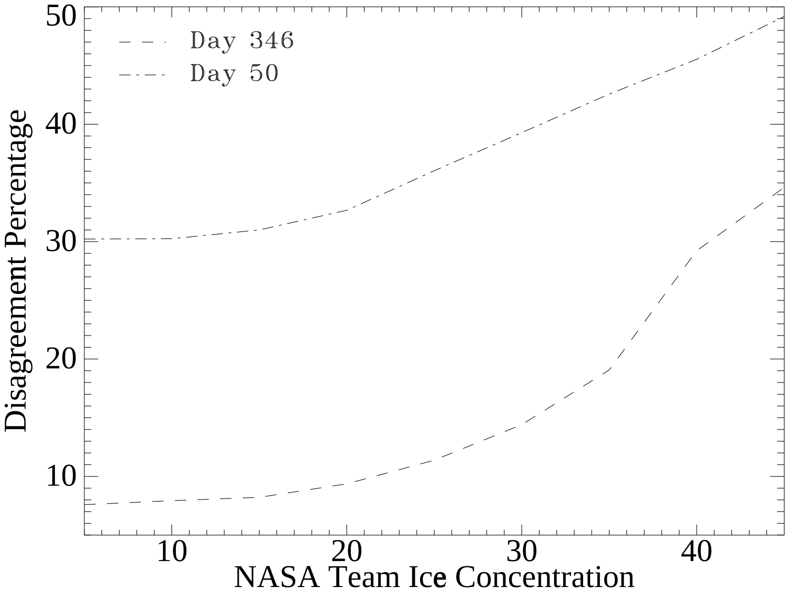

Figure 7.8: Disagreement percentages as a function of NASA Team sea ice concentration for two sample images during rapid ice retreat and minimum ice extent. Disagreement is lowest at 5-10%.

correlation is significantly different. Not only are the disagreement percentage values higher, but the minimum is found at very low concentration levels of 5-10% instead of 30-35%.

Higher correlation with lower concentration edges is typical for all image sets after approximately day 300. At this point, the Antarctic sea ice pack begins a rapid retreat as austral summer approaches. Hence, during spring and summer seasons, the SeaWinds edge correlates best with lower NASA Team concentrations. In contrast, the RL-N algorithm was found to best match the 30% level throughout the year. The discrepancies are attributed to the use of different parameters in the classification. Though both SeaWinds and NSCAT are Ku-band scatterometers, the parameter differences are large enough to cause significant changes in ice concentration sensitivity. NSCAT A images are reconstructed at 40° incidence while SeaWinds A images have incidence angles of 46 and 54°. Also, the SeaWinds classification lacks incidence angle dependence parameters.

To further illustrate the edge comparisons, Figure 7.9 shows a SeaWinds A_h^{46} image of the Weddell Sea quadrant of Antarctica for 1999 day 245. Several ice edge contours are superimposed on the figure. The white contour is the SeaWinds-derived edge while the black lines are the 5% and 30% concentration NASA Team edges. The figure shows the high correlation between the SeaWinds and 30% edges though minor differences are observed. A similar image is shown in Figure 7.10 for 2000 day 5. Again, all three edges are plotted. While the closest correlation is observed between the SeaWinds and 5% contours, significant discrepancies exist. In particular, the SeaWinds edge is further north than low NASA Team concentrations. Fetterer et al. (1992) observed similar trends in comparing GEOSAT radar altimeter ice edges with NASA Team ice concentrations during ice ablation [66]. Fetterer found that the radar-derived extent was consistently larger than the SSM/I-derived product. These results indicate differences in active and passive microwave sensitivities to sea ice concentrations as the ice edge recedes.

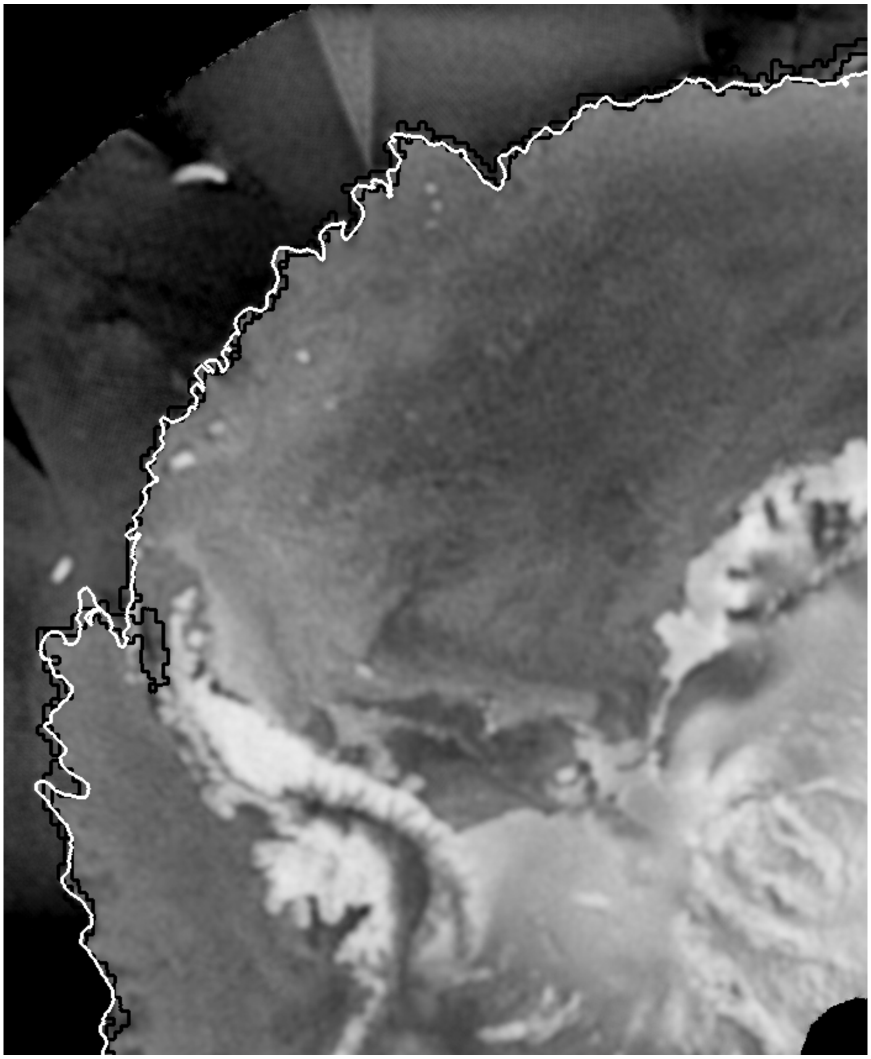

Figure 7.9: Sea ice edge comparisons in the Weddell Sea quadrant of Antarctica for 1999 day 245. The NASA Team 5% and 30% ice edges are plotted in black with the 5% edge north of the 30% contour. The white contour is the SeaWinds edge.

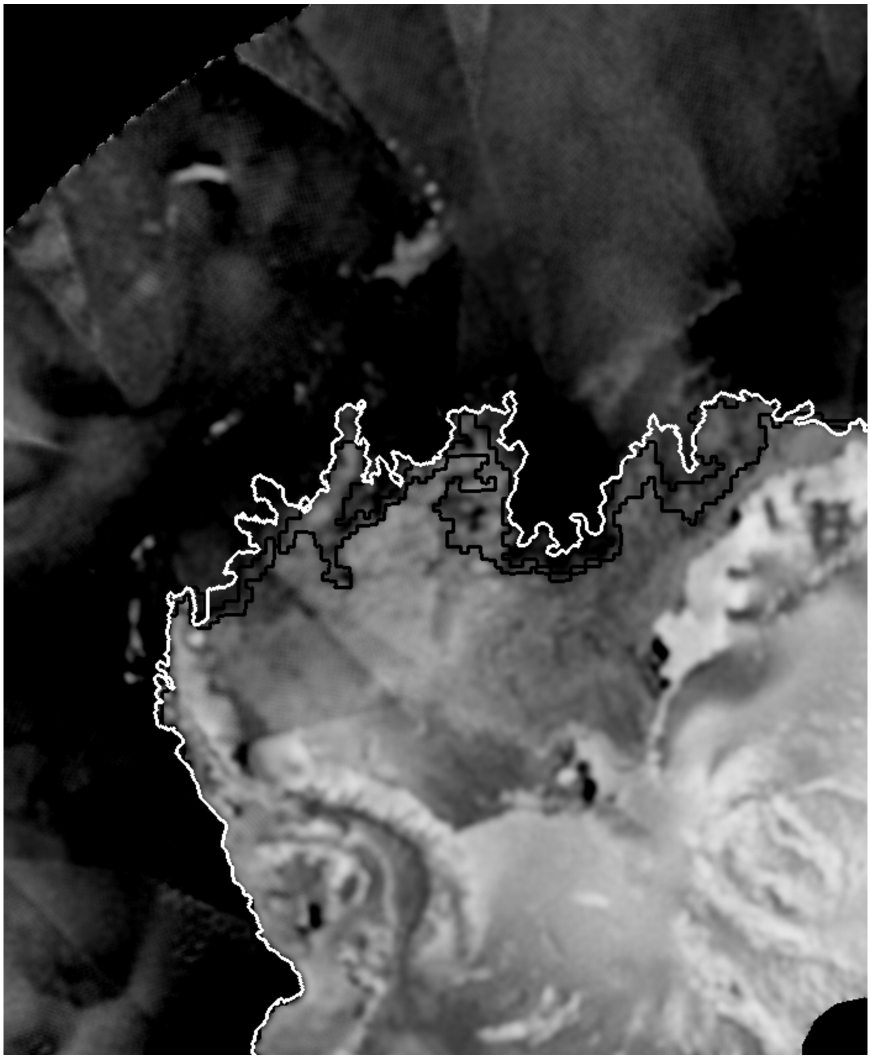

Figure 7.10: Sea ice edge comparisons in the Weddell Sea quadrant of Antarctica for 2000 day 5. The NASA Team 5% and 30% ice edges are plotted in black with the 5% contour north of the 30% contour. The white contour is the SeaWinds edge.

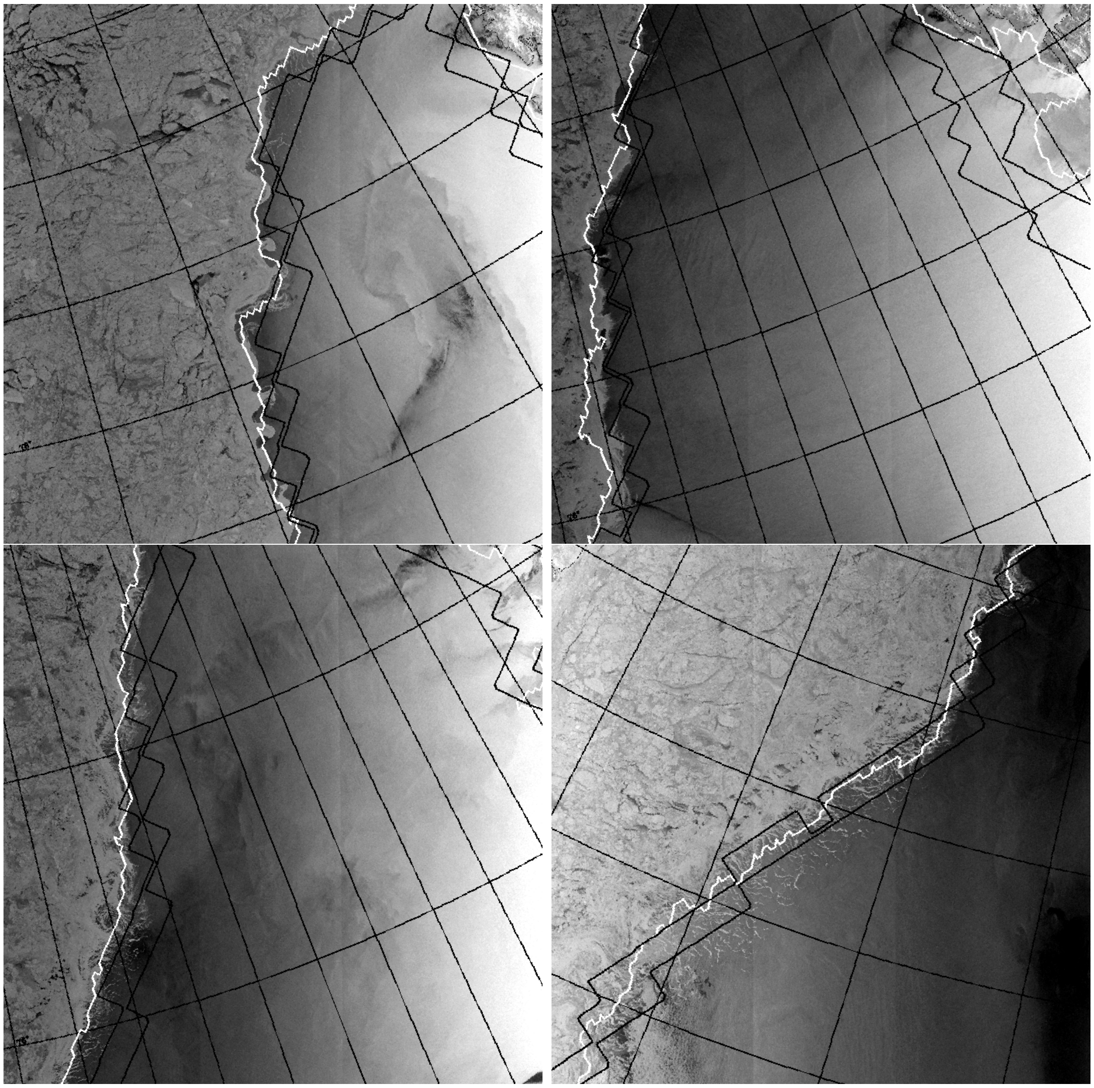

Figure 7.11: Radarsat images with SeaWinds (white), NASA Team 5% (black), and NASA Team 30% (black) edge estimates. Images acquisition days are (from top left to bottom right): 2000 day 37, day 38, day 48, and day 51. (Radarsat images © Canadian Space Agency.

Comparison with Arctic Radarsat SAR Imagery

With high spatial resolution but limited coverage, SAR imagery can be beneficial for ice edge validation in small localized regions. SAR instruments have produce imagery Though SAR imagery of sea ice edges are scarce in the Antarctic, an abundance of image frames are available in the Arctic. For this study, a number of Radarsat hh-pol C-band SAR image frames were obtained from the National Ice Center. The images cover sea ice edge regions near Greenland during February 2000. Several sample Radarsat images are shown in Figure 7.11. Superimposed on each frame are the SeaWinds and the NASA Team 5% and 30% ice edge estimates. In general, the observed Radarsat and SeaWinds edges are highly correlated, matching each other within approximately 10 km. The NASA Team algorithm edge contours also provide good estimates of the sea ice edge albeit at a lower resolution.

While the Radarsat images are essentially instantaneous "snapshots" made as the satellite passed over the region, the SeaWinds and NASA Team edges were created using a full day of microwave data. Consequently, the SeaWinds and SSM/I edges represent averages over the entire day. Some differences are expected since sea ice edges can be very dynamic, moving tens of kilometers in a single day.

Figure 7.11 also illustrates the behavior of the algorithm under different edge conditions. For example, the algorithm's performance varies when the sea ice edge is hard rather than diffuse. When the sea ice edge is clearly defined, the technique estimates the location of the edge relatively well. As the edge becomes more diffuse the SeaWinds edge does not identify the lowest concentrations as sea ice. This is consistent with the finding that the SeaWinds edge correlates well with the 30-35% NASA Team ice edge during this portion of the yearly cycle.

Sea Ice Extent Evolution

An important geophysical parameter, total sea ice extent area, can be obtained from the ice-masked imagery. This parameter is computed by summing the areas of all ice flagged pixels in the SeaWinds or NASA Team images. The data set used in this study represents only a portion of the complete yearly cycle and more comprehensive analyses can be made once more SeaWinds data becomes available. To illustrate the temporal dependence of sea ice extent, Figure 7.12 shows the SeaWinds-derived total sea ice extent area from 1999 day 200 to 2000 day 50. Days when the instrument was not in operation are not shown in the plot. This figure illustrates sea ice extent during the final portion of ice growth through most of the melt period in 1999-2000. The NASA Team 30% ice extent is also plotted for the 74 day period in which full NASA Team image coverage was available. As the plot indicates, a high correlation exists between the two estimates of total sea ice extent area. The day range covered in this interval represents the final period of ice growth until a maximum extent is reached. Unfortunately, the processing errors in the Amundsen Sea quadrant of the NASA Team Antarctic imagery preclude an accurate computation of total sea ice extent after day 273.

Figure 7.13 illustrates a comparison between the NSCAT ice extent estimate in 1996-1997 and the corresponding SeaWinds estimate in 1999-2000. Overlapping days of the year are only available in the period representing the initiation of sea ice ablation to the point of minimum sea ice extent. Though both exhibit the same seasonal trend, significant differences are observed. Throughout this period, the NSCAT estimate is consistently lower, attributed primarily to the interannual variability of sea ice extent.

The other contributing factor to observed differences in sea ice extent between the two data sets is the different sensitivities to sea ice concentration. As previously noted, NSCAT was found to closely correlate to the NASA Team 30% concentration level throughout the NASA mission. On the other hand, the SeaWinds estimate more closely matches the 5-10% ice concentration during periods of rapid sea ice retreat.

7.1.5 Ice Extent Conclusions

Previous studies have shown that Ku-band scatterometer data is capable of effectively discriminating between open ocean and sea ice. This study demonstrated

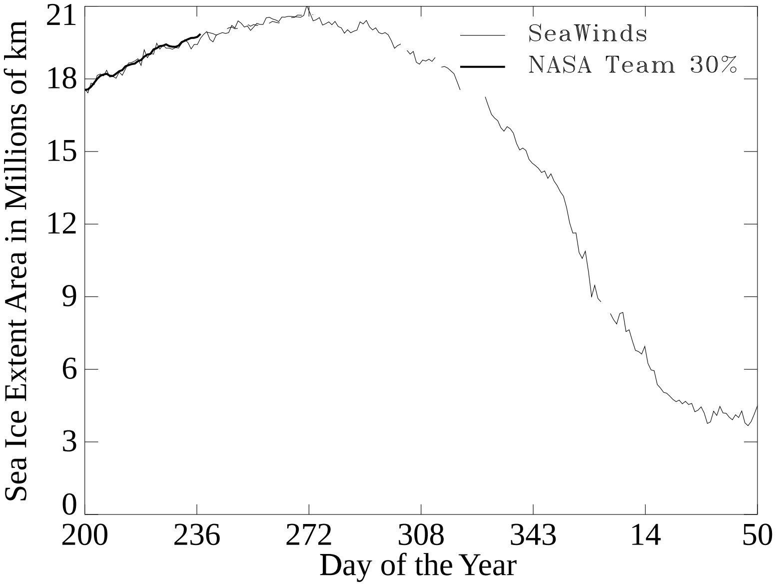

Figure 7.12: SeaWinds total sea ice extent estimate from 1999 day 200 to 2000 day 50. The NASA Team 30% ice concentration estimate is also plotted from 1999 day 200-273 indicating high correlation with SeaWinds in ice edge detection.

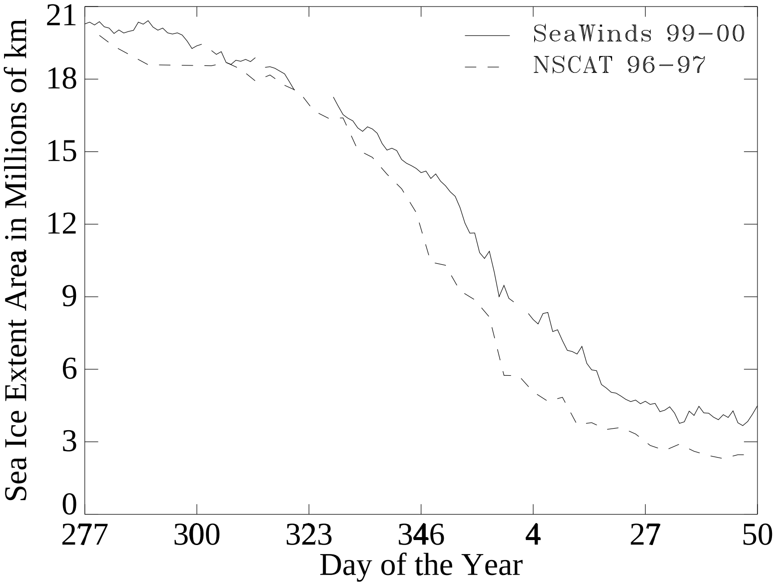

Figure 7.13: SeaWinds vs. NSCAT ice extent comparison during the sea ice ablation period. Differences are due primarily to differing ice concentration sensitivities (SeaWinds: 5-10%, NSCAT: 30%).

the development and implementation of a new algorithm for use with SeaWinds scatterometer data. The technique is fully automated and adapts to temporally changing surface signatures. The resulting ice edges correlate best with the NASA Team 30-35% ice concentration edge during ice advance and 5-10% during sea ice retreat. In contrast, a strong correlation with the 30% contour was observed previously in an NSCAT ice mapping study for both ice advance and retreat periods [8]. The method works effectively for Antarctic and Arctic regimes as demonstrated by comparisons with SSM/I-derived NASA Team ice maps and high resolution Radarsat SAR imagery.

Four microwave parameters are used in the classification: the modified polarization ratio, the SeaWinds h-pol σ^o, and the dual-polarization σ^o estimate error standard deviations. The combination of these parameters are proven effective in identifying sea ice versus ocean regions in enhanced resolution polar imagery. This study showed that the SeaWinds κ images contain more information about sea ice spatial distribution than their NSCAT counterparts. This is primarily due to the one day SeaWinds imaging interval which reduces temporal dependence of the metric and effectively increases sensitivity to azimuthal variations.

The SeaWinds edges are considered superior to the NSCAT product for several reasons. First, the former have significantly better temporal resolution of (one day rather than six days). Next, the ability to include the two κ parameters increases the overall quality of ice edge estimates. In addition, the quadratic boundary classification is improved using maximum likelihood techniques rather than the Mahalanobis distance. Finally, an additional post-processing step is added to the SeaWinds method to incorporate a sea ice edge growth/retreat constraint.

The development of the described technique has resulted in the ability to generate enhanced resolution sea ice extent maps on one day intervals. These products can be applied in a variety of studies including ocean wind processing, sea ice extent evolution, and global climate and weather studies. This research showed that the SeaWinds and NSCAT sea ice extents were significantly different during the 1996-1997 and 1999-2000 melt cycles. In particular, the SeaWinds extent is consistently higher throughout the sequence. This is due to interannual variability in sea ice extent as well as differing sensitivities of SeaWinds and NSCAT to sea ice concentration. While the NSCAT edge correlates best with the 30% NASA Team edge throughout the year, the SeaWinds edge matches lower concentrations during sea ice ablation. While the current available data set is relatively short, future SeaWinds data from the instruments on the currently flying QuikSCAT platform and the future ADEOS-II satellite will permit extended Ku-band polar sea ice mapping.

7.2 Ice Classification Using SeaWinds and SSM/I

In addition to the sea ice extent mapping methods of Chapter 5, SeaWinds data can also be used with the sea ice classification techniques discussed in Chapter 6. This section discusses the application of multisensor ice classification to image sets which, among others, contain SeaWinds σ^o data. In the following section, various instrument combinations are considered for the implementation of the method. In Section 7.2.2 principal component imaging of the chosen image set is considered. Section 7.2.3 describes the implementation of the algorithm. Conclusions of this study are given in the final section.

7.2.1 SeaWinds-SSM/I Ice Classification Data Sets

For the ice edge detection discussed in the preceding section, significant changes in the original algorithm were required to facilitate its use with SeaWinds data. In contrast, no modifications are needed to apply the new data set to ice classification. Consequently, this portion of the chapter focuses soley on analysis of the new classification results. The reader is referred to Chapter 6 for a detailed description of the sea ice classification theory and procedure.

For the classifications implemented in Chapter 6, observations collected from three instruments were used: NSCAT, ERS-2, and SSM/I. The combination of active/passive, dual-polarization, multifrequency measurements proved to have great utility in identifying six major types of sea ice in Antarctica. The loss of NSCAT precludes the use of this technique in current and future studies of polar sea ice packs.

However, the Ku-band SeaWinds scatterometer provides a good substitute for ice classifications. SeaWinds reconstructed imagery consists of A_v^{54} and A_h^{46} parameters. Unfortunately, the incidence angle parameters B_v and B_h cannot be estimated from fixed-incidence angle SeaWinds data. Still, the improved temporal resolution offers a reduction in blurring effects caused by ice motion during the imaging interval.

The one-day imaging interval for SeaWinds has several implications in choosing data sets from other sensors for inclusion in the ice classification. First, the ERS-2 AMI scatterometer requires six days of data to acheive full coverage of the polar regions. To maintain the one-day temporal resolution, ERS-2 is not used in the following ice classification experiments. It is expected that the loss of observations at the lower ERS-2 frequency (5.3 GHz) will result in less ability to correctly segment ice types in the imagery. Such lower frequency observations have greater ability to penetrate the sea ice surface and observe the underlying ice structure. Subsurface features are important in determining ice types.

The 85 GHz channels are also excluded from the classification data set. High frequencies are more sensitive to atmospheric distortions such as cloud cover and precipitation. In the ice classifications of Chapter 6, six days of data are used to produce the SSM/I images. Consequently, the effects of transient atmospheric phenomena are significantly reduced. However, for one day image reconstruction, this is not the case. While the methods presented in Chapter 4 are designed to remove distorted measurements, one day does not provide enough SeaWinds data for the technique to be effective. For similar reasons, the SSM/I 22V channel is also excluded. This frequency is at a region in the microwave spectrum for which atmospheric absorption due to water vapor is unusually high [29]. Without the temporal averaging of a longer imaging interval, the 22V reconstructed imagery have significant atmospheric corruptions that may cause classification errors.

7.2.2 Principal Component Imaging of SeaWinds-SSM/I Data

The resulting ice classification data set consists of two SeaWinds parameters (A_v^{54} and A_h^{46}) and four SSM/I parameters (19V, 19H, 37V, and 37H). Thus, the

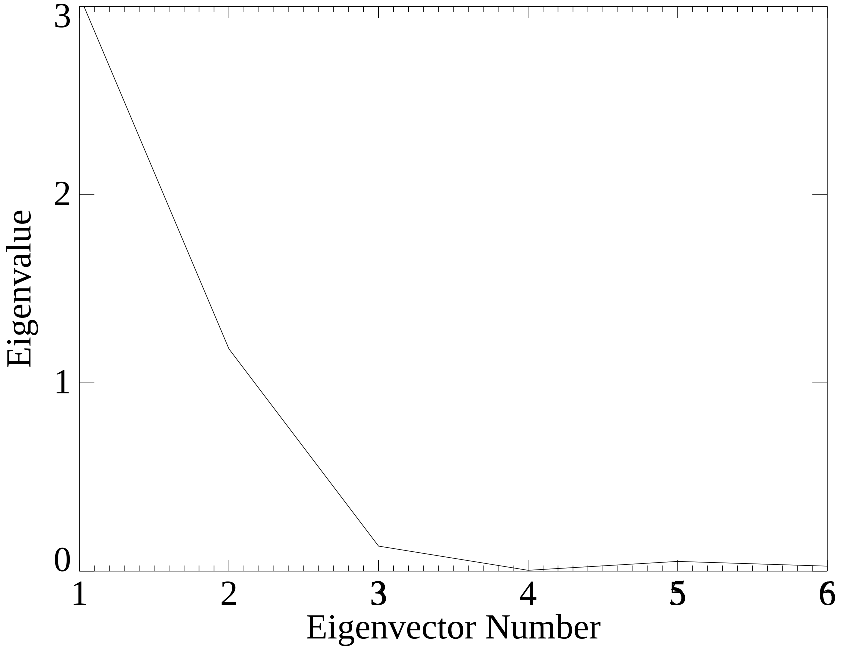

Figure 7.14: Eigenvalue spectrum for the SeaWinds-SSM/I Antarctic data set during 1999 day 200.

sea ice observations reside in a six-dimensional space. The dimensionality of the data space is reduced using principal component analysis (PCA). The PCA eigenvalue spectrum contains the variances spanned by the associated eigenvectors. A sample SeaWinds-SSM/I spectrum for 1999 day 200 is shown in Figure 7.14 which can be compared with a similar spectrum in Figure 6.3. The plot demonstrates that the top few principal components span a large majority of the variance in the data. In fact, 98% of the data variance is contained in the top three components. Consequently, the lower three components are discarded in the classification.

Figure 7.15 shows an RGB composite image of the top three principal components. The red, green, and blue images are the first, second, and third components, respectively. This image illustrates the ability of the three-dimensional data set in identifying sea ice types. Day 200 represents a period before which residual perennial ice from the last season's melt is completely swept out of the Weddell Sea. Remaining

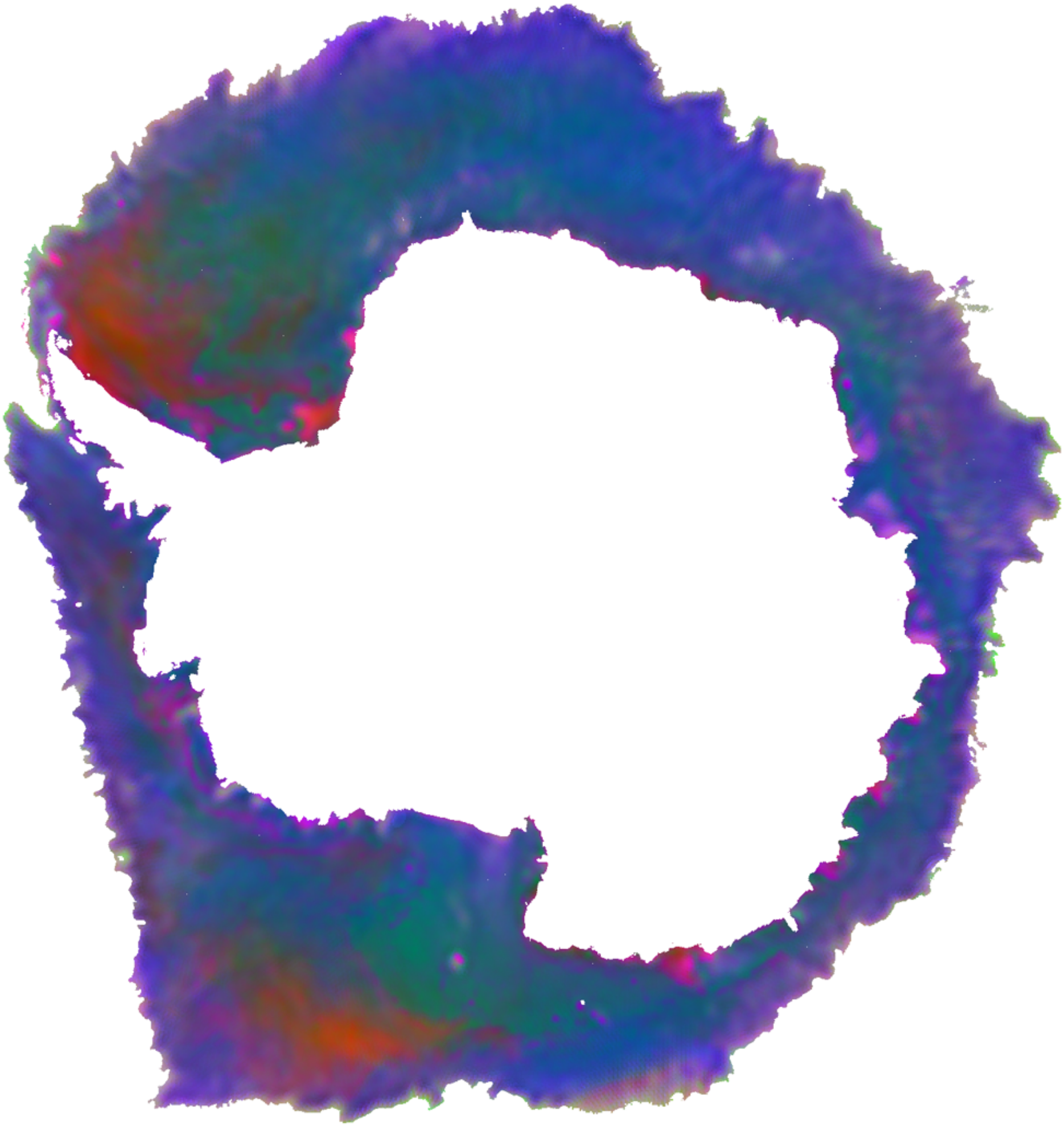

Figure 7.15: RGB composite image of the first three principal components for 1999 day 200. The red channel is the top principal component image, the green is second, and blue is third. This image is useful in evaluating ice type information contained in the top three PCA scores.

perennial ice east of the Antarctic peninsula can be observed in the RGB image in orange hues. Pancake ice regions in the outer Ross Sea have a similar orange signature indicating the inability of the data set to differentiate between these two types. The loss of the σ^o incidence angle dependence, ERS-2, and SSM/I 22 and 85 GHz parameters appears to have impeded the ability to distiguish between these types. Accordingly, perennial and pancake ice forms are considered the same type for the implementations discussed in the following section.

Other ice types can also be identified in Figure 7.15. Ice bergs and ice shelves appear as bright pink regions. An example is the large ice berg, A22, northeast of the tip of the peninsula. Smooth first year ice is evident in regions of green and blue-green while rougher first year ice is shown as darker shades of blue. Finally, gray regions denote the marginal ice zone and large polynyas.

7.2.3 Ice Classification Results

The three-dimensional principal component data space contains various clusters representing different ice classes. These clusters can be segmented using the *maximum a posteriori* (MAP) methods presented in Chapter 6. The recursive MAP ice classification algorithm is implemented with several sample SeaWinds-SSM/I image sets to identify five general ice types: ice bergs (IB), perennial/pancake ice (PER/PNC), rough first year ice (RFY), smooth first year ice (SFY), and the marginal ice zone (MIZ).

Ice classifications are performed for 1999 day 201, 203, and 205 to show short-term changes in the ice pack. The resulting Antarctic ice classification maps are shown in Figure 7.16. The images reveal that the classification has moderate success in identifying the spatial distribution of sea ice types. For example, residual perennial ice is located in the Western Weddell Sea as it is slowly swept out to sea by the Weddell Gyre. Ice berg A22 as well as several grounded ice bergs near the eastern extent of the Ronne ice shelf are correctly identified. The rough first year ice regime surrounds the smooth first year ice area. This result is consistent with the findings in Chapter 6 and [73]. Areas labeled as marginal ice zone are primarily located at

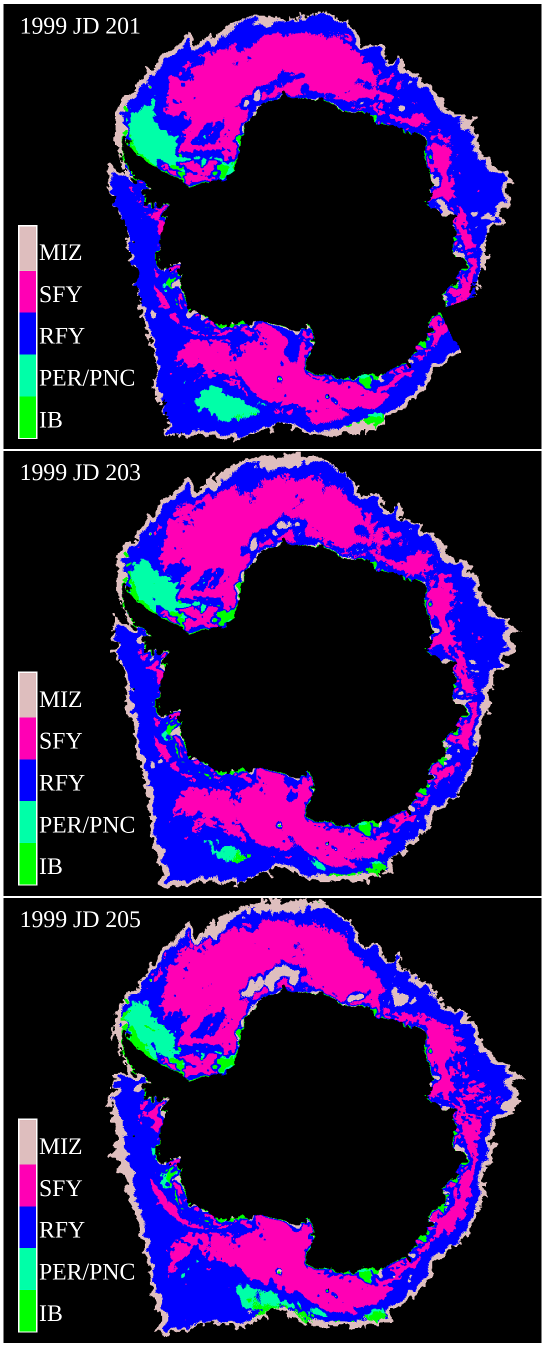

Figure 7.16: MAP ice classification of the image series for 1999 days 201, 203, and 205.

the periphery of the ice pack as expected. A few exceptions are evident in polynya regions within the ice pack. Since polynyas have characteristics very similar to the MIZ, the algorithm appears to chosen correctly in these regions. In fact, the image series illustrates the rapid formation of large polynyas north of New Schwabenland.

Unfortunately, errors are also evident in the classification. For example, in the latter two images, significantly large regions are classified as ice bergs just east of the Antarctic peninsula and in the outer Ross Sea. This error indicates that the clusters for IB, PER, and PNC have significant overlap in the data space. Through the image sequence, the clusters get increasingly confused by the algorithm. Since this phenomenon did not occur in the NSCAT-ERS2-SSM/I data set of Chapter 6, it is concluded that the error is due to excluding the previously discussed parameter sets (ERS-2 A, SSM/I 22V, 85V, and 85H) and the lack of incidence angle dependence parameters (B_v and B_h).

The conclusions of Chapter 6 included a brief discussion about extending the current method to a fuzzy classifier which estimates percentages of ice type. This allows for the estimation of ice type concentrations in each pixel rather than assign each pixel exclusively to a single class. Using SeaWinds data, a first step in this direction is taken using the current methods. Instead of ice type concentrations, the following method provides the spatial distributions of MAP probabilities for each ice type. That is, each pixel contains the estimated MAP probability that it belongs to a particular ice type cluster. This is obtained from the MAP distance metric in Eq. (6.12). Hence, an image is produced for each ice type.

Sample fuzzy classification images for 1999 day 200 are shown in Figure 7.17. In this case, a six-cluster classification was performed (PER and PNC types are considered separately). The image illustrates the transitional regions between different ice types. The transition from one ice type to another is expected to occur relatively gradually rather than in the distance of a single pixel as predicted by the hard classification. In order to increase the utility of these products, more research is needed to relate the MAP probabilities to ice type concentrations. Without significant amounts of *in situ* data, this portion of the study must be left to future studies.

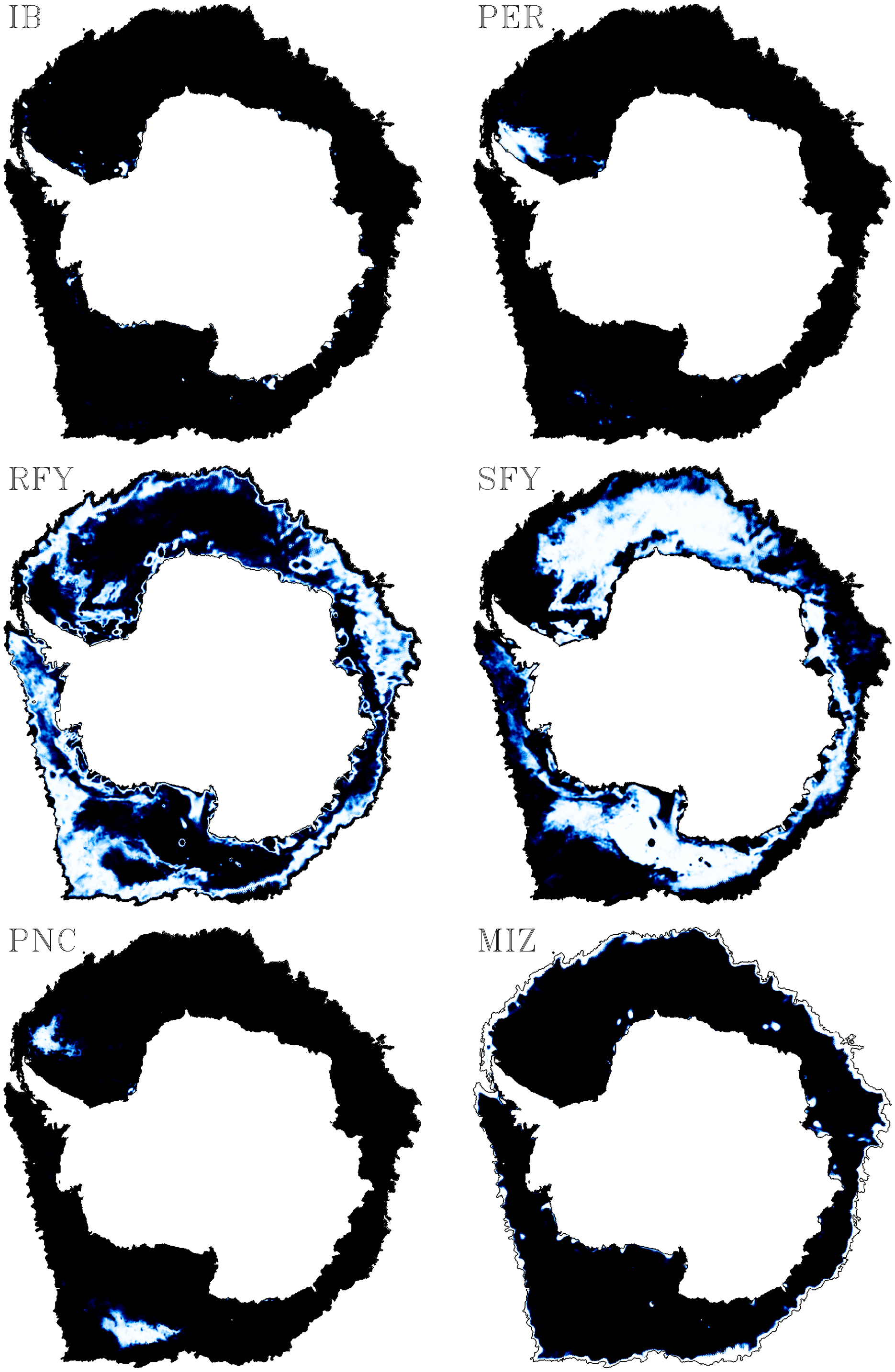

Figure 7.17: Fuzzy classification results for 1999 day 200. The images contain the MAP probabilities of ice type membership. Light values denote high probability while black is low.

7.2.4 Ice Classification Conclusions

This study has presented results from the application of the ice classification algorithm derived in Chapter 6 to current data sets which include SeaWinds scatterometer imagery. The SeaWinds one day imaging interval precluded the use of ERS-2 data as well as SSM/I 22 and 85 GHz channels. While the resulting classifications demonstrated a moderately good segmentation of various ice types, classification errors are noted which are attributed to the parameter exclusion.

A first step toward fuzzy classification is also considered in the study. This allows for the estimation of ice type concentrations and allows for a greater understanding of sea ice type dynamics and evolution. Resulting images illustrate the MAP probability that each pixel belongs to a particular ice class. Since the MAP distance metrics have not been conclusively related to ice concentrations, more research is needed in this area.

Chapter 8

Large Scale Ku-band Backscatter Inverse Modeling

8.1 Introduction

The primary goal of cryosphere remote sensing is the extraction of key sea ice surface characteristics from the observed signatures. Preceding chapters have addressed the estimation of critical sea ice characteristics such as sea ice extent and ice type. The various sensors used in the studies each contributed in different ways to improve estimate quality. In this chapter, the theory and methods for the extraction of other important surface parameters are presented. In particular, surface characteristics closely related to microwave scattering mechanisms are estimated based on the inversion of a well established forward scatter model. The research described in this chapter has been submitted to the *Journal of Geophysical Research* and is currently in review.

Several satellite instruments have proven the utility of scatterometers in monitoring the Arctic and Antarctic regions. The first was the Seasat-A scatterometer (SASS). Though the SASS mission was short, SASS data illustrated that Ku-band measurements are sensitive to the presence of sea ice and show valuable variations within the ice pack that relate to surface features [2, 14, 15, 16]. Later, the AMI scatterometers aboard the European Remote Sensing Satellites (ERS-1 and ERS-2) demonstrated the value of C-band active scatterometer data in monitoring sea and glacial ice regions [9, 14, 18]. The NASA scatterometer (NSCAT) flew aboard the Advanced Earth Observation Satellite (ADEOS) platform from approximately August 1996 through June 1997. Ku-band NSCAT data have been used in a number of cryosphere studies [4, 8, 14, 26]. When the NSCAT mission was prematurely terminated due to a solar panel failure, the NASA-built SeaWinds instrument aboard QuikSCAT filled the gap of active Ku-band data in mid-1999. SeaWinds data is used to monitor sea ice extent [80].

The described instruments have produced a large set of active multi-frequency, dual-polarization microwave scatterometer measurements of sea ice spanning many years. These observations can be interpreted through accurate backscatter modeling. Forward scattering models have been developed to relate key surface parameters to these observed signatures. Many critical sea ice parameters are of interest to the field of cryosphere remote sensing [81]. Several studies have sought to extract information about the surface from observed signatures. For example, the NASA Team algorithm was developed to estimate sea ice concentration from passive radiometer data collected by the Special Sensor Microwave/Imager (SSM/I) [31, 36]. Various studies have developed methods for extracting sea ice type and extent from single and multisensor data sets [8, 9, 62, 69]. Model inversion techniques have also been employed to determine the scattering components reponsible for observed microwave signatures [2, 74]. While directly estimating the parameters mentioned can be difficult, this study proposes a step in this direction through a better understanding of large-scale sea ice scattering properties. Rather than deal with small-scale ice characteristics, a simplified modeling approach is adopted to infer key electromagnetic scattering characteristics. These are, of course, related to the desired physical properties of the sea ice.

Thus, this chapter describes the development and implementation of a large-scale model inversion methodology based on a simple forward scattering model. The goal of the study is to provide an automated means for the inversion of microwave scattering models over vast regions rather than small individual homogeneous regions. The resulting sea ice parameter maps allow for interpretation of the evolution of scattering mechanisms over the entire cryosphere. The chapter is organized as follows: In the next section, the necessary background information is presented. Sea ice scattering is discussed along with variable order image reconstruction of NSCAT data.

In Section 8.3, forward electromagnetic modeling of sea ice backscatter (σ^o) is considered. The model used for the large-scale inversion is described along with the associated surface parameters. Section 8.4 presents the inversion method and discusses its strengths and weaknesses. Next, in Section 8.5 simulations are described to gauge the capability of the technique to extract surface ice characteristics from noisy measurements. The method is implemented using NSCAT data in Section 8.6 to produce imagery of surface parameters over a temporal series during the early portion of the NSCAT mission. Various phenomenon observed in the Antarctic and the Arctic are analyzed using the model inversion products. Last, conclusions are given.

8.2 Variable Order NSCAT Image Reconstruction

Microwave σ^o signatures of sea ice contain important information about surface characteristics. The goal of inverse modeling is to extract or estimate those parameters from σ^o measurements. The observed signatures are also a function of instrument design and measurement collection specifications such as frequency, polarization, and incidence angle. In previous chapters, data collected by NSCAT has demonstrated its sensitivity to sea ice features. In this section, the reconstruction of variable order NSCAT imagery is considered. These images function as inputs to the inverse model of Section 8.4.

Multiple NSCAT passes over the polar regions are used to reconstruct σ^o imagery. To improve the nominal resolution of NSCAT measurements, resolution enhancement algorithms can be applied to generate images. These methods rely upon a parameterization of the dependence of σ^o on incidence angle. Chapter 3 discussed the generation of scatterometer imagery based on a linear (first-order) σ^o vs. θ model. However, in an effort to more accurately represent this dependence, various higher order models can be used with increasing sensitivity to noise as order is increased. In general, σ^o (in dB) can be modeled with by

$$\sigma^\circ(dB) = A + B(\theta - 40^\circ) + C(\theta - 40^\circ)^2 + D(\theta - 40^\circ)^3 + \ldots \tag{8.1}$$

where θ is the incidence angle, A is σ^o normalized to 40°, B is the linear incidence angle dependence of σ^o, C is the quadratic incidence angle dependence of σ^o, and so forth. Equation (2.2) is a special case of the generalization in Eq. (8.1) above. Though, NSCAT σ^o is found to have a nearly linear dependence on θ for a limited range of incidence angles (20°-60°), higher order models can be used to more accurately represent the dependence though the higher coefficients become increasingly sensitive to noise.

Several reconstruction methods exist for the generation of scatterometer imagery. For this study a polar stereographic projection was used in all image products. The first reconstruction method consists of binning σ^o measurements into 22.25 x 22.25 km grid cells. For each cell, a polynomial fit of a chosen order is applied to model the θ dependence of σ^o. Hence N+1 binned images are produced where N is the polynomial order. Since the nominal NSCAT resolution is 25 km, this technique does not improve measurement resolution but is less prone to reconstruction artifacts and noise.

The AVE algorithm (see Chapter 3) is another reconstruction technique for scatterometer image production [39]. Like the binning method, a polynomial fit is used for each pixel to estimate the pertinent coefficients. However, the AVE method uses a higher resolution 4.45 x 4.45 km grid and produces images with an effective resolution of 12-15 km. For a particular pixel, the polynomial fit measurement set consists of all the measurements whose spatial footprint response include that pixel. AVE images are produced for each polynomial coefficient. Sample ice masked AVE images of the Antarctic during 1996 day 270-275 are shown in Figure 8.1 in which a second order model was employed. The images are ice masked using an NSCAT-derived method described in [8]. Significant detail relating to surface parameters is evident in varying A, B, and C pixel values. The images also demonstrate that higher order terms are increasingly sensitive to measurement and reconstruction noise.

The final image reconstruction method is the scatterometer image reconstruction (SIR) algorithm [39] as described in Chapters 2-3. SIR is a modified multivariate multiplicative algebraic reconstruction technique which uses multiple passes of a satellite instrument to increase spatial resolution. Like the AVE algorithm, a

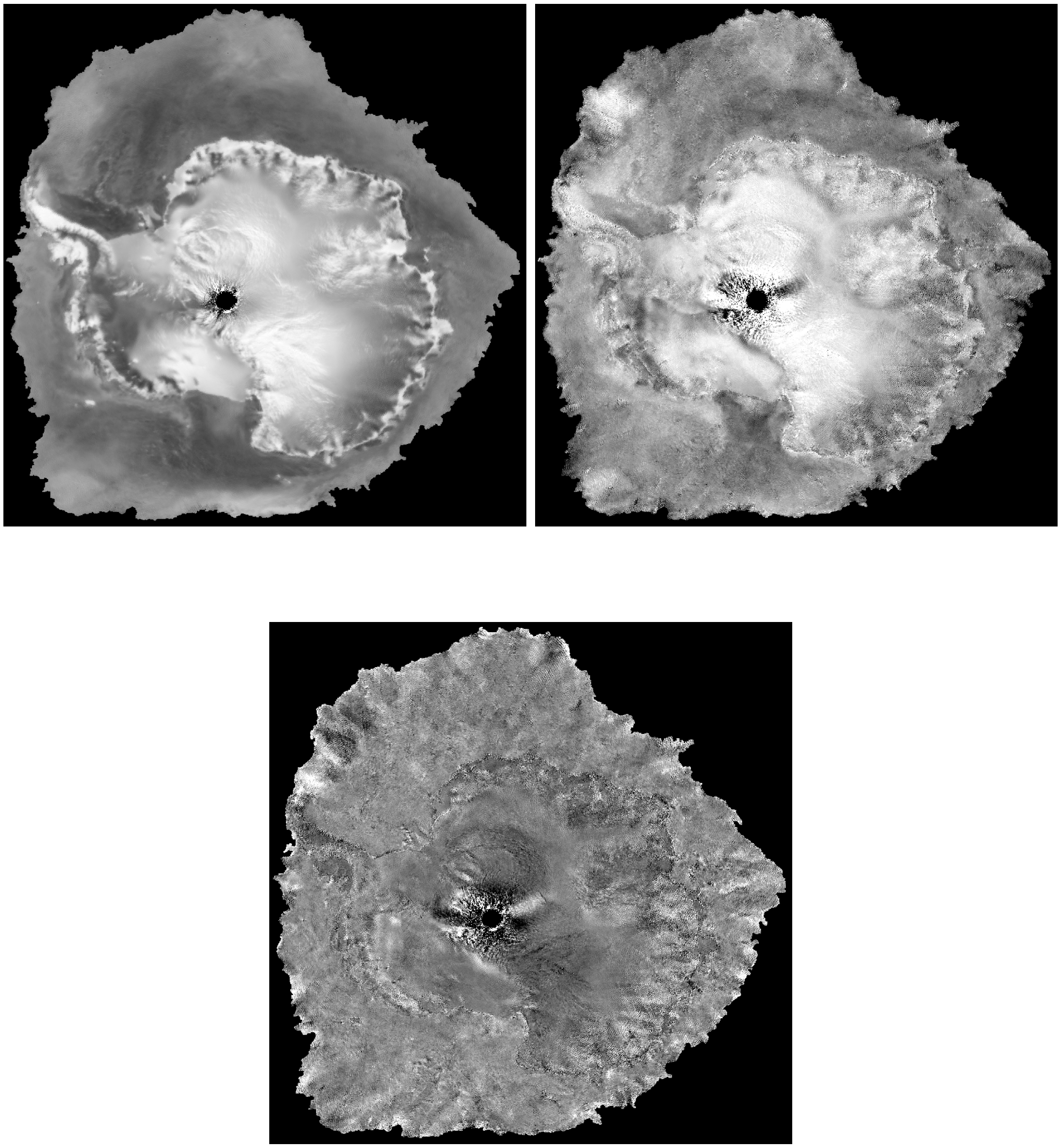

Figure 8.1: Sample ice masked NSCAT AVE v-pol imagery for 1996 days 270-275. The images are, from top left, A_v, B_v, and C_v, respectively. The original images contain 1940 x 1940 pixels with a nominal pixel spacing of 4.45 km.

4.45 km nominal pixel spacing is used. SIR reconstructed images produce an effective resolution of approximately 10 km instead of the nominal 25-50 km resolution of the instrument [40]. SIR results in increased reconstruction artifacts as well as increased resolution. For this reason, only the first order σ^o vs. θ model is used for SIR imagery.

Each of the described reconstruction algorithms have inherent strengths and weaknesses. The binning images have the lowest resolution, but less noise in higher order coefficients. The AVE images have medium resolution also with lower noise levels. The SIR reconstructed images have the highest resolution but are more sensitive to noise in the high order coefficients. For the Antarctic and Arctic regions, all of these methods require 6 days included in the image generation to achieve full v- and h-pol coverage with a range of incidence angles in each pixel. Ice motion during the imaging interval can cause blurring in the final image products particularly in the AVE and SIR images.

8.3 Large-scale Forward Modeling of Sea Ice Backscatter

Forward models of sea ice backscatter have been developed which predict σ^o as a function of incidence angle and important surface parameters. Various sea ice characteristics affect observed signatures. For example, surface roughness reduces specular reflections and increases backscatter. Geophysically, this parameter is important in modulating wind sheering forces on the ice pack and can be an indicator of internal stresses. Liquid water content also influences backscatter signatures. Increased water content results in less penetration by incident microwave pulses. Hence, the backscatter is dominated by the surface scattering response. Snow cover adds another layer to the multilayer structure. Very dry snow appears electrically transparent at many microwave frequencies. However, as snow liquid water content increases, the sea ice signature is increasingly masked. In addition, sea ice salinity plays a role in determining backscatter responses. Brine pockets increase the effective permitivitty and provide volume scattering elements. Since brine pockets are commonly ellipsoidal in shape, the orientation of these inclusions influence the σ^o polarization response. Both snow cover and brine pocket distribution are closely related to sea ice age. Older ice forms typically have greater accumulated snow cover. Also, sea ice aging results in increased brine drainage. Volume scattering air bubbles often remain in the place of old brine inclusions.

A better understanding of scattering from sea ice enhances the ability to estimate geophysical parameters through inverse modeling. Current research in the field has focused on mathematically modeling the complex process of scattering from sea ice on small scales as a function of the previously described parameters. The complexity is due in part to the anisotropic nature sea ice permitivitties. A particular source of anisotropy is the vertically oriented brine pockets caught within the ice crystal lattice. In addition, sea ice is a multilayer medium with rough surface and volume scattering contributions to the backscatter signature. Multilayer anisotropic scattering models have been proposed using a dyadic Green's function as well as the first-order Born approximation to predict backscatter coefficients [82]. Tjuatja et al. developed a scattering model for snow-covered sea ice using radiative transfer theory [83]. While several radiative transfer techniques have been proposed in the past, Tjuatja's model is considerably more robust by accounting for non-Rayleigh particle sizes and close spacing between scatterers. An example of sea ice forward scatter modeling is the work of Nghiem et al. [84] in which a polarimetric backscattering model is derived. Nghiem relates ice, brine, air, and salinity properties to backscatter signatures.

Two primary factors limit the use of such models in large-scale inversion studies. First, these models assume the region of interest has relatively homogeneous scattering properties. Some randomness is allowed in the form of random surface height or other parameters with specified variances but, in general, the region is considered to be spatially homogeneous. This may be appropriate for SAR imagery where the resolution is a few tens of meters, but scatterometer footprints have 5-50 km resolution and thus can often cover very heterogeneous regions. Also, the detailed models are very computationally complex. Inversion of the models on large fields of measurements is not computationally feasible. Consequently, a model for use at the lower resolution found in scatterometer imagery must be based on more general, average, large-scale parameters. Computational complexity of the forward model must be simple enough to allow for inversions of large data sets in relatively short time frames.

One such simple model assumes that sea ice scattering consists of incoherently summed surface and volume scattering responses [85, 86, 87],

$$\begin{aligned} \sigma_m^\circ &= \sigma_s^\circ + \sigma_v^\circ \\ \sigma_m^\circ &= \sigma_s^\circ + t^2\left(\frac{n\sigma_b}{2\alpha}\right) cos\theta_i \end{aligned} \tag{8.2}$$

where

σ_m° measured σ^o,
σ_s° surface scattering σ^o,
σ_v° volume scattering σ^o,
θ_i measurement incidence angle,
t plane wave power transmission coefficient at $\theta = \theta_i$,
n number density of subsurface scatterering elements,
σ_b σ^o per particle,
α volume attenuation coefficient.

This bulk model does not require a detailed description of the ice medium. Instead, several large scale parameters are used to represent the mean response in the region of interest. Following Swift [86] three primary volume scattering parameters are combined into one variable, the volume scatter albedo given by

$$\eta = \frac{n\sigma_b}{\alpha}. \tag{8.3}$$

Though it is a general parameter, η is related to sea ice features such as the number of volume scattering brine pockets and air bubbles. It is also sensitive to the effective permitivitty of the sea ice layers below the surface. Highly saline brine pockets have higher σ_b than air bubbles resulting in greater η values for the same number density, n.

This simple volume scattering model assumes only single scattering. While multiple scattering certainly occurs in a sea ice medium, the model assumes these are

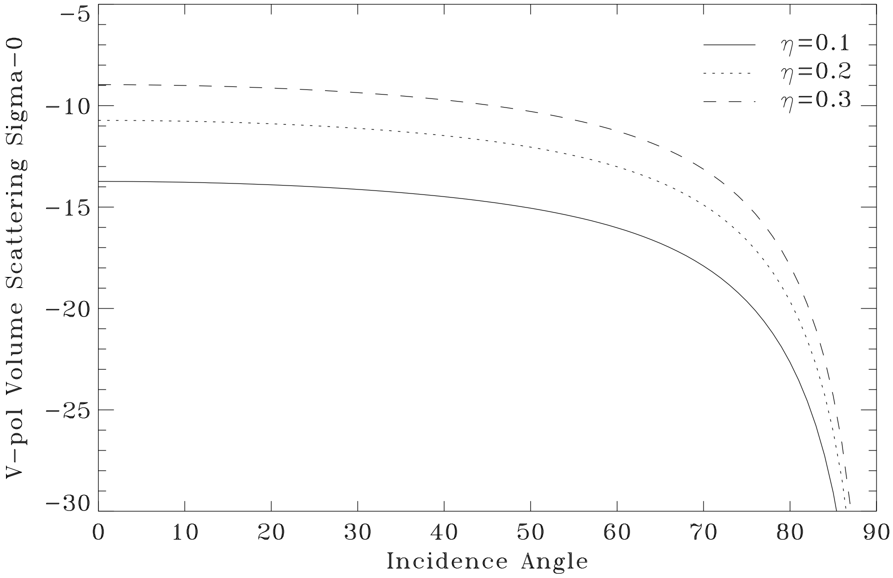

Figure 8.2: Model generated volume scattering v-pol σ^o responses vs. incidence angle. Various volume scattering albedo values are used to show the σ^o dependence on η.

negligible compared to the direct backscatter response. Figure 8.2 shows v-pol volume backscatter as a function of incidence angle for various η values. The signatures exhibit low dependence on incidence angle. As η increases, the level of σ^o also rises. Volume scattering occurs primarily in ice types containing numerous inhomogeneities and low loss such as multiyear ice. Snow layers containing crystallized structures can also result in strong volume scattering contributions. Hence, in the model inversion, multiyear ice forms are expected to have relatively high η when compared with younger ice types such as first year ice.

Surface scattering is also an integral component of the backscatter model. Assuming that the surface can be modeled as an ensemble of reflective facets with Gaussian slope distributions, a geometric optics solution can be used [86, 88] so that,

$$\sigma_s^\circ = \frac{r(0)e^{-tan^2\theta_i/2S^2}}{2S^2cos^4\theta_i}, \tag{8.4}$$

where

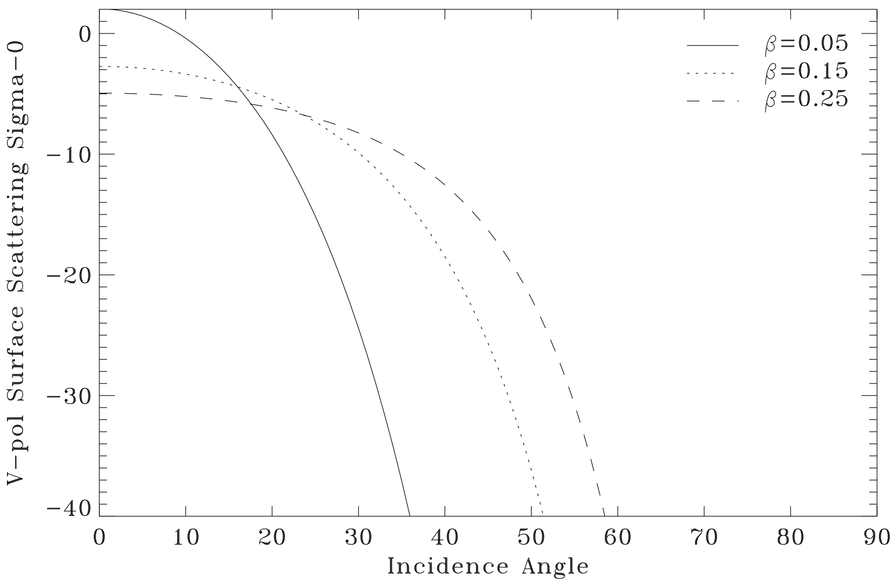

Figure 8.3: Model generated surface scattering v-pol σ^o responses vs. incidence angle. The parameter β is related to RMS surface slope and is defined in the text. For these plots, the reflectivity, $r(0)$, is 0.08 corresponding with a dielectric constant of 3.2.

$r(0) = 1 - t(0)$	surface power reflection coefficient at nadir,
S	RMS surface slope.

The geometric optics solution is derived under the assumption that the wavelength is significantly smaller than the typical roughness dimensions. At 14 GHz, the corresponding wavelength is approximately 2.1 cm. Hence, the model accounts for roughness features which are much larger than this, while smaller roughnesses may not be fully accounted for in the model. It is expected that large surface roughness due to wave action and ice pack sheering forces are within the bounds of this assumption. However, very small-scale roughness due to such phenomena as wind roughening and small surface inhomogeneities are not accounted for in the model.

For the purposes of this chapter, a new parameter is defined, $\beta = 2S^2$, to simplify the model inversion. Figure 8.3 illustrates the theoretical v-pol scattering responses for various values of β. The plots show that as surface slope increases, the σ^o response broadens in incidence angle. For very smooth surfaces, a significant portion of the response occurs below 20° incidence. Since 20° is used as the lower cutoff for the NSCAT measurements used in the image reconstructions, it is expected that the inversion will have limited capability in accurately identifying very low β.

At Ku-band, surface scattering dominates young and first year ice responses which have relatively high water and brine content. These types have significant conductivity and, hence, high loss. Surface melting masks lower level volume scattering and creates greater relative dependence on surface scattering contributions. Inverse modeling of σ^o images should result in relatively high β in regions of significant surface deformation and low values over smoother ice forms.

The two fundamental parameters in the surface scatter model, $r(0)$ and β, are both related to important surface features. The Fresnel reflectivity coefficient, $r(0)$, is directly related to the effective permitivitty of sea ice. It has been shown that lossless sea ice permitivitties are roughly between 3.0 and 4.5 [85, 89] in the Ku-band portion of the spectrum resulting in $r(0)$ values within the range of 0.072-0.13. However, the forward model assumes that the sea ice is lossless. While this applies reasonably well for older ice forms such as ice bergs and multiyear ice in winter, internal water content or surface melt introduces conductivity and loss to the medium. Hence, dielectric constants should not be directly computed from estimates of $r(0)$ derived from the inverse model described in the following section. Nevertheless, $r(0)$ can be used to obtain a general idea of effective relative permitivitties throughout the ice pack.

Figure 8.4 shows the total scattering v-pol responses for sample $r(0)$, β, and η values. The plots illustrate that the theoretical σ^o vs. θ signatures can not always be fit with a linear approximation between 20° and 60°. A linear model is appropriate for plot (a), but (b) and (c) clearly require higher order terms to accurately represent the incidence angle dependence. In general, the linear dependence assumption does not fit well in scenarios with relatively low β values. Swift was able to fit such plots to SASS σ^o observations of multiyear ice in the Arctic [86], demonstrating the ability to invert the model and estimate the three fundamental parameters.

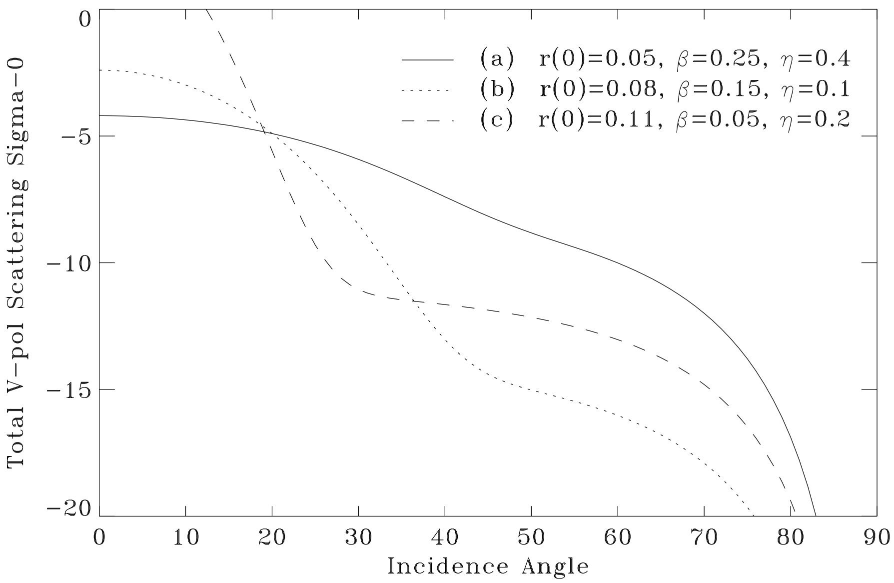

Figure 8.4: Model generated composite (volume + surface) v-pol scattering responses for sample combinations of $r(0)$, β, and η. The curves show the nonlinear nature of σ^o as a function of incidence angle.

The three forward model parameters ($r(0)$, β, η) can be used as proxy values in the interpretation of polar imagery. A close relationship is expected to exist between these values and sea ice type. Consequently, the parameter estimates can be used in ice classification efforts.

8.4 Model Inversion Methodology

The theoretical scattering model parameters, $r(0)$, β, and η can be estimated from observed NSCAT σ^o signatures given sufficient incidence angle sampling. In this section, an automated inversion technique is presented for determining the three parameters from NSCAT reconstructed imagery.

The inversion approach consists of the automated steepest descent optimization of an objective function. The objective function provides a measure of the error between observed signatures and estimated model parameters,

$$\begin{aligned} J(\sigma^\circ, r(0), \beta, \eta) &= \sum_{\theta_i=20}^{60} [\sigma^\circ(\theta_i) - \sigma^\circ_m(\theta_i)]^2 \\ J(\sigma^\circ, \vec{h}) &= \sum_{\theta_i=20}^{60} \Big[\sigma^\circ(\theta_i) - 10log_{10}\Big(\frac{r(0)e^{-tan^2\theta_i/2S^2}}{2S^2cos^4\theta_i} + t^2\Big(\frac{\eta}{2}\Big)cos\theta_i\Big)\Big]^2 \quad (8.5) \end{aligned}$$

where

J	total squared modeling error,
$\sigma^\circ(\theta_i)$	observed backscatter cross section at θ_i,
$\sigma^\circ_m(\theta_i)$	modeled backscatter cross section at θ_i
$\vec{h}$	vector of model parameters $[r(0), \beta, \eta]^T$.

Hence, $J(\sigma^\circ, \vec{h})$ is a measure of the accuracy of the model parameters in predicting the observed signature. The $\sigma^\circ(\theta_i)$ response is computed given the σ^o vs. θ variable order polynomial fit coefficients for a particular pixel in the reconstructed imagery. Since total squared error is a sufficient statistic for mean squared error, the inversion method is a minimum mean squared error technique.

In an effort to detemine the convexity of the objective function, J was computed for all parameter values in the ranges given in Eq. (8.10) for several sample σ^o signatures. The resulting objective function cube is then analyzed by observing multiple two-dimensional "slices" through the cube at various levels. These analyses indicate that the function has a well defined single minimum within the range of expected $r(0)$, β, and η. Hence, the optimal parameters are found at the $\vec{h}$ yielding minimum $J(\sigma^\circ, \vec{h})$.

One method of automated optimization of an objective function is the steepest descent approach. Steepest descent locates the minimum of a function in an iterative fashion through the estimation of the local slope. The slope is obtained from the partial derivatives of the objective function,

$$G(\sigma^\circ, \vec{h}) = \Big[-\frac{\partial}{\partial r(0)}J(\sigma^\circ, \vec{h}), \ -\frac{\partial}{\partial \beta}J(\sigma^\circ, \vec{h}), \ -\frac{\partial}{\partial \eta}J(\sigma^\circ, \vec{h})\Big]^T \qquad (8.6)$$

where $G(\sigma^\circ, \vec{h})$ is the direction vector. The partial derivatives in Eq. (8.6) are analytical functions of $\sigma^\circ(\theta)$, $r(0)$, β, and η given any location in the objective function.

Consequently, $G(\sigma^\circ, \vec{h})$ can be computed for any location vector $\vec{h}$ and points in the direction of steepest descent.

A recursive algorithm for computing the model parameters, and thus searching for the minimum of $J(\sigma^\circ, \vec{h})$ is given by,

$$\vec{h}(m+1) = \vec{h}(m) + \Delta(m) \odot G(m), \qquad m =, 0, 1, 2, \ldots \tag{8.7}$$

where

Δ	vector of step sizes for each model parameter,
$\odot$	Schur element by element vector product operator.

The step size Δ can be chosen in a number of ways. Steepest descent algorithms often use step sizes that are a function of the objective function. Hence, smaller steps are taken closer to the minimum. For this study, a fixed step size is used,

$$\Delta = [0.001,\ 0.002,\ 0.002]^T \tag{8.8}$$

yielding model parameter estimate resolutions of 0.001, 0.002, and 0.002 for $r(0)$, β, and η, respectively.

The algorithm is initialized with arbitrary $\vec{h}(0)$. Simulations indicate that the minimum is found as long as $\vec{h}(0)$ is in the range of possible sea ice parameter values. For a given image set of polynomial fit coefficients, the algorithm is run for each pixel. The resulting products are images of $r(0)$, β, and η used in determining the spatial distribution of important surface parameters.

The algorithm has various strengths that make it useful in model inversion. First, the proposed algorithm is fully automated. Many previous inverse modeling studies focusing on fitting observed and forward modeled signatures have relied on user interaction to manually perturb the model parameters until a satisfactory match is obtained. The technique presented in this chapter requires no user interaction and quickly estimates model parameters given an observed σ^o vs. θ response. This facilitates the production of model parameter image sequences from scatterometer imagery. In addition, if the the σ^o incidence angle dependence model is sufficient (of

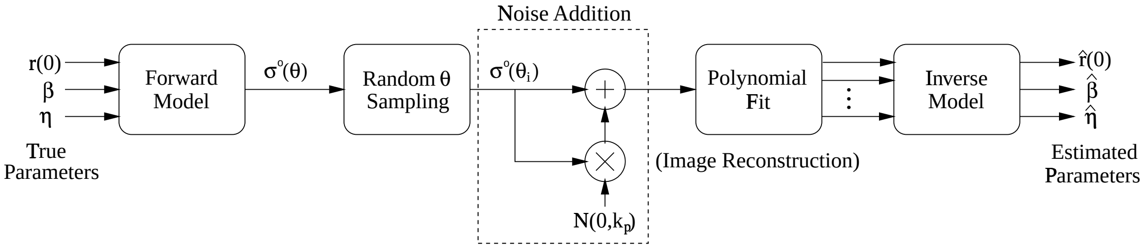

Figure 8.5: Flowchart illustrating the inverse model simulation process.

high enough order) the algorithm finds the best parameters in the minimum mean squared error sense.

The estimated parameters provide, in effect, the mean responses over the pixel region. These are useful on a macroscopic level when viewing entire sea ice packs. However, the products of the inversion technique have limited utility on very small scales. Because the model is based on a specific forward model, the quality of the resulting parameter estimates are directly related to the quality of the original forward model. Some error is expected since the forward model does not account for such things as complex sea ice permitivitties and small-scale roughness features.

8.5 Inverse Model Simulations

To evaluate the capability of the inversion technique, simulations are designed and implemented. The simulation methodology is outlined in Figure 8.5. First, the "ground truth" model parameters $r(0)$, β, and η are run through the forward model to produce a σ^o vs. θ response. This signature is then sampled in incidence angle between 20° and 40° to simulate scatterometer measurement collection. At this point, Monte Carlo scatterometer noise is added to each measurement using the noise model,

$$\sigma_n^\circ(\theta_i) = \sigma^\circ(\theta_i)(1 + N(0, k_p)) \tag{8.9}$$

where

$\sigma_n^\circ(\theta_i)$ noise-added σ^o at incidence angle θ_i,

$\sigma^\circ(\theta_i)$ original noiseless σ^o,

$N(0, k_p)$ normally distributed random variable with standard deviation k_p.

The noise-corrupted measurements are used to obtain polynomial fit coefficients. Variable degree polynomials are used to determine the effect of model order on the inversion. The coefficients are then input to the inverse model resulting in surface parameter estimates. Error analysis is performed with the original parameter values and the inverse model results.

For the purposes of illustration, model inversion is considered using the total scattering cases in Figure 8.4. The inverse model is first evaluated in the absence of noise with ideal incidence angle sampling consisting of samples at each degree from 20° to 60°. For each case, the simulation is implemented using polynomial fit orders from one to four to illustrate the algorithm's performance. The first case to be inverted is example (a) from Figure 8.4. Table 8.1 contains the resulting estimates for all three parameters using different reconstruction model orders. These values demonstrate that virtually all polynomial orders provide good estimates of the true values. Since the response is close to linear in the 20°-60° range which the inverse model considers, even the first order model performs reasonably well. Figure 8.6 shows a comparison of the true σ^o signature with the estimated signatures at each of the considered orders. The vertical lines at 20° and 60° incidence angle bound the range over which the signature matching is performed. The plots are virtually indistiguishable demonstrating the proper performance of the algorithm.

The case (b) inversion illustrates the inverse model's performance with nonlinearities in the true σ^o vs. θ signature. In Table 8.1 it is evident that the first-order model performs poorly. The β estimate is particularly erroneous. However, at order two and above, the estimates are close to the actual values. Figure 8.7 offers a graphical interpretation of the inversion case. The plots clearly show the poor performance of the first-order model values.

The true response in case (c) exhibits extreme nonlinearities. While such a case is not expected to be common, it is included to show the inverse model's performance in extreme circumstances. For this scenario, third or fourth order model

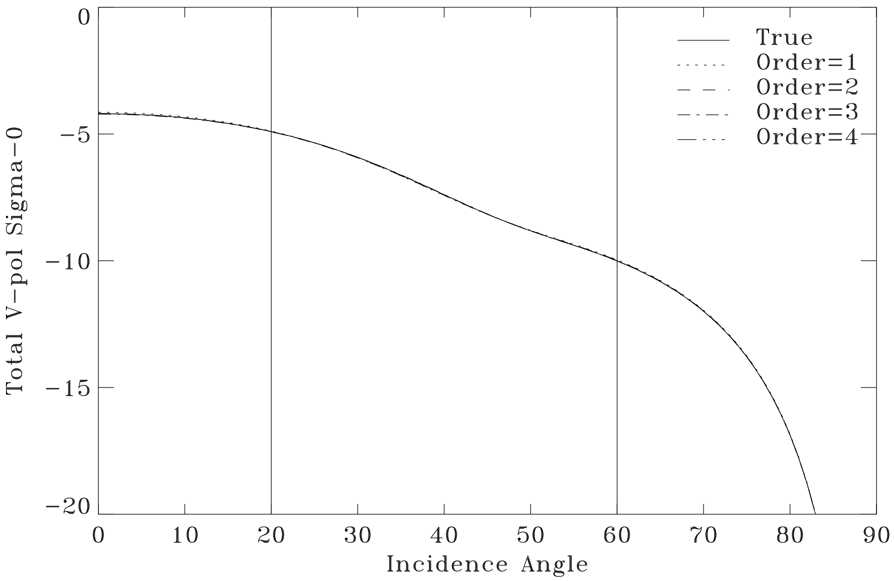

Figure 8.6: Comparison of inverse model-derived responses at various orders with the true response for case (a) in Figure 8.4.

coefficients are required as inputs to the inverse model to provide reasonable estimates of the surface parameters. Figure 8.8 illuminates the situation further. These plots show the difficulty encountered by first and second order inputs in matching the true signature. The sharp "elbow" in the response can only be accounted for by third or fourth order polynomial fits. A greater range of incidence angles included in the model would conceivably yield better estimates at all orders. Unfortunately, scatterometers like NSCAT do not collect measurements over such a broad range of viewing angles.

These three simulations demonstrate that the inverse model performs properly in the absence of noise given sufficient incidence angle sampling and satisfactory polynomial fit coefficient inputs. In actual scatterometer image reconstructions, such ideal incidence angle sampling is not common. For 6 day NSCAT images generated at the SIR and AVE spatial resolutions of 4.45 km, average pixel regions usually encounter at least 10 hits. Hence, for the remaining simulations, incidence angle sampling is performed randomly from a uniform distribution between 20° and 60°

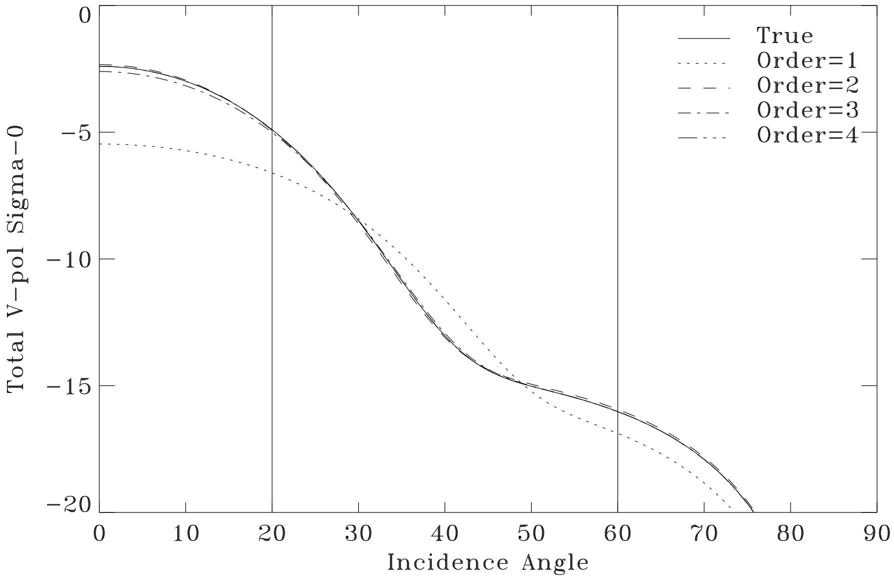

Figure 8.7: Comparison of inverse model-derived responses at various orders with the true response for case (b) in Figure 8.4.

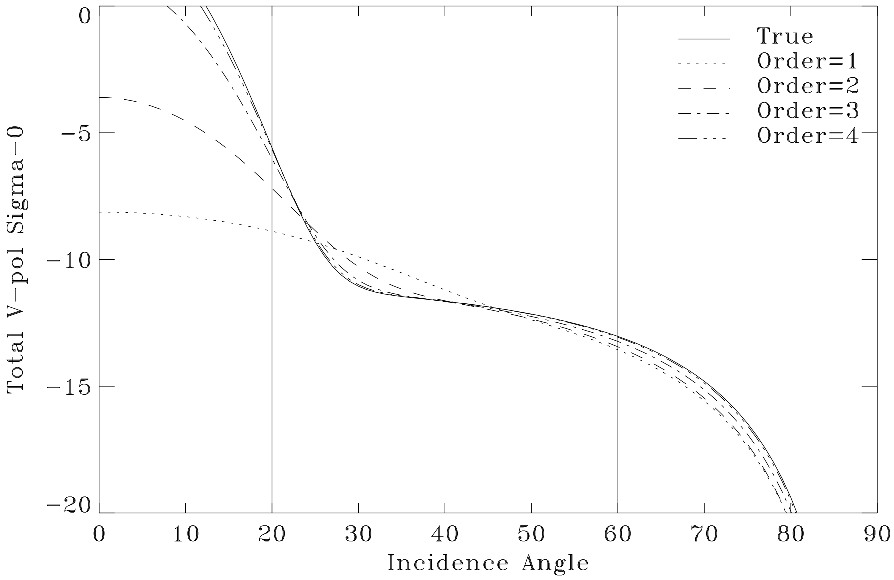

Figure 8.8: Comparison of inverse model-derived responses at various orders with the true response for case (c) in Figure 8.4.

Table 8.1: Inverse model simulation examples in the absence of noise and with incidence angle sampling at each degree in the range $\theta \in [20°, 60°]$.

	Case (a)			Case (b)			Case (c)		
	r(0)	β	η	r(0)	β	η	r(0)	β	η
True	0.05	0.25	0.4	0.08	0.15	0.1	0.11	0.05	0.2
Order=1	0.049	0.242	0.404	0.06	0.242	0.082	0.015	0.222	0.178
Order=2	0.049	0.246	0.402	0.079	0.146	0.102	0.033	0.094	0.182
Order=3	0.05	0.252	0.4	0.078	0.154	0.1	0.073	0.06	0.19
Order=4	0.05	0.25	0.4	0.08	0.15	0.1	0.101	0.052	0.198

with 10 samples for each realization. In addition, measurement noise is simulated using Eq. (8.9) and various k_p values. Typical NSCAT k_p levels are in the range 0 to 0.1. In fact, for the NSCAT Antarctic v-pol data collected from 1996 day 270 to 275, 97% of the k_p values are below 0.1 and 86% are below 0.05.

To offer more comprehensive simulations which consider a broad range of ($r(0)$, β, η) triplet combinations, synthetic "ground truth" images are constructed of each parameter that represent all possible sample combinations of the parameters within the ranges,

$$\begin{aligned} r(0) &\in [0.01, 0.3], \\ \beta &\in [0.05, 0.4], \\ \eta &\in [0.05, 0.4]. \end{aligned} \tag{8.10}$$

These values represent ranges which cover typical sea ice surface parameters. The images are generated using 25 evenly spaced samples of each parameter resulting in 25^3 combinations. Figure 8.9 shows the truth images which are used in the simulation process. Noise-corrupted polynomial coefficient images are simulated which become inputs to the inverse model.

The simulations are run using the incidence angle sampling described previously. Noise levels (k_p) are considered at 0.02 increments from 0 to 0.1. The results are summarized graphically in Figures 8.10-8.12. In Figure 8.10, the $r(0)$ estimates are shown with k_p values of 0, 0.04, and 0.08. The image frames demonstrate the

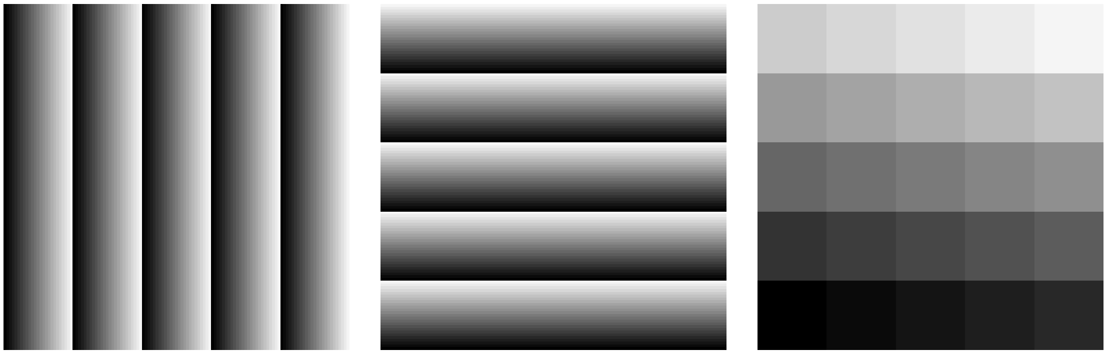
(a) $r(0)$ (b) β (c) η

Figure 8.9: "Truth" parameter images, $r(0)$, β, and η, used in the model simulations.

increasing ability of the algorithm to accurately represent the left-to-right increasing gradient as the model order increases. Nearly all images show that the algorithm has difficulty in areas corresponding with very low β values. As previously noted, extremely low β correspond to scattering responses that are primarily contained below the 20° incidence angle limit for NSCAT data. The images also exhibit that higher order models are increasingly sensitive to noise as evident by the speckling in the estimate frames. Thus, a trade off exists between ability to estimate parameters accurately (on average) and sensitivity to measurement noise.

The performance of the algorithm in estimating β is shown in Figure 8.11. The image panels reveal that first-order coefficients are not sufficient to accurately represent the surface roughness induced characteristics of the forward scattering model. The first-order frames are nearly constant in value. In contrast, the second to fourth-order models are much more successful in reproducing the upward β gradients in the truth image. Like $r(0)$, the β estimates are increasingly sensitive to noise as order increases.

Estimates of the final parameter, η, are shown in Figure 8.12. Similar trends with order exist for η estimates as with the previous two. The first-order

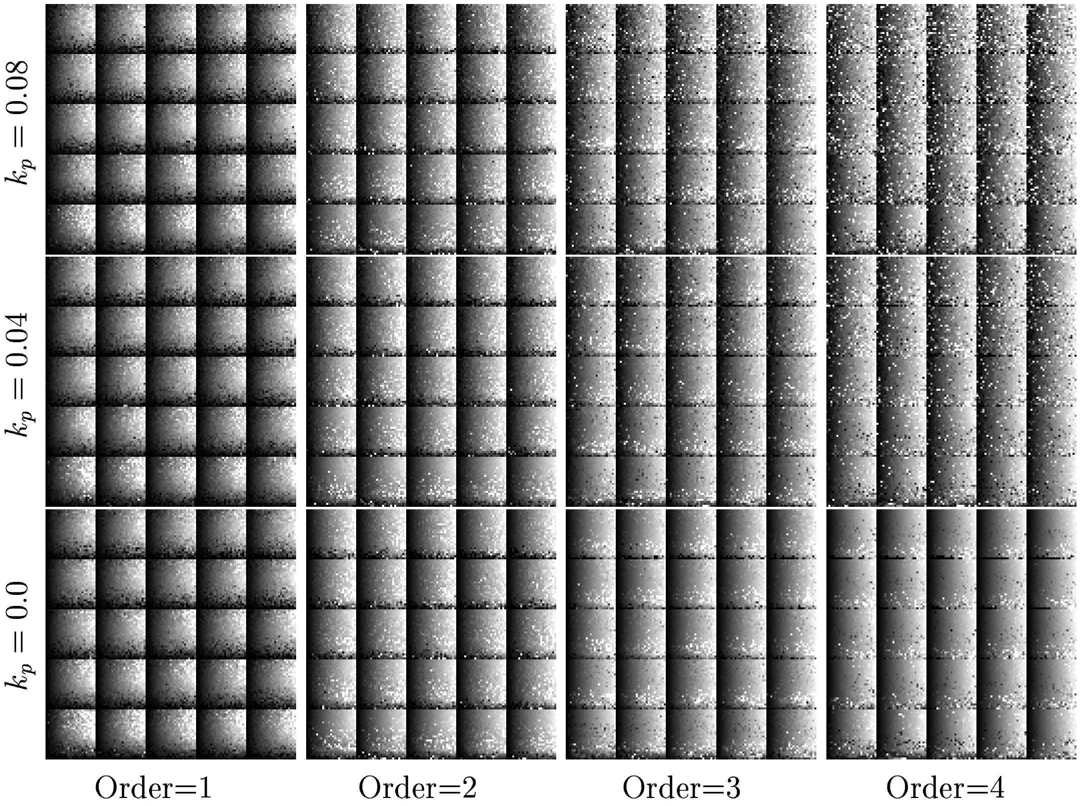

Figure 8.10: Inverse model $r(0)$ parameter estimates at various σ^o vs. θ model orders and noise levels.

model has difficulty generating the constant frames in the truth image. However, all of the higher order models appear to perform relatively well.

In order to provide a quantitative measure of algorithm performance over all the possible parameter combinations, the median absolute error is used. This metric is computed for each parameter as the median of the ensemble of absolute errors over the entire truth image. The estimate images have few very large errors caused by poor sampling or extreme noise. However, the few outliers can skew an average error metric. The median absolute error is used to reduce the confusing effects of theses outliers.

Figures 8.13-8.15 illustrate the error metric for the three forward scattering model parameter estimates as a function of k_p. All of the plots indicate that parameter

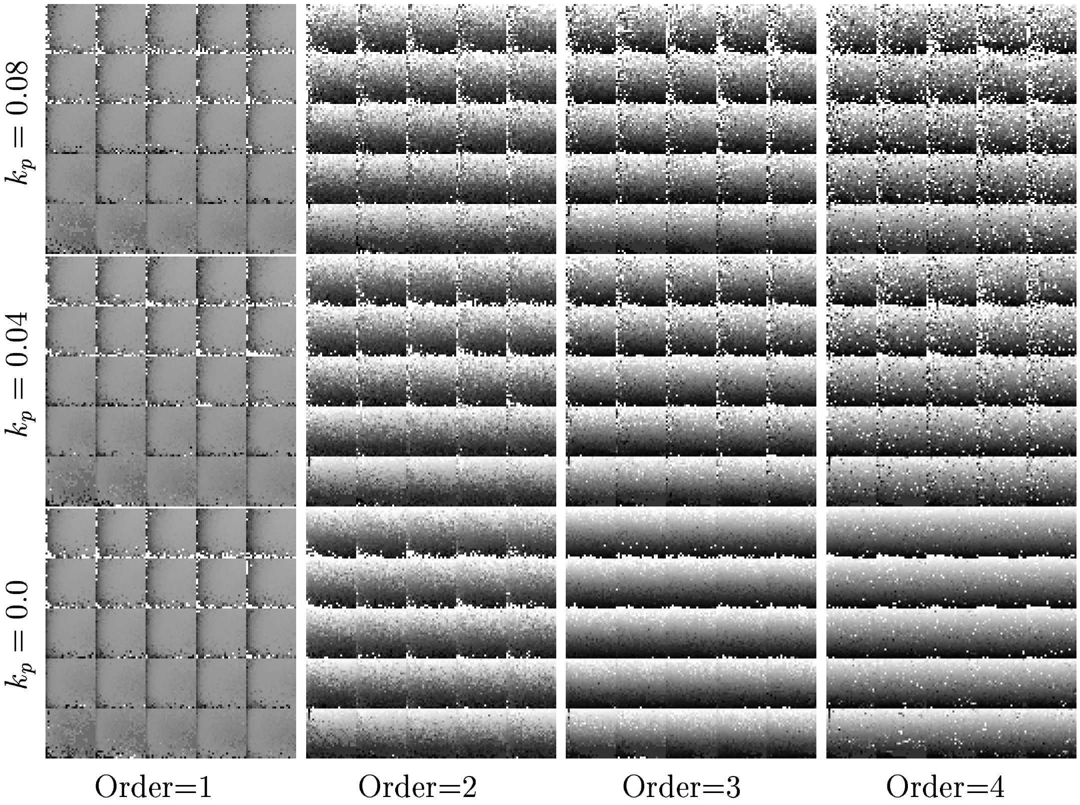

Figure 8.11: Inverse model β parameter estimates at various σ^o vs. θ model orders and noise levels.

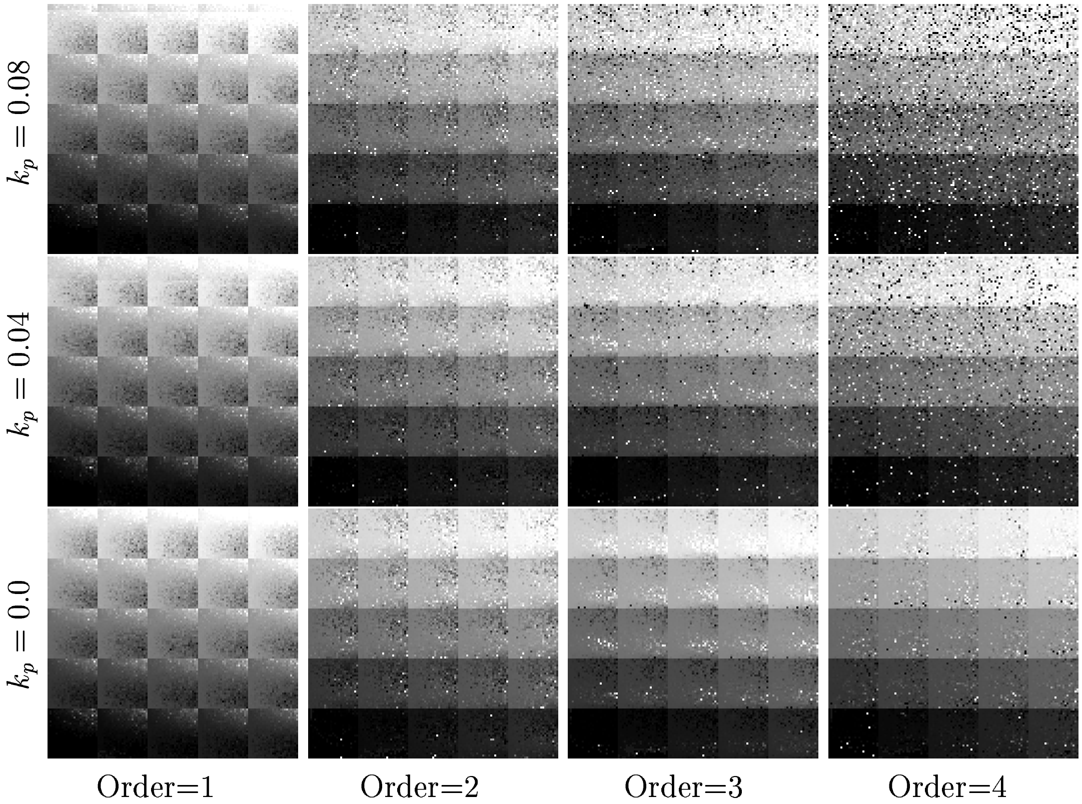

Figure 8.12: Inverse model η parameter estimates at various σ^o vs. θ model orders and noise levels.

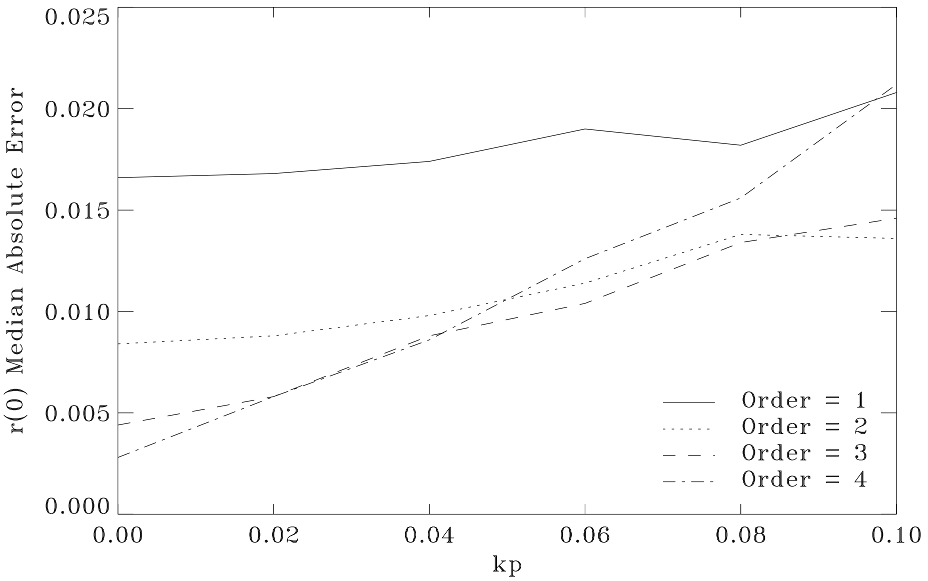

Figure 8.13: Median absolute error of $r(0)$ estimates as a function of measurement noise parameter k_p and model order.

estimate error is lower for higher order models in the absence of noise. However, as k_p rises, the second or third-order estimates have the lowest median absolute error. The curves also show that higher order models are increasingly sensitive to k_p, evident in steeper slopes in the error plots. The first-order model is relatively insensitive to k_p in all three figures since this model performs the most averaging. The results in Figures 8.13-8.15 indicate that the second or third order σ^o vs. θ polynomial coefficients provide the best inputs to the inverse model in the presence of noise. Since both offer similar error characteristics, the second order model is used with actual NSCAT data as presented in the following section.

8.6 Results

The inversion method is applied to second-order NSCAT reconstructed v-pol AVE imagery (A_v, B_v, and C_v) to study the behavior of the technique and to interpret phenomenon observed in the reconstruction σ^o images. First, the inversion

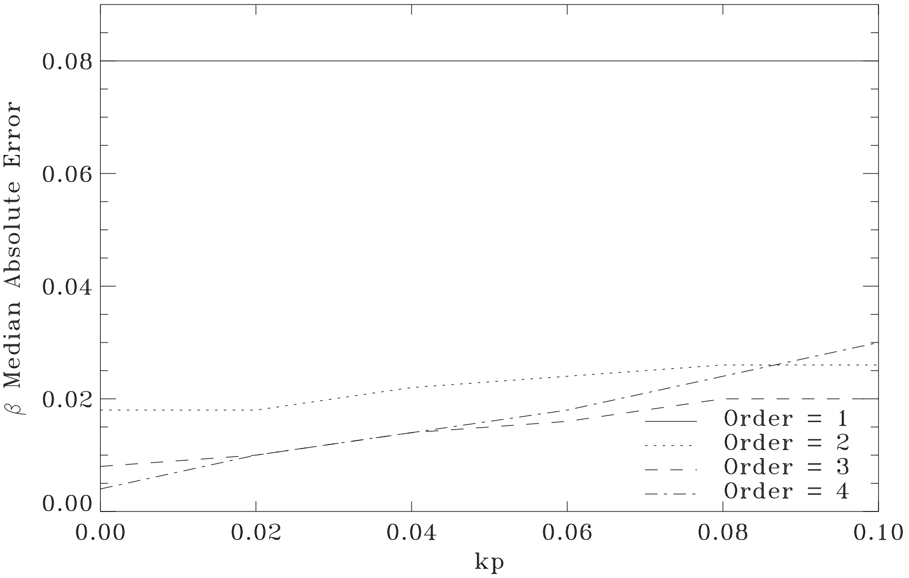

Figure 8.14: Median absolute error of β estimates as a function of measurement noise parameter k_p and model order.

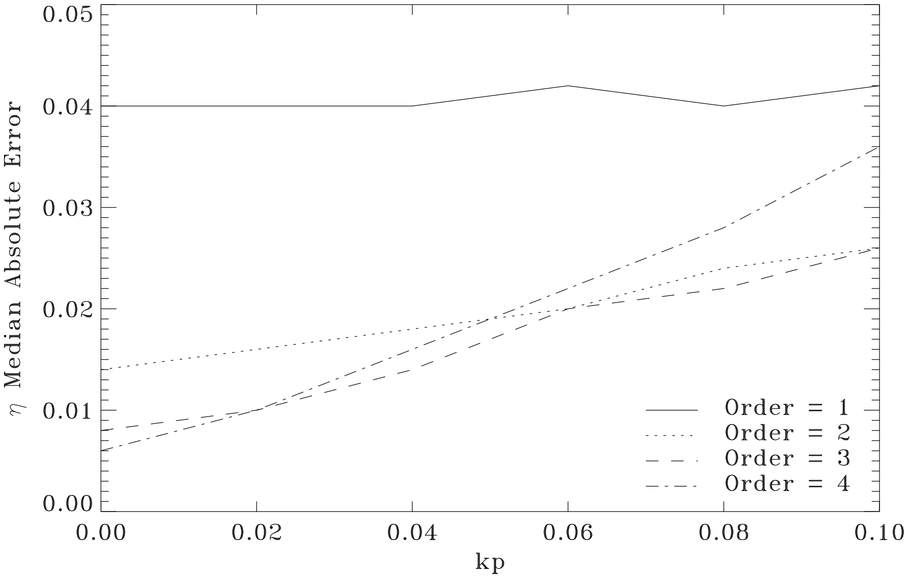

Figure 8.15: Median absolute error of η estimates as a function of measurement noise parameter k_p and model order.

is performed on Antarctic image sequences. Three six day Antarctic SIR images are shown in Figure 8.16. The images are ice masked using an NSCAT-derived ice edge algorithm [8]. The three frames each show significant σ^o detail within the ice pack. The goal of the inversion is to extract useful surface features from these variations and to provide maps of them. An interesting phenomenon illustrated in this image sequence is the "blooming" of σ^o values near the ice perimeter. That is, the A_v values increase significantly in a very short period of time in localized regions. An example is shown near the ice edge in the outer Weddell Sea. The A_v values in this region during the day 279-284 image are significantly higher than the previous two images. SSM/I radiometer brightness temperatures drop significantly in the bloom area. As described below, the inverse model is used to provide a physical interpretation of this phenomenon.

The inverse model is implemented for the Antarctic AVE image sets corresponding the images in Figure 8.16. Figure 8.17 shows the spatial distribution of $r(0)$ estimates for each time interval. Several large ice bergs with very high $r(0)$ are clearly observed in the images such as B10A in the lower-left quadrant of the image and several grounded ice bergs near the eastern limit of the Ronne Ice Shelf. First year ice dominates much of the Antarctic ice pack. These regions have typically low $r(0)$ levels compared with ice bergs and several regions near the ice edge. The Weddell Sea bloom is evident in increased $r(0)$ indicating an increase in the effective permitivitty in the area.

The Antarctic β estimate images are shown in Figure 8.18. The β estimates are visually more noisy than $r(0)$. Areas of very smooth first year ice have low β values in the images. One example is near the western edge of the Ronne ice shelf which is a region of new ice growth as older ice forms are drawn northward along the peninsula by the Weddell Gyre. The area surrounding the previously discussed grounded bergs have high β consistent with sea ice deformations caused as the ice pack collides with the bergs. The bloom area does not indicate any obvious change in this parameter.

The η parameter images are shown in Figure 8.19. The highest volume scattering albedo values are found in pixels covering ice bergs. Since ice bergs are

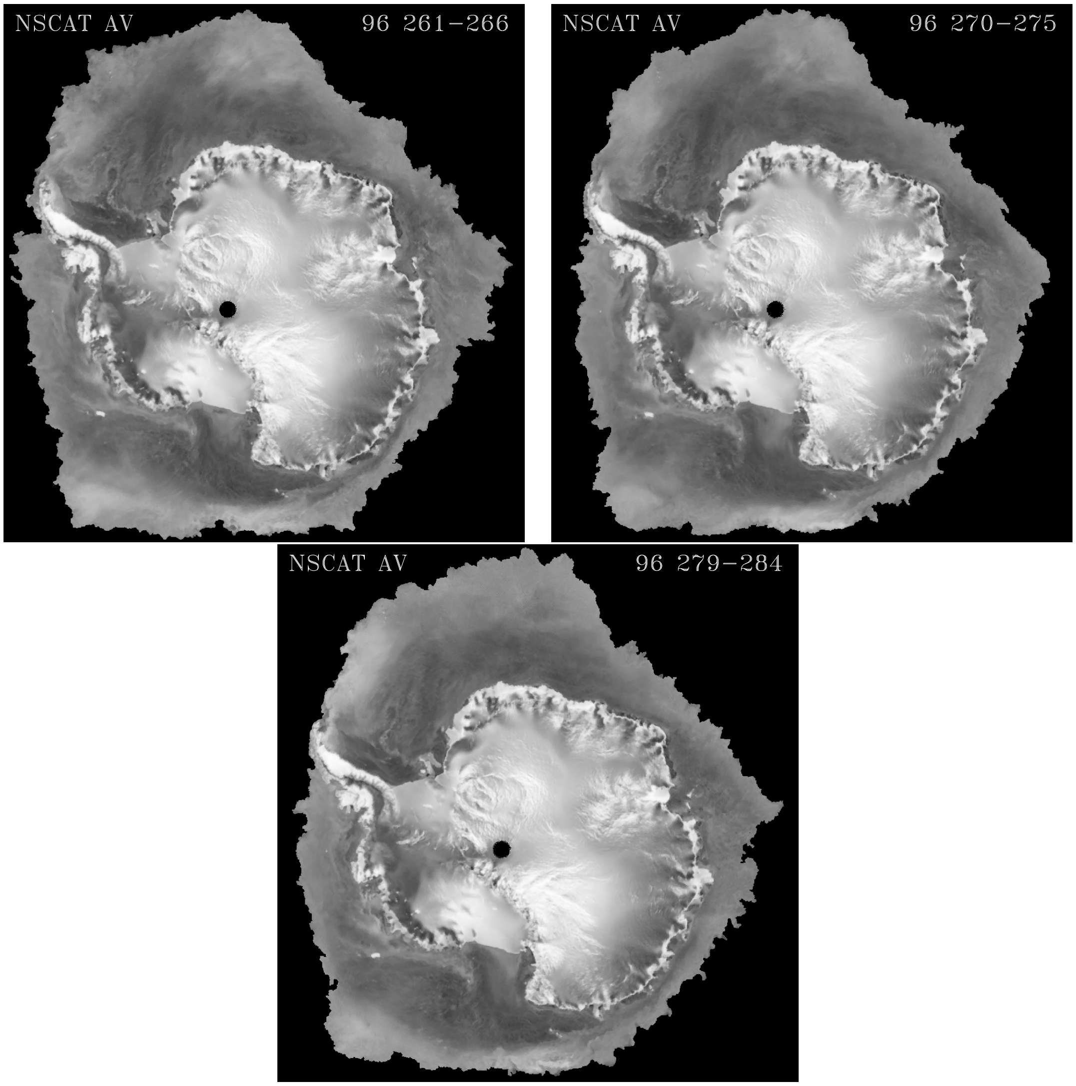

Figure 8.16: Ice masked NSCAT Antarctic A_v SIR image series.

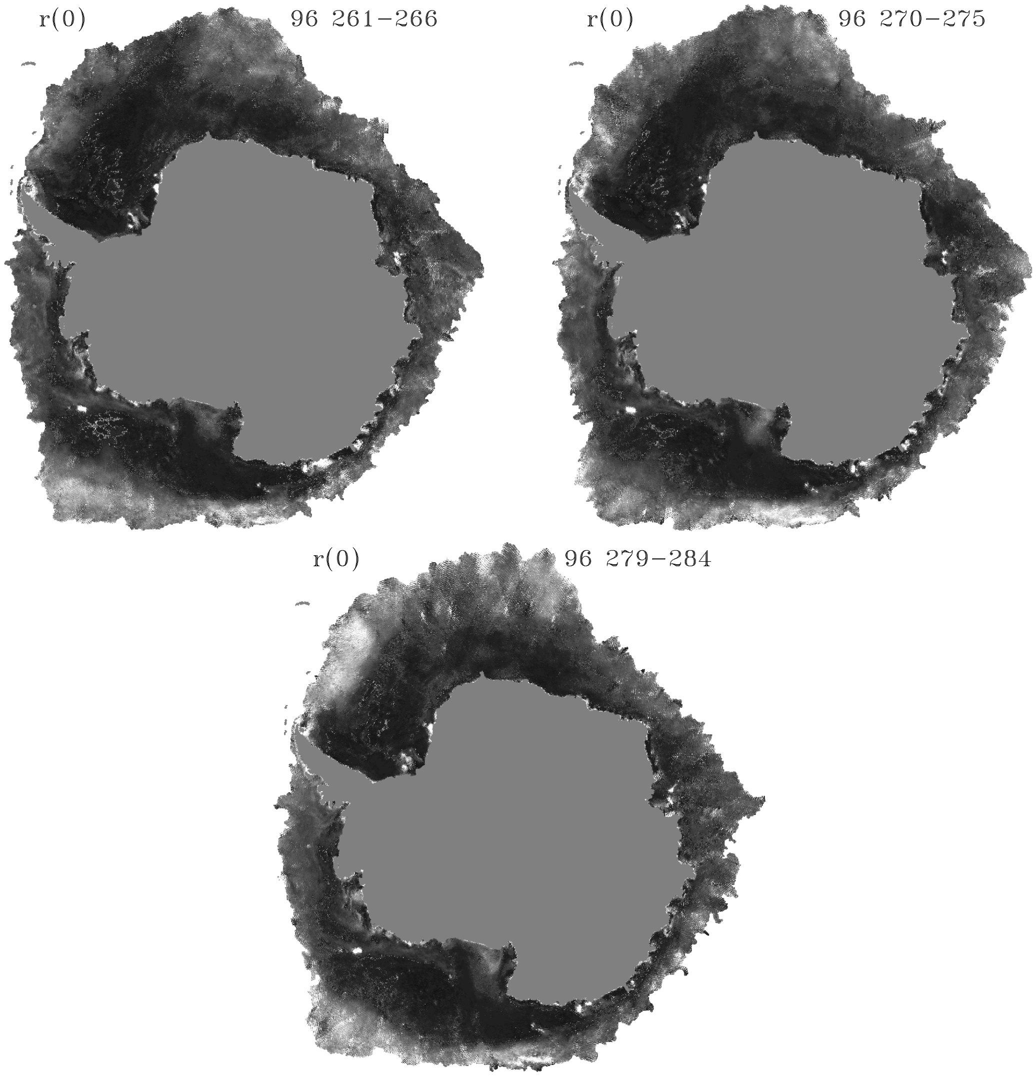

Figure 8.17: Inverse model estimates of Antarctic $r(0)$. The greyscale image display range is $r(0) \in [0,0.12]$.

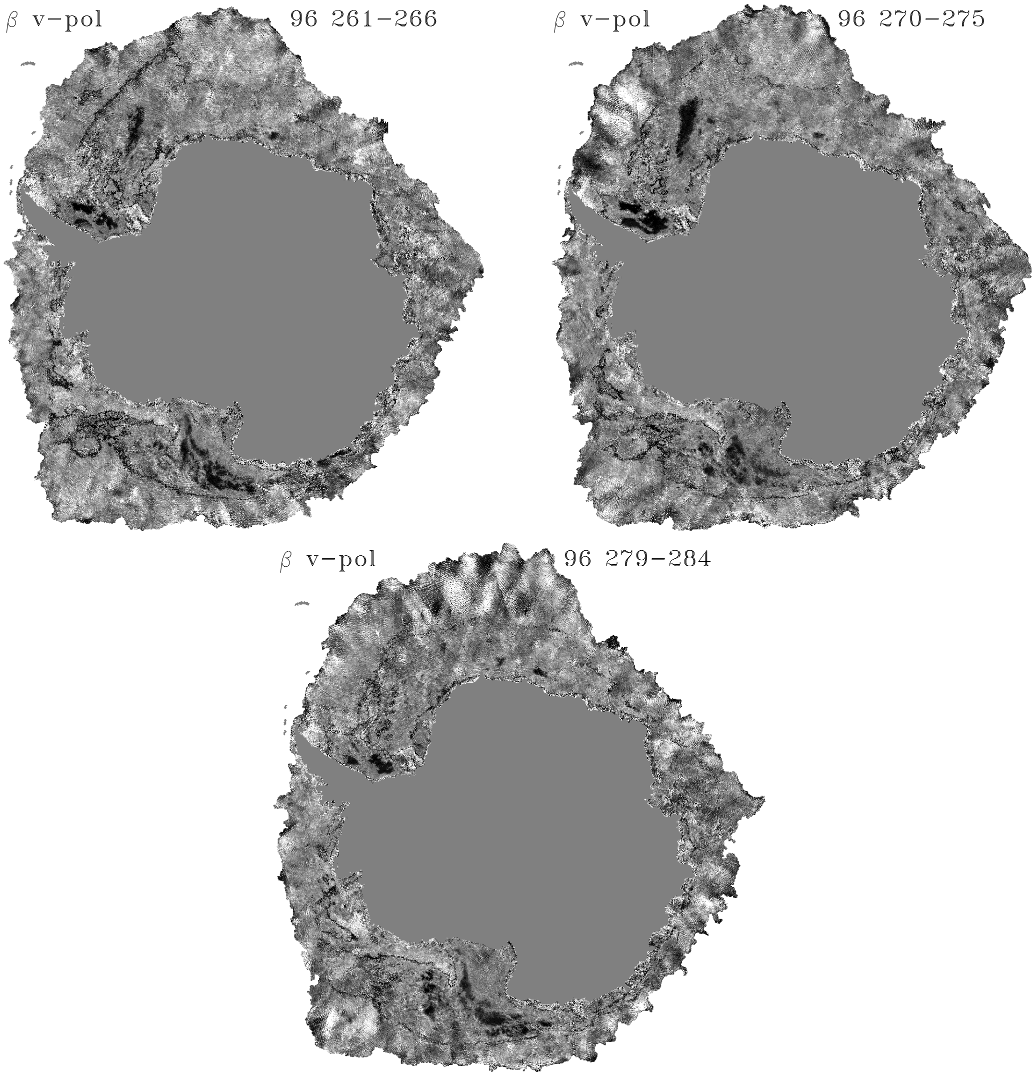

Figure 8.18: Inverse model estimates of Antarctic β. The greyscale image display range is $\beta \in [0.1, 0.4]$.

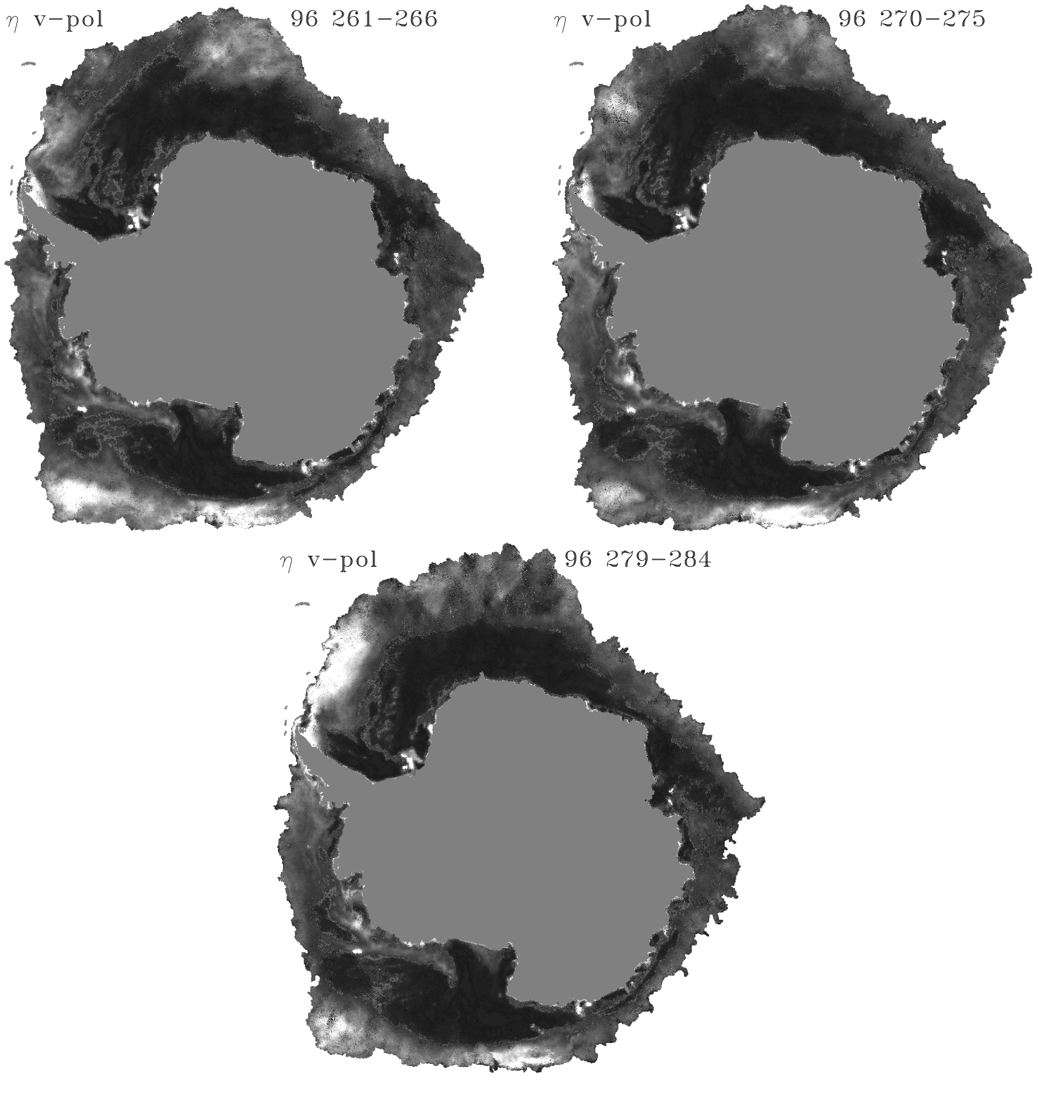

η v−pol 96 261−266

η v−pol 96 270−275

η v−pol 96 279−284

Figure 8.19: Inverse model estimates of Antarctic η. The greyscale image display range is $\eta \in [0,0.3]$.

composed of glacial ice, they have virtually no salinity and, thus, low loss. Microwave frequency pulses, therefore, are sensitive to scattering from subsurface inhomogeneities. A small region of multiyear ice near the tip of the peninsula also appears very bright in the image. A narrow stream of older deformed ice with medium η values is also evident running through the middle of the Weddell Sea parallel to the Ronne Ice Shelf. This line is created by the Weddell Gyre motion pulling ice debris away from the grounded ice bergs near the shelf. Much of the remaining ice pack, consisting primarily of various forms of first year ice, have low volume scattering albedo. The only exception to this are in various bloom regions. In the final image, the increased A_v in the Weddell bloom is accompanied by a sudden rise in η. A local refreezing event could cause the observed change in volume scattering.

These results can be compared with the ice type classifications of Chapter 6 as shown in Figure 8.20. This figure illustrates the ice classification for 1996 day 261-266 along with the corresponding estimates of the three model parameters. Correlation between ice type and the scattering parameters is observed. For example, PER ice has relatively high $r(0)$ and η values. High volume scattering albedo is expected for this ice class since PER ice has very low loss and hence, high volume scattering contributions. On the other hand, RFY and SFY ice types have much lower $r(0)$ and η values. While some correlation is observed in the β image compared to the RFY and SFY regimes, the β estimates are clearly noisier than $r(0)$ and η.

The distributions of $r(0)$, β, and η for each ice type are shown in Figures 8.21-8.23. These plots characterize typical parameters ranges that are observed for the various ice classes. Figure 8.21 illustrates that the IB and PER types exhibit a broad range of reflectivity. Of the remaining ice types, PNC has the highest $r(0)$ followed by MIZ, RFY, and SFY, respectively. In Figure 8.22, similar distributions are shown for β. IB and PER ice types have a large range of surface slopes. PNC and RFY ice are expected to exhibit higher surface roughnesses than SFY and MIZ. The PNC and RFY distributions are, in fact, shifted toward higher β though significant overlap is observed. The high variability of the β distributions indicate that the inverse model estimates contain more noise than the $r(0)$ and η estimates. Finally, Figure 8.23

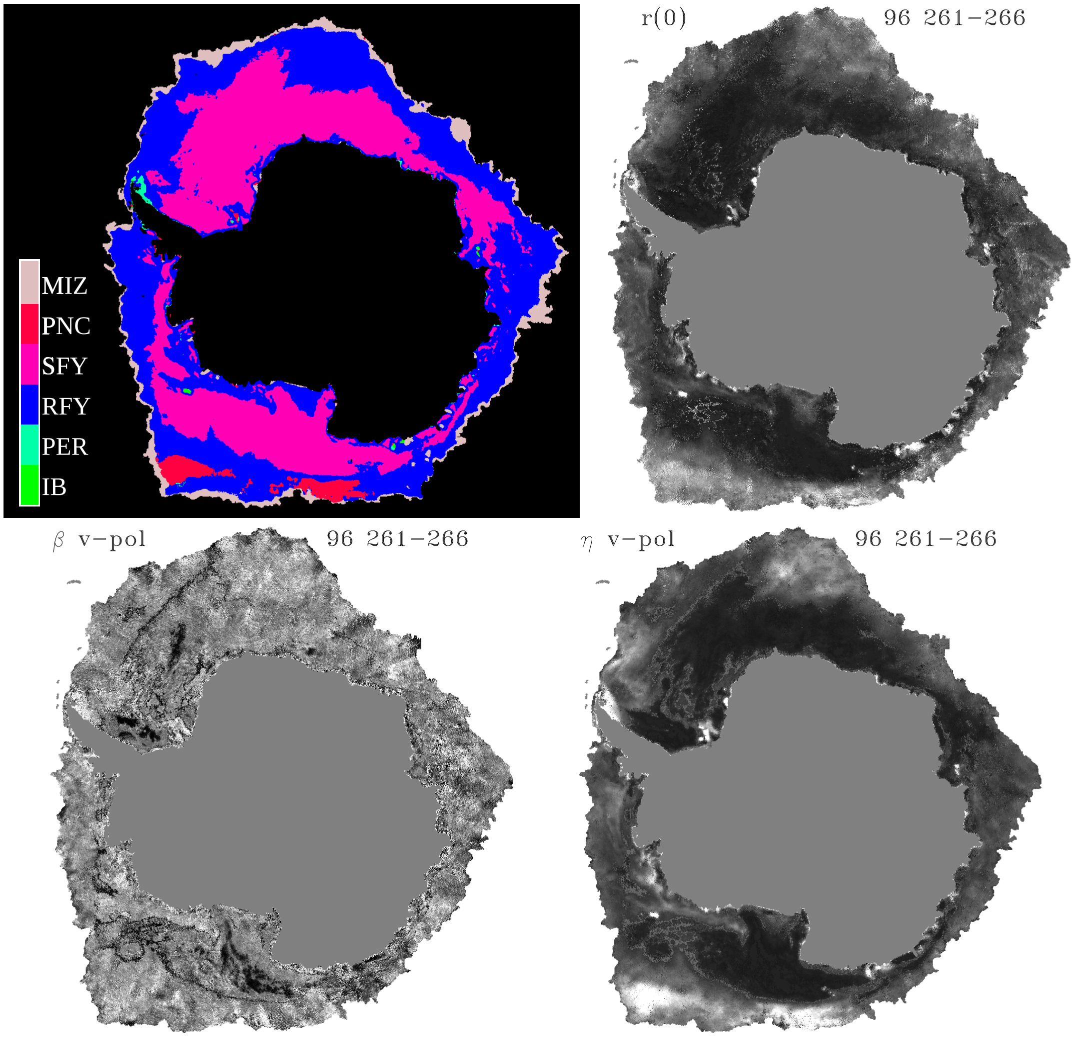

Figure 8.20: Comparison of a sample Antarctic ice classification image with the corresponding surface parameter estimates (1996 day 261-266).

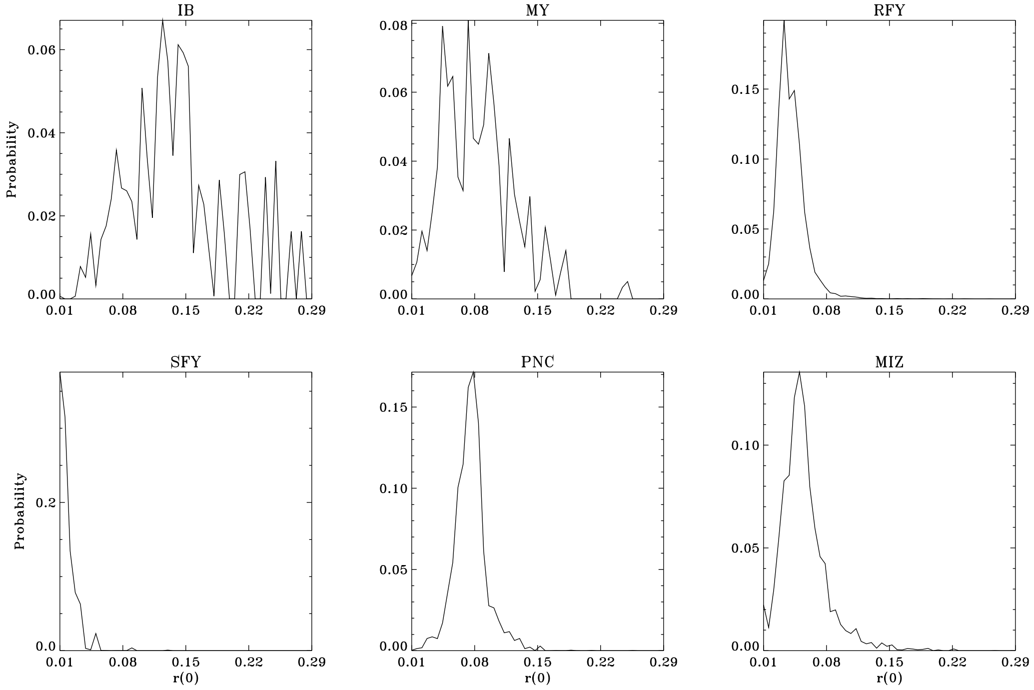

Figure 8.21: Normalized histograms of $r(0)$ for each ice type in the 1996 day 261-266 ice type classification.

shows the distributions of volume scattering albedo, η, for each classified ice type. The plots demonstrate that IB and PER ice have higher η values as expected. These types have very low loss resulting in greater volume scattering contributions to the observed signatures. Ice classes with greater loss (due to increased salinity and water content) such as RFY, SFY, and MIZ have much lower η values.

The inversion method is also applied to Arctic data. A four AVE image set series representing the onset of Arctic summer is used as inverse model inputs. The ice masked image series is illustrated in Figure 8.24. The Arctic ice pack is characterized by large regions of multiyear ice exhibiting high A_v values near the centers of the images. Younger forms of ice have lower A_v signatures. The phenomenon examined in this sequence is the annual drop in σ^o observations due to the passage of warm fronts over the ice pack inducing significant surface melting. While the first few images have very high multiyear σ^o signatures differentiating this ice type from lower σ^o first

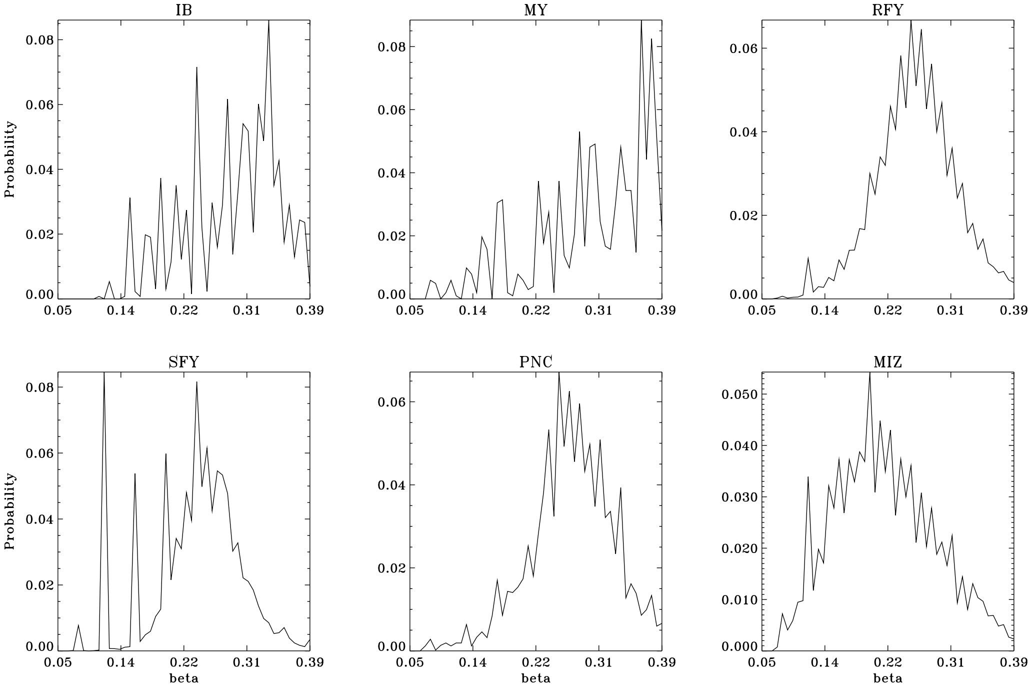

Figure 8.22: Normalized histograms of η for each ice type in the 1996 day 261-266 ice type classification.

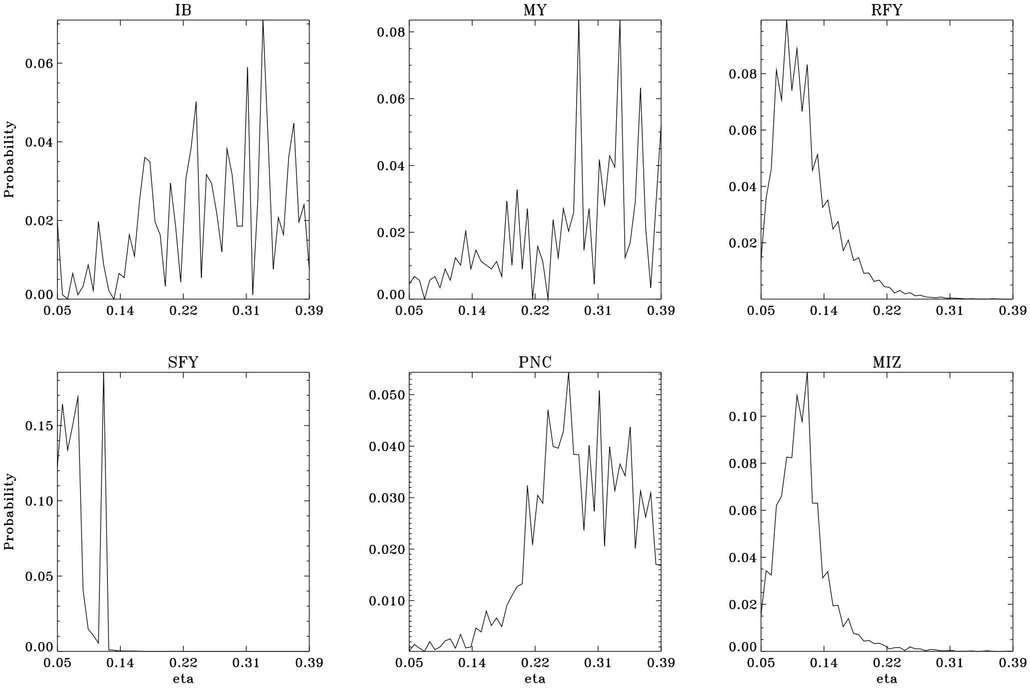

Figure 8.23: Normalized histograms of β for each ice type in the 1996 day 261-266 ice type classification.

year ice, by the end of the image sequence the two types are virtually indistiguishable.

Figure 8.25 contains the image estimates of Arctic $r(0)$. The noisy values near the pole are due to insufficient incidence angle sampling caused by satellite orbit geometry and the NSCAT measurement collection configuration. Unsatisfactory sampling of the incidence angle spectrum results in poor estimates of polynomial fit coefficients in the image reconstruction. Consequently, very low confidence is placed on the near-pole parameter estimates. The general trend in the $r(0)$ imagery consists of relatively high and low values for multiyear and first year sea ice, respectively. The melt event causes $r(0)$ to drop quickly over the entire multiyear area.

The distribution of β surface roughness values are shown in Figure 8.26. Multiyear ice has typically high β levels in contrast to lower observations over first year ice. Newer ice forms are typically less deformed than old ice that has been subjected to wave deformation, ice pack sheering, and large-scale roughness caused by melt/refreeze cycles. As the sequence progresses, β values drop until nearly the entire multiyear region appears similar to the first year β observations. The source of the change may be due to surface smoothing of features due to melting and the creation of melt ponds.

The estimate images of Arctic volume scattering albedo η is shown in Figure 8.27. These images illustrate the intense volume scattering contributions characteristic of multiyear ice. Varying levels of η within multiyear regions can be related to the number density of volume scatterers and mean volume scattering element cross sections. Areas of younger ice have much lower η due to higher salinity and dielectric loss. The image progression shows η decreasing as temperature rises and surface melting occurs. In the last image frame, volume scattering has been almost completely masked by increased water content which reduces penetration depth. Such signature masking makes the various ice types competely indistiguishable at Ku-band.

These results illustrate the utility of the inverse model in interpretting the sources of scattering phenomena observed in reconstructed NSCAT imagery. Since the model inversion method is fully automated, large ensembles of measurements

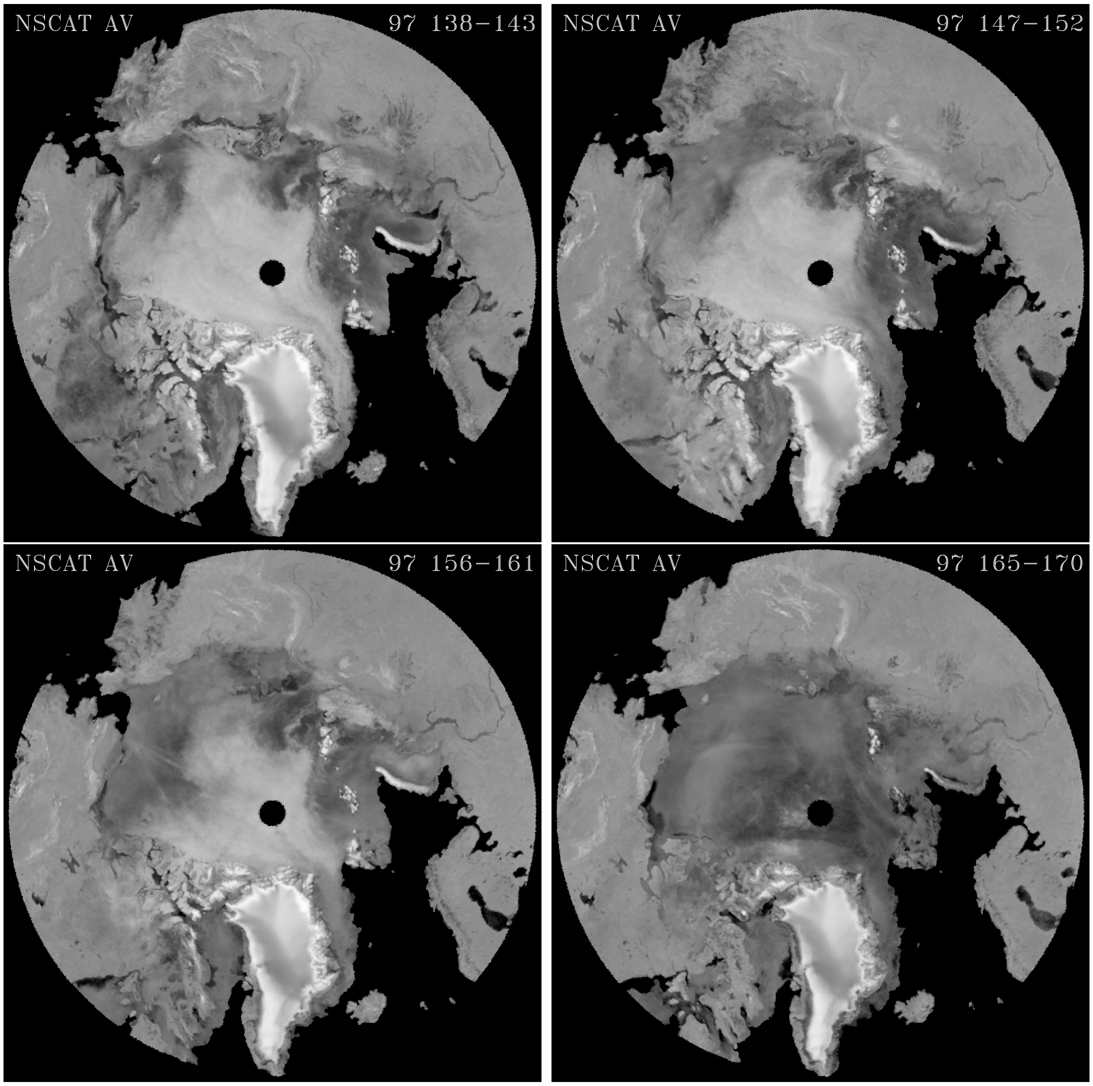

Figure 8.24: Ice masked NSCAT Arctic A_v SIR image series.

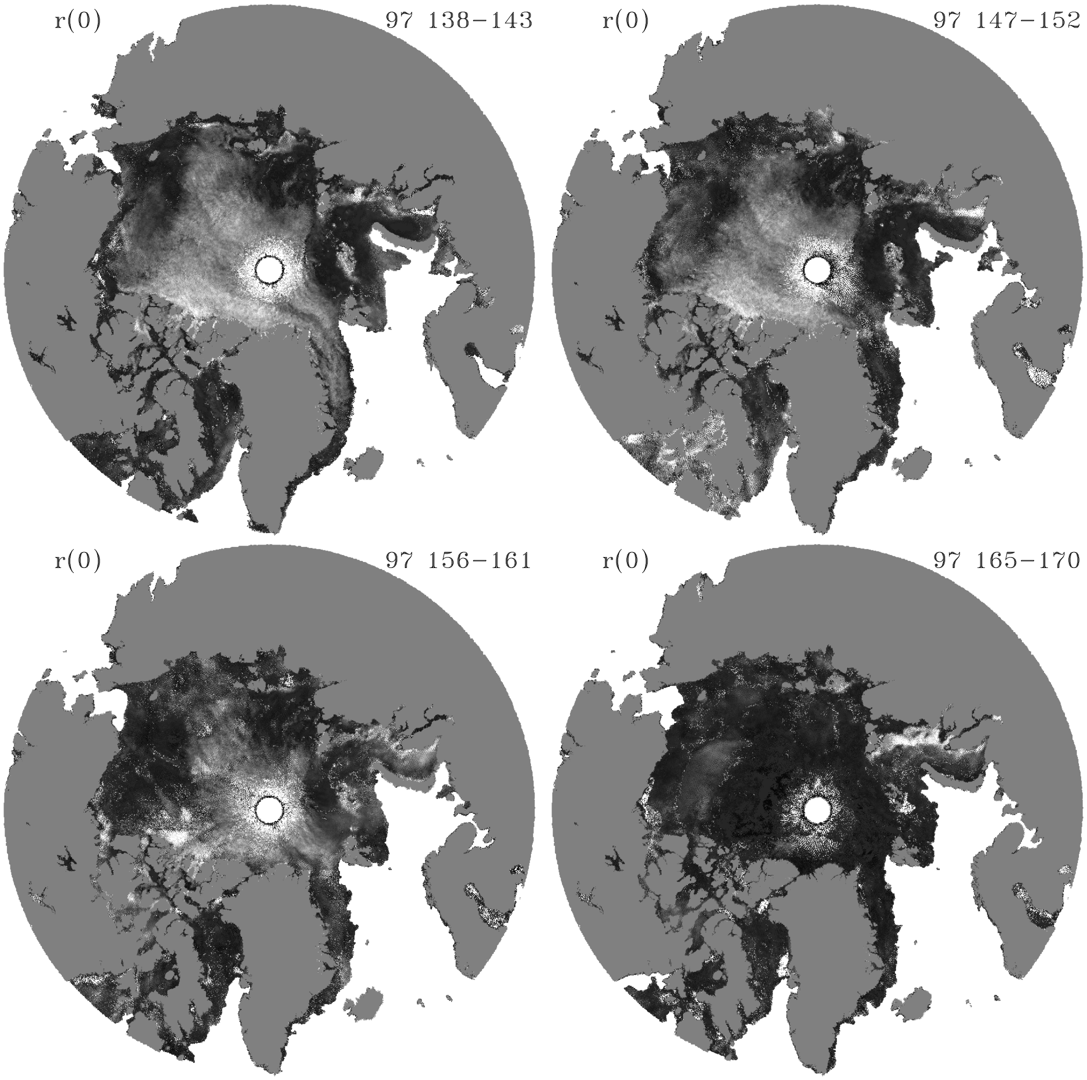

Figure 8.25: Inverse model estimates of Arctic $r(0)$. The greyscale image display range is $r(0)\in[0,0.1]$.

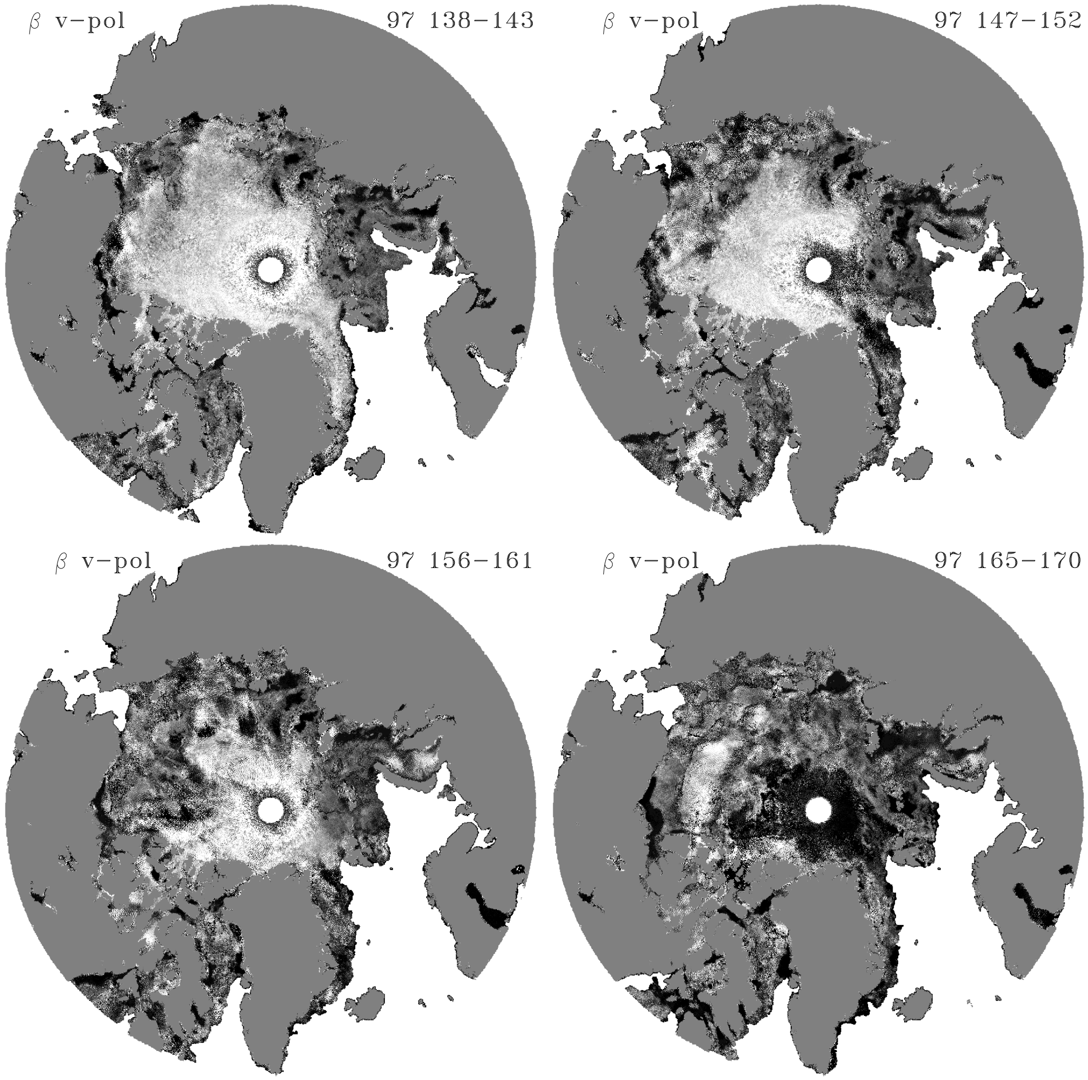

Figure 8.26: Inverse model estimates of Arctic β. The greyscale image display range is $\beta\in[0.1,0.45]$.

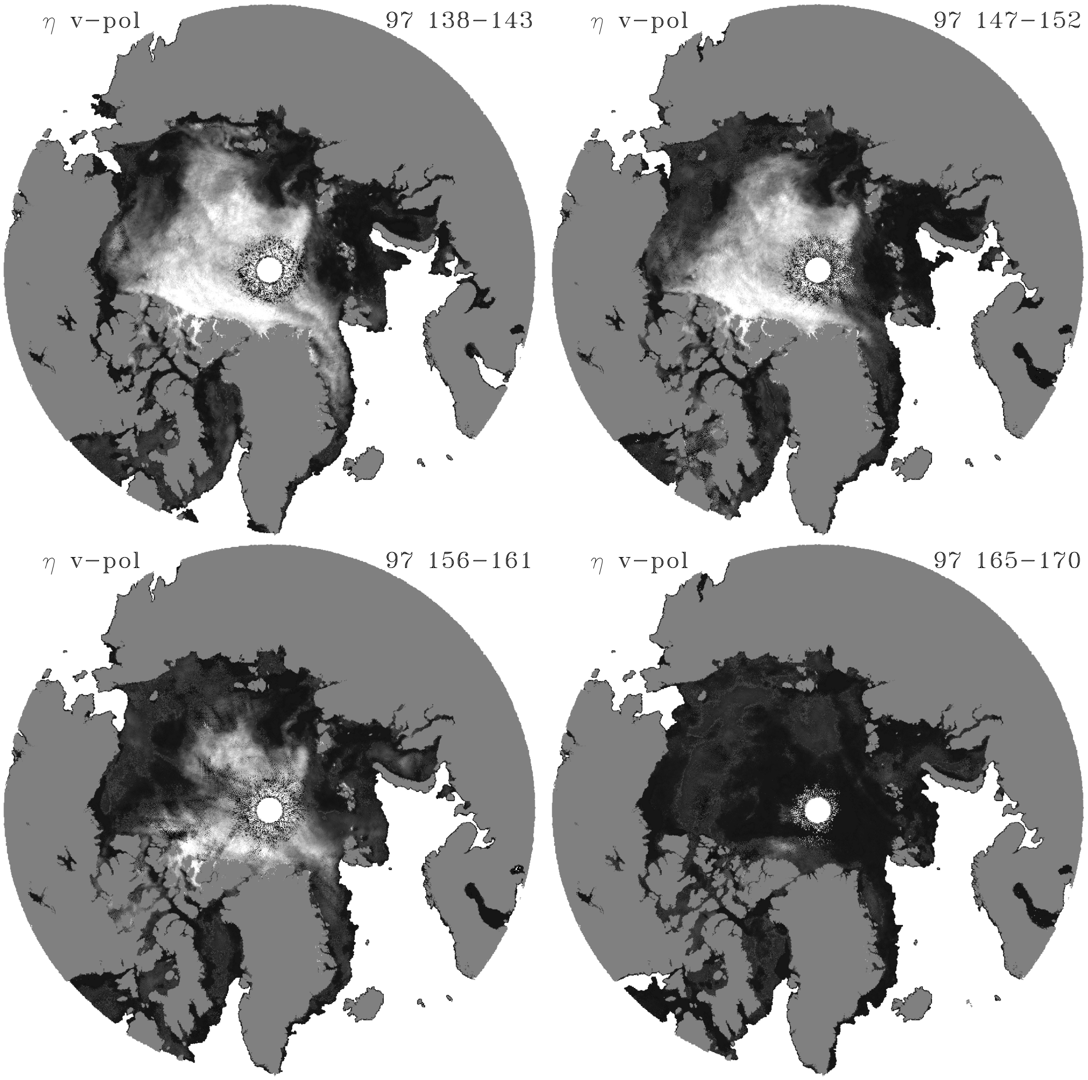

Figure 8.27: Inverse model estimates of Arctic η. The greyscale image display range is $\eta \in [0, 0.45]$.

can be inverted providing estimates of the spatial distribution and magnitude of important surface parameters. These parameters can then be related to sea ice types as previously described. In general, older ice types such as multiyear ice exhibit very high $r(0)$ and η values in the absence of significant surface melt. In contrast, first year ice and other relatively young ice types have much lower $r(0)$ and η. Smoother ice types have typically lower β levels. Temporal variations in the parameters can be used to understand the evolution of scattering mechanisms within the various ice types as considered in this section.

8.7 Conclusions

This study has presented an inversion technique applied to a simple, but robust forward scattering model. The method is fully automated requiring no user interface. Consequently, large scatterometer polynomial fit coefficient images representing the incidence angle dependence of σ^o can be used as inputs to the inverse model. The algorithm is used to determine the spatial distribution of three important surface parameters, the power reflection coefficient at nadir, $r(0)$, the RMS surface slope, S (represented by $\beta = 2S^2$ in the inverse model), and the volume scattering albedo, η.

Simulations of the method demonstrate the capability of the algorithm. Higher order incidence angle dependence models yield better estimates of the surface parameters in the absence of noise. When noise is introduced, a trade-off exists between the capability to estimate a wide range of possible parameter combinations and sensitivity to noise. The first order model performs reasonably well for $r(0)$ and η estimation but cannot effectively reproduce true β values. A good balance is found in using a second order model.

The inverse model is applied to NSCAT Antarctic and Arctic image sequences. The results show that the parameter images have consistent spatial distributions. The image products are used to interpret σ^o "blooming" phenomena in the Antarctic. An increase in $r(0)$ and η is observed in the bloom regions with little change in β. The method is also used to analyze drastic σ^o decreases over multiyear ice in the Arctic as the summer season begins. The accompanying surface melt causes all three parameters to decrease abruptly. Surface roughness appears to be reduced and increased water content masks the volume scattering contribution that give multiyear ice its characteristically high σ^o signature.

The results of this study demonstrate the utility of one technique in inverting simple forward scattering models for sea ice surfaces. Validation data of surface roughness parameters, dielectric properties, and volume scattering element characteristics are needed to accurately measure the algorithm's effectiveness. Regardless, the method aids in the interpretation of important polar geophysical phenomena.

Chapter 9

Conclusion

Microwave remote sensing is a valuable tool in monitoring many critical surface characteristics and geophysical processes in the earth's cryosphere. The preceding chapters described several studies which address critical issues in this relatively young field. Following a brief background of the history of polar remote sensing, various image reconstruction issues were considered such as the optimization of SIRF for NSCAT, azimuthal modulation of Ku-band scatterometer data over Antarctic sea ice, and inter-sensor calibration for the ERS scatterometers. These studies ensure the quality image reconstruction required before enhanced resolution imagery can be applied to studies of surface characteristics and geophysical processes.

In the next chapter, methods were developed to reduce the adverse effects of atmospheric distortion in reconstructed radiometer imagery. A hybrid technique was derived which provides quality estimates of the true surface response in the presence or absence of cloud cover and precipitation. Though developed in tropical regions, the techniques can be used in cryosphere studies as well. The technique enables the filtered imagery to be used with greater confidence in studies of surface brightness temperatures.

In Chapter 5, the automated mapping of sea ice extent from NSCAT data was addressed. An adaptive algorithm was derived which identifies the ice edge using only NSCAT data. The resulting ice edges correlate well with the SSM/I-derived NASA-Team algorithm 30% ice extents. The ice masked imagery was also validated using high resolution Radarsat SAR imagery in the Arctic which showed high levels of correlation between the SeaWinds and actual ice edges.

The next chapter considered the large-scale identification of sea ice types within the Antarctic ice pack using multisensor NSCAT, ERS-2, and SSM/I imagery. Maximum likelihood and *maximum a posteriori* recursive statistical methods were proposed and implemented. The MAP algorithm was found to perform the best and was shown to be functionally equivalent to a modified k-means clustering technique. The resulting ice type maps are consistent with general sea ice dynamics and the results of previous investigators.

The application of the ice extent and ice classification methods to more current data sets containing SeaWinds imagery was discussed in Chapter 7. Due to significant differences in the NSCAT and SeaWinds instruments, multiple modifications are required in the sea ice extent algorithm for application to SeaWinds. Like the NSCAT products, the SeaWinds-derived edges correlate well with NASA-Team estimates. For the ice classification, it was found that the SeaWinds-SSM/I combination had slightly less ability in segmenting imagery into ice types.

Finally, Chapter 8 discussed the theory and development of large-scale inverse modeling. A simple forward scattering model was inverted using an automated steepest descent approach to estimate surface and volume scattering parameters. Images of these parameters were then used to determine the sources of various polar σ^o phenomenon observed in reconstructed NSCAT imagery.

9.1 Contributions

Several significant contributions have been made to the remote sensing community through the work presented in this dissertation. The following sections briefly summarize each of the major contributions of this dissertation. Much of this work has already appeared in journal papers prepared as part of this research.

9.1.1 Image Reconstruction

Enhanced resolution image reconstruction of microwave scatterometer and radiometer measurements has great utility in a number of land and ice research studies. However, several steps must be taken to ensure the integrity of the data in order to facilitate their application in analyses of surface characteristics. Chapter 3 addressed several of the critical issues such as

1. The optimization of SIRF for NSCAT data,
2. Ku-band azimuthal modulation of σ^o over Antarctic ice,
3. Inter-instrument calibration for ERS-1 and ERS-2.

The results can be used to ensure the proper generation and interpretation of enhanced resolution microwave imagery.

9.1.2 Atmospheric Distortion Removal

An important issue in the reconstruction of microwave imagery is measurement distortion effects caused by cloud cover and precipitation. In Chapter 4, methods were developed and presented which reduce the corrupting effects of these phenomena in radiometer imagery. The resulting hybrid technique ensures that the best possible brightness temperature estimates are obtained in cloudy or clear scenarios. The approach is particularly useful when applied to higher frequency microwave radiometer measurements which exhibit high sensitivity to atmospheric distortions. Consequently, the method greatly increases the utility of these data in studies of surface characteristics. This work was published in the *IEEE Transactions on Geoscience and Remote Sensing* [7].

9.1.3 Sea Ice Extent Mapping

An important contribution of this dissertation is the development and analysis of a sea ice extent estimation algorithm for NSCAT σ^o data. The method is fully automated and adapts to the temporal variations of sea ice and ocean microwave responses. The algorithm is also adapted to work for SeaWinds scatterometer imagery allowing for current and future studies of polar sea ice extent. The operational technique is currently being used by the Jet Propulsion Laboratory in their near-real time wind processing and by the National Ice Center for sea ice evolution studies. This research was published in the *Journal of Geophysical Research* [8]. A manuscript on the SeaWinds adaptation of the algorithm has been submitted to the same journal and is currently in review [80].

9.1.4 Multisensor Sea Ice Classification

While several studies have pursued the classification of sea ice on small-scales with single instruments such as synthetic aperture radars, relatively few have addressed this problem on large-scales using multiple sensors. However, in Chapter 6 the theory, development, and implementation of a recursive statistical classifier is discussed. The method combines several active and passive microwave instruments to determine the spatial distribution of sea ice in the Antarctic sea ice pack. The adaptive nature of the algorithm allows it to adjust to seasonally varying microwave signatures of various ice types. The ice classification research has been accepted for publication in the *IEEE Transactions on Geoscience and Remote Sensing* [9].

9.1.5 Large-scale Backscatter Inverse Modeling

The primary focus of many electromagnetic inverse modeling studies has been on determining scattering mechanisms from small homogeneous regions. Unfortunately, spaceborne scatterometer footprints usually cover very heterogeneous mixes of scattering features. In an effort to address this problem, an inverse modeling approach was developed and analyzed in Chapter 8. The method is used to invert a simple, but robust forward scattering model which parameterizes the observed scattering using three large-scale surface and volume scattering metrics. Through the automated optimization of an objective function, the inverse model is able to generate imagery of these scattering parameters for use in the study of large-scale geophysical characteristics as shown in Chapter 8. This work has been submitted to the *Journal of Geophysical Research* and is in review.

9.2 Future Research

This dissertation has developed a number of useful cryosphere techniques. Various lines of research represent natural extensions to the work presented. These are briefly discussed in the following sections.

9.2.1 Atmospheric Distortion Studies

Chapter 4 discussed the removal of atmospheric distortion effects in passive microwave radiometer observations of vegetated land areas. These regions were chosen since they exhibit significant corruptions due to water vapor and hydrometeors. A natural extension to this work is a study of the application of the proposed methods in glacial ice regions and with different sensors.

9.2.2 Ice Extent Mapping Extensions

In Chapter 5, the utility of an NSCAT-derived sea ice extent mapping technique is demonstrated. As discussed in the chapter, researchers have also developed methods for identifying sea ice extent using passive radiometers such as the SSM/I though at a lower resolution. Both the active and passive sea ice edge estimates have their individual weaknesses. For example, the scatterometer ice extents may encounter problems in areas of sustained high winds near the ice edge. SSM/I extents have been shown to underestimate the ice edge during the ice ablation phase. A promising line of research may be to use sensor fusion to combine enhanced resolution scatterometer and radiometer data to produce daily estimates of sea ice extent. It is anticipated that the iterative techniques used in the NSCAT and SeaWinds methods can be extended to higher dimension data sets containing both active and passive observations of the polar regions and produce higher fidelity ice extent estimates.

9.2.3 Sea Ice Classification

The results of Chapter 6 demonstrate the ability of the described approach in correctly identifying various general sea ice types in Antarctica. Several lines of research can be followed to refine this work. The first involves further investigation of the fuzzy classification concepts introduced in Chapter 7. A fundamental requirement is the availability of *in situ* measurements of sea ice type concentrations. With this information, MAP probabilities can be related to concentration. Hence, the percentage of each constituent ice type can be estimated for image pixels enhancing the ability to understand sea ice type formation and evolution.

Another promising line of research is the use of data from future instruments in polar ice classification. In Chapter 7, it was found that the SeaWinds-SSM/I combination yielded moderately good results in segmenting the ice pack into ice types. However, limitations were evident due to the exclusion of several important parameters. Thus, current and future sensors must be identified that can provide high confidence estimates of sea ice type distribution. One such potential combination is found on a single satellite platform, ADEOS-II. This satellite will carry another SeaWinds scatterometer as well as the Advanced Microwave Scanning Radiometer (AMSR). The SeaWinds-AMSR combination has great potential in sea ice classification. For example, AMSR will be a dual-polarization radiometer observing T_B at 6.9, 10.7, 18.7, 36.5, and 89 GHz. The broad spectrum of observations increases the ability of AMSR to detect subsurface scattering mechanisms which distinguish several sea ice types. In addition, since SeaWinds and AMSR will be aboard the same platform, σ^o and T_B measurements will be coregistered in time as well as space. Hence, differences due to transient effects and diurnal variations will be eliminated.

Another extension to the ice classification research is long-term analysis of the sea ice algorithm's behavior. Since the sea ice signatures are only well defined during Antarctic winter, only a very limited portion of the NSCAT data set could be used in ice classification. Current and future instruments that observed scattering and emission properties of the sea ice over many years can be used to monitor the evolution of sea ice type signatures.

9.2.4 Large-scale Inverse Modeling

The large-scale backscatter inverse modeling study described in Chapter 8 represents a first step in determining sea ice parameters over very large image fields.

While the method showed great utility in interpreting various observed cryosphere phenomena, more validation is needed. In particular, *in situ* measurements of sea ice permittivity, roughness, and volume scattering element characteristics are needed to quantify the quality of the inverse model estimates. Also, validation data may facilitate the relation of the parameters which can be estimated from the current technique to other important sea ice characteristics such as ice age, thickness, and type. Such a relationship enables the indirect estimation of these parameters as well. While the inversion method was applied to a relatively simple forward electromagnetic scattering model, the concepts can be extended to more complex models.

Bibliography

[1] W.F. Budd, "Antarctic sea ice variations from satellite sensing in relation to climate," *IEEE Trans. on Geosci. and Rem. Sens.*, vol. 15, pp. 417–426, 1975.

[2] D. Long and M. Drinkwater, "Greenland Ice-Sheet Surface Properties Observed by the Seasat-A Scatterometer at Enhanced Resolution", *Journal of Glaciology*, vol. 40, no. 135, pp. 213–230, 1994.

[3] F.D. Carsey, Ed., *Microwave Remote Sensing of Sea Ice,* Washington, D.C.: American Geophysical Union, 1992.

[4] D.G. Long and M.R. Drinkwater, "Cryosphere Applications of NSCAT Data," *IEEE Trans. on Geosci. and Rem. Sens.*, vol. 37, no. 3, pp. 1671–1684, 1999.

[5] Q.P. Remund and D.G. Long, "Optimization of SIRF for NSCAT," *MERS Tech. Rep. 97-03*, 37 pp., BYU Microwave Earth Remote Sensing Lab., Provo, UT, 1997.

[6] Q.P. Remund, D.S. Early, and D.G. Long, "Azimuthal Modulation of Ku-Band Scatterometer σ^o Over the Antarctic," *MERS Tech. Rep. 97-02*, 24 pp., BYU Microwave Earth Remote Sensing Lab., Provo, UT, 1997.

[7] D.G. Long, Q.P. Remund, and D.L. Daum, "A Cloud-Removal Algorithm for SSM/I Data," *IEEE Trans. on Geosci. and Rem. Sens.*, vol. 37, no. 1, pp. 54–62, 1999.

[8] Q. Remund and D. Long, "Sea-Ice Extent Mapping Using Ku-Band Scatterometer Data," *J. of Geophys. Res*, vol. 104, no. C4, pp. 11515-11527, 1999.

[9] Q.P. Remund and D.G. Long, "An Iterative Approach to Multisensor Sea Ice Classification," *in press, IEEE Trans. on Geosci. and Rem. Sens.*, vol. 38, no. 4, July 2000.

[10] D. G. Long and P. J. Hardin, "Vegetation Studies of the Amazon Basin Using Enhanced Resolution Seasat Scatterometer Data", *IEEE Transactions on Geoscience and Remote Sensing*, vol. 32, pp. 449–460, 1994.

[11] A. R. Hosseinmostafa, V. I. Lytle, K. C. Jezek, S. P. Gogineni, S. F. Ackley, and R. K. Moore, "Comparison of Radar Backscatter from Antarctic and Arctic Sea Ice", *Journal of Electromagnetic Waves and Applications*, vol. 9, no. 3, pp. 421–438, 1995.

[12] F.T. Ulaby, R.K. Moore, and A.K. Fung, *Microwave Remote Sensing – Active and Passive*, Vol. 2, Norwood, MA: Artech House Inc., 1983.

[13] W.L. Grantham, E.M. Bracalente, W.L. Jones, and J.W. Johnson, "Seasat-A Satellite Scatterometer," *IEEE J. of Oceanic Eng.,* vol. OE-2, no. 2, pp. 200-206, Apr. 1977.

[14] M.R. Drinkwater, and D.G. Long, "Seasat, ERS-1/2 and NSCAT Scatterometer Observed Changes on the Large Ice Sheets," *Proc. IGARSS '98*, vol. 4, pp. 2252–2254, Seattle, Washington, July 6-10, 1998.

[15] M.R. Drinkwater and F.D. Carsey, "Observations of the late-summer to fall transition with the 14.6 GHz SEASAT scatterometer," *Proc. IGARSS '91 Symposium,* vol. 3, pp. 1597-1600, Espoo, Finland, June 3-6, 1991.

[16] C.P. Winebrenner, D.G. Long, and B. Holt, "Mapping the Progression of Melt Onset and Freeze-Up on Arctic Sea Ice Using SAR and Scatterometry," in *Analysis of SAR Data of the Polar Oceans,* C. Tsatsoulis and R. Kwok, Eds. Berlin: Springer, 1998, pp. 129-144.

[17] E. Attema, "The Active Microwave Instrument Onboard the ERS-1 Satellite," *Proceedings of the IEEE*, vol. 79, no. 6, pp. 791–799, 1991.

[18] F. Gohin, and A. Cavanie, "A first try at identification of sea ice using the three beam scatterometer of ERS-1," *Int. J. Remote Sensing,* vol. 15, no. 6, pp. 1221-1228, 1994.

[19] F. Gohin, "Some active and passive microwave signatures of Antarctic sea ice from mid-winter to spring 1991," *Int. J. Remote Sensing,* vol. 16, no. 11, pp. 2031–2054, 1995.

[20] M. Drinkwater, D. Long, and D. Early, "Enhanced Resolution ERS-1 Scatterometer Imaging of Southern Ocean Sea Ice", *ESA Journal*, vol. 17, pp. 307–322, 1993.

[21] P. Lecomte, A. Cavanie, and F. Gohin, "Recognition of Sea Ice Zones using ERS-1 Scatterometer Data", in *Proceedings of IGARSS 93.* IEEE, 1993, pp. 855–857.

[22] L. Ulander, A. Carlstrom, and J. Askne, "Effect of Frost Flowers, rough saline snow and slush on the ERS-1 SAR Backscatter Signatures of Thin Arctic Sea Ice," *Int. J. Remote Sens.,* vol. 16, no. 17, pp. 3287–3305, 1995.

[23] F.M. Naderi, M.H. Freilich, and D.G. Long, "Spaceborne Radar Measurement of Wind Velocity Over the Ocean–An Overview of the NSCAT Scatterometer System," *Proceedings of the IEEE*, vol. 79, no. 6, pp. 850–866, June 1991.

[24] D.S. Early and D.G. Long, "Image Reconstruction and Enhanced Resolution Imaging from Irregular Samples," in press, *IEEE Trans. on Geosci. and Rem. Sens.,* 2000.

[25] S.H. Yueh, R. Kwok, S. Lou, and W. Tsai, "Sea Ice Identification Using Dual-Polarized Ku-Band Scatterometer Data," *IEEE Trans. on Geosci. and Rem. Sens.,* vol. 35, no. 3, pp. 560–569, 1997.

[26] M.R. Drinkwater and X. Liu, "Observing Interannual Variability in Sea-Ice Dynamics using NSCAT," *Proceedings of NSCAT Science Team Workshop,* Honolulu, Hawaii, 23-24 Jan., 1997, JPL Tech. Pub., Jet Propulsion Laboratory, 4800 Oak Grove Drive, Pasadena, CA 91109, 1997.

[27] M.W. Spencer, C. Wu, D.G. Long, "Tradeoffs in the Design of a Spaceborne Scanning Pencil Beam Scatterometer: Applications to SeaWinds," *IEEE Trans. on Geosci. and Rem. Sens.,* vol. 35, no. 1, pp. 115–126, 1997.

[28] R. Massom, *Satellite Remote Sensing of Polar Regions,* 307 pp., Belhaven Press, London, 1991.

[29] F.T. Ulaby, R.K. Moore, and A.K. Fung, *Microwave Remote Sensing – Active and Passive*, Vol. 1, Norwood, MA: Artech House Inc., 1981.

[30] H. Zwally, J. Comiso, C. Parkinson, W. Campbell, F. Carsey, and P. Gloersen, "Antarctic sea ice, 1973-1976: satellite passive-microwave observations," *NASA Report SP-459,* NASA, Washington, D.C., 1983.

[31] D.J. Cavalieri, P. Gloersen, and W.J. Campbell, "Determination of sea ice parameters with the Nimbus-7 SMMR," *J. of Geophys. Res.,* vol. 89 no. D4, pp. 5355–5369, 1984.

[32] J. Comiso, "Sea ice effective microwave emissivities from satellite passive microwave and infrared observations," *J. of Geophys. Res.,* vol. 88, no. 7, pp 686-704, 1983.

[33] J.P. Hollinger, J.L. Pierce, and G.A. Poe, "SSM/I Instrument Evaluation," *IEEE Trans. Geosci. Remote Sensing*, Vol. 28, No. 5, pp. 781-790, Sept. 1990.

[34] J. Hollinger, "DMSP Special Sensor Microwave/Imager Calibration/Validation, Final Report, Volume 1," Naval Research Laboratory, Washington, D.C., July 1989.

[35] J. Hollinger *et al.*, "Special Sensor Microwave/Imager User's Guide," Naval Research Laboratory, Washington, D.C., Dec. 14, 1987.

[36] D.J. Cavalieri, J.P. Crawford, M.R. Drinkwater, D.T. Eppler, L.D. Farmer, R.R. Jentz, and E.C. Wackerman, "Aircraft active and passive microwave validation of sea ice concentration from the Defense Meteorological Satellite Program Special Sensor Microwave Imager," *J. of Geophys. Res.,* vol. 96 no. C12, pp. 21989–22008, 1991.

[37] M.R. Farrar and E.A. Smith, "Spatial Resolution Enhancement of Terrestrial Features Using Deconvolved SSM/I Brightness Temperatures," *IEEE Trans. Geosci. Remote Sensing*, Vol. 30, no. 2, pp 349-355, March 1992.

[38] D.G. Long and D.L. Daum, "Spatial Enhancement of SSM/I Data," *IEEE Trans. Geosci. Remote Sens.*, vol. 36, pp. 407–417, 1997.

[39] D. Long, P. Hardin, and P. Whiting, "Resolution Enhancement of Spaceborne Scatterometer Data", *IEEE Transactions on Geoscience and Remote Sensing*, vol. 31, pp. 700–715, 1993.

[40] Q.P. Remund and D.G. Long, "Validation of the SIRF Resolution Enhancement Algorithm for Scatterometer Data Using SAR Imagery," *Proc. IGARSS '98,* vol. 2, pp. 1309–1311, Hamburg, Germany, June 28 - July 2, 1999.

[41] Y. Censor, "Finite Series-Expansion Reconstruction Methods," *Proceedings of the IEEE*, Vol. 71, No. 3, pp. 409-419, Mar. 1983.

[42] F. Remy, Ledroit, and J. F. Minster, "Katabatic Wind Intensity and Direction over Antarctica Derived from Scatterometer Data", *Geophysical Research Letters*, vol. 19, pp. 1021–1024, 1992.

[43] D.G. Long and M.R. Drinkwater, "Azimuth Variation in Microwave Scatterometer and Radiometer Data over Antarctica," in press *IEEE Transactions on Geosci. and Rem. Sens.,* vol. 38, no. 4, July, 2000.

[44] J. Comiso, T. Grenfell, M. Lange, A. Lohanick, R. Moore, and P. Wadhams, "Microwave Remote Sensing of the Southern Ocean Ice Cover", in *Microwave Remote Sensing of Sea Ice*, F. D. Carsey, Ed., chapter 12. American Geophysical Union, Boston, 1992.

[45] M. A. Lange, S. F. Ackley, P. Wadhams, G. S. Diekmann, and H. Eicken, "Development of Sea Ice in the Weddell Sea", *Annals of Glaciology*, , no. 12, pp. 92–96, 1991.

[46] M.R. Drinkwater and C. Haas "1994, Snow, Sea-ice and Radar Observations during ANT X/4: Summary Data Report," *AWI Berichte aus dem Fachbereich Physik*, 53, Alfred Wegener Institut fr Polar- and Meeresforschung, July 1994, 58pp.

[47] A. K. Liu and S. Häkkinen, "Wave Effects on Ocean-Ice Interaction in the Marginal Ice Zone", *Journal of Geophysical Research*, vol. 98, no. C6, pp. 10025–10036, 1993.

[48] T.J. Jackson and T.J. Schmugge, "Algorithm for the Passive Microwave Remote Sensing of Soil Moisture," in *Microwave Radiometry and Remote Sensing Applications* (P. Pampaloni, ed.), (Zeist), pp. 3-17, VSP, 1989.

[49] P. Pampaloni and S. Paloscia, "Microwave Emission and Plant Water Content: A Comparison Between Field Measurement and Theory," *IEEE Trans. Geosci. Remote Sensing*, Vol. 24, pp. 900-904, November 1986.

[50] M.J. McFarland, R.L. Miller, and C.M.U. Neale, "Land Surface Temperature Derived From the SSM/I Passive Microwave Brightness Temperatures," *IEEE Trans. Geosci. Remote Sensing*, Vol. 28, pp. 839-845, September 1990.

[51] A.S. Jones and T.H.V. Haar, "Passive Microwave Sensing of Cloud Liquid Water Over Land Regions," *Journal of Geophysical Research*, Vol. 95, pp. 16673-16683, September 1990.

[52] N.C. Grody, "Classification of Snow Cover and Precipitation Using the Special Sensor Microwave/Imager," *Journal of Geophysical Research*, Vol. 94, pp. 7423-7435, April 1991.

[53] R.H. Thomas, R.A. Bindschadler, R.L. Cameron, F.D. Carsey, B.Holt, T.J. Hughes, C.W.M. Swithinbank, I.M. Whillans, and H.J. Zwally, "Satellite Remote Sensing for Ice Sheet Research," *NASA Technical Memorandum*, 86233, 27, 1985.

[54] B. Choudhury and C. Tucker, "Satellite Observed Seasonal and Inter-Annual Variation of Vegetation Over the Kalahari, The Great Victoria Desert, and The Great Sandy Desert: 1979-1984," *Remote Sensing of Environment*, Vol. 23, pp. 233-241, 1987.

[55] R.W. Spencer, H.M. Goodman, and R.E. Hood, "Precipitation Retrieval over Land and Ocean with the SSM/I: Identification and Characteristics of the Scattering Signal," *Journal of Atmospheric and Oceanic Technology*, Vol. 6, pp. 254-273, April 1989.

[56] C.M.U. Neale, M.J. McFarland, and K. Chang, "Land-Surface-Type Classification Using Microwave Brightness Temperatures From the Special Sensor Microwave/Imager," *IEEE Trans. Geosci. Remote Sensing*, Vol. 28, pp. 829-838, September 1990.

[57] S.D. Prince and B.J. Choudhury, "Interpretation of Nimbus-7 37 GHz Microwave Brightness Temperature in Semi-arid Southern Africa," *International Journal of Remote Sensing*, Vol. 10, no. 10, pp. 1643-1661, 1989.

[58] J.D. Gibbons, *Nonparametric Statistical Inference*, 2nd Ed. New York, NY: Marcel Dekker, 1985.

[59] A.K. Jain, *Fundamentals of Digital Image Processing*, Englewood Cliffs, NJ: Prentice-Hall, 1989.

[60] P.M. Narenda, "A Separable Median Filter for Image Noise Smoothing," *IEEE Transactions on Pattern Analysis and Machine Intelligence*, Vol. 3, pp. 20-29, January 1981.

[61] M.R. Drinkwater, "Active Microwave Remote Sensing Observations of Weddell Sea Ice," in *Antarctic Sea Ice: Physical Processes, Interactions and Variability, Antarctic Research Series* M.O. Jeffries, Ed. Washington, D.C.: American Geophysical Union, 1998, pp. 187–212.

[62] J.W. Rouse, "Arctic Ice Type Identification by Radar," *Proceedings of the IEEE,* vol. 57, no. 4, pp. 605–611, 1969.

[63] D.S. Early and D.G. Long, "Azimuthal Modulation of C-Band Scatterometer σ^o over Southern Ocean Sea Ice," *IEEE Trans. on Geosci. and Rem. Sens.*, vol. 35, no. 5, pp. 1201-1209, 1997.

[64] R.O. Duda and P.E. Hart, *Pattern Classification and Scene Analysis,* John Wiley and Sons, New York, New York, 1973.

[65] J.C. Rush, *The Image Processing Handbook, 2nd Ed.*, 674 pp., CRC Press, Boca Raton, Florida, 1995.

[66] F.M. Fetterer, M.R. Drinkwater, K.C. Jezek, S.W.C. Laxon, R.G. Onstott, L.M.H. Ulander, Sea Ice Altimetry, in *Microwave Remote Sensing of Sea Ice,* edited by F.D. Carsey, pp. 111–135, AGU, Washington, D.C., 1992.

[67] P. Gloersen, W.J. Campbell, D.J. Cavalieri, J.C. Comiso, C.L. Parkinson, H.J. Zwally, *Arctic and Antarctic Sea Ice, 1978-1987: Satellite Passive-Microwave Observations and Analysis,* 290 pp., Scientific and Technical Information Program, National Aeronautics and Space Administration, Washington, D.C., 1992.

[68] D.T. Eppler, L.D. Farmer, A.W. Lohanick, and M. Hoover, "Classification of Sea Ice Types With Single-Band (33.6 GHz) Airborne Passive Microwave Imagery," *J. of Geophys. Res.*, vol. 91, no. C9, pp. 10,611–10,694, 1986.

[69] R. Kwok, E. Rignot, B. Holt, and R. Onstott, "Identification of Sea Ice Types in Spaceborne Synthetic Aperture Radar Data," *J. of Geophys. Res.*, vol. 97, no. C2, pp. 2391–2402, 1992.

[70] E. Rignot and M.R. Drinkwater, "Winter Sea-Ice Mapping from Multi-parameter Synthetic-Aperture Radar Data," *J. of Glaciology*, vol. 40, no. 134, pp. 31-45, 1994.

[71] H. Hra, R.G. Atkins, R.T. Shin, J.A. Kong, S.H. Yueh, and R. Kwok, "Application of Neural Networks for Sea Ice Classification in Polarimetric SAR Images," *IEEE Trans. on Geosci. and Rem. Sens.*, vol. 33, no. 3, pp. 740–748, May 1995.

[72] M. Wensnahan, G.A. Maykut, and T.C. Grenfell, "Passive Microwave Remote Sensing of Thin Sea Ice Using Principle Component Analysis," *J. of Geophys. Res.*, vol. 98, no. C7, pp. 12,453–12,467, 1993.

[73] M. Drinkwater, "Satellite Microwave Radar Observations of Antarctic Sea Ice," in *Analysis of SAR Data of the Polar Oceans*, C. Tsatsoulis and R. Kwok, Eds. Berlin: Springer-Verlag, 1998, pp. 145-188.

[74] M. Golden, D. Borup, M. Cheney, E. Cherkaeva, M.S. Dawson, K. Ding, A.K. Fung, D. Isaacson, S.A. Johnson, A.K. Jordan, J.A. Kong, R. Kwok, S.V. Nghiem, R.G. Onstott, J.Sylvester, D.P. Winebrenner, and I.H.H. Zabel. "Inverse Electromagnetic Scattering Models for Sea Ice," *IEEE Trans. on Geosci. and Rem. Sens.*, vol. 36, no. 5, pp. 1675–1704, 1998.

[75] W.J. Krzanowski, *Principles of Multivariate Analysis: A User's Perspective,* Claredon Press, Oxford, England, 1988.

[76] C.T. Haas and H. Eicken, "Sea Ice Conditions during the Winter Weddell Gyre Study 1992 ANT X/4 with R/V Polarstern: Shipboard Observations and AVHRR imagery," *AWI Berichte aus dem Fachbereich Physik*, 34, Alfred Wegener Institut fr Polar- and Meeresforschung, Dec. 1992.

[77] N.W. Young, "Antarctic Iceberg Drift and Ocean Currents Derived from Scatterometer Image Series," *ESA SP-424*, pp 125–132, Nov. 1998.

[78] M. Drinkwater and G. Crocker "Modelling changes in the dielectric and scattering properties of young snow-covered sea ice at GHz frequencies," *J. of Glaciology,* vol. 34, no. 118, pp. 274–282, 1988.

[79] W.K. Pratt, *Digital Image Processing, 2nd Ed.*, John Wiley and Sons, New York, NY, 1991.

[80] Q.P. Remund and D.G. Long, "Iterative Mapping of Polar Sea Ice Using Ku-band SeaWinds Scatterometer Data," in review*J. of Geophys. Res.,* 2000.

[81] F. Carsey, "Review and status of remote sensing of sea ice," *IEEE Journal of Oceanic Engineering,* vo. 14, pp. 127-137, 1989.

[82] J.K. Lee, and J.A. Kong, "Active Microwave Remote Sensing of an Anisotropic Random Medium Layer," *IEEE Trans. on Geosci. and Rem. Sens.*, vol. GE-23, no. 6, pp. 910–923, 1985.

[83] S. Tjuatja, A.K. Fung, J. Bredow, "A Scattering Model for Snow-Covered Sea Ice," *IEEE Trans. on Geosci. and Rem. Sens.,* vol. 30, no. 4, pp. 804–810, 1992.

[84] S.V. Nghiem, R. Kwok, S.H. Yueh, and M.R. Drinkwater, "Polarimetric signatures of sea ice, Theoretical model," *J. of Geophysical Research,'* vol. 190, no. C7, pp. 13665–13679, 1995.

[85] F.T. Ulaby, R.K. Moore, and A.K. Fung, *Microwave Remote Sensing – Active and Passive*, Vol. 3, Norwood, MA: Artech House Inc., 1985.

[86] C.T. Swift, "Seasat Scatterometer Observations of Sea Ice," *IEEE Trans. on Geosci. and Rem. Sens.,* vol. 37, no. 2, pp. 716-723, Mar. 1999.

[87] C.T. Swift, P.E. Hayes, J.S. Herd, W.L. Jones, and V.E. Delnore, "Airborne microwave measurements of the sourthern Greenland ice sheet," *J. Geophys, Res.,* vol. 90, no. B2, pp. 1983-1994, Feb. 1985.

[88] D.E. Barrick, "Rough Surfaces," in *Radar Cross-Section Handbook,* G.T. Ruck, Ed. New York: Plenum, 1970, pp. 671-772.

[89] M.R. Vant, R.O. Ramseier, and V. Makois, "The Complex Dielectric Constant of Sea Ice at Frequencies in the Range 0.1-40 GHz," *J. of Applied Physics,* v. 49, pp. 1264-1280, 1978.